https://doi.org/10.15388/vu.thesis.70
https://orcid.org/0000-0003-0475-788X

VILNIUS UNIVERSITY
CENTER FOR PHYSICAL SCIENCES AND TECHNOLOGY

Matas
JANULEVIČIUS

Engineering of Lanthanide Orthophosphate Functional Nanomaterials

DOCTORAL DISSERTATION

Natural sciences,
Chemistry N 003

VILNIUS 2020

This dissertation was written between 2015 and 2019 at Vilnius University
The research was supported from the EU Structural funds.

Academic supervisor – Prof. Dr. Artūras Katelnikovas (Vilnius University, Natural sciences, Chemistry, N 003).

This doctoral dissertation will be defended in a public meeting of the Dissertation Defence Panel:
Chairman – Prof. Habil. Dr. Rimantas Ramanauskas (Center for Physical Sciences and Technology, Natural sciences, Chemistry, N 003).
Members:
Prof. Dr. Rasa Pauliukaitė (Center for Physical Sciences and Technology, Natural sciences, Chemistry, N 003);
Prof. Dr. Almira Ramanavičienė (Vilnius University, Natural sciences, Chemistry, N 003)
Dr. Vladimir Sivakov (Leibniz Institute of Photonic Technology, Natural sciences, Chemistry, N 003);
Assoc. Prof. Dr. Linas Vilčiauskas (Center for Physical Sciences and Technology, Natural sciences, Chemistry, N 003).

The dissertation shall be defended at a public meeting of the Dissertation Defence Panel at 2 p.m. on 11 September 2020 at Auditorium of Inorganic Chemistry at the Faculty of Chemistry and Geosciences of Vilnius University.

Address: Naugarduko street, 24, LT-03225, Vilnius, Lithuania
Tel. +370 5 2193105; e-mail: info@chgf.vu.lt

The text of this dissertation can be accessed at the libraries of Vilnius University and Center for Physical Sciences and Technology, as well as on the website of Vilnius University: www.vu.lt/lt/naujienos/ivykiu-kalendorius

https://doi.org/10.15388/vu.thesis.70
https://orcid.org/0000-0003-0475-788X

VILNIAUS UNIVERSITETAS
FIZINIŲ IR TECHNOLOGIJOS MOKSLŲ CENTRAS

Matas
JANULEVIČIUS

Lantanoidų ortofosfatų funkcinių nanomedžiagų inžinerija

DAKTARO DISERTACIJA

Gamtos mokslai,
Chemija N 003

VILNIUS 2020

Disertacija rengta 2015 – 2019 metais Vilniaus universitete.
Moksliniai tyrimai remti ES struktūrinių fondų lėšomis.

Mokslinis vadovas – prof. dr. Artūras Katelnikovas (Vilniaus universitetas, gamtos mokslai, chemija – N 003).

Gynimo taryba:
Pirmininkas – **prof. habil. dr. Rimantas Ramanauskas** (Fizinių ir technologijos mokslų centras, gamtos mokslai, chemija – N 003).
Nariai:
prof. dr. Rasa Pauliukaitė (Fizinių ir technologijos mokslų centras, gamtos mokslai, chemija – N 003);
prof. dr. Almira Ramanavičienė (Vilniaus universitetas, gamtos mokslai, chemija – N 003);
dr. Vladimir Sivakov (Leibnico Fotoninių technologijų institutas, gamtos mokslai, chemija – N 003);
doc. dr. Linas Vilčiauskas (Fizinių ir technologijos mokslų centras, gamtos mokslai, chemija – N 003).

Disertacija ginama viešame Gynimo tarybos posėdyje 2020 m. rugsėjo mėn. 11 d. 14 val. Vilniaus universiteto Chemijos ir geomokslų fakulteto Neorganinės chemijos auditorijoje. Adresas: Naugardukog. 24, LT-03225, Vilnius, Lietuva tel. +37052193108 ; el. paštas info@chgf.vu.lt.

Disertaciją galima peržiūrėti Vilniaus universiteto bei Fizinių ir technologijos mokslų centro bibliotekose ir VU interneto svetainėje adresu: *https://www.vu.lt/naujienos/ivykiu-kalendorius*

CONTENTS

LIST OF ABBREVATIONS

CTAB	Cetrimonium bromide
CTB	Charge-transfer band
DC	Downconversion
DLVO	Derjaguin, Landau, Vervey, and Overbeek theory
DOTA	Dodecane tetraacetic acid
DOX	Doxorubicin
DS	Downshifting
DTPA	Diethylenetriaminepentaacetic acid
EG	Ethylene glycol
EPR	Enhanced permeability and retention
ET	Energy-transfer
LED	Light emitting diode
MEMA	2-methoxyethyl methacrylate
MRI	Magnetic resonance imaging
PCL	Polycaprolactone
PEG	Polyethylene glycol
PEO	Polyethylene oxide
PLA	Polylactic acid
PLGA	Poly(lactic-co-glycolic) acid
PMAM	Polymethacrylamide
PMMA	Poly(methyl methacrylate)
PPAm	Phenyl-polyacrylamide
PVA	Poly(vinyl alcohol)
PVP	Polyvinylpyrrolidone
RGB	Red, green, blue
SERS	Surface-enhanced Raman spectroscopy
UV/VIS	Ultraviolet/Visible

1. INTRODUCTION

Nanomaterial science is unquestionably one of the most important directions in modern science. Investigation and development of various luminescent inorganic nanomaterials holds a significant part of this field. Material scientists have spent years in engineering various nanomaterials and nanostructures to study new unique chemical and physical properties, which emerge when material size is downgraded to nanoscale. Besides, not only the size but shape as well may be responsible for some unique parameters of the materials [1, 2]. Particularly, inorganic nanomaterials based on lanthanides (such as lanthanide fluorides, lanthanide oxides, lanthanide phosphates) have high expectations due to their large applicability range and potential multifunctionality emerging from their outstanding properties [3, 4].

For the last two or three decades, lanthanide based materials and ceramics were forefront materials responsible for many high-tech advancements such as LED technologies, laser development, magnetic compounds and so on. Even though synthesis and investigation of new lanthanide bulk materials remains important, development of lanthanide based nanoparticles is introduced as new trending field in material science [5]. It is known that nanoparticles and nanostructures can possess different or even enhanced properties apart from their equivalent bulk materials. A good example is a decrease of luminescence efficiency as the size of lanthanide based inorganic material is reduced to nanoscale [6, 7]. However, lanthanide based inorganic nanoparticles have benefits too. If compared to QD's or organic phosphors, luminescent lanthanide nanoparticles do not suffer from photobleaching effect. Another benefit is that inorganic lanthanide-based nanoparticles are more durable over time in comparison to, for example, carbon dots or organic phosphors, since they can degrade and oxidize over time. Also, lanthanide based nanoparticles (and materials) have distinct emission, which has characteristic narrow emission lines meanwhile QD's and organic materials tend to have very broad emission lines, which often overlap [8-10].

Among lanthanide based nanomaterials, particularly interesting class of materials is lanthanide doped orthophosphates ($LnPO_4$). Interest in nanostructured rare-earth orthophosphates is consistently growing as they are offering a wide range of advantages and show huge potential to be applied as drug carriers and luminescent biomarkers in medical field, luminescent nanophosphors, up-conversion nanomaterials, catalysts, and so on [11-14].

There are numerous ways (conventional hydrothermal synthesis, co-precipitation, reverse-micelle growth, sonochemical, microwave-assisted

hydrothermal treatment and other methods) reported in literature to obtain lanthanide orthophosphate nanoparticles. Since lanthanide orthophosphates, investigated in this thesis, were obtained under hydrothermal conditions, hydrothermal approach will be discussed in great detail [15-19].

Owing to their wide diversity, lanthanide orthophosphates are very interesting materials to study. Firstly, depending on lanthanide ionic radius and synthesis method used, lanthanide orthophosphates offer several possible crystalline structures – trigonal rhabdophane, monoclinic monazite, tetragonal xenotime [20]. The morphology of lanthanide orthophosphate particles can be manipulated much more easily and in relatively wide range (fibers, nanorods, hexagonal nanoprisms, urchin-like particles, spherical shaped particles, hollow spheres, submicrostars, etc.) if compared to some other lanthanide-based inorganic compounds (fluorides, oxides, etc.) [15, 21-26]. Another important features of lanthanide orthophosphates are their good thermal and chemical stability, low solubility in aqueous media (which can be beneficial property for biological and nuclear waste management applications), absence of toxic precursors during the synthesis and, like most phosphates, biological inertness [27-29]. Moreover, lanthanide orthophosphate nanoparticles can also possess magnetic properties [26, 30]. $GdPO_4$ is well known to have magnetic properties, since Gd^{3+} ions have seven unpaired electrons in its inner 4f shell. Due to this unique electronic configuration Gd^{3+} based systems (both organic and inorganic) are often promoted as potential magnetic resonance contrast, multifunctional or dual mode imaging probes ($GdPO_4$, GdF_3, $NaGdF_4$, Gd_2O_3) [31-33].

During the period of this thesis, various $LnPO_4$ nanostructures with different morphologies and properties have been engineered. The obtained lanthanide orthophosphate materials were characterized and investigated. It is expected that engineering of various lanthanide orthophosphate nanostructures, conducted during this thesis, will enable better understanding in formation and applicability of lanthanide orthophosphate materials and open new prospects to their further development in material science.

The aim of this thesis was to obtain various lanthanide nanoparticles and evaluate their possible application as functional nanomaterials. In order to fulfill this aim, the following tasks were formulated:

1. Development of simple synthetical approach, which allows to obtain monodisperse lanthanide orthophosphate particles of high quality with effective control over particle growth and morphology.
2. Investigation and evaluation of lanthanide orthophosphate nanoparticle stability in aqueous colloids.

3. Ensuring long term lanthanide orthophosphate nanoparticle colloidal stability in biological media.

Statements for defense:

1. Hydrothermal synthesis is suitable approach for efficient synthesis of monodisperse lanthanide orthophosphate nano and submicro particles. It is possible to very effectively control the growth and morphology of particles by significantly altering the phosphorus source and lanthanide ions molar ratio in the range from 1 to 100.
2. $GdPO_4$ particles of different morphologies have different zeta-potential values. Hence, it is possible to achieve electrostatic stability of $GdPO_4$ particles in a wide range of pH values by altering the particle morphology.
3. $GdPO_4$ nanoparticles modified with p(METAC-*stat*-PEO_{19}MEMA) show superior colloidal stability in comparison to bare $GdPO_4$ particles and show no signs of agglomeration over time.
4. p(METAC-*stat*-PEO_{19}MEMA) modified $GdPO_4$ nanoparticles can be redispersed from dry-state which is both commercially and practically useful property since most of commercial nanoparticles are sold in colloidal state and typically cannot be redispersed from dry state.
5. Hydrothermally synthesized $GdPO_4$ nanofibers enabled preparation of novel nanofibrous $GdPO_4$ aerogel. Such aerogel shows magnetic properties and is ultralight.

2. Types and classification of nanomaterials

It is important to understand the classification and origin of nanoscale materials in order to get better understanding about them and also to be able to see and compare differences between such materials. Therefore, a brief overview of nanomaterial classification is given in this section.

International Organization for Standardization (ISO) suggests using prefix nano with objects who's dimension ranges approximately from 1 to 100 nm [34]. Contradictory, the British Standards Institution proposed that nanoscale materials in size range approximately from 1 to 1000 nm can be considered nanoscale materials [35]. To get better understanding of such dimensions, nanoparticles and nanostructures with their size can be similar in size in comparison to viruses (size of SARS-CoV-2 virus is ca. 70-90 nm), proteins (size of single hemoglobin molecule is ca. 5 nm), antibodies (ca. 10 nm) [36-38]. Numerous different nanoparticles and nanostructures of different origin exist – micelles, liposomes, dendrimers, carbon based nanoparticles (for example, carbon dots, fullerenes, carbon nanotubes, graphene sheets), inorganic nanoparticles (for example, Au, Ag, Fe_3O_4, $LnPO_4$, Ln_2O_3, LnF_3). However, this review will be focused mostly on inorganic nanoparticles and nanostructures, since their properties, possible application, and functionalization are closely related to the experiments conducted during this thesis.

One of the possible approaches to classify nanomaterials is classification depending on material dimensions – 0D, 1D, 2D, 3D. Visual representation of such classification is provided in Figure 1. Lanthanide orthophosphates are given as examples in Figure 1 in order to highlight wide diversity of such materials. Probably the most common representation of 0D nanomaterials would be various nanoparticles, which do not exceed 100 nm in any direction. As will be discussed in detail later on, nanoparticles can be very different, exhibit different shapes and forms, possess either single either polycrystalline domains and can be of various origins and compositions. Typically, 0D materials are isotropic, meanwhile their 1D, 2D, and 3D counterparts, in most cases, are anisotropic.

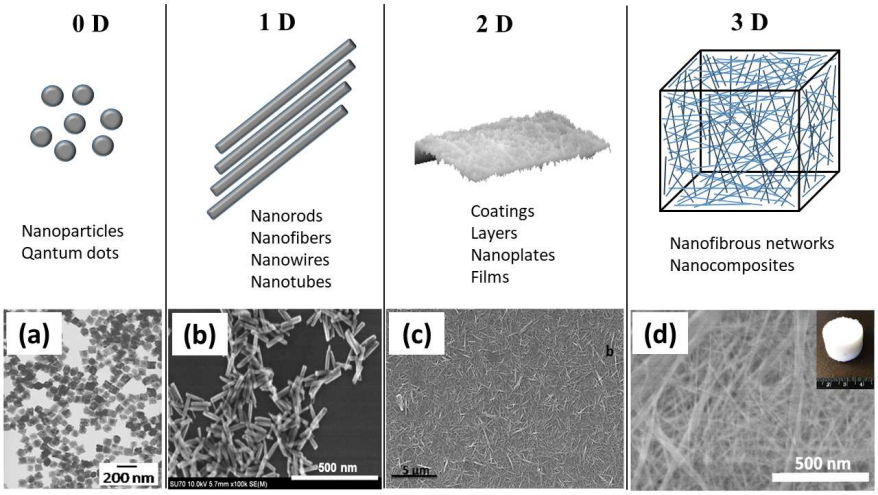

Figure 1. Nanomaterial classification regarding of their dimensions. SEM micrographs show examples of represented dimensional classification. (a) $GdPO_4$ nanocubes; (b) $GdPO_4$ nanorods; (c) hydrophobic $LaPO_4$ coating on silica glass surface; (d) $GdPO_4$ aerogel; Images adopted from (a) [39] (b) [15] (c)[40] (d)[41].

Probably the most popular and well-defined representation of 1D nanomaterials, along with various nanofibers and needle like particles, could be nanorods. Interestingly, depending on the aspect ratio, nanorods are on the boundary between 0D and 1D nanomaterials. One of 1D nanomaterials dimensions can be over 100 nm, whilst other two dimensions should remain in nanoscale, typically below 100 nm. The "longer" 1D nanomaterial gets, the more aspect ratio increases. Similarly to nanoparticles (0D nanomaterials), 1D nanomaterials can be of different origin (metallic, organic/polymeric, ceramic, etc.). Speaking of two dimensional nanomaterials, two of the 2D nanomaterial dimensions can exceed 100 nm, whilst one of the dimensions remain within nanoscale (<100 nm). Good example of 2D material could be various nanocoatings and nanolayers, which are typically introduced on various substrates in order to enhance material functionalities [40, 42]. 3D nanomaterials can be referred to as nanostructured bulk materials. Good examples of 3D nanomaterials would be various three dimensional structures made from nanoscale objects (for example submicron stars, urchin-like particles), nanoparticle assemblies or nanofibrous aerogels [23, 26, 41].

Another noteworthy approach to nanomaterial classification would be categorizing nanomaterials based on their chemical composition/origin. These can be carbon based nanomaterials, organic nanomaterials and inorganic nanomaterials. Also, latest progress in nanoscience is focused on hybrid

nanomaterials, where unique multifunctional properties are achieved by combining both organic and inorganic nanoparticles. These hybrid materials will also be discussed shortly in this paragraph.

1) **Carbon-based nanomaterials.** Carbon is the key element of all life forms on earth. Carbon also has its own class of nanomaterials (see Figure 2) – fullerenes, carbon nanotubes, graphene, carbon nanofibers, carbon dots, nanodiamonds and so on [43]. Such a variety is possible due to carbon ability to bond other elements (including carbon itself) in several ways (different hybridizations). Fullerenes and carbon nanotubes can be described as hollow nanostructures formed from graphene sheets shaped into a sphere/tube.

   Fullerenes are interesting nanomaterials, which were discovered more than 30 years ago [43, 44]. Fullerenes consist of hexagonal (or pentagonal) sp^2 hybridized carbon rings. First fullerenes were synthesized by vaporizing carbon using laser beam under inert atmosphere. However, drawback of such approach was very low yield. In considerably bigger quantities fullerenes are now obtained by using two carbon electrodes in a helium or neon atmosphere, where during arc heating of graphite fullerenes are formed [45]. One of the most iconic fullerenes is Buckminsterfullerene, often referred to as C60. With a chemical formula C_{60}, this fullerene is made of 60 carbon atoms and, besides being strong electron acceptor, has a good thermal stability and strong resistance to pressure (owing to his unique cage-like structure). Comparatively high chemical reactivity of fullerenes enables further functionalization of such compounds [44, 46, 47].

   Carbon nanotubes, differently from fullerenes, are elongated hollow cylinders made from hexagonal carbon (also sp^2 hybridized) rings. These can be up to tens of nanometers in diameter and structurally are similar to graphene sheet "rolled into" cylindrical shape. Carbon nanotubes can be obtained via three main different approaches – carbon-arc discharge, laser ablation of carbon or chemical vapor deposition [48]. Besides their electrical conductivity, carbon nanotubes are known for their other noteworthy properties, such as high degree of stiffness, large aspect ratio and brilliant resilience. These properties combined makes carbon nanotubes interesting materials. Carbon nanotubes can be additionally classified into different categories: such as single or many walled carbon nanotubes. More information on carbon nanotubes can be found in the following reviews [49-53].

Graphene is well-known example of carbon based nanomaterial. Individual layers of graphite are called graphene, which, along with fullerenes and carbon nanotubes, consist of sp^2 hybridized carbon atoms. Graphenes are known for their unique, single atom thick, layered 2D structure. For the first time graphene was obtained by removing it mechanically as a layer from graphite by using adhesive tape. Since this approach was very simple and cheap and the material itself at a time was unique and novel – interest in graphene grew exponentially. Nowadays graphene is mainly obtained via chemical vapor deposition (CVD) [54]. Yet, various methods, such as mechanical exfoliation, thermal exfoliation, chemical reduction and epitaxial growth, exist to obtain graphene layers [55-57]. Graphene materials are interesting as they possess good electrical conductivity. Graphene layers, due to relatively large surface area, can accommodate considerable amount of defects, which are electroactive sites. In comparison to fullerenes and carbon nanotubes, graphene electric properties are fully comparable on the same scale. Scientific evidence suggests graphene as a promising candidate for electrochemical biosensors, even more suitable than carbon nanotubes [58-60].

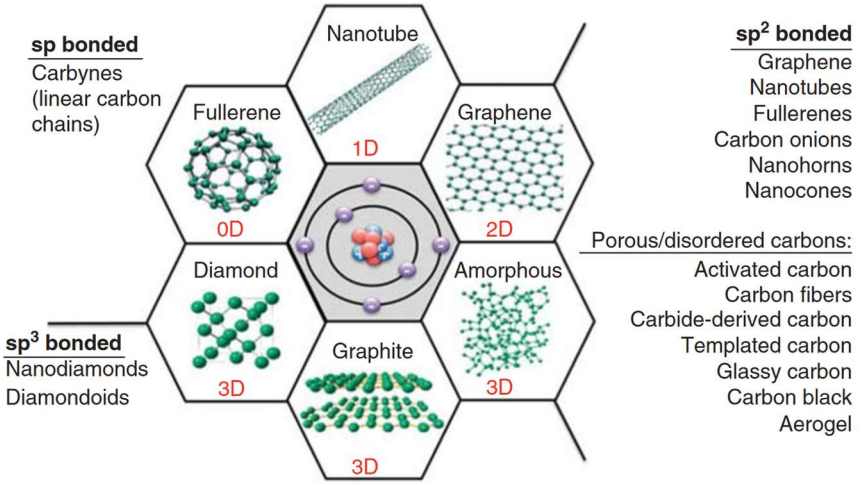

Figure 2. Visual representation of the most common carbon nanomaterials classification, based on carbon hybridization and dimensions (0D, 1D, 2D, 3D). Image adopted from [61].

2) **Organic nanomaterials.** These are typically made from organic molecules and are often studied as potential drug carriers. Classical

examples of organic nanoparticles would be dendrimers, liposomes, micelles, polymeric nanoparticles (depicted in Figure 3).

Dendrimers can be defined as a highly branched nanostructures, which can be obtained in via diverent approaches, when synthesized from the core and via convergent approaches, when synthesis of dendrimer starts from exterior formation [62]. Dendrimers can be obtained with very good monodispersity and high number of functional groups, which can further be functionalized in order to alter their physicochemical properties. Dendrimers can be made from various organic materials and polymers such as PMAM, PEG, PPAm and so on. Numerous studies about dendrimers reveal their potential use in wide range of applications, such as drug delivery and release, MRI contrast agents, sensor development and so on [63, 64]. Due to their suitability for biologically active molecule and drug storage, transportation and controlled release, dendrimers lately are often referred to as very attractive drug delivery nanoplatforms. Such claims are confirmed by over 29 thousands articles and over 600 reviews related to drug delivery systems based on dendrimers (source WOS, January 09-2020, [65]).

Liposomal nanoparticles (or nanoliposomes) are type of nanoparticles, which can shortly be defined as spherical bilayer lipid vesicles with sizes varying from 50 nm to micrometers. Various methods (mechanical dispersion methods, solvent dispersion methods, detergent removal methods) to obtain liposomes were systemically reviewed by Akbarzadeh et al. [66]. Depending on materials chosen for liposome formation, different types of liposomes can be formed: conventional liposomes, sterically stabilized liposomes, cationic liposomes, targeted liposomes, etc. [67, 68]. Liposomal nanoparticles can be produced either using natural (for example cholesterol or other natural nontoxic lipids) or synthetic lipids. Thanks to their unique composition and outer lipid layer, liposomes are, in a way, comparable to membranes of a living organism cell and are known to possess very high biocompatibility. This feature makes liposomes an interesting platform for such purposes as carrier systems for various drugs, particles (for example QD's), genetic material [69]. As a matter of fact, liposomal nanoparticles are already applied in medicine, for example for cancer drug delivery [70]. Good example is DOXIL®, liposomal doxorubicin, which is surface-coated with PEG in order to prolong in-vivo circulation and enhance biocompatibility of liposomal surface [71].

Micelles (nanomicelles) are another type of colloidal nanoparticles with their size ranging from several to around 100 nm. Structurally speaking, nanomicelles can be described as spherically shaped assembly of amphiphilic molecules (monomers). Approaches for nanomicelle preparation can be divided into two categories – direct dissolution, and solvent casting. Furthermore, nanomicelles can be obtained by using either surfactants or synthetic block polymers. Surfactants used for nanomicelles formation can be ionic (for example anionic sodium dodecyl sulfate or cationic dodecyltrimethyl ammonium bromide), nonionic, zwitterionic (for example dioctanoyl phosphatydyl choline, which has both cationic and anionic groups in its structure) [72]. Depending on what particular molecules were used to form micelles, these globular nanostructures can have either hydrophilic or hydrophobic surface and, therefore, be able to exist either in aqueous or in non-aqueous media. Simply speaking, micelles enables solubilization of hydrophobic molecules (for example drugs) into aqueous media (or vice versa).

Similarly to liposomes, nanomicelles are also suggested as potent nanocarrier platforms as they offer size of nanoscale, structural stability, low toxicity, ability to entrap and carry various molecules, for example, cyclosporine A delivery to cornea [73]. More information on nanomicelles, their preparation methods and other properties can be found in literature [74-76].

Polymeric nanoparticles are likely the most diverse class of all organic NP examples given before. Since a vast amount of different polymers exist, both physical, chemical and functional properties of such particles can be altered regarding of polymers used. Nasir et al. reviewed synthetical approaches to obtain polymeric NP's and divided those in to two segments: 1) chemical methods (conventional emulsion polymerization, surfactant free emulsion polymerization, microemulsion polymerization, radical polymerization); 2) physical methods (spray drying, solvent evaporation, nanoprecipitation and so on) [76]. Each and all natural (for example chitosan, albumin, dextran), synthetic (PLA, PLGA, PCL), commercially available, and custom-made polymers can be used for development of polymeric NP's. Another noteworthy aspect is that polymeric nanoparticles can be prepared using biodegradable polymers (for example PLA, PLGA, PCL) [77, 78]. Polymeric NP's are also interesting candidates to be used as a drug carrier nanoplatforms, since they offer ability of controlled drug release in specifically targeted

area; can encapsulate DNA, RNA, proteins. Besides, further surface modifications of such particles remains possible. Polymeric NP's are known to exhibit good *in vitro* and *in vivo* stability [79]. Biodegradable polymeric NP's are especially preferred as drug delivery systems as they can break down over time both in living organisms and environment [77, 80, 81]. Polymeric nanoparticles, prepared from nonbiodegradable polymers (such as PMMA, PS, PAM or various polyacrylates), are also applied in drug delivery, wound healing, and are used as antimicrobial agents. Also, it is important that nonbiodegradable NP's have effective clearance from the organism, for example via urine or feces, to avoid long-term toxic effects and accumulation in organism [79].

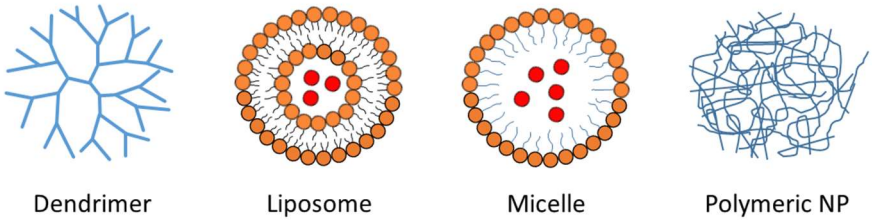

Figure 3. Visual representation of organic nanoparticle classification.

3) **Inorganic nanoparticles.** This section will be discussed in the most detail, since this thesis is based on inorganic (lanthanide orthophosphate) nanoparticles.

Different inorganic nanoparticles due to their unique and tunable properties are very likely more functional if compared to all clases of nanomaterials discussed before [82, 83]. Properties of inorganic nanoparticles are dependent on their size and shape, crystalline phase, surface modifications, doping and so on. It is known that some physicochemical properties of inorganic materials (for example, surface plasmon resonance (SPR) emerges in gold NPs, and superparamagnetism in Fe_3O_4 NP's) emerge as their size decreases and surface-to-volume atom ratio becomes significantly large [82, 84, 85]. Inorganic nanoparticles can further be divided into several subcategories:

Metal nanoparticles. A wide variety of metallic nanoparticles exists. The most widely studied examples of metal NP's include gold, silver, platinum, palladium, iron, copper and other, not mentioned in this list, metal nanoparticles [86-89]. Metal nanoparticles, as will be discussed later in this paragraph, have potential to be applied in a wide range of

applications. As shown in Figure 5, metallic nanoparticles come in a variety of shapes and sizes, and compositions (alloys for example). This variety is also associated to physicochemical and optical properties of these nanoscale materials. Some of the changes in these properties are due to quantum effects – variation in the electronic structure, due to large number of surface atoms (Figure 4). Moreover, the band gap is also dependent on the particle size [90].

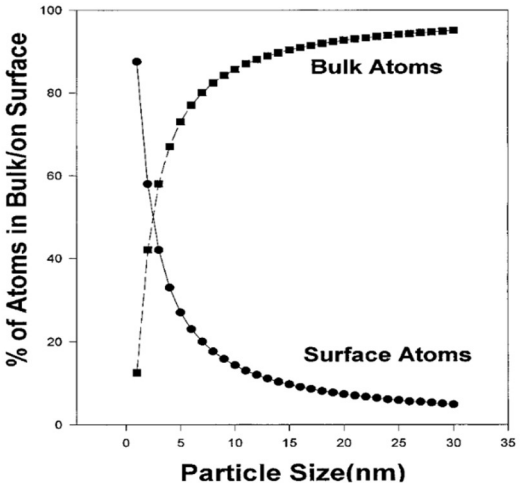

Figure 4. Calculated surface to bulk atom ratios for solid metal particles versus size. Image adopted from [91].

Various methods are used obtain metal nanoparticles: electrochemical synthesis, laser ablation, evaporation-condensation technique, various chemical methods (based on reduction of metal salts under different synthesis parameters), thermal decomposition, and even green approaches, where nanoparticle formation is a result of microorganism activity [90, 92, 93].

Due to their biological inertness and surface plasmon resonance, gold and silver nanoparticles are applied in bioimaging, metamaterials, theranostics, cancer therapy, and SERS [94-98]. Silver nanoparticles can be potentially be used as antimicrobial agents in various products and textile industry, promote wound healing when applied on wounds, as conductive materials (for example in conductive inks) and other applications [90, 93, 99-101]. Also, similarly to gold, silver NP's are promising materials for SERS [102].

Platinum nanoparticles show potential in biomedical, catalysis, and sensing applications [103-105]. Palladium are important in catalysis of organic reactions and also show potential in future biomedical applications [106-108].

Copper nanoparticles are known for they catalytic properties, which enables their applicability as biosensors [109]. Besides that, copper nanoparticles find application in heat transfer systems, as antimicrobial materials, electronics and so on [92, 110, 111].

Selenium nanoparticles are promising tool for fighting CNS disorders. They also possess antibacterial, anticancer and immunomodulatory properties, are non-toxic and biocompatible [112-114]

Nanoparticles of metal alloys also exist, for example, AuAg, AuPt, and other alloys. These alloys have different optical, catalytic, electronic properties if compared to their monometallic counterparts [98, 115].

Metal oxide nanoparticles are materials of great technological importance and future prospects. Metal oxides such as TiO_2, ZnO, Ag_2O, CuO, Fe_3O_4, SnO_2, ZrO_2, along with numerous other unmentioned metal oxides, exhibit different properties from their bulk counterparts. The existing metal oxide nanoparticle synthesis methods include thermal decomposition, microwave-assisted synthesis, solvothermal synthesis, chemical deposition, sol-gel synthesis, and other methods [116-118]. The diversity and application range of metal oxide nanoparticles is very wide. In contrast to metal nanoparticles, metal oxide nanoparticles are mainly focused not on biomedical field, but rather on technological applications, such as gas sensors (anisotropic metal oxide nanoparticles are referred to as perfect building blocks for a wide range of nanoscale chemical sensing devices), magnetic storage devices, MRI contrast agents, antibacterial materials, battery and solar cell components, and so on [118, 119].

TiO_2 nanoparticles are probably the most widely applied metal oxide nanoparticles. To begin with self-cleaning surfaces and catalysis and to end with being dye pigments, food and drug colorant [120, 121]. ZnO nanoparticles are mainly focused on industrial and technological application, i.e., to enhance properties of rubbers, paints, and coatings. However, lately ZnO nanoparticles are being considered as promising materials for biomedical applications [122-124]. Also, both ZnO and TiO_2 nanoparticles are comprehensively used as UV “filters” in cosmetics [125]. Ag_2O nanoparticles can be applied as antibacterial and antiviral agent [126, 127]. CuO nanoparticles are used in biomedical field, development of supercapacitors, as a component in magnetic

storage devices, sensors, catalysts, and semiconductors [128-130]. Iron oxide (Fe_3O_4) nanoparticles are known for their biocompatibility and superparamagnetic properties; therefore, they are suitable inorganic platforms to be applied in numerous biomedical applications such as drug delivery, MRI imaging, hyperthermia, tumor ablation, and theranostics [131, 132]. Another noteworthy example of oxide nanoparticle would be silicon dioxide. Silicon dioxide nanoparticles are inert and can be synthesized in wide range of sizes and morphologies followed by large variety of possible surface modifications [133, 134]. Also, some of silicon dioxide nanoparticles are known to possess large number of pores, which can be used for drug, or other molecule, loading, thus making such particles interesting for biomedical applications [134].

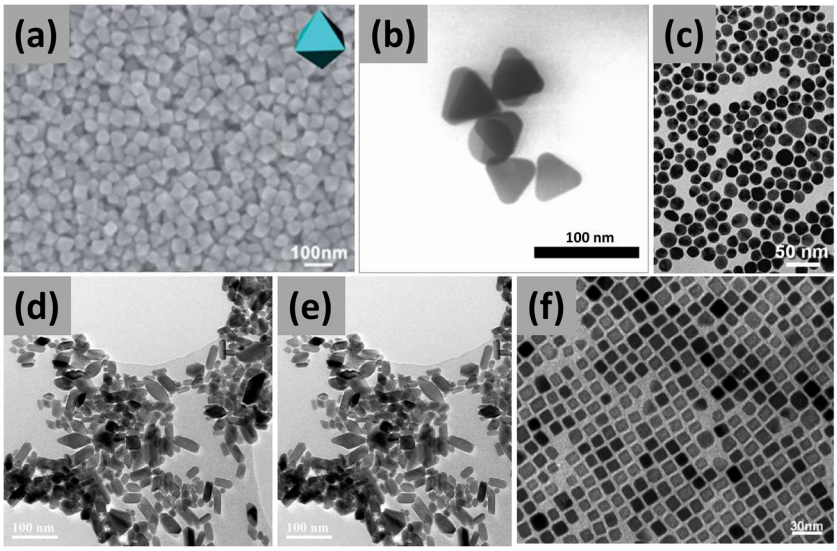

Figure 5. Examples of metal (a-c) and metal oxide (d-f) nanoparticles: Au (a), Ag (b), Cu (c), TiO_2 (d), ZnO (e), Fe_3O_4 (f). Images adopted from: (a) [135]; (b) [136]; (c) [137]; (d) [138]; (e) [139]; (f) [140].

Quantum dots (QDs) can be characterized as zero dimensional inorganic nanoparticles, which are tailored from semiconducting materials. Probably the most recognized examples of quantum dots would be ZnS, ZnSe, CdS, CdSe. Various methods, such as sol-gel processes, microemulsion processes, hot solution decomposition method, wet chemical methods (including precipitation and hydrothermal synthesis), are used to obtain quantum dots [141].

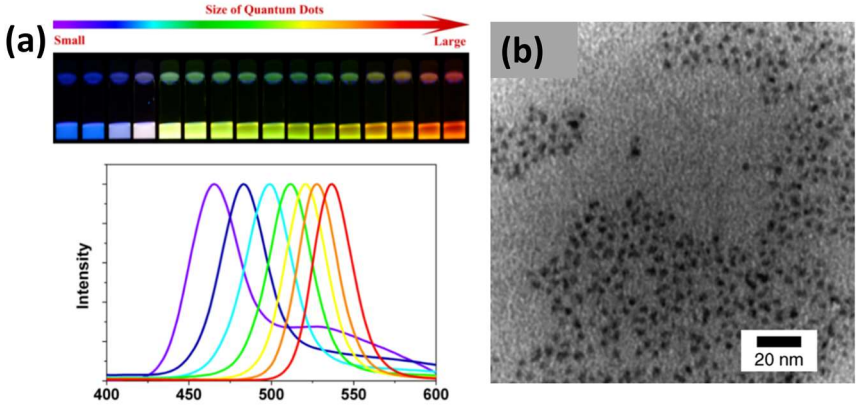

Figure 6. Size dependent emission colour of CdSe quantum dots from small (blue) to large (red) (a). Photoluminescence spectra of some CdSe QD's are given below. TEM image of CdSe quantum dots is represented in (b). Images adopted from: (a) [142] and (b) [143].

In case of QD's, as they get small enough (<~30 nm), some of their properties become size dependent: optical absorption, exciton energies and electron-hole pair recombination. In order to exploit these properties with full potential, highly selective and controlled synthesis is needed, since these emerged unique properties are dependent not only on QD size, but also their shape, crystallinity, concentration of defects and impurities. Such QD properties dependence on size can be related to change of surface-to-volume atom ratios and quantum confinement effects. It is well known that QD's exhibit different color depending on the size of the QD. Size dependent emission of CdSe QD's is shown in Figure 6 [142]. The potential of quantum dots is mainly arising from their unique luminescence (see Figure 6) and is focused on biomedical applications (bioimaging, biosensing, theranostics), LED development, solar cells, and so on [142, 144, 145].

Lanthanide-based inorganic nanoparticles, due to their magnetic and luminescent properties, are perfect candidates to be used as multifunctional nanoparticles. In inorganic materials lanthanides typically exist as trivalent cations [146]. Lanthanide ions are known for their relatively long emission lifetime, narrow luminescence (both excitation and emission) spectral lines (except Ce^{3+}, Eu^{2+} and partly Pr^{3+}) and low toxicity [147, 148]. Lanthanide-based nanoparticles are considered as core materials suitable to be exploited as multifunctional luminescent nanoparticles. Their luminescent properties are mostly

dependent on dopant ions, their concentrations and the host material, they are embedded in. Typically, lanthanide ions are chosen to be embed into oxide-type (oxides, phosphates etc.) hosts, but in some cases, for example, in upconversion luminescence, fluorides as host materials are more preferred. In order to exploit full potential of lanthanide-based inorganic nanoparticles, a controlled synthesis of various hosts is still important to achieve in order to obtain these nanoparticles with good monodispersity, desired sizes, shapes, good crystallinity and so on [3, 149]. The most extensively studied lanthanide-based inorganic nanoparticle systems will be briefly discussed in this section.

Lanthanide oxides are known to be used in LED and tricolor (RGB) display industry. As an example Y_2O_3:Eu^{3+} and Gd_2O_3:Eu^{3+} phosphors are typically excited with radiation corresponding to ultraviolet (UV) region below 300 nm. Such short wavelength radiation excites Eu^{3+} through charge transfer band (CTB), where charge migrates between Eu^{3+} and surrounding O^{2-} pairs ($Eu^{3+} + O^{2-} \leftrightarrow Eu^{2+} + O^{-}$). This excitation mode is is known to be very effective, therefore, quantum yield in such bulk materials can be close to 100% [150]. Ln_2O_3 nanophosphors could be used for enhancement of display panel resolution and are also considered as appropriate candidates for bioimaging since they are known to exhibit strong emission intensity. Additionally, depending on synthesis route, lanthanide oxides are known to possess relatively large specific surface area, which is really useful property for possible catalytic applications. In this case, CeO_2 nanoparticles can be given as a good example, since they are commercially used as component in exhaust fume catalysts in automobile industry. Furthermore, due to their high magnetic moment and paramagnetic nature, some of the lanthanide oxides are considered as promising nanoparticles to be used as T1 and T2 MRI contrast agents [151, 152]. Lanthanide oxides can be obtained by hydrothermal, sol-gel, sonochemical methods, microemulsion synthesis or via solid-state synthesis followed by ball milling [153-155]. Ball milling, laser ablation in liquid (LAL), thermal decomposition, hard template synthesis and other methods are known to be used for lanthanide oxide particle synthesis [3, 156].

Lanthanide-based fluoride nanoparticles can be divided into LnF_3 and $NaLnF_4$. Lately, both of these fluoride hosts are intensively investigated as suitable for development of upconverting fluorescent materials. Both LnF_3 and $NaLnF_4$ can be obtained as really small nanoparticles (as small as around 10 nm). Due to their low phonon energy, which is preferable

for up-conversion materials, and small sizes, lanthanide fluorides seem to be brilliant candidates as multifunctional nanoprobes [157, 158].
$NaLnF_4$ nanoparticles can be obtained in two different crystalline phases – cubic (α) and hexagonal (β). The hexagonal phase is considered more suitable for UC applications, since it has lower phonon energy if compared to α-$NaYF_4$ (or LnF_3). Therefore, $NaLnF_4$ nanoparticle research is generally focused mostly on application in UC nanoprobes [159].

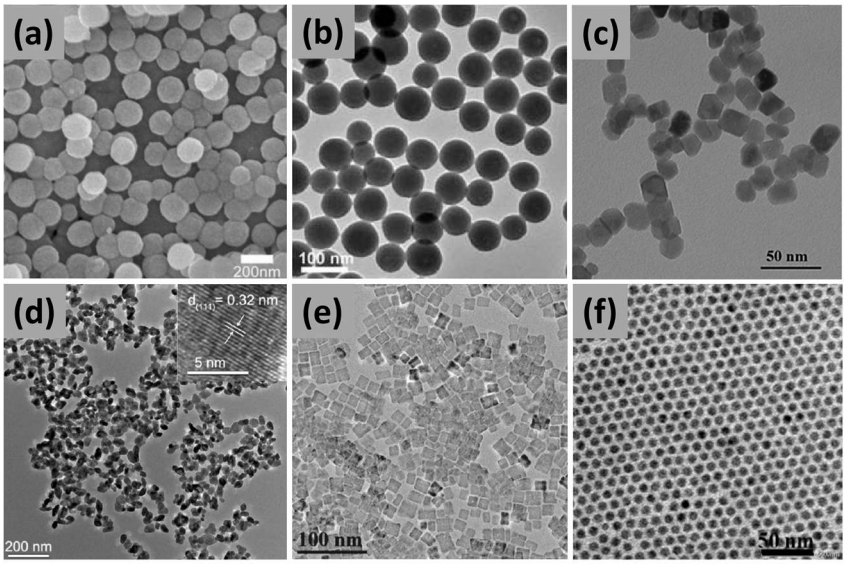

Figure 7. Examples of lanthanide oxide (a-c) and lanthanide fluoride (d-f) nanoparticles: Y_2O_3 (a) [a], $Gd_2O_3:Eu^{3+}$ (b), CeO_2 (c), GdF_3 (d), α-$NaGdF_4:Yb^{3+}/Er^{3+}$ (e), β-$NaYF_4:Yb^{3+}/Er^{3+}$ (f). Images adopted from: (a) [160]; (b) [161]; (c) [162]; (d) [163]; (e) [164]; (f) [165].

Probably the most frequent approaches, used to obtain lanthanide-based fluoride nanoparticles, are either solvothermal synthesis or thermal decomposition method. However, some other approaches also exist, for example, reverse micelle synthesis or co-precipitation [166, 167]. If synthesized without any surfactant, bare fluoride nanoparticles tend to agglomerate immediately and, therefore, are not suitable for biological applications. Thus, they are frequently prepared using oleylamine or oleic acid to prevent agglomeration or can be coated with surfactant/polymer afterwards [168]. The particle surface coated with these surfactants is hydrophobic, hence, particles are extremely unstable in aqueous media. It goes without saying that some additional particle surface modification

is necessary to make them stable in aqueous media. Furthermore, a surfactant attached on the particle surface can not only decrease luminescence efficiency but also limit accessibility of surface atoms, what can negatively affect further functionalization of nanoparticle surface [168, 169].

Lanthanide orthophosphate nanoparticles are another example of extensively studied lanthanide-based nanomaterials. They are attractive due to their thermal and chemical stability, low toxicity, and luminescence stability [27, 28, 170]. Lanthanide orthophosphates are also very versatile materials and offer several possible crystalline phases (hexagonal, monoclinic and tetragonal). Moreover, lanthanide orthophosphates can be synthesized in a wide range of particle shapes (rods, hexagonal prisms, spheres, cubes and so on – see Figure 18) [171]. Due to such versatility, lanthanide orthophosphate nanoparticles are exciting materials from scientific point of view and are considered as attractive candidates for MRI nanoprobes for (for their short relaxation times), bio-imaging, catalysis, laser materials, luminescent nanophosphors and so on [14, 31, 172, 173].

Numerous methods (for example, sol-gel [174, 175] sonochemical [18, 176, 177], co-precipitation [178, 179], solvothermal [180-182], and microwave-assisted hydrothermal [39, 183, 184] for lanthanide orthophosphate nanoparticle synthesis have been developed (please refer to section 4 for the detailed review of synthesis methods). Most popular approaches to synthesize lanthanide orthophosphates are wet chemical methods, since lanthanide orthophosphates are known to have poor solubility in water. These methods are based on precipitation and growth of lanthanide orthophosphate nanoparticles when lanthanide cations meet phosphate anions in the reaction media. The growth of the particles is then determined by reaction conditions, i.e., temperature, pressure, concentration, pH, solvent, the used coordinating agent, and so on [15, 27]. As mentioned before, good control of particle growth, shape, size, and monodispersity is highly desired. It is also preferable that the obtained particles do not have any surfactant attached on the particle surface, since use of surfactants during synthesis has significant drawbacks (decreased solubility in water; reduced accessibility of particles surface, since surfactants remain attached on it and particle surface is blocked from further modifications in order to develop multifunctional nanoparticles). Hydrothermal method enables such

control and probably is the most common method to obtain lanthanide orthophosphates [185-187].

Hybrid nanomaterials. The growing demand of multifunctional nanomaterials or materials with novel properties has accelerated the development of novel hybrid nanomaterials – composites of two or more nanomaterials. There are virtually endless possible combinations to obtain various hybrid nanomaterials. Generally speaking, hybrid nanomaterials can be any combinations of previously discussed carbon, organic, and inorganic nanoparticles. Depending on composition, hybrid nanomaterials can offer combined properties [188, 189].

Surface functionalized nanoparticles (DOX-loaded $GdPO_4$ particles), composite nanoparticles (carbon submicrospheres functionalized with γ-Fe_2O_3 and $GdPO_4$ nanoparticles), core-shell nanoparticles ($NaYF_4$:Yb^{3+},Er^{3+}@SiO_2@Au), liposomal-QD hybrid nanoparticles – all these examples can be referred to as hybrid nanomaterials [190-192]. The variety of hybrid nanomaterials is so wide that it would require separate review for decent discussion.

Nanostructured lanthanide-based inorganic aerogels

Liebner et al. defined aerogels as solids, which feature very low density, high specific surface area and consist of a coherent open porous network of loosely packed, bonded particles or fibers [193]. Aerogels are known as materials with a set of outstanding properties, such as extremely low density, large surface area, low thermal conductivity, and so on. Despite the wide variety of materials that can be processed to obtain porous and low-density aerogel-like substances, there is still plenty room for specifically tailored and multifunctional systems [194].

Gesser et al. described aerogel preparation as an art, where much skill is required to achieve the specific end product [195]. A variety of different organic and inorganic substances can be used to produce aerogels, though most of the industrial production of aerogels relies on silica-based and carbon-based aerogels [194]. Besides, organic aerogels are gaining more and more attention lately. For example, cellulose aerogels, made from nanofibrous cellulose, are very versatile and are suitable for obtaining composite aerogels just by incorporating various nanostructures in cellulose-based aerogel as template [196].

Aerogels are obtained from gels. The initial gel, which is used to obtain aerogel, can be either organic or inorganic (for example, fibers) material,

which under suitable conditions is capable to form stable 3D network (gel) in a suitable solvent (preferably water, methanol or ethanol). Aerogels are then obtained when liquid is removed from the gel, either by critical drying process or by dry-freezing (Figure 8). As-prepared aerogels, obtained via freeze-drying, can be referred to as cryogels, since cryogenic conditions are involved in drying procedure [195].

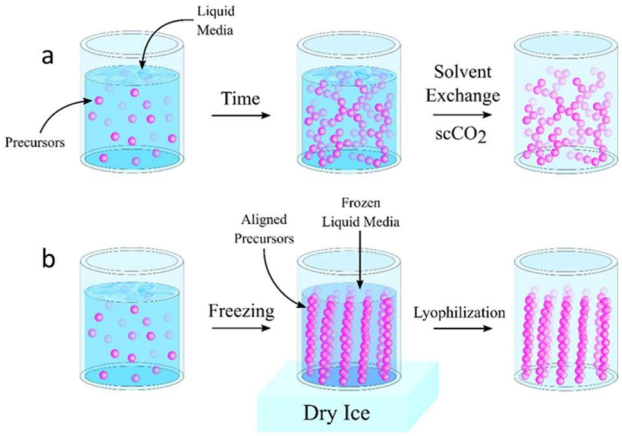

Figure 8. Comparison of different aerogel preparation strategies – supercritical drying (a) and freeze-drying (b). Adopted from [197].

Supercritical drying is a widely used approach to dry gels in order to obtain aerogels. This approach exploits the use of liquid-gas transition occurring in supercritical conditions, depending on the liquid used (ethanol, methanol, etc.) [198]. The main idea of such approach is that under high enough pressure, solvent reaches state of supercritical fluid; therefore, as shown in Figure 9, such "supercritical" liquid evaporation from liquid to gaseous state occurs. Such supercritical liquid evaporation avoids crossing liquid-gas phase boundary (Figure 9). Supercritical drying process is known to yield highly porous, undamaged aerogel structures [196, 199]. However, from the practical point of view, in comparison to freeze-drying approach, use of supercritical drying can produce limited size aerogels due to use of autoclaves, meanwhile freeze-drying approach does not require autoclave. Therefore, bigger bulk aerogels can be obtained, for example, to be used as transparent window insulation material [197, 200].

Freeze-drying is another alternative approach used to obtain aerogels. In this case, solid (frozen liquid, typically water) under low temperature and pressure evaporates by directly going to gaseous phase (Figure 9). In other

words, sublimation of frozen solvent occurs, while maintaining the volume and structure of 3D network, formed by organic/inorganic precursors. Such sublimation, where liquid phase is absent, enables to avoid capillary forces, which may break and collapse the forming aerogel [194, 197].

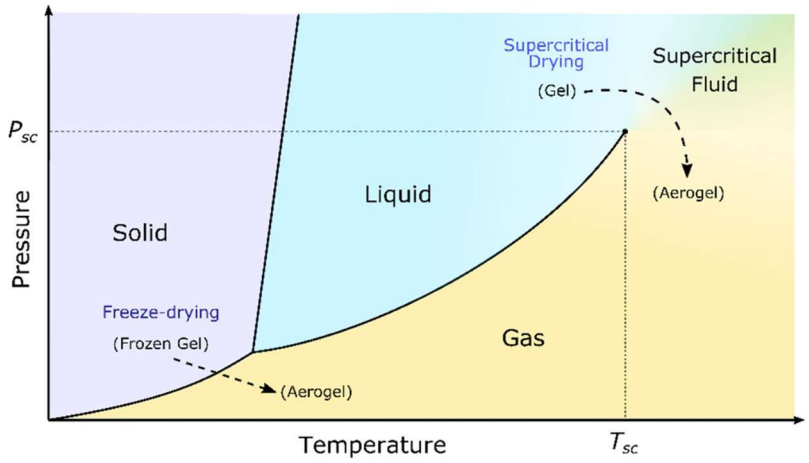

Figure 9. Phase diagram representing supercritical drying and freeze-drying methods used to obtain aerogels. Solid-gas transition (sublimation) yields aerogel in case of freeze-drying. Supercritical drying includes transition from liquid to gas during state of so called supercritical fluid and requires rise in temperature and pressure as main goal of this approach is to "avoid" boundary between liquid and gas. Adopted from [197].

Aerogels are considered as promising materials for application in numerous fields ranging from tissue engineering and bio-sensing to catalysis and aerospace applications [201-207]. Introducing porosity in anisotropically structured magnetic materials would lead to the perfect supports for magnetic separations in biotechnology or for magnetic field-assisted chemical reactions.

Typically, aerogels which are made from anisotropic particles (rods, fibers, wires, etc.) are intertwined in all directions chaotically. The result of such chaotic interweaving of magnetic fibers is a fully compensated overall magnetic moment; therefore, magnetic properties of such anisotropic aerogel would be fully quenched. Thus, obtaining magnetic anisotropic aerogel as a homogenous system with magnetic properties still remains a challenge. For this reason, the most recent papers report magnetic aerogels as composite materials, where magnetic properties are introduced by incorporating magnetic nanoparticles into originally non-magnetic aerogel matrix [208-211].

Rare-earth elements can be used to bring a whole new class of aerogels. Most importantly, lanthanide orthophosphates are suitable for preparation of

nanofibrous aerogels since their tendency of one dimensional growth is well known. Rare-earth elements would enable to obtain homogenous aerogel platforms with both magnetic and optical properties, not to speak about possibilities to composites based on such aerogels as templates. Also, Gd^{3+} containing inorganic materials usually are magnetic due to strong paramagnetic nature of Gd^{3+} ions. Up to now there is only one scientific paper published in this field by Yorov et al., where $CePO_4$ aerogel was successfully obtained and characterized [212]. However, the $CePO_4$ aerogel synthesis procedure, reported in this work, needed various organic solvents, was very time consuming (more than 10 days), and required sophisticate supercritical drying in CO_2. Additionally, to the best of our knowledge, there is no information describing synthesis or preparation of homogenous anisotropically structured magnetic rare-earth aerogels therefore such materials can be considered as innovation.

Thus, the more environmentally friendly and time effective synthesis route for rare-earth phosphate aerogel preparation still needs to be developed. The synthetic approach to obtain lanthanide aerogels reported in this thesis can be applied to obtain lanthanide-based composite aerogels too, simply by incorporating different nanomaterials into hydrogel, which further is used to produce aerogels. In such way, gadolinium phosphate based aerogels can be easily doped with other rare-earth ions (for example Nd^{3+}, Eu^{3+}, Ce^{3+}) in order to tailor or enhance the desired properties.

A unique approach for homogenous fibrous magnetic $GdPO_4$ aerogel preparation is presented in this thesis. Method is simple, scalable, eco-friendly and does not require any exotic precursors or harsh conditions. The main characteristics of the synthesized $GdPO_4$ aerogels are evaluated and presented in paragraph 12.

3. Crystal structure of rare-earth orthophosphates

Crystalline structure is very important factor determining mechanical and physicochemical properties of materials. The same compound possessing different crystalline structures may have remarkably different physicochemical properties and even different intended applications. Orthophosphates consist of isolated PO_4 tetrahedrons and are partially structurally similar to orthosilicates. Apatites (fluorapatites, hydroxyapatites, etc.) and lanthanide orthophosphates are among the most commonly studied orthophosphate materials [213]. Lanthanide orthophosphates are found in nature in form of monoclinic monazite or tetragonal xenotime minerals. More rarely – in partially hydrated trigonal rhabdophane or monoclinic churchite forms. The crystalline phase of lanthanide orthophosphates is determined by ionic radius of lanthanide ion and the chosen synthesis method [20, 214].

Lanthanides from La to Dy tend to crystallize in trigonal rhabdophane phase ($LnPO_4 \cdot nH_2O$, space group $P3_121$) when synthesized via hydrothermal or aqueous co-precipitation route [213, 215]. Another known crystalline form of hydrated lanthanide orthophosphates is churchite ($LnPO_4 \cdot 2H_2O$), which crystallizes in a similar crystalline structure as gypsum ($CaSO_4 \cdot 2H_2O$) and has a monoclinic structure with a space group C2/c [216]. Meanwhile, heavier lanthanides from Ho to Lu (including Y) tend to form xenotime phase (tetragonal structure, space group $I4_1/amd$) under the same conditions [213].

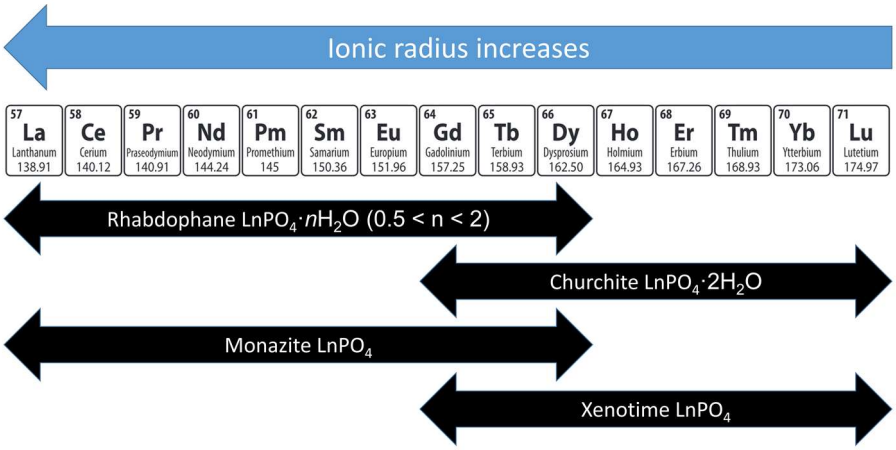

Figure 10. Possible crystalline phases of lanthanide orthophosphates.

Under anhydrous synthesis conditions (e.g., glycothermal synthesis), lighter lanthanides (from La to Gd) tend to form anhydrous monazite

(monoclinic) phase with a space group $P2_1/n$. On the contrary, heavier lanthanides (from Dy to Lu, including Y) tend to crystallize in the tetragonal xenotime phase, same as during aqueous syntheses [214, 217]. The three lanthanides – Gd, Tb and Dy – are known to be able to crystallize (under certain conditions) in all four mentioned phases [39, 216]. Due to such structural diversity, synthesis of single phase Gd, Tb or Dy orthophosphates sometimes can be challenging [218]. The possible crystalline structures of lanthanide orthophosphates are shown in Figure 10.

The majority of scientific papers related to synthesis and development of lanthanide orthophosphate nanoparticles are focused on luminescent properties. Due to the popularity of wet chemical synthesis methods (as will be discussed later), larger portion of these papers study nanoparticles of rhabdophane phase. A hexagonal structure with a space group of $P6_222$ was initially proposed for the rhabdophane phase, but later the space group was revised to be trigonal $P3_121$ [219]. The crystal structure of rhabdophane phase $GdPO_4 \cdot nH_2O$ is provided in Figure 11 a.

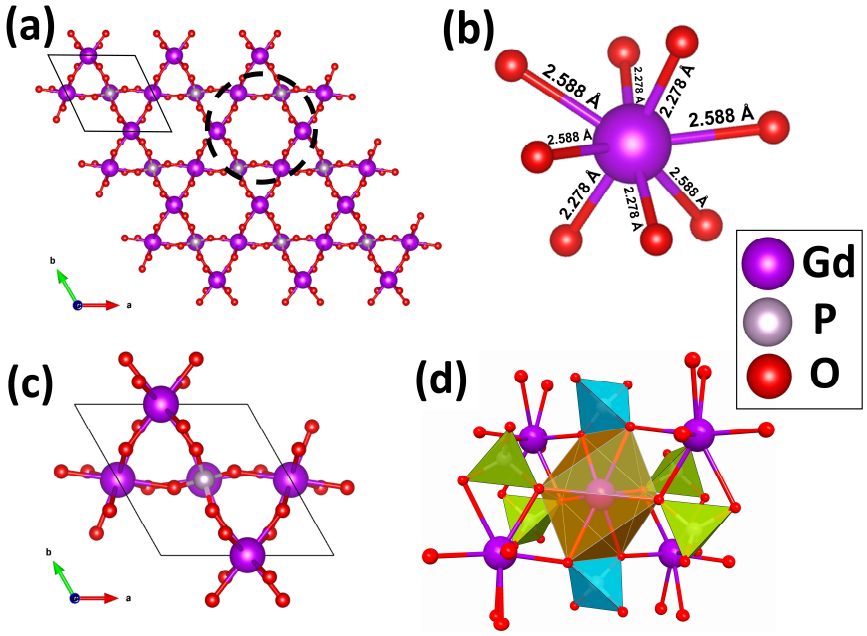

Figure 11. Crystal structure model of trigonal rhabdophane $GdPO_4 \cdot nH_2O$ phase. (a) Crystalline structure of trigonal rhabdophane phase. Dashed line points out presence of zeolitic channel. View of the structure is along c direction; (b) Gd site in rhabdophane structure with CN = 8; (c) Unit cell of trigonal rhabdophane $GdPO_4 \cdot nH_2O$. View of the unit cell is along c direction; (d) Building block in trigonal rhabdophane $GdPO_4 \cdot H_2O$ structure. Cyan and green tetrahedra show edge and vertex sharing PO_4, respectively.

Each Gd atom is forming 8 coordination bonds with oxygen atoms of phosphate group, thus forming GdO_8 polyhedrons (Figure 11 b). Such GdO8 polyhedron, in turn, share its edges with four other GdO_8 polyhedrons and two PO_4 tetrahedrons (visual representation of such building block is given in Figure 11 d). Trigonal rhabdophane structure consists of infinite chains of such GdO_8 polyhedrons and phosphate tetrahedrons connected together along *c* axis, thus forming so called zeolitic channels, which also go along *c* axis (depicted in Figure 11 a with dashed circle). These zeolitic channes are known to contain crystalline water.

In the monoclinic $GdPO_4$ structure, Gd^{3+} ions are nine-coordinated with 9 oxygen atoms (Figure 12 b) resulting in GdO_9 polyhedrons. Each GdO_9 polyhedron shares edges with six other GdO_9 polyhedrons and two PO_4 tetrahedra and vertexes with five PO_4 tetrahedrons [220]. The visual representation of this building block is given in Figure 12 d.

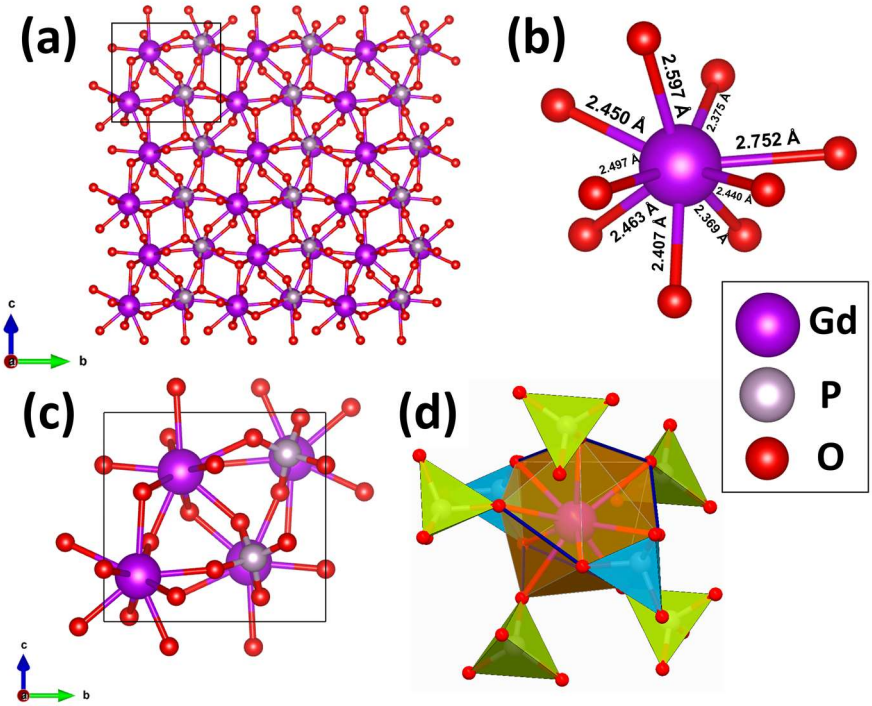

Figure 12. Crystal structure model of monoclinic monazite $GdPO_4$ phase. (a) Crystalline structure of monoclinic monazite phase. View of the structure is along a direction; (b) Gd site in monazite structure with CN = 9; (c) Unit cell of monoclinic monazite $GdPO_4$. View of the unit cell is along a direction; (d) Building block in monoclinic monazite $GdPO_4$ structure. Cyan and green tetrahedra show edge and vertex sharing PO4, respectively. The edges of GdO_9 polyhedron, that are shared with other six GdO_9 polyhedrons, are marked in blue.

Correspondingly, the tetragonal xenotime structure of $GdPO_4$ is depicted in Figure 13 a. Local environment of Gd ion in tetragonal xenotime structure is shown in Figure 13 b. As can be seen, the trivalent gadolinium ions in the tetragonal xenotime structure are coordinated by eight oxygen atoms which are provided by the phosphate groups. GdO_8 polyhedras in tetragonal xenotime structure are interconnected with PO_4 tetrahedras by edge and corner sharing Figure 13 d [221].

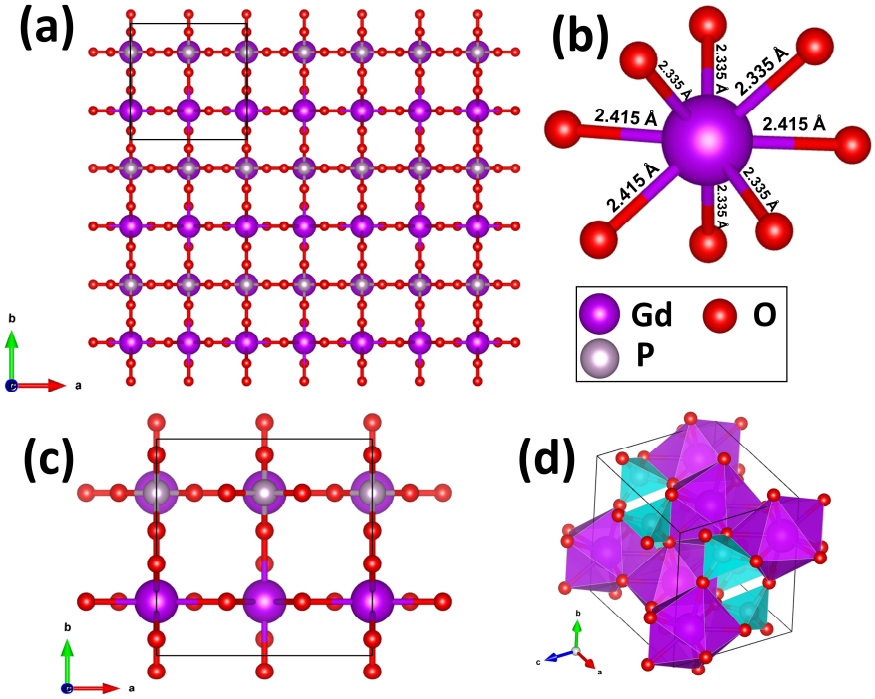

Figure 13. Crystal structure model of tetragonal xenotime $GdPO_4$ phase. (a) Crystalline structure of tetragonal xenotime phase. View of the structure is along c direction; (b) Gd site in xenotime structure with CN = 8; (c) Unit cell of tetragonal xenotime $GdPO_4$ (view is along c direction); (d) Polyhedral version of tetragonal xenotime phase unit cell.

The crystal structure of monoclinic churchite $GdPO_4$ is depicted in Figure 14. Trivalent gadolinium ions in monoclinic churchite structure are coordinated with 8 oxygen atoms resulting in GdO_8 polyhedra. 6 of these coorination bonds are formed with oxygen atoms provided by phosphate groups and other two oxygens (depicted as blue beads in Figure 14) are "provided" by water molecules [222]. As can be seen from Figure 14 c churchite is layered structure. Alternating chains formed by GdO_8 polyhedrons interconnected with PO_4 tetrahedrons going along *a* axis (as

shown in Figure 14 c) form infinite layers which are stacked along *b* axis. Water molecules are positioned in between those layers (Figure 14 c). These hydrogen bonds originating from these water molecules contribute to "holding" these layers together [216].

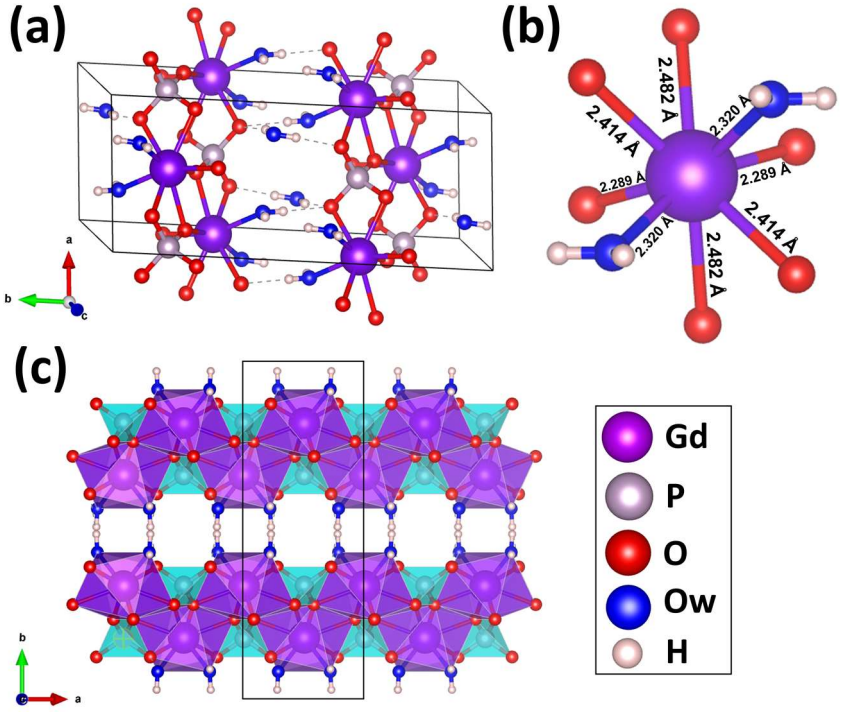

Figure 14. Crystal structure model of monoclinic churchite phase. (a) Unit cell of $GdPO_4 \cdot 2H_2O$; (b) Gd site in churchite structure with CN = 8; (c) View of the churchite structure along c direction.

Notably, coordination number of lanthanide ions in monoclinic monazite structure is 9. On the contrary, in trigonal rhabdophane, tetragonal xenotime and monoclinic churchite phases coordination number of lanthanide ions is 8. This is because coordination of the additional, 9th oxygen atom in the structure becomes spatially difficult [223].

3.1. Water content and thermal behaviour of lanthanide orthophosphates

The water in lanthanide orthophosphates can be either crystalline water positioned in zeolitic channels or physically adsorbed water from air humidity

[15]. The amount of water in lanthanide orthophosphates can differ quite strongly. The exact amount of water is dependent on the crystal structure of the orthophosphate, the morphology of the particles, synthesis approach used to obtain the particles, and so on [20].

Some of the water in zeolitic channels is structurally bound, meaning that it is responsible for structural stability of lanthanide orthophosphates of rhabdophane ($LnPO_4 \cdot nH_2O$) phase. According to Mooney et al., the unit cell of rhabdophane phase can accommodate 1.5 water molecules. Since unit cell accommodates three $LnPO_4$ formula units, it can be concluded that there are 0.5 molecules of water in the unit cell for each Ln^{3+} on. On the contrary, lanthanide phosphates of tetragonal xenotime and monoclinic monazite structures cannot contain crystalline water in their structure, but may have physically adsorbed water molecules on their surface [218].

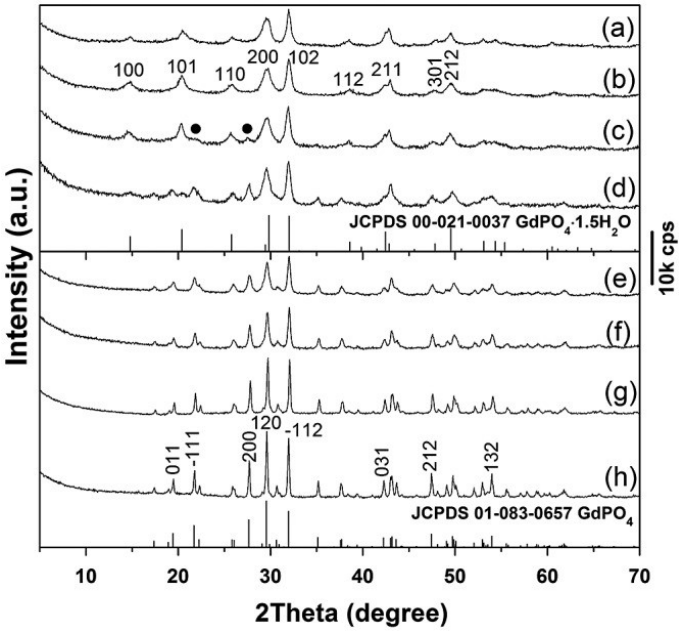

Figure 15. Powder XRD patterns representing calcination of rhabdophane phase $GdPO_4$ under different temperatures: (b) 500 °C, (c) 600°C, (d) 800°C, (e) 900°C, (f) 1000°C, (g) 1100°C, and (h) 1200 °C. The black dots in (c) indicate monoclinic monazite phase. Image adopted from [224].

Trigonal rhabdophane phase is known to be meta-stable low temperature phase. Lanthanide orthophosphates of rhabdophane phase are known to recrystallize into more thermodynamically stable monoclinic monazite or

tetragonal xenotime phases when annealed [213, 218]. Phase transformation from rhabdophane to monazite begins from ca. 600 °C. Such phase transformation process of $GdPO_4$ is shown in Figure 15.

It can be seen that starting from 600 °C diffraction peaks of monoclinic phase emerges (Figure 15 c). Pure monoclinic phase is formed after calcination under 900 °C (Figure 15 c) [225]. Water loss is observed during annealing process of rhabdophane phase. The loss of physically adsorbed water is observed at lower temperatures, meanwhile at higher temperatures the loss of crystalline water positioned in zeolitic channels begins. When water loss is sufficiently high phase transformation from trigonal rhabdophane to monoclinic monazite phase is observed [226].

Interestingly, partially dehydrated lanthanide orthophosphates with rhabdophane phase can easily rehydrate (even from air humidity at room temperature). During this dehydration/rehydration no significant changes in crystalline structure are observed; therefore, it was concluded that the water in rhabdophane phase is of zeolitic nature [219, 227, 228].

As mentioned before, the rhabdophane phase forms when synthesis is carried out in aqueous media. Rhabdophane phase forms easily without the need or high temperatures, pressure or any other exceptional synthesis parameters. Hence, lanthanide orthophosphates of rhabdophane phase are often chosen as precursors to obtain monoclinic monazite phase samples by annealing. Lanthanide orthophosphates possessing tetragonal structure are known to be thermodynamically stable, therefore, their phase remains unchanged when annealing under higher temperatures [229]. Interestingly, water loss is also observed when annealing tetragonal lanthanide orthophosphates synthesized in aqueous media. For example, tetragonal YPO_4 nanoparticles synthesized by Hernandez et al. shown 6% mass loss when annealed. $GdPO_4$ nanoparticles possessing tetragonal phase shown weight loss of 3%, and tetragonal $LuPO_4$ particles – 11% weight loss when heat treated [39, 230, 231]. Authors off all given examples attribute this mass loss to the loss of physically adsorbed water. Despite the considerable water loss and high annealing temperature, annealed orthophosphates of tetragonal phase (obtained by synthesis in aqueous media), show no significant changes in the crystalline phase in comparison to their pre-annealed „hydrated“ form. Hence, it can be concluded that lanthanide phosphates of tetragonal xenotime phase synthesized in aqueous media are partially hydrated. However, the origin of water is still unclear. Most likely the water content can be attributed to physically adsorbed water [20, 219].

It is known that in absence of water (solid-state synthesis), lighter lanthanides from La to Dy tend to form monoclinic monazite phase and heavier lanthanides from Ho to Lu (including Y) form tetragonal phase [214].

It can be summarized that when synthesized in aqueous media, lanthanides from La to Gd crystallize in their stable low-temperature rhabdophane phase. Interestingly, depending on conditions, Dy are known to crystallize in both rhabdophane and tetragonal phase [232]. On the contrary, lanthanides from Ho to Lu will crystallize in their most thermodynamically stable tetragonal xenotime phase. The stable high-temperature phase for lanthanides from La to Gd is monoclinic (space group $P2_1/n$), meanwhile for lanthanides from Ho to Lu most stable phase is tetragonal.

3.2. Anisotropic nature of lanthanide orthophosphates

The hydrothermal method presented in this thesis is an efficient way to synthesize (hydrothermally crystallize) various oriented nanostructures of lanthanide orthophosphates – nanotubes, nanostrips, nanowires, nanofibers, etc. (will be discussed in detail later) [223]. The anisotropic nature of lanthanide orthophosphates may be related to their crystalline structure. Besides, monoclinic phase lanthanide orthophosphates (for instance, $LaPO_4$, $CePO_4$, $NdPO_4$) are also known to have anisotropic nature. Although not as much pronounced as in the case of rhabdophanes [222]. Fang et al. studied tetragonal lanthanide orthophosphates and concluded that lanthanide orthophosphate nanoparticles have isotropic nature and does not have any preferential growth direction [217].

Even though there are many publications related to the synthesis of anisotropic $LnPO_4$ nanoparticles, there is still limited number of fundamental studies that have thoroughly investigated relationship between crystalline phase, synthesis parameters and the anisotropic growth of $LnPO_4$ nanoparticles. There are some speculations explaining this anisotropic nature of lanthanide orthophosphates, for example that the anisotropic growth of nanocrystals of lanthanide phosphate could be attributed to their specific crystalline structures and different chemical potentials on crystalline planes. According to Gibbs Thomson's theory, the relative chemical potential of a crystal is directly proportional to surface to volume atom ratio, which is proportional to the number of "hanging" bonds per atom [233]. Wang et al. reported solvothermal synthesis and investigation of lanthanide orthophosphates of both monoclinic monazite and trigonal rhabdophane

structures tend to grow anisotropically due to lower activation energy for growth along *c*-axis [27].

According to Boakye et al., anisotropic nature of rhabdophane phase can be related to surface energy anisotropy of the structure, with a base *(ab*) plane having higher surface energy than other planes, which is in tact with Wulff's theorem [234]. Wulff construction enables to determine the most thermodinamically stable shape of a crystal without any difficult mathematical calculations. This suggests that elongated shape of rhabdophane phase crystal is, likely, the most thermodinamically stable. Even though one-dimensional growth of lanthanide phosphates is preferable, the particle growth can be significantly influenced by altering the synthesis parameters (pH, solvent, surfactants, coordinating agent) [235]. The changes in system parameters can affect surface energy on specific crystal planes resulting in reduced surface anisotropy [234].

4. Typical synthetical procedures to obtain lanthanide orthophosphate nanoparticles and nanostructures

First serious fundamental studies towards nanoparticle synthesis and properties were reported back 1980‘s [236-238]. As depicted in Figure 16, methods for obtaining nanoparticles can roughly be divided into top-down and bottom-up approaches. Top-down methods are based on downsizing bulk material down to nanoscale dimensions. This usually requires relatively expensive equipment (for example ball-mill in case of ball-milling or sophisticated laser in case of laser ablation). Often, nanoparticles obtained via top-down approaches do not have good monodispersity, defined morphology, and have many surface defects. Due to these drawbacks, applicability of such particles may be limited in some cases. Contrary, nanoparticles obtained via bottom-up approaches typically have better monodispersity, and more defined morphology. Also, in comparison to top-down methods, bottom-up approaches are often technologically simpler [239-241].

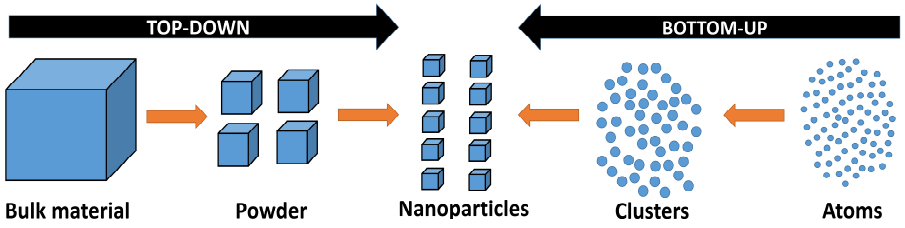

Figure 16. Principle of bottom-up and top-down synthesis of nanomaterials.

Large part of bottom-up approaches are mostly based on wet chemical synthesis methods, which are often simple, easy controllable, inexpensive and easy scalable. In order to get better understanding of advantages and disadvantages of wet chemical synthesis methods, it is necesarry to shortly review each of them [116, 242].

The controlled synthesis of nanoparticles is very important in order to obtain monodisperse particles of the desired morphology and size, which would be suitable for intended applications. In order to achieve good control of nanoparticle growth, it is important to understand the nucleation and growth mechanisms of the particles themselves and other ongoing processes and also to understand how synthesis parameters correlate with the growth of the particles [243, 244]. In terms of the practical applicability of nanoparticles, it is important that the chosen synthesis method would have good reproducibility and could be upscaled easily if necessary.

Wet chemical synthesis methods remain very popular for the synthesis of various lanthanide nano and microparticles. The main advantage of wet chemical synthesis methods is the ability to control the nucleation of particles growing in solution starting from the atomic level. Up to this day, probably the most popular and the best known wet chemical synthesis methods remain the hydrothermal, microwave assisted, thermal decomposition, co-precipitation and microemulsion methods [245-248].

As was discussed in the previous section, various crystalline phases of lanthanide orthophosphates are possible. Crystalline phase of the obtained lanthanide orthophosphates can be dependent on the synthesis method and synthesis parameters chosen. The morphology of synthesized nano and micro particles of lanthanide orthophosphates can be manipulated by altering and modifying various synthesis parameters, such as temperature, pressure, pH, precursors and their concentrations, coordinating agents, surfactants and so on [15, 19, 249]. The main wet-chemistry based methods, used to obtain lanthanide orthophosphate particles, will be discussed in the following section.

4.1. Hydrothermal/Solvothermal synthesis

Compounds synthesized via the hydrothermal/solvothermal approach are widely applied in electronics, catalysis, data storage devices, (bio)medicine and so on. The particles of various compounds, including telurides, silicates, carbonates, phosphates, sulfides, selenides and so on, can be synthesized via the solvothermal synthesis method [250]. Also, wide range of possible morphologies can be obtained via solvothermal synthesis: nanotubes, nanowires, nanofibers, nanorods, nanoplates and so on [251]. Even in 2020 solvothermal synthesis remains a popular synthesis method to innovatively obtain lanthanide orthophosphates [15, 252, 253]. During solvothermal synthesis, nanoparticles are synthesized under high temperature and pressure in a closed reaction vessel. The matrix (solvent) used for hydrothermal synthesis can be anything from water (hydrothermal synthesis) to ammonia (ammonothermal), alcohol (alcothermal, glycothermal), or any other organic or inorganic solvent [254]. Many different nanostructures have been synthesized by hydrothermal synthesis to this day [254, 255].

Concept of hydrothermal process was adopted from geosciences, where it was used since 19th century in order to describe hydrothermal water circulation. During such process, hot pressurized water circulates in the earth's crust and this process is responsible for the formation of many new minerals and rocks [256]. Over time, chemists have also become interested in

hydrothermal processes and the first „official“ hydrothermal syntheses (of „$BaCO_3$ and $SrCO_3$) were reported in 1839 by scientist named Robert Bunsen. Shortly afterwards, E. Schafhautl described the hydrothermal synthesis of small quartz crystals. These researchers provided the induction for the beginning of a wide field of research on hydrothermal syntheses [257].

Speaking of recent times, the “revival” of hydrothermal synthesis occurred in the 1990s and can be related to the breakthrough in nanomaterials science [258]. Additional new studies focused on modification of hydrothermal synthesis (microwave assisted, acoustic wave induced, mechanical mixing introduction, electrochemical synthesis under hydrothermal conditions) attracted the attention of many chemists and materials scientists and, thus, contributed to popularity of hydrothermal synthesis. Up to this day hydrothermal synthesis remains popular approach in development and synthesis of various innovative (nano)materials [250, 259]

Hydrothermal synthesis is a crystallization process during which crystallization of material and chemical reactions occur in a closed reaction vessel under elevated temperature and pressure. Hydrothermal method principle is based on that under hydrothermal conditions chemical processes and interactions start to occur, which are not observed under normal conditions: solubility of insoluble materials increases, the change of physicochemical properties of the water is also observed. Characteristics (such as ionic product, density, viscosity, thermal conductivity, heat capacity, boiling point) of chosen solvent are important and can define the properties and formation of the final product. Also, solvent properties can also be dependent on solvothermal conditions. As a result, during hydrothermal syntheses, under elevated temperature and pressure water can act not only as reaction medium, but also as a solvent and even catalyze reactions that occur during hydrothermal synthesis [250].

The most frequently used lanthanide ion precursors in hydrothermal syntheses of lanthanide orthophosphates are solutions of simple lanthanide salts – chlorides, nitrates or soluble organic lanthanide salts [15, 19, 39, 260]. Depending on specific synthesis, additional compounds, such as surfactant or coordinating agents, can be introduced into reaction system as well [235, 261].

There are numerous advantages, which make hydrothermal synthesis of lanthanide orthophosphates attractive: high reproducibility, good control over synthesis parameters, high monodispersity of obtained particles, colloidal stability of the obtained particles, surfactant-free surface of the obtained particles, hence the surface of nanoparticles remains accessible for further functionalization [15, 22, 27, 235].

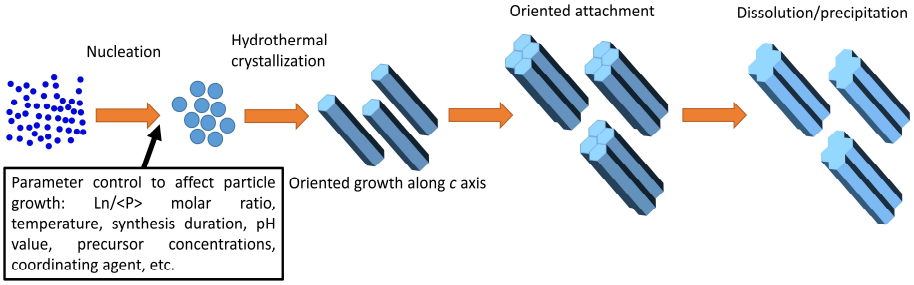

Figure 17. Principal scheme for hydrothermal growth of rhabdophane $LnPO_4 \cdot nH_2O$ nanoparticles.

Hydrothermal synthesis of lanthanide orthophosphates is a complex process during which, besides nucleation and (nano)particles growth, various additional processes and side reactions take place. Changes in each of them may affect the nucleation and growth of nanostructures [262, 263]. Hence, possible nanoparticle nucleation mechanism remains very complex and delicate process and is covered by numerous papers and theories (classical nucleation, LaMer, diffusion theory and so on) [243, 264, 265]. During nucleation process, $LnPO_4$ nuclei are formed which further hydrothermally crystallize into defined nanoparticles with their properties depending on the synthesis parameters. Further particle formation may be affected by Ostwald ripening and oriented attachment, which under appropriate conditions can result in fusion of contact surfaces of agglomerated particles (via dissolution + precipitation) forming one bigger nanoparticle (as shown in Figure 17). Ostwald ripening process is based on dissolution-precipitation phenomenon and difference of chemical potential (excess surface energy) between smaller and bigger growing particles. Due to this effect, bigger particles growth is promoted at an expense of smaller particle dissolution, since these are more soluble [266]. Another possible process happening may be oriented attachment (shown in Figure 17). Oriented attachment and Ostwald ripening processes are independent of each other [266]. Oriented attachment is different from random aggregation, since oriented attachment typically happens along the specific crystallographic directions of nanoparticles offering a unique approach to design nanomaterials [267]. As discussed previously, rhabdophane phase lanthanide orthophosphates have tendency of oriented growth (along *c*-axis). It is seen in papers that anisotropic lanthanide orthophosphate nanoparticles have a tendency to agglomerate parallel to each other, along *c*-axis [27, 30, 172]. Such behaviour of rod-like particles is also a form of oriented attachment or so called self-organization [267, 268]. Another process happening to particles during hydrothermal growth is

redissolution and reprecipitation, which also may affect size and shape of the resulting particles as shown in Figure 17 [257].

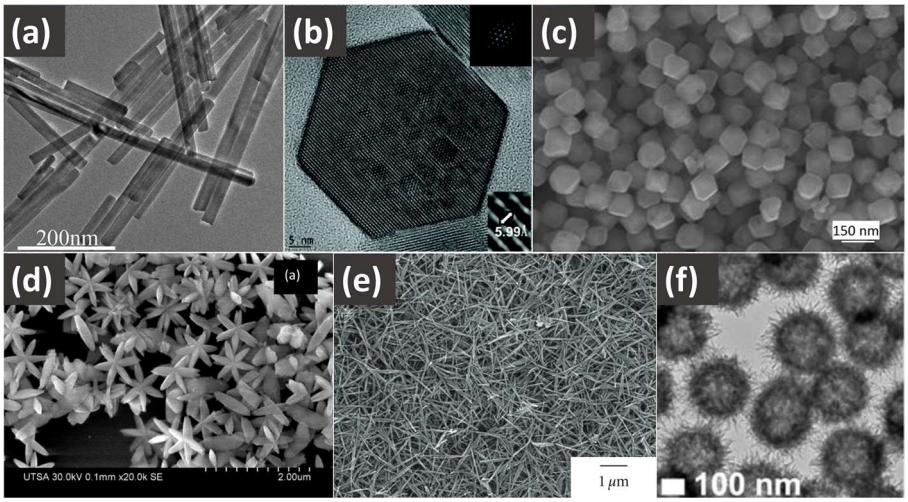

Figure 18. Various $LnPO_4$ nanoparticles obtained via solvothermal synthesis method. $CePO_4$ nanorods (a), $TbPO_4$:Ce nanoprisms (b), GdPO4:Tb^{3+} nanocubes (c), $GdPO_4$:Nd^{3+} submicron stars (d), $CePO_4$ nanofiber (e), $GdPO_4$:Ce/Tb hollow spheres (f). Images adopted from: (a) [180]; (b) [181]; (c) [182]; (d) [26]; (e) [21]; (f) [192].

Diverse variety of $LnPO_4$ particles can be obtained via hydrothermal synthesis route. Zhu et al. reported hydrothermal synthesis (150 °C for 12 hours) of luminescent $CePO_4$ nanorods (Figure 18 a). $CePO_4$ nanorods possessed rhabdophane phase. Authors suggested potential possibility to use these nanorods as UV absorbers in personal care products since they exhibited strong UV absorption [180]. Kuang et al. synthesized multifunctional core-shell $TbPO_4$:Ce^{3+}@$TbPO_4$:Gd^{3+} hexagonal nanoprisms (Figure 18 b) of rhabdophane phase for magnetic resonance and bioimaging [181]. Particles were obtained at pH value of 1.5 under hydrothermal treatment for 12 hours at 150 °C temperature. Liviano et al. published a paper on synthesis of rhabdophane $GdPO_4$:Tb^{3+} submicron cubes (Figure 18 c), which had size of ca. 150 nm [182]. These cubes were obtained from nitrate precursors, whereas hydrothermal conditions were maintained at 180 °C for 20 hours. Kumar et al. reported synthesis of Nd^{3+} doped $GdPO_4$ monoclinic monazite phase submicron stars (ca. 600 nm) [26]. Submicron stars (Figure 18 d) were obtained from nitrate precursors dissolved in EG, reaction media was heat treated in autoclave at 130 °C temperature for 12 hours. Ekthammathat et al. reported synthesis $CePO_4$ fibers (Figure 18 e). Nanofibers were obtained under hydrothermal conditions (200 °C for 12 h). Obtained $CePO_4$ nanofibers

possessed monoclinic crystalline phase [21]. Yi et al. reported fabrication of $GdPO_4$:Ce/Tb hollow spheres (Figure 18 f) corresponding to rhabdophane phase. These hollow spheres were obtained under hydrothermal conditions (200 °C for 15 h) using $Gd(OH)CO_3$:Ce/Tb as Gd precursor/template and, interestingly, the surface of these hollow spheres was loaded with drug doxorubicine [192].

The given examples demonstrate that hydrothermal approach is suitable to obtain monodisperse nano and micro sized lanthanide orthophosphate particles with a wide range of different morphologies. Due to higher synthesis temperature, lanthanide orthophosphates prepared via hydrothermal approach have relatively high crystallinity. Hydrothermal synthesis remains a promising synthesis method that allows the efficient control of many reaction parameters yielding single phase, highly crystalline, and homogeneous compounds.

4.2. Microwave-assisted hydrothermal/solvothermal synthesis

Microwave-assisted solvothermal (and hydrothermal) synthesis is another attractive, but not as popular synthesis approach to obtain lanthanide orthophosphate nanoparticles. Due to the microwave radiation, reaction mixture reaches needed temperature faster if compared to conventional solvothermal synthesis. As a result, microwave-assisted syntheses are faster in comparison to regular solvothermal syntheses. The main disadvantage is that rapid heating of the reaction mixture builds up solvent vapor pressure very fast, which increases the risk of explosion and/or possible damage to the equipment [250, 269].

Rodriguez-Liviano et al. reported the microwave-assisted solvothermal synthesis of $GdPO_4$:Eu^{3+} nanocubes of around 75 nm in size (Figure 19 a) [39]. Butylene glycol was used as a solvent during synthesis and organic acetylacetonate salts of corresponding lanthanides were used as Ln^{3+} precursors. Microwave assisted hydrothermal synthesis (120 °C for 20 min) of $LaPO_4$ nanorods was reported by Colomer et al. [183]. Lanthanum nitrate was used as precursor for La^{3+} ions and H_3PO_4 was used as phosphorus source during the synthesis. No surfactants or coordinating agents were used to control the growth of $LaPO_4$ nanorods (Figure 19 b). Samsonova et al. reported synthesis of Nd^{3+} doped YPO_4 nanoparticles via microwave assisted hydrothermal route (200 °C for 2 hours) [184]. Nitrate salts of corresponding lanthanides were used as precursors and $K_2HPO_4 \cdot 3H_2O$ as phosphorus source, no organic molecules were used to affect the growth of YPO_4 nanoparticles.

According to this paper, such $YPO_4:Nd^{3+}$ particles exhibit tetragonal xenotime phase and are of ca. 50 nm in size (Figure 19 c).

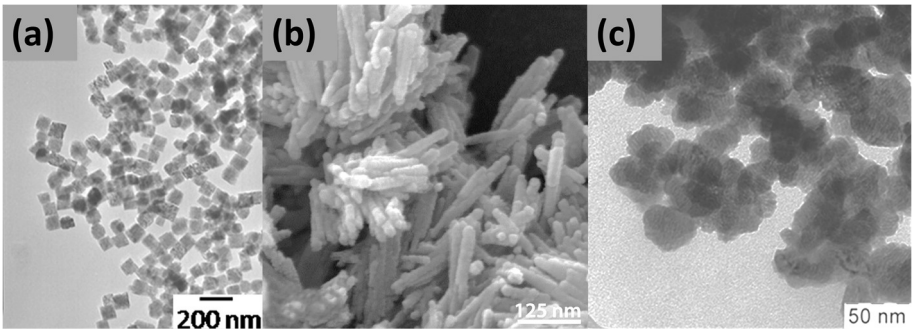

Figure 19. Various $LnPO_4$ nanoparticles obtained via microwave-assisted solvothermal synthesis method. (a) $GdPO_4$ nanoparticles (image adopted from [39]); (b) $LaPO_4$ nanorods (image adopted from [183]); (c) $YPO_4:Nd^{3+}$ nanoparticles (image adopted from [184]).

4.3. Co-precipitation

Co-precipitation methods are probably the cheapest and simplest methods to synthesize lanthanide-based nanoparticles. This method is popular for its simplicity, relatively mild reaction conditions, low cost (simple equipment) and short reaction times.

Co-precipitation from aqueous solutions. During such syntheses, solutions of water-soluble salts are mixed, resulting in the formation of water-insoluble compounds such as lanthanide orthophosphates, lanthanide fluorides and so on. Nanoparticles, obtained via co-precipitation from aqueous solutions, typically suffer from low crystallinity. Low crystallinity can negatively affect luminescent properties of nanoparticles [16, 48, 179, 270]. Hence, further annealing of synthesized nanoparticles is needed in order to increase the luminescence intensity. However, particles tend to agglomerate irreversibly when heated, hence their possible applicability is narrowed [270].

Powder XRD patterns depicted in Figure 20 indicate that the crystallinity of lanthanide orthophosphates obtained via co-precipitation from aqueous solutions is low. It can be seen from Figure 20 a that as-coprecipitated $LaPO_4$ nanoparticles have low crystallinity and their diffraction peaks correspond to rhabdophane phase. Though, when $LaPO_4$ particles are annealed under temperature of 400 °C crystallinity is notably increased. As expected, further increase in annealing temperature results in phase transformation, where from 900 °C temperature pure monoclinic phase is observed. Even though

as-coprecipitated nanoparticles tend to have low crystallinity, it can be improved along with the increase of reaction media temperature. It can be seen from Figure 20 b that as-coprecipitated (30 °C) $LaPO_4$ nanowires have relatively low crystallinity. On the contrary, LaPO4 nanowires obtained under 60 and 90 °C temperature are more crystalline. Interestingly, when reaction media temperature reaches 100 °C additional peaks of monoclinic phase are observed.

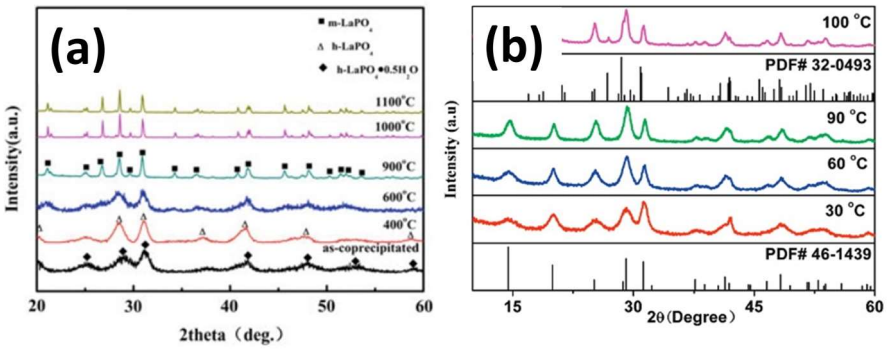

Figure 20. XRD patterns of various $LnPO_4$ nanoparticles obtained via co-precipitation. (a) $LaPO_4$ nanoparticle XRD patterns. Image adopted from [178]; (b) XRD patterns of $LaPO_4:Ce^{3+}$ nanowires precipitated under different temperatures. Image adopted from [179].

Co-precipitation from organic solvent/polyalcohol (polyol mediated synthesis) is a variation of precipitation type synthesis when polyalcohols (for example ethylene glycol) are used as a solvent. Due to the higher boiling point of the solvents used, higher synthesis temperatures are possible. As a result, it is possible to obtain particles of higher crystallinity. Because these syntheses are practically anhydrous, the obtained lanthanide orthophosphate nanoparticles (depending on lanthanide and synthesis parameters) tend to crystallize either in monoclinic monazite or in tetragonal xenotime phase. Since both phases formed and reaction media are anhydrous, the luminescence efficiency of the nanoparticles is not affected by the presence of any physically adsorbed or crystalline water. Compared to co-precipitation from water, precipitation from organic solvents has a disadvantage, since sometimes it can be challenging to remove organic solvent residues from nanoparticles [271, 272].

One of the first syntheses of lanthanide orthophosphate nanoparticles, where EG was used as a solvent, was reported by Feldman et al. in 2002. Authors of this paper synthesized (180 °C, 4 h) spherical $LaPO_4$ (Figure 21 a) and $CePO_4$ nanoparticles with diameters ranging (depending on the synthesis

parameters and lanthanide ion) from 30 to 180 nm. Acetate salts of corresponding lanthanides were used as lanthanide ion precursors [271]. Correspondingly, Nunez et al. reported synthesis of various $LnPO_4$ (Ln = La, Ce) submicrospheres doped with Eu, Ce, Ce+Tb. Depending on the synthesis parameters, diameter of the obtained spherical particles was ranging from 150 to 500 nm. An image of $LaPO_4:Ce^{3+}/Tb^{3+}$ submicrospheres is depicted in Figure 21 b. These particles were synthesized using EG (120 °C, 1.5 h) as solvent and crystallized in monoclinic monazite phase [24]. Becerro et al. synthesized $LuPO_4:Eu^{3+}$ nanoparticles possessing tetragonal xenotime phase (Figure 21 c) by precipitation in EG (180 °C, 30 min). Synthesized $LuPO_4:Eu^{3+}$ particles were rice-shaped, approximately 80 nm in length and 40 nm in width. Due to the significantly higher reaction temperature (compared to aqueous co-precipitation syntheses) obtained particles have higher crystallinity [231].

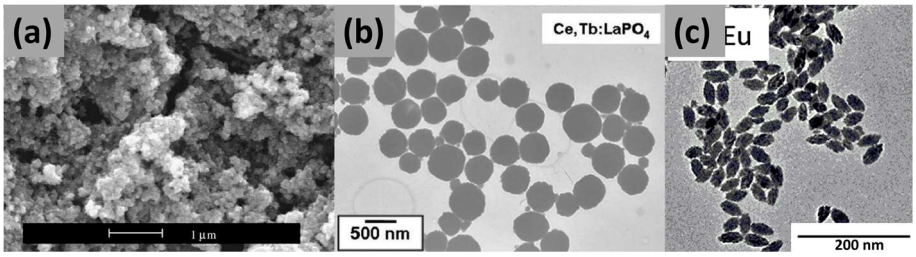

Figure 21. Various $LnPO_4$ nanoparticles obtained via co-precipitation from polyols. (a) $LaPO_4$ nanoparticles (adopted from [271]); (b) $LaPO_4:Ce^{3+}/Tb^{3+}$ submicrospheres (TEM image adopted from [24]); (c) $LuPO_4:Eu^{3+}$ nanoparticles (adopted from [231]).

Microwave-assisted co-precipitation. Ma et al. prepared $LaPO_4:Ln^{3+}$ ($Ln^{3+} = Ce^{3+}$, Eu^{3+}, Tb^{3+}) nanorods (Figure 22 a). Synthesis of corresponding particles was performed in aqueous solution via microwave-assisted co-precipitation. Domestic microwave oven (650 W, 2.45 GHz) was used as microwave source, reaction media was heated at 60% of the maximum microwave oven power for 20 min under reflux) [273]. Nitrates of corresponding lanthanides were used as Ln precursors, $NH_4H_2PO_4$ was used as phosphorus source. The reported nanorods crystallized in rhabdophane phase, had 6-30 nm diameter and were up to 400 nm in length. Ekthammathat et al. reported another microwave-assisted co-precipitation synthesis of uniform rhabdophane phase $LaPO_4$ nanorods (Figure 22 b) [274]. $LaCl_3$ salt was used as source of lanthanum ions and Na_3PO_4 was used as phosphorus source. Syntheses of $LaPO_4$ nanorods were performed in aqueous media, Electrolux EMS 2820 2.45 GHz microwave oven was used as microwave

source, reaction mixture was heated for 60 min using 180 W power. Fabrication of highly luminescent $LaPO_4:Ce^{3+}/Tb^{3+}$ nanoparticles (Figure 22 c) with sizes of ca. 21 nm were reported by Bühler et al. [275]. Chlorides of corresponding lanthanides were used as Ln^{3+} precursors, H_3PO_4 was used as phosphorus source. Notably, ionic liquid ($[MeBu_3N][(SO_2CF_3)_2N$) was used as a reaction media. Aim of the authors was to use fast heating (which was possible due to usage of ionic liquid as solvent) to achieve fast precipitation and, therefore, growth of monodisperse crystalline nanoparticles of corresponding lanthanide orthophosphate. Temperature of reaction mixture was elevated to 300 °C and maintained for 10 s.

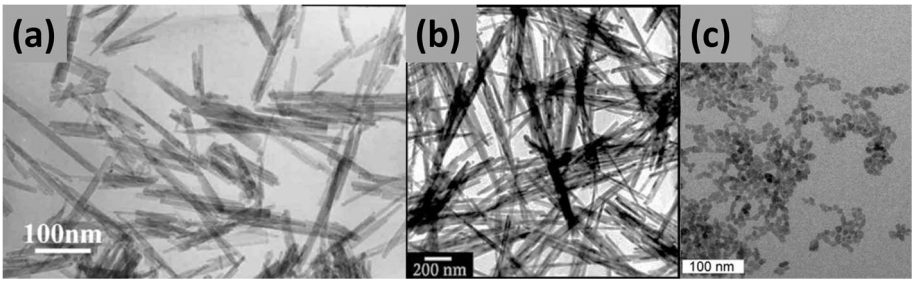

Figure 22. Various $LnPO_4$ nanoparticles obtained via microwave-assisted co-precipitation method. (a) $LaPO_4:Eu^{3+}$ nanorods (TEM image adopted from [273]; (b) $LaPO_4$ nanorods (TEM image adopted from [274]; (c) $LaPO_4:Ce^{3+}/Tb^{3+}$ nanoparticles (TEM image adopted from [275].

4.4. Sol-gel method

Sol-Gel method is a convenient approach to obtain various inorganic materials (glasses, ceramics, composites). During sol-gel synthesis, aqueous colloids are prepared from the precursors, which are then aged to obtain a colloidal gel. These colloidal gels are then heated to remove volatile compounds (solvent, organics) and crystallize the desired material [276]. Sol-gel synthesis is suitable approach to obtain large variety of porous nano and micro structures, thin films, glasses, foams, fibers. Sol-gel approach is suitable for low-temperature synthesis. Such low-temperature products tend to have relatively low crystallinity, hence additional calcination of the product is often needed in order to increase crystallinity of the final product [277, 278].

Recently, Ahmadzadeh et al. reported sol-gel synthesis and detailed investigation of synthesis parameters to $LaPO_4$ nanoparticle formation [175]. $LaPO_4$ nanorods obtained under pH value of 2 are given in Figure 23 a. After

synthesis, $LaPO_4$ particles were dried for 24 hours (80 °C) and then dehydrated at 400 °C. Interesting approach to obtain Eu^{3+} doped $LaPO_4:Eu^{3+}$ nanotubes (Figure 23 b) synthesis via sol-gel method was reported by Fisher et al. [279]. These $LaPO_4:Eu^{3+}$ nanotubes were obtained by using a template for growth. The obtained nanotubes reflect the shape of the template used (alumina membrane). Rajesh et al. reported the sol-gel synthesis of $LaPO_4$ nanorods [174]. $LaPO_4$ nanorods were obtained from $La(NO_3)_3$ and H_3PO_4 as precursors and exhibited rhabdophane phase as-prepared. Phase transformation from rhabdophane to monoclinic was observed during calcination process. Authors of this paper demonstrated a versatile application of such method and particles as functional nanocoatings by preparing a $LaPO_4$ coating on glass surface (see Figure 23 c).

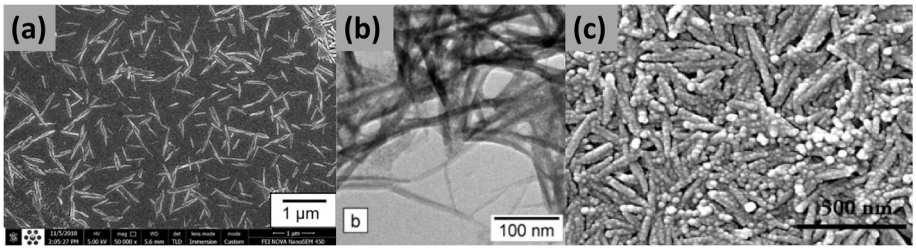

Figure 23. Various $LnPO_4$ nanoparticles obtained via sol-gel method. (a) $LaPO_4$ nanorods (TEM image adopted from [175]); (b) $LaPO_4$ nanorods (TEM image adopted from [279]); (c) $LaPO_4$ nanorods (TEM image adopted from [174]).

4.5. Sonochemical method

The sonochemical synthesis method allows to rapidly yield lanthanide orthophosphates. This method is based on ultrasonic treatment of reaction media. During sonication process, ultrasound energy diffuses in the reaction media. As a result, small bubbles are produced within reaction media. Due to acoustic cavitation in reaction media, localized spots of high energy (reaching nearly 5000 K temperature and 20 MPa pressure) are generated by the bubbles. Therefore, these high spots of high energy induce crystallization and growth of nanoparticles within reaction media [280, 281].

Sonochemical synthesis of $LaPO_4$ and $CePO_4$ nanorods was reported by Phuruangrat et al. [18]. Nitrates of corresponding lanthanides were used as precursors and Na_3PO_4 was used as phosphorus source during the synthesis. SEM image of $CePO_4$ nanorods is given in Figure 24 a. These nanorods possessed rhabdophane phase and were synthesized by simply mixing the solutions of precursors, setting pH value to 1and treating ultrasonically for

4 h. Various lanthanide orthophosphates were prepared via sonochemical approach by Yu et al. [176]. $GdPO_4$ nanorod bundles of rhabdophane phase, reported in this paper, are represented in Figure 24 b. Morphologies, crystalline phases and some of the luminescent properties of lanthanide orthophosphates were evaluated by the authors as well. Bundles were around 100 nm in diameter and were up to 500 nm in length. Last example of sonochemical synthesis, represented in Figure 24 c, are $CePO_4:Tb^{3+}@LaPO_4$ core-shell nanorods reported by Zhu et al. Obtained nanorods had 10-30 nm diamaters and were up to 200 nm in length [177]. Both $GdPO_4$ nanorod bundles depicted in Figure 24 b and $CePO_4:Tb^{3+}@LaPO_4$ core-shell nanorods depicted in Figure 24 c were synthesized using using nitrate salts of lanthanides and lanthanide precursors and H_3PO_4 as a phosphorus source.

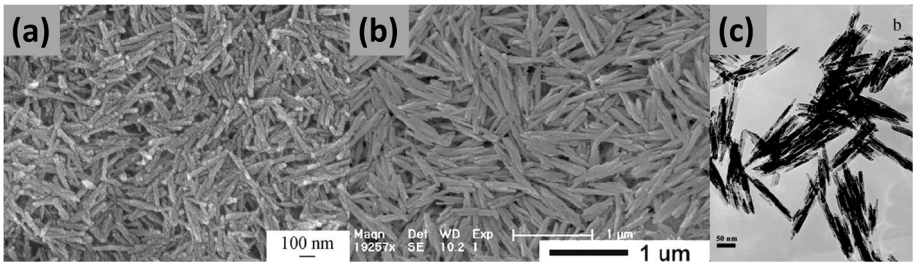

Figure 24. Various $LnPO_4$ nanoparticles obtained via sonochemical method. (a) $CePO_4$ nanorods (SEM adopted applied from [18]); (b) $GdPO_4$ nanorod bundles (SEM image adopted from [176]; (c) $CePO_4:Tb^{3+}@LaPO_4$ nanorods (TEM image adopted from [177]).

4.6. Microemulsion-based synthesis

Microemulsion-based synthesis. Even though there are only few reports of microemulsion-based synthesis of lanthanide orthophosphates, this distinctive synthesis method is worth mentioning. Inverse microemulsion (water in oil) is a stable solution, where small water droplets are dispersed throughout the volume of reaction media, which is mostly “oil” phase. These water droplets are surrounded by surfactant monolayer and can be referred to as “reverse-micelles”. These reverse-micelles are dispersed in this “oil-rich” reaction media. These reverse-micelles with the water inside act as confined spaces for nanoparticle growth [282, 283].

$LaPO_4:Eu^{3+}$ nanorods represented in Figure 25 a were synthesized via microemulsion synthesis by Filho et al. [284]. $La(NO_3)_3$ solution was used as precursor for Ln^{3+} ions and $NaH_2PO_4 \cdot H_2O$ was used as phosphorus source. Citric acid was used as complexing agent, cetyltrimethylammonium bromide

(CTAB) and 1-butanol were used as surfactant and co-surfactant, respectively. The reaction system was kept under reflux for 24 hours.

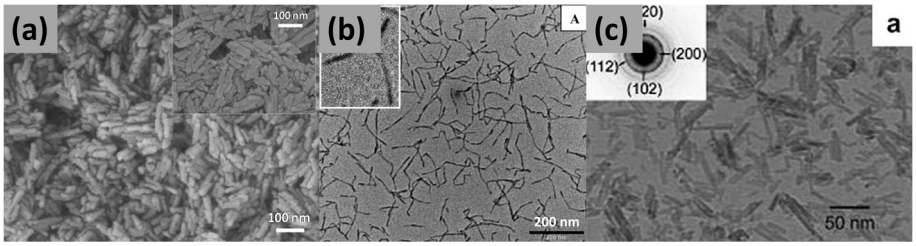

Figure 25. Various $LnPO_4$ nanoparticles obtained via microemulsion-based method. (a) $LaPO_4:Eu^{3+}$ nanorods (TEM image adopted from [284]); (b) $CePO_4$ nanorods (TEM image adopted from [17]); (c) $La_{0.45}Ce_{0.45}Tb_{0.1}PO_4$ nanorods (TEM image adopted from [285]).

Xing et al. reported microemulsion synthesis of $CePO_4$ nanowires (Figure 25 b) [17]. In a typical synthesis authors used cerium nitrate and NaH_2PO_4 solutions as precursors. Dioctyl sulfosuccinate sodium salt (or NaAOT) isooctane solution was used as surfactant solution to form microemulsion. However, the described particular approach is not convenient due to long formation times, since the $CePO_4$ nanowires shown in the Figure 25 b took one month to form. A very interesting variation of microemulsion method was described by Chai et al. [285]. Authors of this report obtained Ce and Tb doped $LaPO_4$ nanorods (Figure 25 c) using methyl methacrylate as "oil" phase (CTAB was used as surfactant), which was later on polymerized (2,4,6-trimethylbenzoyldiphenylphosphine oxide was used as photoinitiator). As a result, highly luminescent, transparent $LaPO_4:Ce^{3+}$, Tb^{3+}/PMMA composite was obtained. Nitrate salts of corresponding lanthanides were used as Ln^{3+} source and $(NH_4)_2HPO_4$ was used as a phosphorus source. Notably, nanorod formation in this case took around 1 hour under 50 °C temperature, nanorods crystallized in rhabdophane phase. Authors report that obtained nanorods were around 2-6 nm in diameter and their lengths varied from 10 to 55 nm.

5. Basics of colloidal nanoparticle stability

Nanoparticles usually possess large surface area and, in order to minimize their surface energy, they tend to agglomerate to achieve the stabilized state [286]. Nanoparticle affinity to agglomerate is dependent on several factors such as particle size, concentration of the colloid, composition of the solution in which particles are dispersed, particle morphology and their surface chemistry, and so on [287-289]. Most importantly, agglomerated particles cannot form stable colloids. Hence, agglomerated nanoparticles cannot even be applied for implied purposes theoretically, not to speak practically. Therefore, stabilization of nanoparticles is needed to prevent formation of nanoparticle agglomerates and ensure their further applicability.

Overall stability of nanoparticle colloids. Colloidal stability of nanoparticles is achieved by preventing nanoparticle aggregation process. So basically by evaluating colloidal stability we just express how much nanoparticles are resistant to return back from their colloidal (dispersed) state to their agglomerated state. In ideal case, the agglomeration should be prevented or occur at adequately slow rate. The main forces responsible for stability/instability of colloids are explained by DLVO (*Derjaguin, Landau, Verwey* ir *Overbeek*) theory [290]. According to DLVO theory, the stability of colloids is determined by *Van der Waals* attraction and repulsion between nanoparticles dispersed within colloid as they approach to each other due to Brownian motion. Overall interaction energy (Φ_T) between nanoparticles can be expressed as a sum of *Van der Waals* attraction force (Φ_A) and electrostatic repulsion force Φ_R [291, 292].

$$\Phi_T = \Phi_A + \Phi_R \quad \text{(Eq. 3)}$$

When electrostatic repulsion force is stronger than *Van der Waals* attraction force then the colloid will be stable and vice versa.

Colloidal stability of nanoparticles can be achieved either electrostatically or sterically. In most cases, electrostatic stabilization, induced by charge repulsion, does not ensure reliable enough stability and prevention from agglomeration. Thus, steric stabilization, achieved by attaching surfactant to particle surface (either by chemical bonds or electrostatic interactions), is more effective and popular, because the created steric barriers prevent particles from approaching too close to agglomerate [293, 294].

Since colloids of nanoparticales are often unstavle, colloidal nanoparticle stability requires to be enhanced. Notably, aggregation is also dependent on the concentration of nanoparticles – the bigger nanoparticle concentration in

the colloid, the more often their collision occurs, the bigger agglomeration rate is [295].

Electrostatic stabilization. The main force responsible for electrostatic stabilization in aqueous media is electrostatic repulsion between nanoparticles. This repulsion force is caused by so called electrical double layer (Figure 27). When nanoparticles of the same charge approach close to each other, their electrical double layers start to overlap. Hence, repulsion force between particles emerges. If this repulsion force is strong enough – nanoparticles are electrostatically stabilized [296, 297].

The driving force for the formation of electrical double layer is surface charge of nanoparticles. When nanoparticles are dispersed in aqueous media, a charge is introduced on nanoparticle surface. Several processes, contributing to surface charge of nanoparticles, can occur on the surface [298]:

- Protonation/deprotonation of functional groups that are present on nanoparticle surface (carboxyl, hydroxyl, amino, etc.). In case of lanthanide orthophosphate both lanthanide oxygen and phosphate oxygen sites on the surface can be protonated [299].

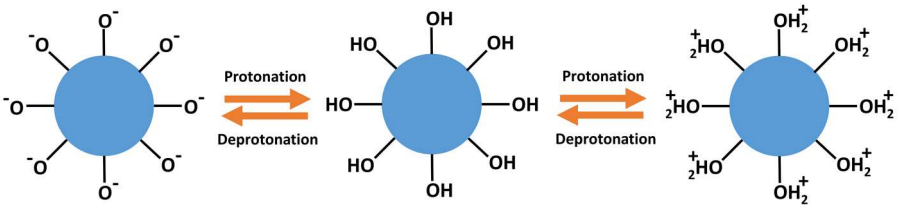

Figure 26. Visual representation of protonation/deprotonation of hydroxyl groups positioned on particle surface.

- Adsorption of ions or low molecular weight ligands (citrate, tartrate, etc.) on the nanoparticle surface [300].

Let's say we have a nanoparticle with a negative surface charge. In that case, when such nanoparticle is in contact with ionic-liquid (for example water), its negative charge is balanced by positively charged counter-ions (ions of opposite charge) originating from the surrounding liquid. These counter-ions form adjacent layer on the nanoparticle surface (Stern layer). Even though additional counter-ions are attracted by negatively charged nanoparticle surface, they are repelled by Stern layer. Additionally, negatively charged ions are also attracted by the positively charged Stern layer. The amount of negative ions attracted by Stern layer gradually decreases until equilibruium is attained, meaning that electric potential constantly changes

throughout the layer. This layer, composed of positively and negatively charged ions, is called diffuse layer and both these layers together (diffuse and Stern) are referred to as electrical double layer (schematic representation of electrical double layer is given in Figure 27) [301, 302].

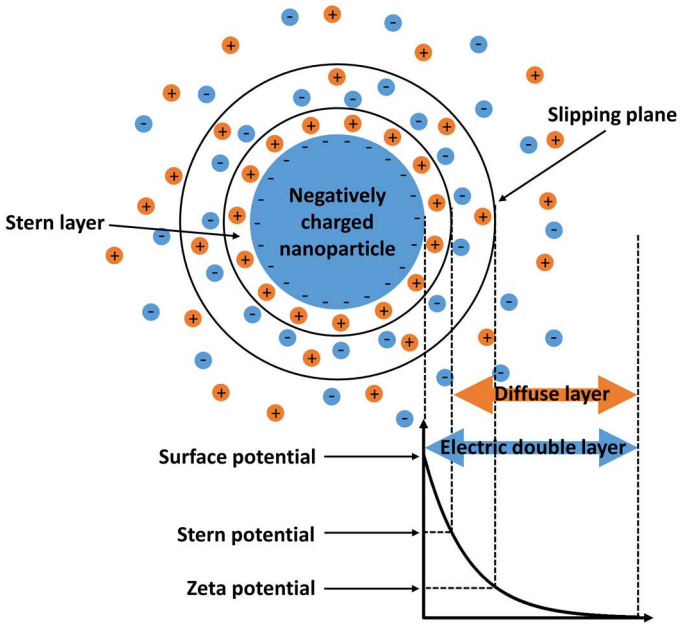

Figure 27. Visual representation of electric double layer.

As visualized in Figure 27, the slip plane is the boundary between Stern and diffuse layers. The electrical potential measured in slip plane is referred to as zeta potential. We judge the stability of electrostatically or electrosterically stabilized nanoparticle colloids based on their zeta potential values. Zeta potential is determined by measuring electrophoretic mobility of nanoparticles in a special cuvette. It is considered that the particles with absolute zeta-potential value higher than 28 mV exhibits colloidal stability, which is induced by electrostatic repulsion. This prevents them from forming agglomerates and coagulates [303, 304].

Potential energy curve between two nanoparticles is depicted in Figure 28 and visually represents the concept of DLVO theory. Based on this curve, we can conclude that stability is closely related to distance between nanoparticles. As long as distance between two nanoparticles is maintained large enough – colloidal stability is ensured. As can be seen from Figure 28, there are two minimum of potential energy observed. Primary minimum is observed when

particles are very close to each other. At this point irreversible aggregation occurs, meaning that such aggregate is not redispersible anymore. Secondary minimum, observed when distance between nanoparticles is larger, is marked by nanoparticle agglomeration. Agglomerated nanoparticles (agglomerates) are redispersible [291, 292].

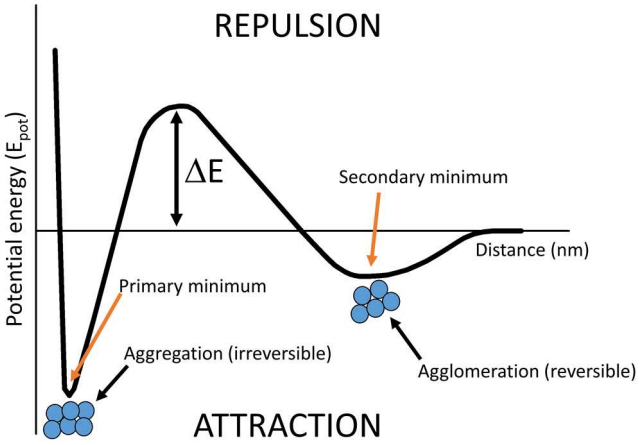

Figure 28. Graphical representation of DLVO theory.

Steric stabilization is rather straightforward, but reliable approach to achieve colloidal stability (represented in Figure 29). In order to achieve steric stabilization, nanoparticles are coated with various macromolecules. Such modified nanoparticles are still attracted to each other by *Van der Waals* forces, but the macromolecules attached on the nanoparticle surface create a physical barrier, which prevents particles approaching close enough to agglomerate [303]. In terms of reliability, steric stabilization is considerably less sensitive to ionic strength of the media, temperature, and pH value in comparison to electrostatic stabilization [305, 306]. Also, usage of polymers can enhance biocompatibility of nanoparticles by preventing/inhibiting the rate of protein corona formation on the nanoparticle surface [307].

Natural polymers, such as chitosan or dextran, or synthetic polymers, such as PEG, PVP, PVA, are often used to achieve steric stabilization. Additionally, low molecular weight surfactants, such as TWEEN, CTAB, TRITON, can also be used to enhance the stability of various nanoparticle systems [308-310]. Polymer (or surfactant) chains must be dense and long enough to overcome attraction force between nanoparticles. If the chains are too short – colloids will be unstable and particles will agglomerate [311].

Electrosteric stabilization (represented in Figure 29) can be described as colloidal stability achieved by combining both electrostatic and steric stabilization mechanisms. Generally, electrosteric stabilization is achieved by usage of charge bearing polymers (polyelectrolytes). Agglomeration of nanoparticles, coated with such polymers, will be prevented not only by physical barrier created by polymers, but also by electrostatic repulsion due to surface charge created by adsorbed polyelectrolyte molecules [303].

Polyelectrolytes of various architectures can be used to achieve electrosteric stabilization – homopolymers, blockcopolymers, graft polymers, etc. It is necessary that polyelectrolytes, used for electrosteric stabilization, bear ionizable functional group(s) in its structure, for example, carboxyl or quaternary amine group [312].

Polyelectrolyte adsorption on nanoparticle surface is also dependent on surface chemistry and charge of the particle. For example, adsorption of cationic polyelectrolyte is favored when nanoparticle surface bears negative charge [294, 313].

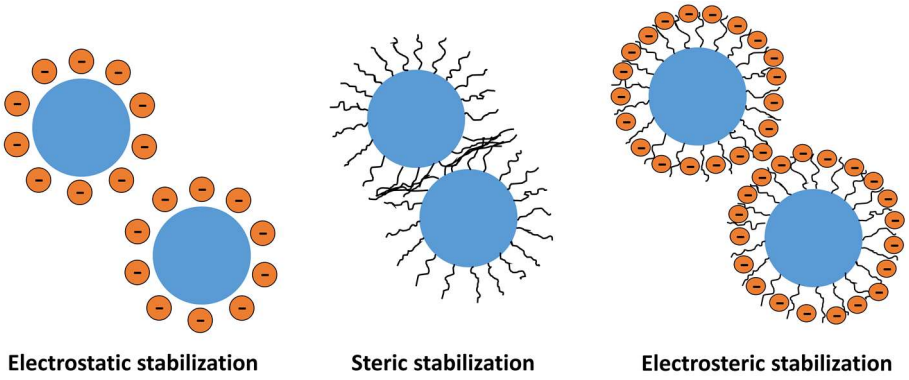

Figure 29. Nanoparticle stabilization mechanisms.

6. Lanthanide orthophosphates as functional nanomaterials

Functional nanomaterials can offer a set of new and unique properties. Hence, a huge focus is given for the development of various inorganic nanoparticles in order to create various functional nanomaterials for application in various fields, the most frequent ones being biomedical and technological fields [314, 315].

6.1. Nanoparticle surface functionalization

Unmodified luminescent nanoparticles usually carry only one intended function. Surface functionalization of nanoparticles can extend nanoparticle functionality by yielding multifunctional nanoparticles. Yet, surface functionalization of nanoparticles remains an rapidly evolving field of nanoscience [316, 317].

Even though functionalization of nanoparticles can be very complex, the material scientists and chemists have successfully functionalized nanoparticles with a variety of different ligands, polymers, and (bio)molecules. These modifications offer wide variety of benefits from increased stability and biocompatibility to drug delivery and selective targeting of cancer cells [318].

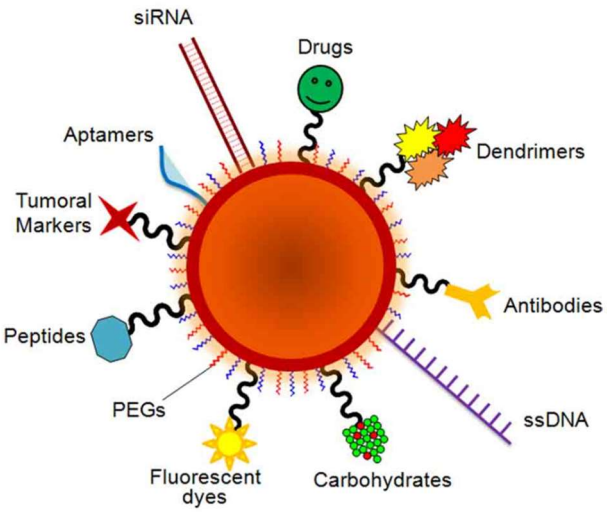

Figure 30. Schematic representation of possible surface modifications. Image adopted from [319].

Among possible candidates for functional nanomaterials, lanthanide-based inorganic nanoparticles are also considered to be very promising hosts. In the next paragraph, the most frequent intended applications of lanthanide orthophosphates will be summarized.

6.2. Applications in nanomedicine

MR imaging. The unpaired electrons in 4f shell of lanthanides are the reason of lanthanide magnetic properties (lanthanides have paramagnetic properties at room temperature). Particularly, Gd^{3+} ions possess seven unpaired electrons in 4f shell. Due to such unique electronic configuration of Gd^{3+} ion, gadolinium chelates are widely used as magnetic resonance (MR) contrast agents in medicine. They are commonly used in chelated forms such as Gd-DTPA (commercial name Magnevist®) or Gd-DOTA (commercial name Dotarem). Gd-based contrast agents are suitable to be used as T1 contrast agents, since they are known to decrease longitudinal relaxation time of water protons. On the contrary, Dy^{3+} and Ho^{3+} contrast agents, having larger magnetic moments than Gd^{3+}, are suitable candidates as T2 contrast agents, since they shorten transverse relaxation time of surrounding water protons [320, 321].

The use of some commercial chelated gadolinium contrast agents on patients with kidney problems was restricted by World Health Organization back in 2009. It is because Gd^{3+} ions are highly toxic and, even in chelated form, there still is a risk of Gd^{3+} release into organism [320, 322]. Gd^{3+} ions are a lot less likely to be released when incorporated into crystalline structure in the form of inorganic Gd-based nanoparticles. Hence, Gd-based lanthanide orthophosphate nanoparticles can be considered as promising T1 contrast agents, since solubility of lanthanide orthophosphates is known to be very low. This was confirmed by Hifumi et al. [31]. He and co-authors reported hydrothermal synthesis of dextran coated $GdPO_4$ nanorods. The obtained nanorods were used for tumor imaging in rabbit. Results indicated that dextran coated $GdPO_4$ nanorods effectively visualized tumors by only using 1/10 amount of clinical dose compared to commercially used Gd-based contrast agent Magnevist® (see Figure 31 for comparison). According to authors, $GdPO_4$ nanorods needed to accumulate for 24 hours for the best contrast. Authors claim that $GdPO_4$ nanorods revealed tumors more visibly due to EPR effect towards nanorods, since Magnevist® molecules are too small to be affected by EPR effect.

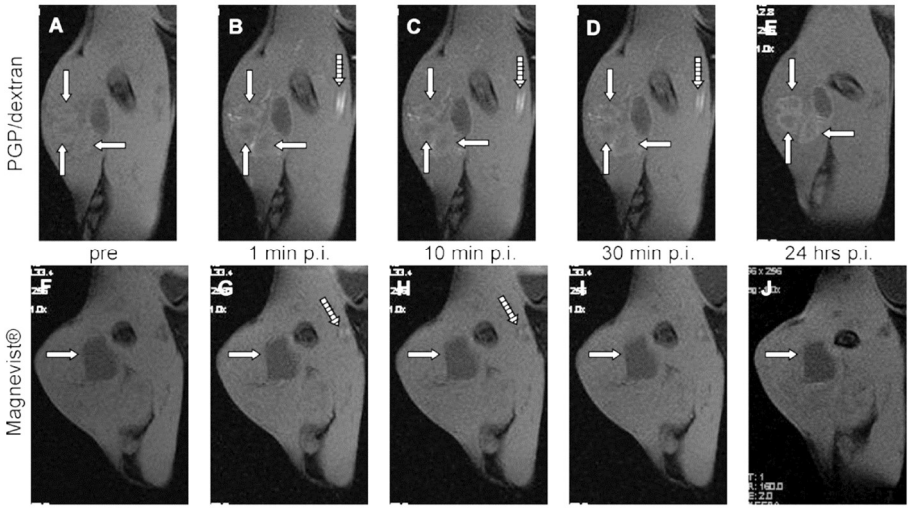

Figure 31. T1 weighted MR images of $GdPO_4$ and Magnevist® of tumour bearing rabbit femorial region at 5 different time points after contrast agent administration. White arrows mark tumour regions. Image adopted from [31].

Multimodal imaging. Depending on composition, nanoparticles, including lanthanide orthophosphates, can have multiple imaging modes. Multimodal imaging is considered as the major advantage, as such multimodal imaging nanoparticles can provide more versatile observation. Therefore, there is a need for development of such particles. One of the examples could be multimodal imaging particles with capability of both T1 and T2 MR imaging. Single mode MR imaging may not always produce MR images of good quality. If both modes are available, more accurate MR monitoring would be possible. For example, Zhan et al. reported mesoporous carbon spheres co-functionalized with γ-Fe_2O_3 and $GdPO_4$ nanoparticles with the purpose for dual mode (T1 and T2) MR imaging [190, 323].

Another example of multimodal imaging could be nanoparticles with possibility to provide combined bioimaging and MR imaging option. Lanthanide orthophosphate nanoparticles, especially $GdPO_4$, are also being investigated as potential multimodal imaging particles. The main advantage of $GdPO_4$ nanoparticles is that gadolinium orthophosphates are a suitable matrix for doping with other optically responsive lanthanides (e.g., europium, terbium, neodymium, etc.). Hence, such lanthanide doped $GdPO_4$ nanoparticles can be considered as possible candidates for multimodal imaging [192, 324-326].

Ren et al. reported synthesis of $GdPO_4$ nanorods as potential dual-mode bioprobes [172]. $GdPO_4$ nanorods were synthesized via PVP assisted hydrothermal approach and were doped with Eu^{3+} ions and Yb^{3+}/Er^{3+} ions. Results indicated potential applicability combined MR and bioimaging (both downconversion and upconversion possibilities were tested, for images see Figure 32).

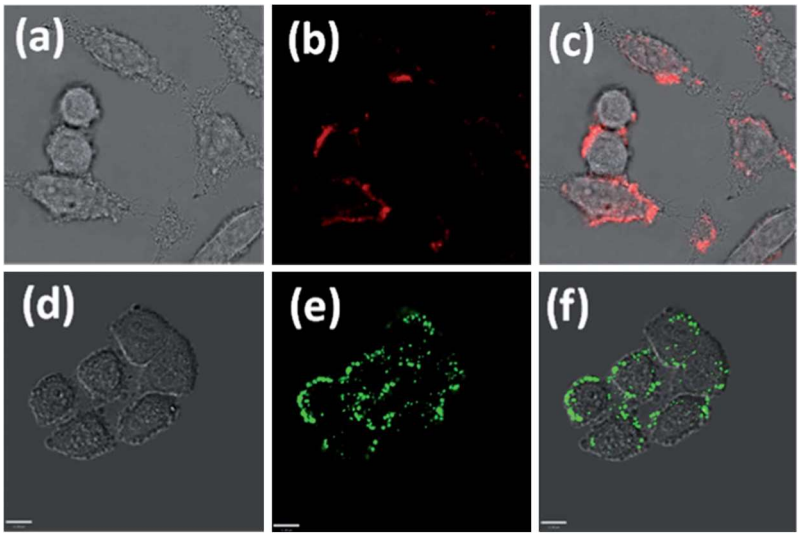

Figure 32. Images of luminescence-based bio-imaging of A549 cells. Bright (a), dark (b) and overlapped (c) images of $GdPO_4:Eu^{3+}$ under UV excitation. Bright (d), dark (e) and overlapped (f) images of $GdPO_4:Yb^{3+}/Er^{3+}$ under 980 nm excitation. Images were adopted from [172].

Therapeutic. Various nanoparticles are being actively exploited as potential platforms for drug delivery [3, 4]. Lanthanide orthophosphate nanoparticles are also being considered as suitable candidates for multifunctional drug delivery platforms, as they may have other pre-installed functionalities, for instance, MR imaging or bio imaging in addition to the intended drug-delivery function [192, 324-326].

A good example would be synthesis of DOX-loaded $GdPO_4:Nd^{3+}$ hollow spheres (visual representation in Figure 33) reported by Yang et al. [324]. The release mechanism of the drug is pH induced, since $GdPO_4$ particle surface charge is known to be strongly pH dependent as will be shown later in this thesis. DOX molecules were loaded on particle surface via interaction between positively charged protonised amino group, present in DOX molecule, and negatively charged surface of the particle. Drug loading and release efficiency along with *in-vivo* NIR and X-ray imaging was investigated

with these multifunctional theranostic probes. The obtained results indicated that 40% of the DOX was "released" from particle surface in period of 10 h under pH value of 5. Also, excellent *in-vivo* NIR and X-ray imaging properties were demonstrated. Authors claim that X-ray imaging quality was even superior in comparison to commercially used iobitridol.

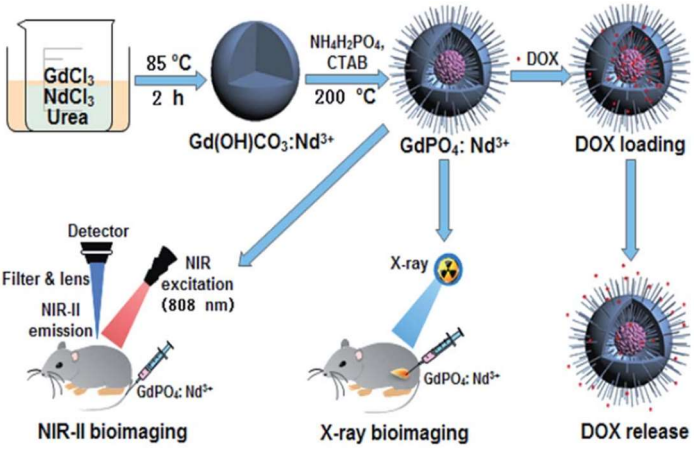

Figure 33. Visual representation of design and application of multifunctional theranostic DOX-loaded $GdPO_4:Nd^{3+}$ probe. Image adopted from [324].

6.3. Lanthanide orthophosphates for nuclear waste management

Due to lanthanide chemical similarity to actinides, lanthanide orthophosphates have long been in the spotlight of scientists as an attractive material for the immobilization and storage of radioactive actinides [327, 328].

The naturally occurring mineral monazite is an orthophosphate composed of a mixture of various lanthanides and actinides (Ce, La, Nd, Th, U) [329]. In general, monazite phase lanthanide orthophosphates are known as chemically and thermodynamically stable compounds. The fact that radioactive actinides, like Th and U, are naturally found bound in the form of monazite-structured minerals, confirms the monazite structure resistance to radiation damage. Lanthanide orthophosphates are also known as chemically stable, and insoluble in water materials [327, 330]. Lanthanide orthophosphates are known to be stable even under very high temperatures and pressures [331, 332]. It is known that lanthanide orthophosphates can successfully immobilize (incorporate) actinides in their structure. In addition, monazite-phase lanthanide orthophosphates have even been proposed as a

potential candidate for immobilization and storage of excess plutonium from nuclear weapons [216].

It is known that a partially hydrated rhabdophane phase forms on the surface of the monazite crystals when stored in water for long durations. This surface layer of rhabdophane phase can also play an important role in controlling the solubility of "captured" actinides. It has been reported that the rhabdophane phase, which, due to interaction with water over a long period of time, was formed on the surface of monazite granules, can act as a protective barrier by helping to inhibit and slow the release of actinides back into solution or the environment [333].

To conclude, lanthanide orthophosphates can be considered as suitable hosts for disposal of actinides by incorporating them into highly stable crystalline structure.

7. Final remarks and conclusions of the literature review

The literature review part was mainly focused to understandably introduce reader to the current situation in nanomaterial science, diversity of nanomaterials, their functionalities, and trends, so that the reader could easily understand the research and achievements presented in this thesis.

In this literature part, possible synthesis methods to obtain lanthanide orthophosphates were systematically reviewed and discussed to govern the current trends and achievements in the synthesis of lanthanide orthophosphates. The discussed synthesis methods can be useful to better understanding the influence of synthesis parameters upon particle formation and also, if needed, to help choosing suitable a synthesis strategy to obtain particles of desired size, phase, and shape. Possible factors responsible for lanthanide orthophosphate anisotropic growth were also discussed. Brief introductions to luminescence and stabilization basics were also provided for better understanding of the experiments presented in this thesis.

Short discussion of possible lanthanide orthophosphate functionalization and applications has also shown that lanthanide orthophosphates are promising hosts to be used as templates for development of multifunctional theranostic probes. The ability to modify and functionalize these particles opened a new prospect for further lanthanide orthophosphate applicability as multifunctional theranostic probes in the field of biomedicine. In my opinion, researchers should continue exploiting multimodal imaging and surface functionalization of lanthanide orthophosphate nanoparticles. Development in the field of functionalized lanthanide orthophosphate nanoparticles may contribute to the treatment and diagnostics of various diseases, including cancer.

To conclude, lanthanide orthophosphate particles are very diverse class of materials with numerous applications which are still emerging. With the recent advances and ongoing efforts in improving particle size and shape, synthesis efficiency, and extending their biomedical applications, it is hopeful that the wide implementation of such particles will take place in the coming years.

8. Experimental section

8.1. Instrumental setup

Hydrothermal synthesis of particles was performed using hydrothermal reactor *highpreactor* by BERGHOF and BTC-3000 Temperature Controller and Data Logger by BERGHOF.

Particles were centrifuged using Centrifuge 5804 by Eppendorf.

Freeze drying of the frozen $GdPO_4$ hydrogel (containing $GdPO_4$ nanofibers) was performed in a *Labconco FreeZone 2.5* freeze-dryer operated at 0.010 mBar pressure and -82 °C temperature. Samples were freeze dried for 48 h

Crystalline phase of the particles was identified by performing powder XRD measurements using following devices:

XRD measurements for Figure 35 were carried out using parallel beam geometry on a Bruker D8 Advance da Vinci design diffractometer. The patterns were analyzed with the software Topas version 4.2 (Bruker AXS).

Rigaku MiniFlexII working in Bragg-Brentano ($\theta/2\theta$) focusing geometry was used for remaining XRD measurements. The 2θ angle was scanned in the range of $10° \leq 2\theta \leq 80°$ (step width 0.02° and scanning speed 5 °/min.) using Ni-filtered Cu Kα radiation.

Cell parameters were calculated using Le Bail method.

Scanning electron microscopy (SEM) images were taken with high-resolution scanning electron microscope (FE SEM) Hitachi SU-70, with accelerating voltage up to 10 kV. Samples for SEM were prepared by dispersing particles in distilled water and adding 20 μL of aqueous dispersion on a Si plate.

Transmission electron microscopy (TEM) was performed using FEI Tecnai F20 X-TWIN transmission electron microscope. Measurements were carried out using 200 kV accelerating voltage, images were obtained using Gatan Orius CCD camera.

Zeta-potential values were measured at 25 °C with Malvern Zetasizer Nano ZS using Smoluchowski model.

Dynamic light scattering (DLS) measurements were carried out using a ZetaSizer Nano ZS (*Malvern*) equipped with a 4 mW He–Ne laser emitting at a wavelength of 633 nm. Measurements were performed at 25 °C and an angle of 173° using noninvasive back-scattering (NIBS) technology. Using this method the particle size detection range is 0.3 nm – 10 μm. The size distribution data was analyzed using Zetasizer software from *Malvern*.

Isoelectric point (IEP) values of bare and modified $GdPO_4$ particles with different morphology were determined by measuring zeta potentials under different pH values in aqueous dispersions. The pH of $GdPO_4$ dispersions were adjusted from 2 to 10 using 0.1 M HNO_3 and 0.1 M NH_4OH solutions, respectively. Zeta-potential values were measured with Malvern Zetasizer Nano ZS using Smoluchowski model at 25 °C temperature.

Thermogravimetry/Differential Thermal Analysis (TG-DTA) measurements of the synthesized particles were performed using Perkin Elmer STA 6000 under air atmosphere. The heating rate was 10 °C/min. The weight of analyzed samples was ca. 5.5 mg.

Fourier transform infrared (FTIR) spectroscopy measurements of rare-earth orthophosphate samples were performed in the range from 520 to 3800 cm^{-1} with resolution of 4 cm^{-1} using Perkin Elmer FT-IR Spectrometer Frontier.

Specific surface area (SSA) was determined by conducting nitrogen adsorption measurements using a Micromeretics ASAP 2020 (Brunauer−Emmett−Teller method) device.

Magnetic properties were evaluated by encapsulating a fixed amount of rod-like $GdPO_4$ nanocrystals compactly into a Teflon tube with the inner diameter of 2.0 mm to increase density of the investigated material and to reduce possible displacement of the nanocrystals under an applied magnetic field. The real part of differential (AC) magnetic susceptibility of the sample, $\chi(H)$, was measured at a fixed frequency (f = 31.5 kHz) using AC susceptometer by under DC magnetic field, H, ranging from –1.0 to 1.0 T and small AC field ($h \sim 10^{-4}$ T) oriented parallel to the applied field H. Coil system of the susceptometer consisted of magnetically coupled primary and secondary coils. The pick up coil consisted of two identical sections wounded in opposite directions and connected in series to make the output signal in the absence of the sample equal to zero. The $M(H)$ curves were obtained numerically by integrating the $\chi(H)$ curves. The measurement equipment has been calibrated by using samples with certified magnetic properties.

Ultraviolet-visible (UV-Vis) spectroscopy measurements were performed using Edinburgh Instruments FLS980 spectrometer. Excitation spectra were were measured in the range from 250 to 550 nm. Emission spectra were measured in the range from 550 to 800 nm. Step width in both type of measurmeents was set to 0.5 nm. Each spectra were corrected using special correction file obtained from tungsten incandescent lamp certified by the National Physics Laboratory, UK (NPL).

8.2. Experimental conditions for controlled synthesis of $GdPO_4$ particles (nanorods, hexagonal nanoprisms, submicrospheres)

The starting materials were Gd_2O_3 (99.99%, Tailorlux), Eu_2O_3 (99.99%, Tailorlux), $NH_4H_2PO_4$ (99.9%, EuroChemicals), 66% HNO_3 (EuroChemicals), concentrated ammonia (EuroChemicals), tartaric acid (99.99%, EuroChemicals). $Gd(NO_3)_3$ was obtained by dissolving Gd_2O_3 in diluted nitric acid. Identically, $Eu(NO_3)_3$ was obtained by dissolving Eu_2O_3 in diluted nitric acid. The obtained transparent solution was evaporated to dryness to remove excessive nitric acid. The dry residue was dissolved in appropriate ammount of distilled water to obtain of 0.8 mmol/L concentration stock solution of $Gd(NO_3)_3$. All chemicals were used as received without any further purification.

The synthesis of nanorods, hexagonal nanoprisms and submicrospheres can be divided into multiple stages. During first stage, 0.5 mL (0.4 mmol) of $Gd(NO_3)_3$ was diluted to 20 mL using distilled water. Subsequently, 8 mmol of tartaric acid was weighted and dissolved in 20 mL of distilled water, added dropwise to $Gd(NO_3)_3$ solution, and then left stirring at room temperature for 30 min in order to Gd-tartaric acid complex to form (solution A). During second stage, pH value was set to 10 using ammonia solution. Afterwards, during third stage, required amount of $NH_4H_2PO_4$ (depending on synthesis) was dissolved in 20 mL of distilled water and added dropwise to solution A under vigorous stirring, while maintaining pH value around 10 forming and left stirring for 15 min. If needed pH was adjusted by using HNO_3 and ammonia solutions and then the volume of reaction mixture was adjusted to 80 mL by adding distilled water. During fourth stage, the reaction mixture was poured into Teflon bottle autoclave which was then sealed and placed into hydrothermal reactor. The hydrothermal reaction temperature in a typical procedure was maintained at 160 °C for 12 h. During fifth stage, after cooling down to room temperature, the reaction product was centrifuged under 7500 rpm (centrifuge model Eppendorph 5804) and washed with distilled water, this procedure was repeated 4 times, then precipitate was left to dry in air at 80 °C. In order to obtain desired morphology (nanorods, hexagonal nanoprisms and nanospheres) – certain $NH_4H_2PO_4/Gd^{3+}$ molar ratios during this synthesis were employed: to obtain nanorods $NH_4H_2PO_4/Gd^{3+}$ molar ratio was set to 10, to obtain hexagonal nanoprisms the molar ratio was set to 50 and in order to obtain nanospheres – molar ratio was set to 100. Note, that stirring during hydrothermal treatment is also very important factor as the

particles obtained would be agglomerated and would have very big distribution in size.

8.3. Experimental conditions for controlled synthesis of urchin-like $GdPO_4$ particles

In order to obtain urchin-like microparticles hydrothermal reactor was used. The conditions are similar as in case with nanorods, only difference is that pH has to be set to 1.7 (HNO_3 33% solution was used for pH control). During the first stage, 0.5 mL (0.4 mmol) of $Gd(NO_3)_3$ was diluted to 20 mL using distilled water. Subsequently, 8 mmol of tartaric acid was weighted and dissolved in 20 mL of distilled water, added dropwise to $Gd(NO_3)_3$ solution, and then left stirring at room temperature for 30 min. in order to Gd-tartaric acid complex to form (solution A). During second stage certain amount of $NH_4H_2PO_4$ was dissolved in 20 mL of distilled water and added dropwise to solution A under vigorous stirring. Finally, the pH value of the reaction mixture was set to 1.7 using HNO_3 solution. The reaction mixture was then transferred to Teflon autoclave and hydrothermally treated for 12 hours under temperature of 160 °C. After cooling down to room temperature, obtained urchin-like particles product were then centrifuged under 7500 rpm and washed with distilled water, this procedure was repeated 4 times, then precipitate was left to dry in air at 80 °C.

8.4. Experimental conditions for synthesis of PEO-MEMA

Materials. Poly(ethylene glycol) methyl ether methacrylate (PEO_{19}MEMA, M_n 950, *Aldrich*) and [2-(methacryloyloxy)ethyl] trimethylammonium chloride (METAC, 80% aqueous solution, *Aldrich*) were purified of inhibitors by passing the monomers through a column filled with basic alumina (type 5016A, *Fluka*). Methanol (MeOH, 99.8%, *Aldrich*), acetone (99%, *Aldrich*), ethylene glycol (EG, 99.5 %, *Fluka*), diethyl ether (Et_2O, 99%, *Aldrich*), carbon disulfide (CS_2, 99.9%, *Aldrich*), 1-butanthiol (99%, *Aldrich*), sodium hydride (NaH, 60% dispersion in mineral oil, *Aldrich*), iodine (I_2, 99.8%, *Aldrich*), and 4,4′-azobis(4-cyanovaleric acid) (ACVA, 98%, *Fluka*) were used as received.

The cationic brush-type polyelectrolytes p(METAC-*stat*-PEO_{19}MEMA) were prepared via RAFT (*Radical Addition Fragmentation Chain Transfer*) polymerization method from three different monomer feeds, METAC:PEO_{19}MEMA = 25:75, 45:55, and 65:35 mol% according to the

previously described procedure [15] with minor modifications (different chain transfer agent 4-(((butylthio)carbonothioyl)thio)-4-cyano-pentanoic acid (BCPA) was used). BCPA was freshly synthesized before use according to the published data) [334]. The synthesis scheme of p(METAC-*stat*-PEO_{19}MEMA) with different morphology is provided in Figure 34.

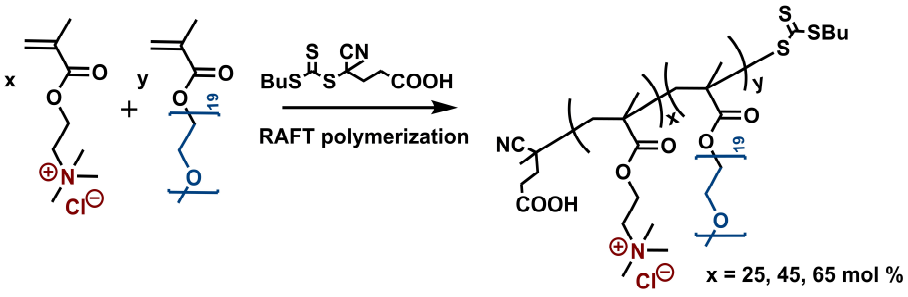

Figure 34. Synthesis scheme of cationic brush-type p(METAC-*stat*-PEO_{19}MEMA) polyelectrolytes via RAFT method.

Table 1. Characteristics of the synthesized p(METAC-*stat*-PEO_{19}MEMA) copolymers.

No.	Copolymer charge	$[METAC]_0$: $[PEO_{19}MEMA]_0$	M_n, kDa*	DP	[METAC]: $[PEO_{19}MEMA]$**
1.	Low	25:75	28.5	38	27:73
2.	Medium	45:55	24.6	41	47:53
3.	High	65:35	19.4	42	65:35

In all three cases, the molar ratio of initial synthesis components $[M]_0$:$[BCPA]_0$:$[ACVA]_0$ was the same, i.e., equal to 100:3:1, where $[M]_0$ represent the sum molar concentration of both monomers in the reaction feed. RAFT copolymerization of METAC and PEO_{19}MEMA was carried out in a round-bottomed flask sealed with silicone septum under an inert N_2 atmosphere in a 70:30 (v/v) mixture of ethylene glycol and water. The polymerization mixtures with an overall 15% monomer concentration were magnetically stirred for 12 h at 70 °C temperature. After synthesis, the mixture was cooled down and the flask was opened to air to quench the polymerization. Synthesized polymers were purified by ultrafiltration (10 kDa MWCO) against a 0.15 M NaCl aqueous solution and, later, against deionized water. Polymer solutions were concentrated using rotary evaporator and separated by freeze-drying. The NMR and SEC techniques were applied to

determine the composition and exact macromolecular parameters (average number molecular weight (M_n), dispersity (Đ), and calculated degrees of polymerization) of the synthesized polymers, respectively. The macromolecular parameter and exact composition of cationic polyelectrolytes used in this study are provided in Table 1.

8.5. Experimental conditions used for nanoparticle modificaton and determination of polymer adsorption

Preparation of dispersions. Colloidal 1 or 10 mg/mL dispersions were prepared by dispersing $GdPO_4$ particles of particular morphology in MiliQ water. The pH of each suspension was set to 10.6 using 1.0 M and then 0.1 M ammonium hydroxide (NH_4OH) solutions. All dispersions were treated by ultrasound in ultrasonic bath for 15 min to disassemble nanoparticle agglomerates. Afterwards, an appropriate amounts of cationic brush-type polyelectrolytes p(METAC-*stat*-PEO_{19}MEMA) were added to dispersion (up to 200 mg of polymer per gram of dry $GdPO_4$ particles) and ultrasonically treated again for 15 min.

Determination of polymer adsorption and surface potential. The adsorbed amount of cationic polyelectrolyte on the surface of $GdPO_4$ particles was evaluated by measuring the change of zeta potential as a function of added polymer to alkaline aqueous (pH 10.6) dispersions. The maximal polymer adsorption is observed at the point where the value of zeta potential reached the plateau. Cationic polyelectrolytes with three different compositions were evaluated and, thus, the effectiveness of all three polyelectrolytes was compared.

8.6. Experimental conditions for $GdPO_4$ nanofiber and aerogel preparation

$GdPO_4$ nanofiber preparation. The starting materials were Gd_2O_3 (99.99%, Tailorlux), $NH_4H_2PO_4$ (99.9%, EuroChemicals), concentrated HNO_3 (EuroChemicals), concentrated ammonia (35%, EuroChemicals), tartaric acid (99.99%, EuroChemicals). $Gd(NO_3)_3$ was obtained by adding concentrated HNO_3 dropwise into Gd_2O_3 dispersion until it becomes transparent. The obtained transparent solution was evaporated to dryness to remove excessive nitric acid. The dry residue was dissolved in appropriate amount of distilled water to obtain of 0.8 mol/L concentration stock solution of $Gd(NO_3)_3$. All chemicals were used as received without any further purification.

The synthesis can be divided into multiple stages. During the first stage, certain amount (0.5 mL (0.4 mmol) in typical experiment) of $Gd(NO_3)_3$ stock solution was diluted to 20 mL using distilled water. Subsequently, 1.200 g (8 mmol) of tartaric acid was weighted, dissolved in 20 mL of distilled water, and added dropwise to $Gd(NO_3)_3$ solution. The obtained solution was stirred at room temperature for 30 min in order to Gd-tartaric acid complex to form solution A. During the second stage, pH value was set to 7.0 using ammonia solution. Afterwards, during the third stage, certain amount of $NH_4H_2PO_4$ (from 0.4 mmol to 0.04 mol, depending on synthesis) was dissolved in 20 mL of distilled water and added dropwise to solution A under vigorous stirring, while maintaining pH value around 10 and left stirring for 15 min. The necessary pH value was adjusted by using HNO_3 and ammonia solutions and then the volume of reaction mixture was adjusted to 80 mL by adding distilled water. During the fourth stage, the reaction mixture was poured into Teflon bottle autoclave, which was sealed and placed into hydrothermal reactor. The hydrothermal reaction temperature in a typical experiment was maintained at 160 °C for 12 h. During the fifth stage hydrothermal reactor was cooled to room temperature, then obtained precipitate was centrifuged at 1500 rpm and washed with distilled water. This procedure was repeated 3 times, then the precipitate was diluted to 10 mL to form hydrogel.

$GdPO_4$ aerogel preparation. Pre-annealed aerogel was prepared by diluting $GdPO_4$ hydrogel to desired volume (10 mL). The diluted hydrogel was then frozen in refrigerator for 6 hours (-24 °C). Frozen $GdPO_4$ nanofiber hydrogel was then lyophilized (freeze-dried) for 48 hours, turning into a highly micro porous three dimensional network of $GdPO_4$ nanofibers (with diameter ranging from 5 to 15 nm) aerogel. Sublimation of water during freeze-drying process enables to avoid water-nanofiber related stresses which would occur during ordinary drying process, typically resulting in the collapse of the structure. As a result, it is possible to obtain three dimensional nanifibrous $GdPO_4$ aerogel of high quality and without any shrinkage or deformation of the initial volume and structure respectively. Obtained as-prepared $GdPO_4$ aerogel was then annealed under 915 °C temperature for 12 hours in order to induce phase transformation from trigonal to monoclinic.

9. Controlled hydrothermal synthesis of $GdPO_4$ particles

$GdPO_4$ particles characterized in this chapter were synthesized according to procedure described in detail in experimental section. During these experiments a novel synthetical approach to selectively obtain $GdPO_4 \cdot nH_2O$ particles of desired size and morphology was developed and published in 2020 [15]. Influence of an array of synthetic conditions on phase composition, morphology and colloidal stability of $GdPO_4 \cdot nH_2O$ particles obtained in hydrothermal solution was studied. It appears that under certain hydrothermal conditions shape and size $GdPO_4$ particles can be manipulated relatively easily, only by altering only one synthesis parameter – molar ratio between Gd^{3+} and phosphorus source. Alteration of this parameter led to formation of GdPO4 particles of various shapes (nanorods, hexagonal nanoprisms and submicrospheres) and sizes. Hydrothermal growth of $GdPO_4$ particles under different conditions and synthetical parameters was investigated. Obtained results are discussed in detail in this chapter. Among the conducted experiments four major series could be marked out varying: 1) PO_4^{3-} /Gd^{3+} molar ratio (for the sake of simplicity further referred to as <P>/Gd ratio), 2) Gd^{3+} absolute concentration, 3) pH, and 4) duration of synthesis.

9.1. Phase composition and thermal behaviour

Phase composition and purity of synthesized gadolinium phosphate particles was investigated by means of XRD. As expected, the selected range of synthetic conditions does not affect the phase composition of final materials. All synthesized samples consist of pure trigonal rhabdophane-type phase with composition $GdPO_4 \cdot nH_2O$. PDF ICDD 00-039-0232 card states that structure possess $P3_121$ space group. Recent precise synchrotron experiments established that rhabdophane phase may actually crystallize in a monoclinic structure. However, in this work the rhabdophane phase will be reffered to as a trigonal structure, due to lack of information such as atomic positions for the monoclinic structure. In order to avoid confusion, it was necessary to notice, that several recent works refer to $GdPO_4 \cdot nH_2O$ phase as monoclinic.

Despite the fact, that the phase is the same regardless the conditions of synthesis, the lattice parameters and the apparent crystallite sizes are different for different samples. XRD patterns of $GdPO_4 \cdot nH_2O$ samples synthesized via hydrothermal route with different <P>/Gd molar ratios (other conditions: 12 h at 160 °C, synthesized amount 0.4 mmol) are presented on Figure 35.

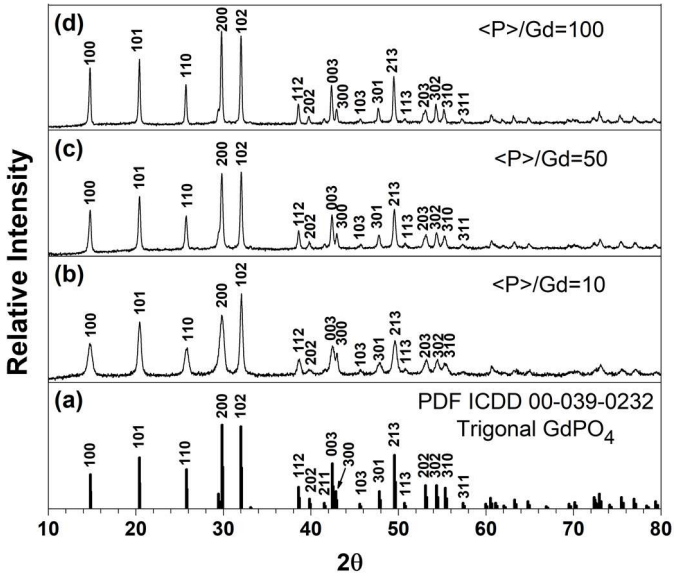

Figure 35. XRD patterns of different $GdPO_4 \cdot nH_2O$ samples (b, c, d) and a reference pattern of $GdPO_4 \cdot H_2O$ (a).

Using Le Bail method, lattice parameters for samples presented on Figure 35 were calculated (see Table 2). Lattice parameter *a* for sample with <P>/Gd ratio = 10 is very close to this parameter in reference structure from ICCD database ($GdPO_4 \cdot H_2O$, PDF ICDD 00-039-0232), but it grows and exceeds this value with the increase of <P>/Gd ratio. Meanwhile parameter *c* for all obtained samples is smaller than reported in ICCD database. It is worthy to note that both cell parameters, and, therefore, the volume of the unit cell, are growing with the increase of <P>/Gd ratio. This result indicates, that, although the phase remains the same, some structural differences between samples exist.

Table 2. Crystallite sizes and unit cell parameters of different $GdPO_4 \cdot nH_2O$ samples. Reference unit cell parameters were taken and can be indexed to trigonal $GdPO_4 \cdot H_2O$ (PDF ICDD 00-039-0232).

<P>/Gd ratio	Crystalite size (nm)	Cell parameter a (Å)	Cell parameter c (Å)
	-	6.905	6.326
10	20 (±3)	6.904 (±0.001)	6.311 (±0.001)
50	29 (±1)	6.918 (±0.001)	6.315 (±0.001)
100	38 (±2)	6.926 (±0.001)	6.320 (±0.001)

The most obvious source of nonstoichiometry for rhabdophane phases is crystalline water. The amount of crystalline water molecules in zeolitic channels of rhabdophane structure can differ and, as the water molecules are neutral, there's no problem with the electroneutrality. To prove this hypothesis and study condition and content of crystalline and absorbed water in samples synthesized in different conditions we conducted their analysis by means of IR spectroscopy and DT/TGA.

The recorded FTIR spectra of as prepared $GdPO_4 \cdot nH_2O$ samples with different <P>/Gd molar ratios of 10, 50 and 100 are given in Figure 36 a, b, and c, respectively.

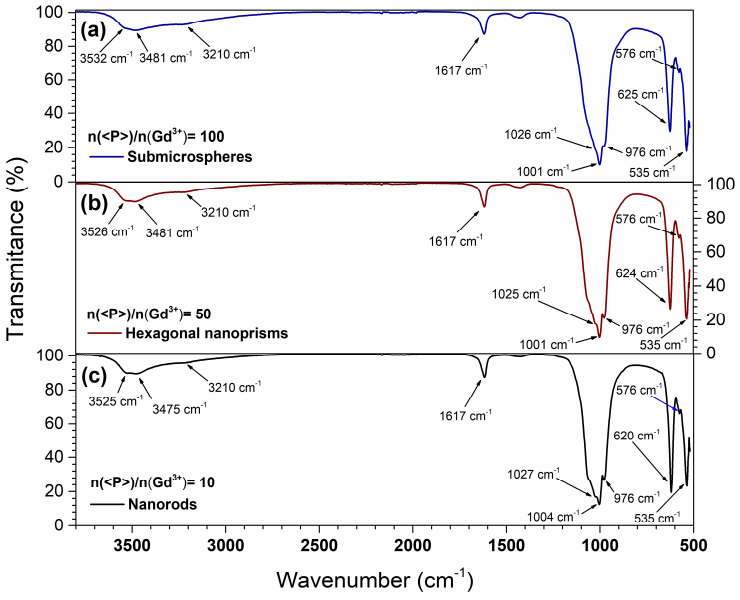

Figure 36. FTIR spectra of $GdPO_4 \cdot nH_2O$ nanorods (a), hexagonal nanoprisms (b) and submicrospheres (c).

The obtained results can be divided into four regions of interest: 300-800 cm^{-1} (corresponding to PO_4 tetrahedron deformation modes), 900-1200 cm^{-1} (originating from the stretching PO_4 vibrations), and two remaining regions related to water: around 1615 cm^{-1} (corresponding to bending H_2O vibrations) and 2500-3800 cm^{-1} (corresponding to stretching H_2O vibrations). Wide vibration band at around 1000 cm^{-1} originates from P-O vibrations within PO_4^{3-} groups and actually consist of three peaks centered at 976 cm^{-1} (could be assigned to symmetrical stretching mode), 1001 cm^{-1} (shifts to 1004 cm^{-1} as <P>/Gd ratio increases to 50 or more,) and

1027 cm^{-1}. Both 1001 and 1027 cm^{-1} vibrational bands could be assigned to asymmetric stretching mode. A pair of sharp bands observed at 625 and 535 cm^{-1} are the result of O-P-O vibrations in PO_4^{3-} groups and can be assigned to bending modes of O=P-O and O-P-O groups. The vibrational bands at 1617 cm^{-1}, ca. 3210 cm^{-1}, ca. 3480 cm^{-1}, ca. 3530 cm^{-1} (position of the bands shifts slightly with the change of <P>/Gd ratio) can be related to both physically adsorbed and bound within crystal structure water molecules. 1617 cm^{-1} band can be assigned to bending vibrations and ca. 3210 cm^{-1}, ca. 3480 cm^{-1}, ca. 3530 cm^{-1} to stretching vibrations of water, respectively. It is noticeable that with the increase of <P>/Gd ratio both bands of OH groups have more and more pronounced splitting and lower energy component emerges (3210 cm^{-1}). These components most likely can be attributed to structurally bound water of different coordination. Phosphate ions are known as one of the strongest positively-binding groups for water molecules and, therefore, significant shift towards lower energies of vibrations is to be expected for crystalline water molecules in orthophosphates. Thus, it is reasonable to suggest, that the increase of <P>/Gd ratio leads to the increase of content of strongly bound, i.e. crystalline, water.

This suggestion is confirmed by results of DT/TGA analysis (see Figure 37). The analyzed samples were heated up to 950 °C with heating speed of 10 °C/min under air atmosphere. The main decrease in mass for analyzed samples was observed until 500 °C.

Weight loss of all analyzed samples contain three main processes – loss of physically adsorbed water, loss of crystalline water from rhabdophane phase and phase transformation, when during dehydration process phase transition from rhabdophane to monoclinic structure occurs. The observed results are similar to those published by T. Anfimova et al. [213, 226].

The loss of physically adsorbed water from the particle surface occurs in the interval from 30 to ca. 145 °C. The observed mass loss in this temperature interval leads to the conclusion that spherical particles contain more physically adsorbed water if compared to rod-like nanoparticles.

The second process, accompanied with an endothermic peak at around 145-200 °C, is observed in temperature range from 150 to 500 °C and is assigned to the loss of crystalline water of $GdPO_4 \cdot nH_2O$ phase.

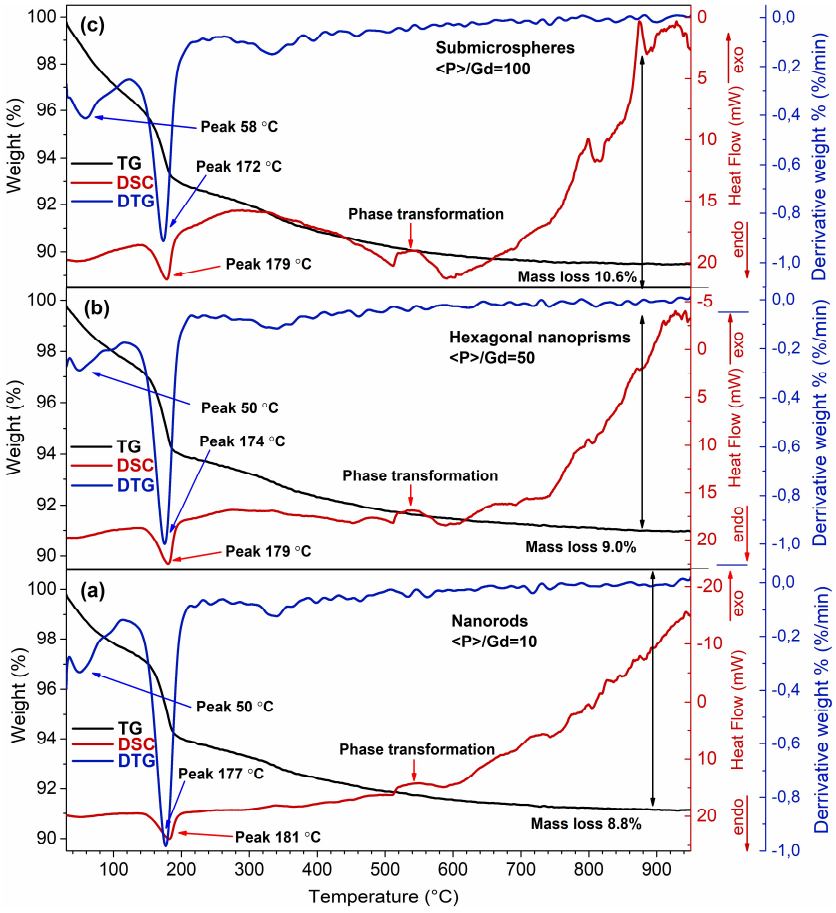

Figure 37. TG-DTG-DSC curves of $GdPO_4 \cdot nH_2O$ nanorods (a), hexagonal nanoprisms (b) and submicrospheres (c).

The third process is attributed to the beginning of rhabdophane phase transformation into the monoclinic phase and starts at around 500 °C and, even though it is not followed by significant weight loss, is accompanied by the exothermic peak observed at temperatures between 500 and 550 °C for all samples representing different morphologies. The weight loss in temperature interval 500-900 °C can be attributed to the remaining crystalline water (or even stronger bound OH groups within zeolitic channels, which is supporting the rhabdophane crystal structure [335].

It was calculated that along with increase of <P>/Gd ratio the amount of physically adsorbed water increases and the amount of crystalline water decreases. The exact formulas for different $GdPO_4 \cdot nH_2O$ morphologies were determined and are summarized in Table 3.

Table 3. Crystalline and physically adsorbed water content within different $GdPO_4 \cdot nH_2O$ samples.

<P>/Gd ratio	$GdPO_4 \cdot nH_2O$	Physically adsorbed water
10	1.07	1.7%
50	1.03	2.1%
100	1.01	3.8%

9.2. Morphology of obtained particles

The choice of synthesis parameters is extremely important in morphology control of obtained $GdPO_4 \cdot nH_2O$ particles. Influence of synthesis parameters such as ratio of <P>/Gd, Gd^{3+} concentration, pH, and synthesis duration were studied during this work. All syntheses were conducted in the presence of tartaric acid. Tartaric acid may affect the growth of $GdPO_4 \cdot nH_2O$ crystals in several ways. It has two carboxylic groups –COOH and two hydroxyl groups –OH in its structure. The presence of these functional groups enables tartaric acid to chelate Gd^{3+} ions by forming TA–Gd^{3+} complex [235]. Therefore, in the presence of tartaric acid, the sedimentation of Gd^{3+} ions with $NH_4H_2PO_4$ proceeds at a slower rate, as Gd^{3+} ions are chelated. On the other hand, the nucleation process is also affected by the presence of tartaric acid. It was shown that short organic molecules (for example citric acid, EDTA, as a coordinating agents or EG as synthesis medium) may bind to *ab* facet and in this way inhibit the particle growth along *c* (001) axis or alter the morphology of forming particles [27, 235, 336]. Thus, one can expect the formation of anisotropic particles in presence of tartaric acid, given that degree of supersaturation is not very high.

This hypothesis was proved by series of experiments with varying <P>/Gd molar ratio (these syntheses were performed for 12 h at 160 °C, pH = 10). Figure 38 and Figure 39 represents SEM images of synthesized $GdPO_4 \cdot nH_2O$ particles. By changing the molar ratio of <P>/Gd from 1 to 100 (in other words increasing the degree of saturation) the following morphologies were obtained subsequently: nanofibers, nanorods, nanoprisms and submicrospheres. At the lowest degree of saturation (<P>/Gd ratio is equal to 1, Figure 39 a) a nanofiber net made from very thin (~10 nm) and long wires up to hundreds of nanometers is formed. As the ratio increases up to 10 (Figure 39 b-d) – a well-shaped and monodisperse nanorods of ca. 100 nm in length and 15 nm in thickness form. These images also reveal that shorter and thicker nanorods are formed if larger <P>/Gd ratio is used.

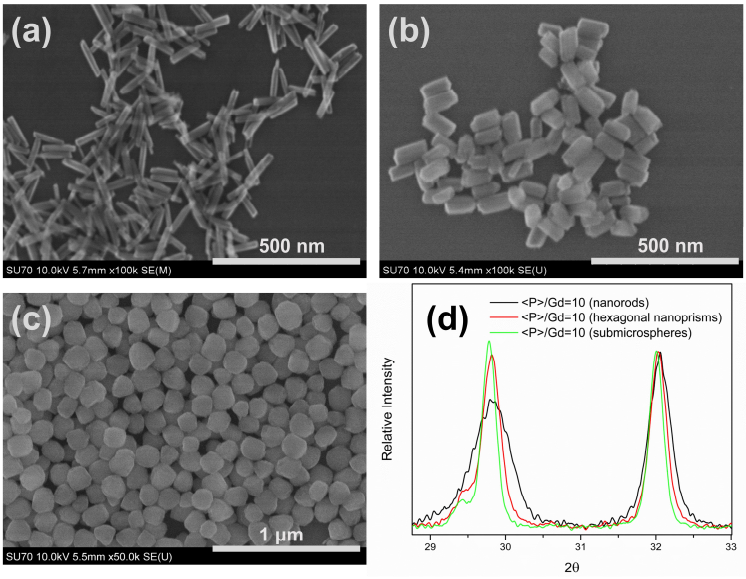

Figure 38. SEM images of $GdPO_4 \cdot nH_2O$ synthesized with different <P>/Gd molar ratio: (a) 10, (b) 50 (c) 100. (d) shows the change of $I_{(200)}/I_{(102)}$ ratio in the XRD patterns of samples with different morphology.

One dimensional growth of rhabdophane structure is well-known [337]. Anisotropic particles (nanorods) of various rare-earth orthophosphates are the result of such anisotropic growth and are reported in numerous papers and is characteristic structural feature of such compounds [27, 223, 337]. Anisotropic nature of lanthanide orthophosphates can be related to their specific crystal structure as is discussed in section 3.2.

However, when the degree of saturation increases (<P>/Gd molar ratio reaches 50, Figure 38 b and Figure 39 f), intensive growth and aggregation of nuclei prevents formation of anisotropic nanoparticles, hexagonal nanoprisms (ca. 80 nm in length and ca. 40 nm in diameter) start to form. Further increase of degree of saturation and, therefore, rate of growth, leads to formation of more and more isotropic particles. The formation of crude submicrospheres is observed when <P>/Gd ratio reached 75 (Figure 39 g) and higher. Eventually, relatively uniform submicrospheres, although not perfect in shape, form if $<P>/Gd^{3+}$ molar ratio reaches 100 (Figure 38 and Figure 39 h) (ca. 100 nm in diameter). The mean size of particles also increased with the increase of the degree of saturation.

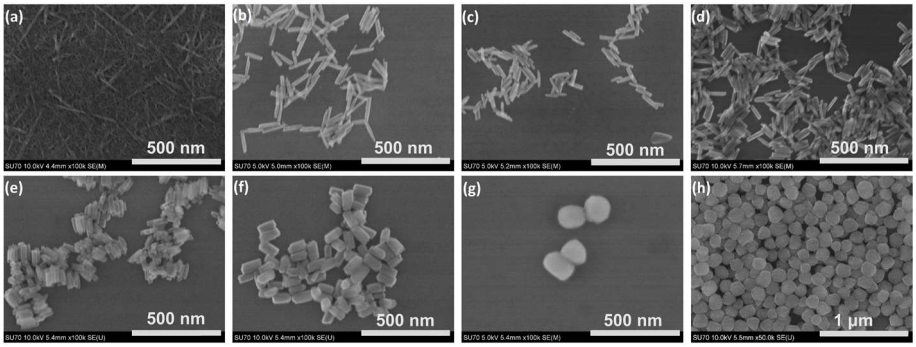

Figure 39. SEM images of $GdPO_4$ under magnification of (a-g) ×100 k and (h) ×50 k. Images represent $NH_4H_2PO_4/Gd^{3+}$ molar ratio impact to particle morphology: (a) ratio 1, (b) 4, (c) 7, (d) 10, (e) 20, (f) 50, (g) 75, and (h) 100.

It is interesting to compare evolution of microstructure and crystallinity of samples synthesized under different degree of supersaturation (Figure 37). As the <P>/Gd ratio increases, the apparent crystallite size, calculated using Scherrer equation, increases too, thus resulting in narrowing of the peaks of corresponding XRD patterns (see Figure 38 d). The mean apparent crystallite sizes for samples with <P>/Gd ratios of 10 (20±3 nm), 50 (29±1 nm) and 100 (38±2 nm) were calculated using Scherrer's equation (see Table 2).

Formation of uniform spherical particles with very narrow size distribution. Usually under such high degree of saturation shapeless micrometer-sized aggregates are formed as a result of unlimited growth and fast aggregation of particles. On the other hand, conditions for formation of uniform spherical particles is low concentration of reagents and minimal degree of supersaturation [338].

In case of this work, the possible explanation of resulting morphology may be the chelating effect of tartaric acid. Binding of Gd^{3+} ions in complex may efficiently limit the speed of growth, therefore, providing conditions for uniform particles formation even at high degree of supersaturation. However, additional experiments should be conducted to support these claims.

It is also noticeable, that $I_{(200)}/I_{(102)}$ changes, indicating specific texture, in this case aggregation of particles. The powder XRD pattern of particles synthesized under <P>/Gd molar ratio of 10 (nanorod shaped) have a diffraction peak (102) a little less intensive than peak (200), i.e., $I_{(200)}/I_{(102)}$ value is 0.732. In the case of sample synthesized under <P>/Gd ratio of 50 (hexagonal nanoprisms, Figure 35 c) intensity values of (200) and (102) peaks become similar as ratio $I_{(200)}/I_{(102)}$ reaches value of 0.977. For sample, synthesized under <P>/Gd molar ratio of 100 (submicrospheres, Figure 35 d)

intensity of (200) peak even exceeds intensity of (102) peak as observed $I_{(200)}/I_{(102)}$ ratio value reaches 1.05. The comparison of (200) and (102) peaks (normalized intensity) is given in Figure 38 d. It is reasonable as nanorods grow along specific crystallographic axis and tend to form stacks of particles with the same orientation. On the other hand, isotropic particles do not have preferable orientation during aggregation.

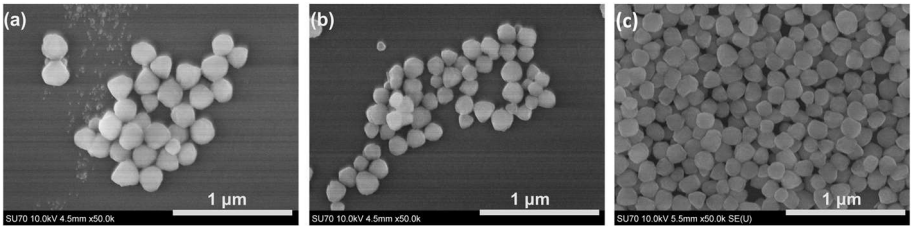

Figure 40. SEM images of $GdPO_4 \cdot nH_2O$ under magnification of x50 k (c). Samples were synthesized with different starting amounts of Gd^{3+} ions: (a) 0.1, (b) 0.2, and (c) 0.4 mmol of Gd^{3+} ions.

It was found out that concentration of Gd^{3+} ions does not affect morphology of the resulting nanoparticles once the <Gd>/P ratio is fixed. The SEM images of $GdPO_4 \cdot nH_2O$ particles obtained for different starting amounts of Gd^{3+} ions with <P>/Gd ratio set to 100 given in Figure 40 (conditions of synthesis – 12 h at 160 °C). This confirms the hypothesis that Gd^{3+} ions are chelated by tartaric acid and the release of Gd^{3+} ions occurs at low speed, which is determined by stability of complex, not the initial Gd^{3+} concentration.

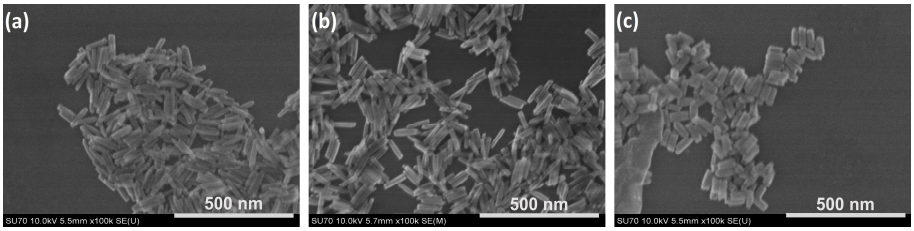

Figure 41. SEM images of $GdPO_4 \cdot nH_2O$ particles under magnification of x100 k. Particles were synthesized at several pH values: (a) 9, (b) 10, and (c) 10.5.

The SEM images, given in Figure 41, represent the impact of pH value (9, 10 and 10.5) on the $GdPO_4 \cdot nH_2O$ particle size and morphology. Hydrothermal synthesis was performed for 12 h at 160 °C and the <P>/Gd ratio was set to 10. It is obvious (Figure 41 a-c) that an increase in pH value causes formation of shorter and thicker nanorods and, therefore, acts in the same way as the

increase of <P>/Gd ratio. Though the concentration of phosphate ions does not change with the increase of pH, hydrolysis equilibria for phosphate ions shifts towards less protonated forms. This increases the activity of phosphate ions in the precipitation process and, therefore, acts the same way as the increase of degree of supersaturation. Additionally, the way how tartaric acid interacts with growing particles may depend on the pH value too, as it affects deprotonisation of tartaric acid molecules [339]. For reference the XRD patterns of specimens synthesized at different pH values are shown in Figure 42.

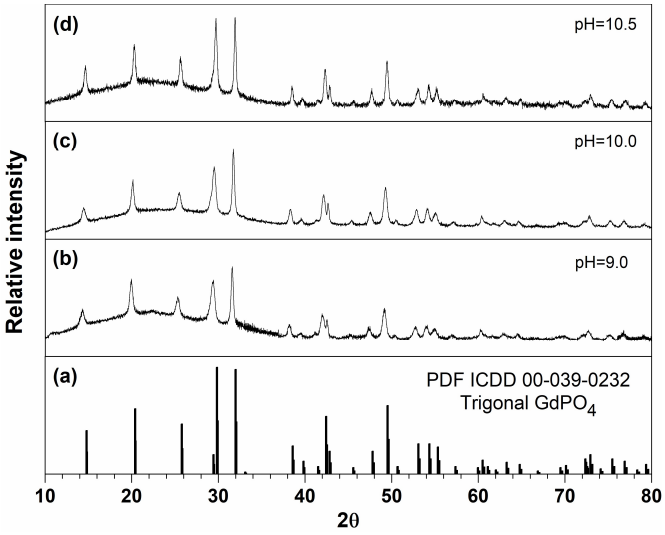

Figure 42. XRD patterns of trigonal $GdPO_4 \cdot nH_2O$ particles upon synthesis pH (b-d) and a reference pattern of $GdPO_4 \cdot H_2O$ (PDF ICDD 00-039-0232).

The influence of synthesis duration on particles morphology was also studied. Figure 43 represent SEM images of $GdPO_4 \cdot nH_2O$ particles synthesized for: 4 (Figure 43 a), 8 (Figure 43 b), 12 (Figure 43 c), 16 (Figure 43 d), 20 (Figure 43 e), and 24 (Figure 43 f) hours, respectively.

These SEM images imply that the best quality nanorods are obtained when synthesis time is in the range of 12 – 16 h. Nanorods synthesized in the time range up to 12 h have broader size distribution and are not perfectly shaped. It indicates that growth and recrystallization of nanorods are not finished yet. On the other hand, particles synthesized with duration over 24 h already are not that well dispersed and tend to agglomerate along *c*-axis, what can actually be called self-assembly of nanorods. In this case, self-assembly occurs in order to minimize the surface area and, thus, defects.

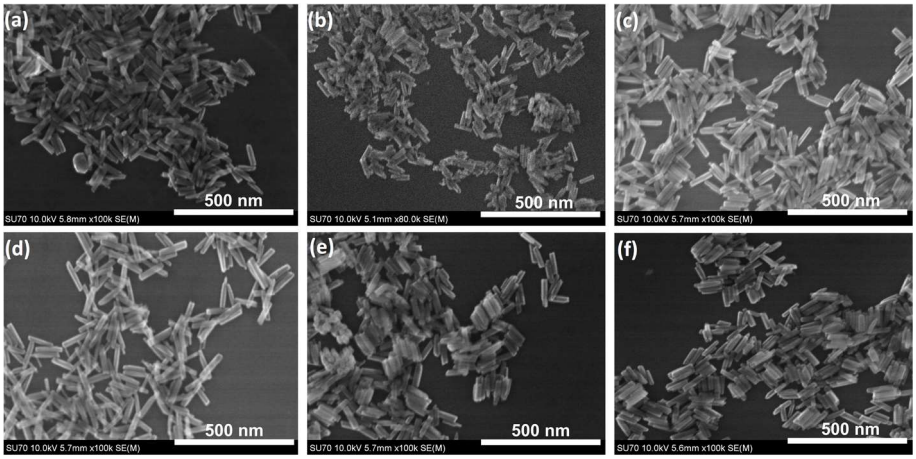

Figure 43. SEM images of $GdPO_4$ under magnification of x100 k under different reaction times: (a) 4, (b) 8, (c) 12, (d) 16, (e) 20, and (f) 24 h.

The XRD patterns of samples synthesized for different time are depicted in Figure 44. The patterns look virtually identical; thus it can be concluded that single phase $GdPO_4 \cdot nH_2O$ compounds are obtained even after 4 h synthesis.

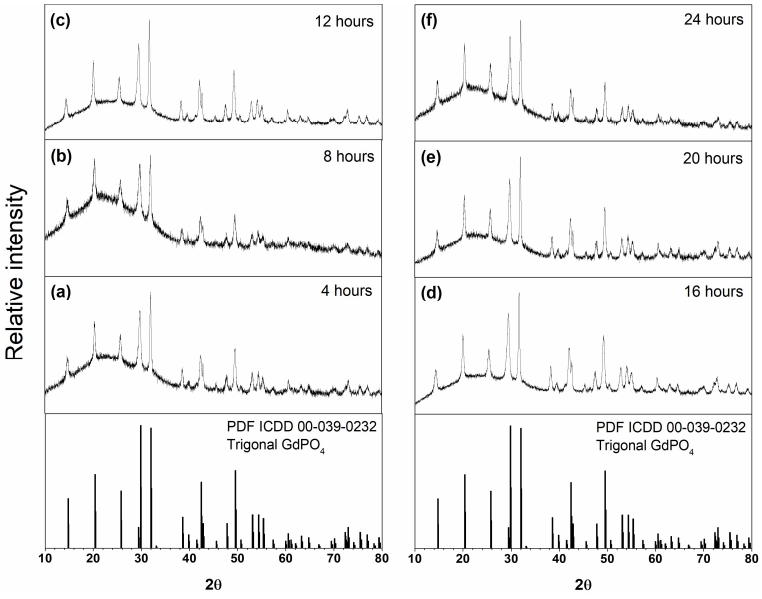

Figure 44. XRD patterns of trigonal $GdPO_4 \cdot nH_2O$ particles upon synthesis length (a-f) and a reference pattern of $GdPO_4 \cdot H_2O$ (PDF ICDD 00-039-0232).

9.3. Electrostatically achieved colloidal stability of $GdPO_4$ nanoparticles with different morphology in aqeuous media

Figure 45 demonstrates the dependence of zeta-potential values of $GdPO_4$ samples with different morphology as a function of pH. Zeta-potential is an important factor determining the stability of electrostatically stabilized nanoparticles. The value of zeta-potential is strongly dependent on pH value and ionic force of the solution. The obtained values of zeta-potentials varied from 52.9 mV at pH value of 2.5 for nanorods up to -65.6 mV at pH value of 10.0 for submicrospheres. According to the literature, the particles with absolute zeta-potential value higher than 28 mV exhibits colloidal stability, which is induced by electrostatic repulsion. This prevents them from forming agglomerates and coagulates [304]. In all cases, the measured zeta-potential values decreased alongside with increase in pH value. It was also noticed that isoelectric point of examined particles is highly dependent on the particles morphology. The isoelectric points of rod-like particles (<P>/Gd = 10), nanoprisms (<P>/Gd = 50), and submicrospheres (<P>/Gd = 100) are at pH values of 6.2, 5.6, and 4.5, respectively.

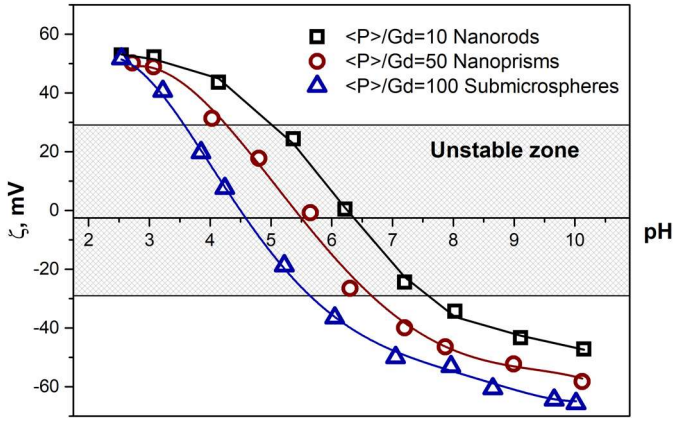

Figure 45. Zeta-potentials of $GdPO_4 \cdot nH_2O$ particles with different morphologies at different pH values.

As was discussed in section 5 (see Figure 26), the main source of surface charge, determining zeta-potential of electrostatically stabilized particles are functional groups exposed to the particle surface. Particularly in this case, at pH value of 2.5, nanorod/hexagonal and nanoprism/submicrosphere shaped particles have very similar zeta-potential values, which are around 50 mV. This surface charge can be related to protonated $-OH_2^+$ groups and is

measured when, under acidic pH value of around 2, most of hydroxyl groups are fully protonated. The change in remarkably different isoelectric points and zeta-potential values under basic pH values of nanoparticles can be explained by different amounts of hydroxyl groups present on the particle surfaces. The difference may come from morphology (different crystal plane may have different number of hydroxyl groups) and different surface areas of particles with different morphologies. Under pH value of around 10, there is an obvious difference between zeta-potentials of investigated particles: -49 mV for nanorods, -58 mV for hexagonal nanoprisms, and -65 mV for submicrospheres. Under this pH value, it is most likely that most of the surface-exposed hydroxyl groups are deprotonated. The more hydroxyl groups are deprotonated – the more negative surface charge is generated, which results in more negative zeta-potential value.

The obtained results suggest that $GdPO_4$ particles can be effectively dispersed in aqueous media forming stable solutions in different ranges of pH values. Furthermore, these morphology/surface area dependent changes in zeta-potential values enable to selectively choose desired morphologies of $GdPO_4$ particles to form stable dispersions under certain pH values.

There are numerous papers reporting various different approaches to obtain $GdPO_4$ nano- and micro- sized particles (nanorods, nanoprisms, submicrospheres, submicrostars, nanocubes). To the best our knowledge there are only two papers reporting controlled growth of $GdPO_4$ nanoparticles. However, both of them have slightly different approaches. In 2018, Z. Wang et al. reported a study of $GdPO_4$ nanocrystals synthesis by solvothermal method, where the impact of pH and ethylene glycol (EG) to the particle morphology has been investigated. This report has shown that increasing EG concentration results in shortening of the obtained nanorods yielding quasi-equiaxed hexagonal $GdPO_4{\cdot}nH_2O$ nanocrystals when high amount of EG was used [27]. However, the control of particle shape was not that simple and, in some cases, particle size distribution was relatively large due to particle agglomeration. In 2019, S. Wu et al. published a research paper where morphology of obtained $GdPO_4$ particles was controlled by altering pH values from 1 to 4. Nanorods and hexagonal nanoprisms were obtained [340]. Authors of this paper also claimed that they have also obtained $GdPO_4$ nanocubes; however, it is more likely that these cubes are the same hexagonal nanoprisms just lying on the side. This observation is also confirmed by the fact, that reported TEM images also contain hexagonal nanoprisms. Both publications discuss possible bio-applicability of obtained nanoparticles;

however, none of them has any stability experiments done to support these claims.

As mentioned before, the surface charge and, therefore, stability range of electrostatically stabilized particles are characterized by zeta potential analysis. This analysis method of particle surface charge provides information about $GdPO_4$ particle stability in aqueous colloids and charge of the particle surface. The isoelectric points and stability range of particles were determined and are given in Figure 45. These results define particle stability and, thus, help to evaluate potential applicability of $GdPO_4$ nanoparticles in biomedical and other possible fields, as particles which are not stable in biological pH range (biological pH value ranges from 7.35 to 7.45) cannot be applied in the fields where colloid stability under discussed pH is required.

There are only few reports discussing stability of $GdPO_4$ nanoparticles. A. Mayence et al. reported nanorods of ca. 300 nm in length and 15 nm in thickness with negative zeta potential values in pH range from 2.0 (around 0 mV) to 10.0 (around -70 mV) [341]. B. Abecassis et al. reported nanorods of 125 nm in length (with 40 nm deviation). According to this paper, the analyzed $GdPO_4$ nanorods possess similar stability range to $GdPO_4$ nanorods reported by us. However, zeta-potential values in this paper are not suitable to achieve colloidal stability for biological applications, as these particles seem not to be stable in biological pH range [30]. F. Mpambani reported research on $GdPO_4$ particle stability in his doctoral thesis. He discussed that instability range of $GdPO_4$ nanorods obtained by his group is between pH values 5.0-10.0 with isoelectric point around pH value of 6. According to thesis author, $GdPO_4$ particles can be considered as possible MRI agents if their stability is increased [342]. Mirzadeh et al. reported $GdPO_4$ particles, which possess -23.88 mV zeta potential values as prepared and -13.03 mV values after the dialysis. $GdPO_4$ particles doped with Eu^{3+} ions are reported to exhibit -28.52 mV zeta potential (deviation 7.78) and after dialysis value of zeta-potential decreased to -18.50 mV [343]. Zeta potential of $GdPO_4$:Eu submicrospheres was reported to be around -6 mV at pH value of 5.0, -15 mV at pH value of 7.4, and -22 mV at pH value 8.0. However, the reported values are not large enough for electrostatically stabilized colloids to form [344].

Some research reporting stability of some other similar $LnPO_4$ systems are also worth mentioning. Hexagonal $LaPO_4$ nanorods (50-100 nm in length and 5-10 nm in thickness) doped with Tb^{3+} and Eu^{3+} ions were reported by T. Grzyb [345]. Particles, reported by his group, possess zeta potential values of 29-34 mV at pH value of 7, which is almost the minimal satisfactory value

for the stability, although if particles are stable - it seems to be suitable for biological applications. In 2015 Becerro et al. reported $LuPO_4$:5%Eu nanoparticles (85 nm in length and 40 nm in thickness) with tetragonal crystal structure. These nanoparticles exhibited zeta potential value of 0.3 mV (very near to the isoelectric point) at pH value of 4.0, and value of -44 mV at pH value of 10.0. In comparison to this result, under similar pH values our particles possess zeta potential values of 30 mV (for nanoprisms) and 50 mV (for nanorods) which is more than enough for stable colloids to be acquired [231].

The pH instability range for particles obtained during this work is 5.0-7.5 for nanorods, 4.5-6.5 for hexagonal nanoprisms and 3.5-5.5 for submicrospheres. According to these results, $GdPO_4$ nanoparticles, which may form stable aqueous colloids at pH values from 2.5 to 5.0 and from 5.5 to 10, may be obtained. These results show, that only at pH interval 5 to 5.5 none of our synthesized nanoparticles form stable aqueous colloids.

Our research was mainly focused on developing novel simple synthesis route allowing to control $GdPO_4$ nanoparticle growth and morphology. Moreover, to prove particle applicability in suggested fields, which require colloid stability in aqueous solutions, stability of colloids was evaluated. Besides, every so often scientific reports provide $LnPO_4$ synthesis routes, which yield $GdPO_4$ particles with large size distribution. These particles are also often agglomerated, possess poor crystallinity or are not single phase, or simply are too large to form stable colloids and to be applied in suggested application fields. It is well known, that colloidal stability of particles in dispersion is highly related to its size. If particles are larger than 1 μm, tendency of sedimentation process is high due to their own weight. However, it is possible to find examples where relatively large particles are stable in aqueous media. Rhodes et. al. reported the florescent SiO_2 particles with diameter of about 1 μm, which are stable in aqueous dispersion (pH 6) without any dispersant added [346]. On the other hand, there are cases reporting that even small particles (~25 nm) in aqueous dispersions exhibits poor stability, despite high values of surface potential (-60 mV) [294].

Such synthetical approach provides simple, clean, eco-friendly and quick synthesis route, which enables not only to obtain relatively small, single phase, monodisperse, well-shaped $GdPO_4$ particles but also to control their growth and morphology with great accuracy and reproducibility. Furthermore, most of the published research related to $GdPO_4$ nano– or micro–sized particle development nearly always mentions possible particle applications such as MRI agents, nanoprobes, security inks and so on. These applications require

colloidal stability. In addition, it is important to note that particle size plays important role in overall applicability of such colloidal systems: smaller colloidal systems made from particles which size varies from several to around 100 nm can potentially be applied in biological fields, whereas size of particles to be applied in development of security inks does not matter at all as long as aqueous colloids of such particles are stable.

However, only very few reports provide any experiments that the obtained particles can be dispersed in aqueous media at all. Such electrostatically achieved colloidal stability results, regardless of desired application (which requires colloidal stability), enable to obtain $GdPO_4$ particles, which will form stable aqueous colloids in a wide range of pH values. Particles are easily synthesized and no surface modification is needed making the synthesis procedure simple, clean and quick. Moreover, particle surface remains unmodified; therefore, further modification of the particles remains possible.

9.4. Doping of $GdPO_4$ particles

Nanocrystalline $GdPO_4$:Eu^{3+} phosphors of various different morphologies: nanofiber, nanorods, hexagonal nanoprisms, nanospheres, and urchin-like microparticles were synthesized in order to check whether $GdPO_4$ nanoparticles can be successfully doped without disrupting their morphologies, crystalline phase and monodispersity. All of the obtained samples were doped with 5% of Eu^{3+} ions.

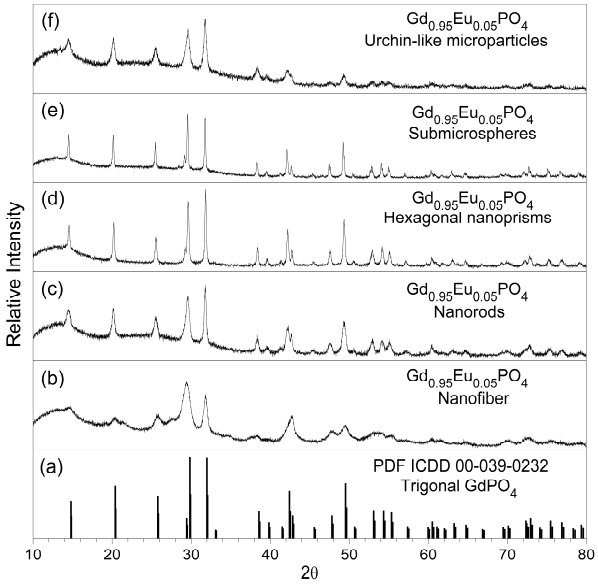

Figure 46. XRD patterns of different morphology $Gd_{0.95}Eu_{0.05}PO_4 \cdot nH_2O$ particles (b-f) and a reference pattern of $GdPO_4 \cdot H_2O$ (a).

Phase purity of synthesized $Gd_{0.95}Eu_{0.05}PO_4 \cdot nH_2O$ particles was confirmed by means of XRD. Figure 46 represents XRD patterns of $Gd_{0.95}Eu_{0.05}PO_4 \cdot nH_2O$ samples with different particle morphology. The broad band observed in the range from 10° to 40° 2θ originates from a glass sample holder. It is evident that XRD patterns of 5% Eu^{3+} doped samples correspond well to reference pattern of trigonal rhabdophane phase of $GdPO_4 \cdot H_2O$ (PDF ICDD 00-039-0232). The main diffraction peaks correspond well to the main crystallographic planes. No impurity peaks are observed. There are noteworthy differences in diffraction peak width suggesting variation in crystallite size of the samples.

In total, particles of 5 different morphologies (nanofibers, nanorods, hexagonal nanoprisms, submicrospheres, and urchin-like microparticles) were

doped with Eu^{3+} ions. SEM images in Figure 47 b-d represent <P>/Ln^{3+} molar ratio impact on $Gd_{0.95}Eu_{0.05}PO_4 \cdot nH_2O$ particle morphology. Discussed particles were synthesized as described in experimental part.

By changing the molar ratio of <P>/Ln^{3+} from 1 to 100, the following morphologies of Eu^{3+} doped particles were obtained: nanofibers, nanorods, hexagonal nanoprisms and submicrospheres. When <P>/Ln^{3+} ratio is equal to 1 (Figure 47 a) – nanofiber, made from thin (~5-15 nm) and hundreds of nanometers in length nanowires forms. Note that in order to successfully obtain nanofibers of good quality – magnetic stirring throughout synthesis must not be used. As <P>/Ln^{3+} ratio increases to 10 (Figure 47 b) – well shaped and monodisperse nanorods form. When <P>/Ln^{3+} ratio reaches 50 (Figure 47 c) – hexagonal nanoprisms are obtained. Formation of crude microspheres is observed when <P>/Ln^{3+} ratio reaches 100 (Figure 47 d). Change in pH value from alkaline 10 to acidic 1.6 yielded urchin-like $Gd_{0.95}Eu_{0.05}PO_4 \cdot nH_2O$ microparticles (Figure 47 e, f). It is evident that the intended morphology of $GdPO_4$ particles is successfully maintained when doping with Eu^{3+} ions.

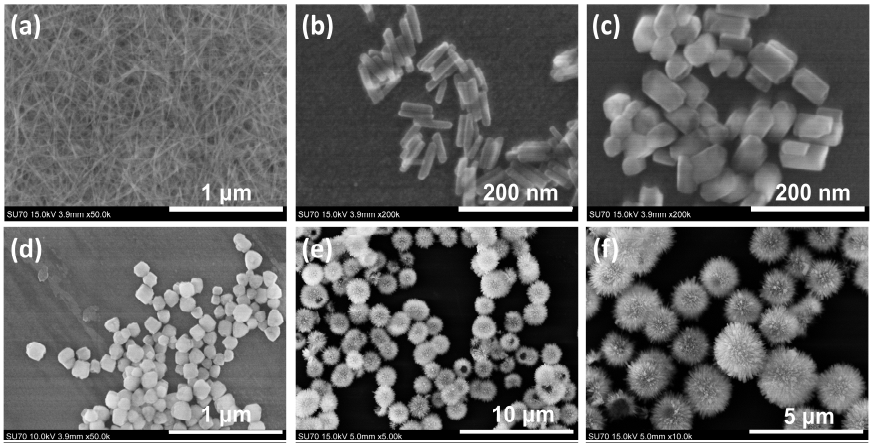

Figure 47. SEM images of $Gd_{0.95}Eu_{0.05}PO_4 \cdot nH_2O$.

Luminescent properties of $Gd_{0.95}Eu_{0.05}PO_4 \cdot nH_2O$ samples of different morphologies are reported in this paragraph. Powder of $Gd_{0.95}Eu_{0.05}PO_4 \cdot nH_2O$ samples possess fine white colour suggesting that all samples have low to no absorption in the visible range. Figure 48 represents excitation (Figure 48 a) and emission (Figure 48 b) spectra of $Gd_{0.95}Eu_{0.05}PO_4 \cdot nH_2O$ samples. Excitation spectra were recorded in range from 250 to 550 nm upon emission wavelength $\lambda_{em} = 592$ nm, which corresponds to $^5D_0 \rightarrow {}^7F_1$ transition. The

high energy part of excitation spectra consists of a broad band up to 270 nm and several sharp peaks located at ca. 275 and 310 nm. The broad band is attributed to charge transfer (CT) and originates from electron transfer from O^{2-} to Eu^{3+}. The excitation lines observed at ca. 275 and 310 nm, in turn, are assigned to $^8S \rightarrow {}^6I_J$, and $^8S \rightarrow {}^6P_J$ transitions of Gd^{3+} ions. The presence of Gd^{3+} excitation lines in excitation spectra monitored for Eu^{3+} ion proves the occurring $Gd^{3+} \rightarrow Eu^{3+}$ energy transfer. The rest of observed excitation lines belongs to Eu^{3+} transitions assigned in the Figure 48 a.

Emission spectra were measured in the range from 550 to 800 nm. The investigated samples were excited under wavelength λ_{ex} = 394 nm which corresponds to $^7F_0 \rightarrow {}^5L_6$ transition of Eu^{3+} ions.

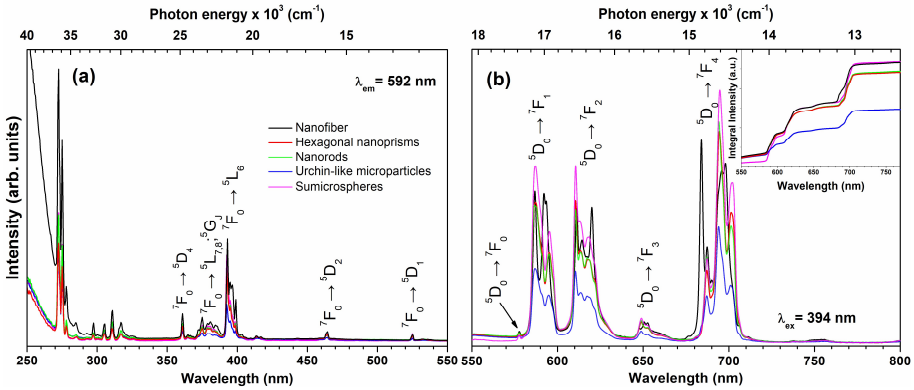

Figure 48. (a) Excitation (λ_{em} = 592 nm) and (b) emission (λ_{ex} = 394 nm) spectra of $Gd_{0.95}Eu_{0.05}PO_4 \cdot nH_2O$ samples with different morphologies. Inset shows emission (λ_{ex} = 394 nm) integral intensity for different samples.

The observed emission (λ_{ex} = 394 nm) was red and consists of several sets of emission lines corresponding to the intraconfigurational transitions of Eu^{3+} ions, namely, $^5D_0 \rightarrow {}^7F_0$ (ca. 577 nm), $^5D_0 \rightarrow {}^7F_1$ (ca. 590 nm), $^5D_0 \rightarrow {}^7F_2$ (ca. 615 nm), $^5D_0 \rightarrow {}^7F_3$ (ca. 650 nm), and $^5D_0 \rightarrow {}^7F_4$ (ca. 690 nm). The intensity of $^5D_0 \rightarrow {}^7F_0$ transition is the weakest, since $J = 0 \leftrightarrow J' = 0$ transitions are always forbidden [347]. Interestingly, the strongest emission was observed for the $^5D_0 \rightarrow {}^7F_4$ (ca. 690 nm), what is in good agreement with other Eu^{3+} doped orthophosphates reported in the literature [348]. The inset in Figure 48 b represents integrated emission intensities (λ_{ex} = 394 nm) of samples with different morphology. It is evident that the highest emission output can be assigned to submicrospheres and nanofiber meanwhile the lowest emission intensity can be attributed to urchin-like microparticles, even though they are the largest particles among samples and, typically, the largest

bulk crystals or agglomerates tend to yield the highest intensity. This can be explained that they consist of long $Gd_{0.95}Eu_{0.05}PO_4 \cdot nH_2O$ nanowires which have one of their end connected to the center of the microparticle, therefore, these particles are not large bulk crystal or agglomerate from point of view of spectroscopy. Hexagonal nanoprisms and nanorods share lower emission output than submicrospheres but larger than urchin-like particles.

10. $GdPO_4$ particle stabilization with cationic brush-type copolymers

In this chapter, $GdPO_4$ particles were modified with custom-made cationic brush-type copolymers and stability of such modified particles was investigated. Polymers of various compositions were synthesized via RAFT polymerization route. Cationic brush-type polymers were used to improve the stability of aqueous $GdPO_4$ particle dispersions. Firstly, the IEP points of $GdPO_4$ particles with different morphology (nanorods, hexagonal nanoprisms and submicrospheres) were determined by measuring zeta potential of bare particle dispersions under various pH values. Afterwards, cationic brush-type polyelectrolytes with different composition were applied for surface modification of $GdPO_4$ particles (negatively charged in alkaline media under pH value of ~10.6). The concentration and composition effects of used polymers on the change of particle surface potential and stability (DLS measurements) in dispersions were investigated and presented in this chapter. The remarkable outcome of this study is redispersable $GdPO_4$ nanoparticle colloids with increased bio-compatibility and stability as well as new insights into possible cationic brush-type polyelectrolyte applicability in both scientific and commercial fields.

10.1. Surface potential and colloidal stability of bare $GdPO_4$ particles with different morphology

The main object for this investigation was $GdPO_4$ particles of three different morphologies, i.e., nanorods, hexagonal nanoprisms and submicrospheres. The change in $GdPO_4$ particle surface potential was evaluated by measuring zeta potential values in aqueous colloidal dispersions in pH range from 2 to 10 (Figure 49 a). Zeta potential values of the synthesized $GdPO_4$ particles slightly differ and are dependent on the particle morphology. For example, the zeta potential value of submicrospheres in aqueous alkaline media (pH 10.6) is -64.7 mV. Under identical conditions, the measured zeta potential values for hexagonal nanoprisms and nanorods are observed to be higher, -53.8 and -43.8 mV, respectively. It is interesting to note that $GdPO_4$ particles of different morphology possess different isoelectric points (isoelectric point is determined by the pH value, where zeta potential is equal to 0, further will be referred as IEP). The determined IEP value for nanorods is 6.53. IEP values of hexagonal nanoprisms and submicrospheres are shifted to lower pH values, 6.03 and 5.61, accordingly. These differences in IEP could be related to

possibly different phosphate group density on differently shaped $GdPO_4$ particle surfaces since surface potential of the particles is related to amount of surface exposed PO_4^{3-} groups. Shape of template $GdPO_4$ particles and, therefore, amount of such surface exposed phosphate groups was manipulated by variation of $NH_4H_2PO_4/Gd^{3+}$ molar ratio by employing hydrothermal synthesis route as reported in previous chapter. The $NH_4H_2PO_4/Gd^{3+}$ molar ratios of 10, 50 and 100 were used for hydrothermal synthesis of nanorods, hexagonal nanoprisms and submicrospheres, respectively.

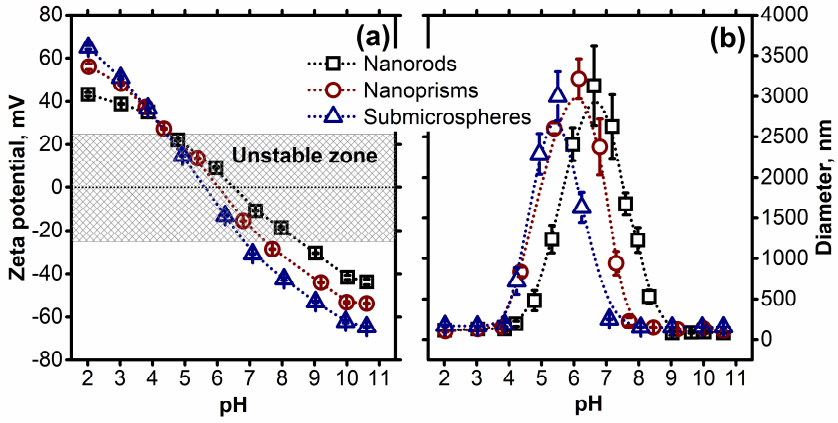

Figure 49. Zeta potential (a) and particle size (b) of different morphology bare $GdPO_4$ particles in aqueous dispersion at various pH values: a) nanorods (□), b) nanoprisms (○) and c) submicrospheres (Δ). Particles were redispersed from dry state.

The colloidal stability of bare $GdPO_4$ particles with different morphology in aqueous media under various pH values were measured using DLS equipment (Figure 49 b). Typical unstable zones were observed during stability measurements of bare $GdPO_4$ particle dispersions. It was observed that agglomeration and fast sedimentation of particles in aqueous dispersion occurred if absolute values of zeta potential of particles were lower than |22| mV.

10.2. Surface modification of different $GdPO_4$ particles using cationic brush-type polyelectrolytes in alkaline media

For the surface modification of $GdPO_4$, three p(METAC-*stat*-PEO_{19}MEMA) polyelectrolytes with different compositions were synthesized. Different polymer compositions were obtained by variation of initial molar ratio of METAC and PEO_{19}MEMA (see Table 1). METAC groups contain positively

charged quaternary ammonium groups that could electrostatically anchor on to the negatively charged surface of $GdPO_4$ particles. Moreover, PEO_{19}MEMA polymer can be additionally defined as inert, biocompatible macromonomer, containing relatively long PEO substituents. These substituents are responsible for a steric barrier that prevents other particles from approaching too close, and, therefore, the agglomeration is avoided. PEO stabilized particles are also known to possess good biocompatibility [349]. According to amount of quaternary ammonium groups in copolymer composition, different p(METAC-*stat*-PEO_{19}MEMA) copolymers were classified as low, medium and highly charged, where low means that copolymer consist of 27 mol%, medium – 47 mol%, and high – 65 mol% of METAC groups in composition.

The adsorption of cationic brush-type polyelectrolyte on oppositely charged surfaces of $GdPO_4$ particles with different morphology were evaluated by measuring the change of particle zeta potential. Measurements were carried out in alkaline media (pH 10.6), where $GdPO_4$ particles have highly expressed negative charge. The copolymer amount effect on the change of zeta potential of $GdPO_4$ particles with different morphology in aqueous dispersions is presented in Figure 50.

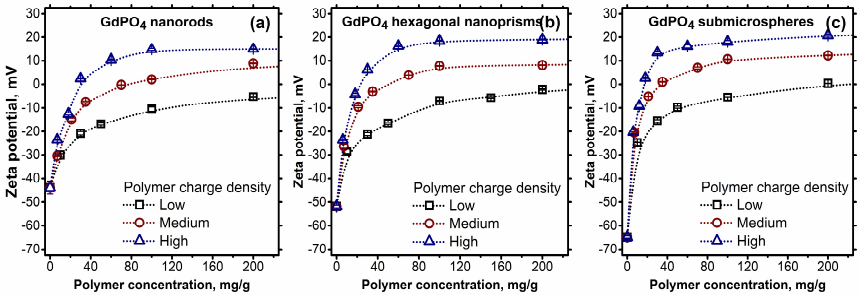

Figure 50. Dependence of zeta potential of 1% $GdPO_4$ particles in alkaline aqueous media (pH 10.6 as a function of polymer concentration: nanorods (a); nanoprisms (b); submicrospheres (c).

During addition of copolymer, the change in zeta potential value and, thus, charge of $GdPO_4$ particle surface is affected by both polymer charge density and particle morphology (Figure 50). Clearly, the charge density of polymers has higher effect. For example, during addition of low charge density polymer to aqueous dispersion with rod-like $GdPO_4$ nanoparticles, the full charge compensation is not achieved, and the surface of $GdPO_4$ nanorods remains negative (-5.1 mV) even using high amount of polymer (200 mg per gram of

$GdPO_4$ particles in dispersion). Different behavior was observed using polymers with medium or high charge density. Surface charge inversion was observed during physical adsorption of polymers with both medium and high densities of positively charged quaternary ammonium groups (METAC units). This behavior is explained in the literature, where the similar structure cationic brush-type polyelectrolytes were applied for stabilization of TiO_2 particles in aqueous media [294]. Charge inversion effect is induced by an excess of METAC groups on the particle surface during adsorption. The surface charge of $GdPO_4$ nanorods after addition of medium and high density polymers (200 mg/g) reached +8.9 and +15.0 mV, respectively. Similar effects were observed during investigation of $GdPO_4$ hexagonal nanoprisms. The zeta potential values of $GdPO_4$ hexagonal nanoprisms treated with low, medium and highly charged p(METAC-*stat*-PEO_{19}MEMA) polyelectrolytes (amount of 200 mg/g) reached -2.1, +8.2, and +19.1mV, respectively. Differently to nanorods and hexagonal nanoprisms, the negatively charged surface of $GdPO_4$ submicrospheres after treatment with polymers was fully compensated (+0.35 mV) using even low charge density (27 mol% of charged groups) polyelectrolyte. The used medium and highly charged p(METAC-*stat*-PEO_{19}MEMA) polyelectrolytes has led to the described charge inversion effect and the zeta potential of submicrosphere $GdPO_4$ particles was +12.2 and +20.8 mV, respectively.

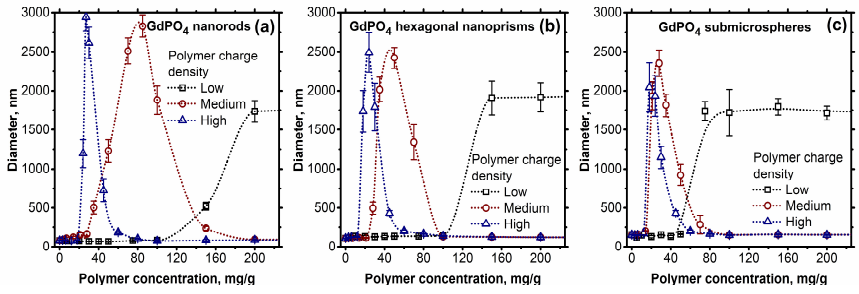

Figure 51. Dependence of $GdPO_4$ particles size in alkaline aqueous media (pH 10.6) as a function of polymer concentration and polymer charge density: nanorods (a); nanoprisms (b); submicrospheres (c).

Colloidal stability was evaluated and observed throughout all $GdPO_4$ particle treatment with p(METAC-*stat*-PEO_{19}MEMA procedure by measuring particle size distribution (PSD) using dynamic light scattering equipment. Colloidal stability evaluation of differently shaped $GdPO_4$ particles are presented in Figure 51. Note that particles were treated using three different

cationic brush-type polymers with different charge densities (low, medium and high).

Regardless the morphology, all $GdPO_4$ particles are stable in alkaline aqueous media (pH 10.6) without polymer added. In such cases the stability of particles is ensured by electrostatic repulsion forces between highly (negatively) charged particles. Zeta potential of $GdPO_4$ with morphology of nanorods, hexagonal nanoprisms and submicrospheres in alkaline media (pH 10.6) was observed to be -43.8, -53.8 and -64.7 mV, respectively. Polymer amount in such dispersions is playing an important role. After addition of a certain amount of polymer, dispersions became unstable. For example, during the treatment of $GdPO_4$ nanorods, particle dispersions were stable up to 100 mg/g of added low charge density polymer. Addition of higher amount of such polymer in dispersion led to formation of agglomerates up to 1800 nm. The addition of medium and highly charged polymers to $GdPO_4$ particle dispersions showed different behavior. In these cases, $GdPO_4$ nanorods dispersions had typical zones of instability if polymer amount in dispersion was insufficient. Instability zone of identical $GdPO_4$ nanorods dispersions stabilized using medium and highly charged p(METAC-*stat*-PEO_{19}MEMA) polymers was determined to be from 30 to 150 and from 20 to 60 mg/g, respectively. In these zones, particles existed in agglomerated state, the measured PSD showed values up to 3000 nm. After increasing polymer amount over these ranges, dispersions of $GdPO_4$ nanorods became stable again. The determined PSD of modified $GdPO_4$ nanorods in alkaline media were ~80 nm using both medium and highly charged polyelectrolytes. The determined PSD values using DLS were relatively close to ones measured using TEM and SEM (Figure 52).

The unstable zones that occurred during study could be related to particle zeta potential. During treatment with polymers, the change of particle surface potential mainly depends from the amount of polymer added and density of positively charged quaternary ammonium groups within polymer itself. It was found out that p(METAC-*stat*-PEO_{19}MEMA) polymers with high charge density had the highest impact to zeta potential values of $GdPO_4$ particles. Lower amount of such polymers was needed to reach the same value of zeta potential in comparison to polyelectrolytes, containing small amount of positively charged groups. Similar results were obtained during stability study of $GdPO_4$ particles with other morphology (hexagonal nanoprisms, submicrospheres) and are summarized in Table 4. It is important to note that instability zones of $GdPO_4$ particles, regardless of particle morphology, are

observed when the absolute zeta potential value of particles was in the range of |12| mV (see Figure 50 and Figure 51).

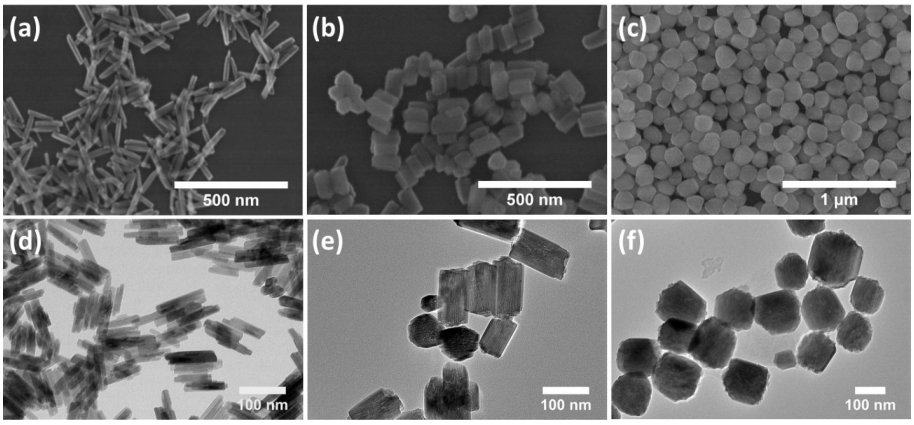

Figure 52. SEM and TEM images of bare $GdPO_4$ particles of different morphologies.

Table 4. Stability results of $GdPO_4$ particles with different morphology during the treatment with different polymers in alkaline aqueous media (pH 10.6).

Polymer charge density	Nanorods		Hexagonal nanoprisms		Submicrospheres	
	Unstable zone		Unstable zone		Unstable zone	
	Polymer amount, mg/g	ζ, mV	Polymer amount, mg/g	ζ, mV	Polymer amount, mg/g	ζ, mV
Low	over 125	over -8.9	over 100	over -8.4	over 50	over -8.7
Medium	35 to 150	-8.5 to 7.4	22.5 to 100	-8.9 to 7,8	15 to 70	-9.3to 7.4
High	20 to 60	-9.5 to 10.9	15 to 50	-8.9 to 11.3	12.5 to 45	-9.1 to 11.9

10.3. Determination of maximal polymer adsorption on $GdPO_4$ particles with different morphology

The equilibrium (in quantity) cationic brush-type polyelectrolyte adsorption on oppositely charged surfaces of $GdPO_4$ particles with three different morphologies (nanorods, hexagonal nanoprisms, submicrospheres) was evaluated by measuring zeta potential values of particles treated with 200 mg/g polymers (low, medium, high charge density). For this purpose, nanoparticles, which were used for these measurements were washed three times by centrifuging and re-dispersing them in MiliQ water employing ultrasonic treatment (see Table 5).

Table 5. Zeta potential and calculated maximal adsorption of cationic polyelectrolytes on $GdPO_4$ particles with different morphology in alkaline aqueous media (pH 10.6).

$GdPO_4$ morphology	Polymer charge density								
	Low			Medium			High		
	ζ^*, mV	ζ^{**}, mV	MA, mg/g	ζ^*, mV	ζ^{**}, mV	MA, mg/g	ζ^*, mV	ζ^{**}, mV	MA, mg/g
Nanorods	-5.2	-17.0	39.2	8.9	-8.3	36.5	15.0	3.2	36.8
Hexagonal nanoprisms	-2.1	-23.3	23.0	8.2	-8.9	21.8	19.1	1.0	23.4
Submicro-spheres	0.35	-32.3	8.7	12.2	-17.3	11.1	20.8	-6.8	13.3

* zeta potential of $GdPO_4$ in alkaline aqueous media (pH 10.6) before wash.

** zeta potential of $GdPO_4$ in alkaline aqueous media (pH 10.6) after wash with MiliQ water (3 times).

*** Maximal adsorption of p(METAC-*stat*-PEO_{19}MEMA) with different charge density on the surface of $GdPO_4$ particles, calculated from curves presented in Figure 50.

The results presented in in Table 5 suggest that the equilibrium adsorption (independently to used polymers) on $GdPO_4$ nanorods is higher in comparison to particles with other morphology (hexagonal nanoprisms, submicrospheres). For example, the equilibrium adsorption of low charge density p(METAC-*stat*-PEO_{19}MEMA) on $GdPO_4$ nanorods is 39.2 mg/g if compared to 23.0 and 8.7 mg/g on hexagonal nanoprisms and submicrospheres, respectively. It can be explained through particle size, because it is well-known that the surface

area of particles is inversely proportional to particles size meaning $GdPO_4$ nanorods are the smallest particles used in this study (see Figure 52). To support this claim, nitrogen gas adsorption using BET (Brunauer-Emmett-Teller) technique was conducted. During this analysis surface area was determined to be 47 m^2/g for nanorods, 24 m^2/g for hexagonal nanoprisms and 20 m^2/g for submicrospheres.

10.4. Surface potential and colloidal stability of modified $GdPO_4$ particles with different morphology

Stable aqueous $GdPO_4$ particle dispersions (1 mg/mL) of each morphology were prepared by using dry $GdPO_4$ particles, which previously were washed and dried. The pH values of prepared $GdPO_4$ dispersions were then adjusted from ~2 to 10.6 using 0.1 M HNO_3 and NH_4OH solutions, respectively. The zeta potential and particle size distribution were measured under different pH values for all $GdPO_4$ particle morphologies and are presented in Figure 51. The determined IEP of particles independently to $GdPO_4$ particle morphology are shifted to the alkaline pH region. The p(METAC-*stat*-PEO_{19}MEMA) containing the highest amount of charge groups (67 mol%) affected IEP of studied particles the most noticeably. For example, the IEPs of $GdPO_4$ nanorods modified with low and medium charged polymers were 7.23 and 8.65, respectively, whereas IEP of nanorods stabilized with highly charged p(METAC-*stat*-PEO_{19}MEMA) was shifted to highly alkaline pH values (>11). The IEPs of $GdPO_4$ hexagonal nanoprisms were 6.99, 8.51 and ~10.60, for particles modified using p(METAC-*stat*-PEO_{19}MEMA) with low, medium and high charge densities, respectively. In the case of $GdPO_4$ submicrospheres, IEPs were determined to be 6.61, 7.96 and 8.98, accordingly.

After $GdPO_4$ particle modification using cationic brush-type p(METAC-*stat*-PEO_{19}MEMA) polymers with different compositions, the stability range of $GdPO_4$ dispersions was expanded. It is important to notice that good stability is observed in biological range (pH 6.6 - 7.4). The best results in stabilization of $GdPO_4$ particles were achieved for rod-like particles. For comparison, bare $GdPO_4$ nanorods (IEP 6.53) were extremely unstable in pH range from 4.2 to 9.1 (Figure 51 b). Hence, after stabilization with polyelectrolytes nanorods demonstrate perfect stability in pH range from 2 up to 5.6, 7.2 and 8.3 using low, medium and highly charged polymers, respectively. The study of $GdPO_4$ particle stabilization with other morphology (hexagonal nanoprisms and submicrospheres) particles has shown comparable

results, which also suggest greatly increased colloidal stability (see Figure 53).

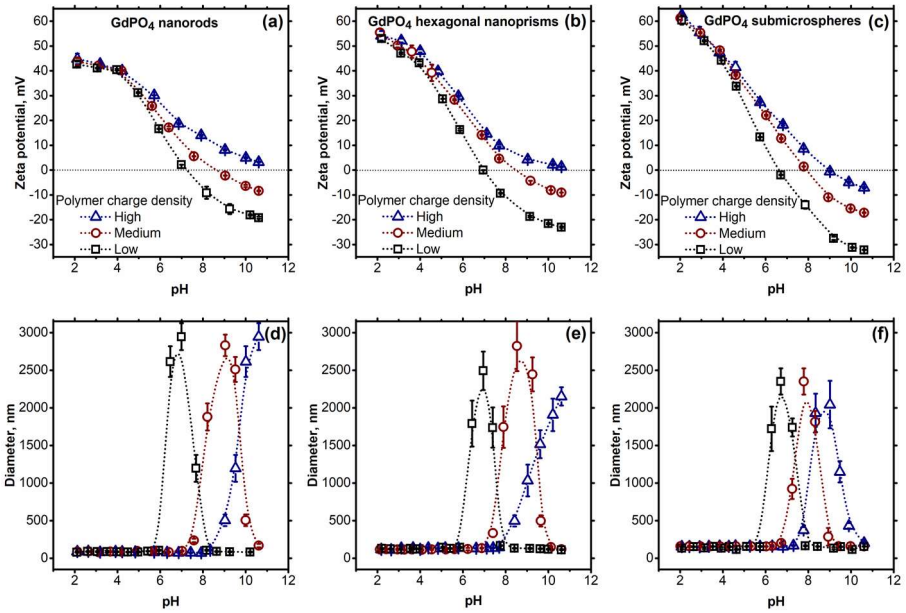

Figure 53. Dependence of zeta potential (a, b and c) and size (d, e and f) of modified $GdPO_4$ particles as a function of media pH: nanorods (a, d); nanoprisms (b, e); submicrospheres (c, f).

Results obtained during this research imply that the most suitable investigated polymer for stabilization of $GdPO_4$ particles tends to be cationic brush-type p(METAC-*stat*-PEO_{19}MEMA) polyelectrolyte with the highest density of positively charged quaternary ammonium groups in its composition (65 mol%). The observed increase in $GdPO_4$ particle stability after surface modification was achieved as combination of both steric and electrostatic stabilization as polymer coated particles tend to possess positive surface charge, which provides additional electrostatic repulsion forces among modified particles. Therefore, this surface charge additionally enhances particle stability.

Nanoparticles are often claimed to be potential candidates for bio-medical (nanoprobes) or anti-counterfeiting (security-inks) applications. Low toxicity and good bio-compatibility are highly desired properties for such nanoparticle systems, whereas superior colloidal stability is an absolute necessity [350-353].

10.5. Long-term empirical stability experiment of modified $GdPO_4$ particles with different morphology

One of the most remarkable results of this study is that, after the relatively simple nanoparticle surface modification, they can be easily re-dispersed from the dry powder and still forms stable colloids. This, however, was not the case for the uncoated nanoparticles. Both nanoparticle preparation and their surface modification procedures are rather quick, easy, simple and most importantly – exhibits nearly perfect reproducibility what is a crucial aspect not only for scientific, but also for commercial applications. It is also very important to notice that $GdPO_4$ particle surface modification using p(METAC-*stat*-PEO_{19}MEMA) polyelectrolyte not only enhances the particle stability, but also improves their bio-compatibility [354]. Hence, the results achieved during this research could have significant importance not only to scientific community working in the field of nanoscience and colloid chemistry, but also could be potentially applied in commercial applications.

In order to support our previous statement regarding nanoparticle stability and re-dispersability, an additional experiment was planned and conducted. The main objective of this experiment was to evaluate colloidal stability and re-dispersability of both bare and modified nanoparticles. For this purpose, aqueous colloids (6 colloids in total) were prepared using bare $GdPO_4$ nanoparticles with different morphologies (nanorods, hexagonal nanoprisms, and submicrospheres) and $GdPO_4$ particles (same morphology) modified with high charge density (65 mol% of quaternary ammonium groups) p(METAC-*stat*-PEO_{19}MEMA) polyelectrolyte. Firstly, in order to evaluate initial dispersability, particles were re-dispersed from dry state in neutral aqueous media (pH = 6.5). It was noticed immediately that bare $GdPO_4$ nanorods, whose isoelectric point value is close to neutral pH values (see Figure 51), were re-dispersed considerably slower than $GdPO_4$ nanorods with modified surface. In a vial on the left hand side there are bare $GdPO_4$ nanorods that were dried, whereas in a vial on the right hand side there are the same $GdPO_4$ nanorods whose surface were modified with the polyelectrolyte. After the shaking of both vials, the bare $GdPO_4$ nanorods precipitate readily, while the surface modified particles disperse into the water and remain stable.

Another experiment was observation of $GdPO_4$ colloidal suspensions stability in a time frame of up to 168 hours (one week). For this purpose, aqueous colloids of $GdPO_4$ particles (both bare and modified) with different morphologies were prepared and documented over the given time. Visual

colloidal stability over the time is represented in Figure 54. All samples were re-dispersed by treating colloids in ultrasonic bath for 5 minutes.

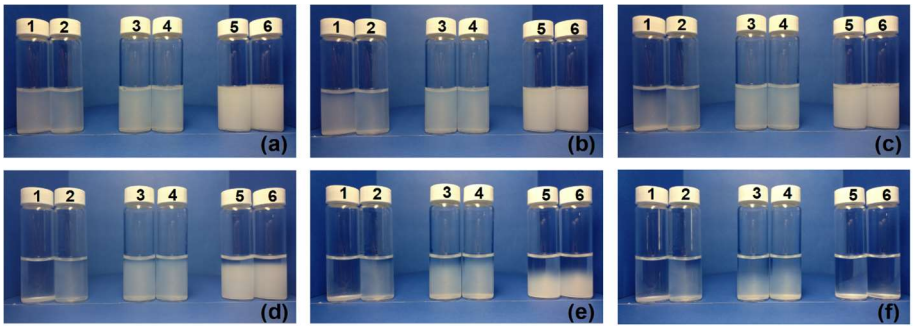

Figure 54. Visual evaluation of aqueous dispersion stability (pH = 6.5) of $GdPO_4$ particles with different morphologies ((nanorods (**1** bare, **2** stabilized), hexagonal nanoprisms (**3** bare, **4** stabilized), submicrospheres (**5** bare, **6** stabilized)) over time: 0 h (a), 1 h (b), 3 h (c), 24 h (d), 72 h (e) and 168 h (f).

It is important to notice that differently shaped $GdPO_4$ nanoparticles possess different zeta potential values under the same pH value. This means that in the same aqueous media (for example during this experiment) they also have to have different zeta-potential values. This is because isoelectric point (therefore – zeta potential value) is dependent on the particle morphology, as discussed above. During this experiment (pH value of aqueous media was set to 6.5), zeta potential values of bare $GdPO_4$ nanoparticles were +0.56, -9.0 and -18.6 mV for nanorods, hexagonal nanoprisms and submicrospheres, respectively. Meanwhile, identical aqueous colloids (pH = 6.5) were prepared by dispersing $GdPO_4$ particles modified with high charge density p(METAC-*stat*-PEO_{19}MEMA) polyelectrolyte. Zeta potential values of such colloids were ca. +22 mV for all morphologies identical as presented in Figure 53 a-c. Because modified $GdPO_4$ particles of all morphologies have almost identical zeta-potential values, it is possible to additionally evaluate the effectiveness of cationic brush-type polymers depends on the shape of modified particles. It is known that due to the electrostatic repulsion forces even insignificant nanoparticle surface charge could affect an overall stability of such particle colloids. Therefore, according to Figure 49 b, bare $GdPO_4$ hexagonal nanoprisms and submicrospheres should exhibit better colloidal stability during this experiment in comparison to bare $GdPO_4$ nanorods.

No obvious visual difference between colloids of same morphology was observed after ultrasonically re-dispersing both bare and modified $GdPO_4$ particles of various morphologies in aqueous media (pH 6.5) (see Figure 54 a).

Though, it should be noticed that aqueous colloid of bare $GdPO_4$ nanorods (Figure 54 a1) was slightly hazier in comparison with colloid obtained by re-dispersing modified $GdPO_4$ nanorods (Figure 54 a2). After one hour (Figure 54 b) a transparent layer developed and is observed in the upper part of bare $GdPO_4$ nanorods colloid (Figure 54 b1). This indicates sedimentation of bare $GdPO_4$ nanorods. This transparent layer broadens over the time and becomes more expressed in image taken after 3 h (see Figure 54 c1). In the case of $GdPO_4$ nanoprisms (3 and 4) and submicrospheres (5 and 6), no obvious differences between bare and modified aqueous colloids were observed in the time frame up to 3 h (Figure 54 c). After 24 h since beginning of the experiment, sedimentation of bare $GdPO_4$ nanorods (Figure 54 d1) becomes even more evident, whilst modified $GdPO_4$ nanorods colloids show no signs of sedimentation (Figure 54 d2). Controversially, dispersions of both bare and modified $GdPO_4$ hexagonal nanoprisms (3 and 4) even after 24 h remain in the state of stable aqueous colloids (Figure 54 d3 and d4). Slight settling is observed for both bare and modified $GdPO_4$ submicrospheres (Figure 54 d5 and d6). Visual observations after the 72 h from the beginning of experiment revealed that bare $GdPO_4$ nanorods have completely precipitated, whereas modified $GdPO_4$ nanorods colloid remained stable. Both bare and modified hexagonal nanoprism colloids show signs of sedimentation after 72 h of experiment, though modified prism settling is less expressed in comparison with bare prisms (Figure 54 e3 and e4). Regardless modified or bare, particle weight-related settling of submicrospheres still continues after 72 h of experiment (Figure 54 e5 and e6). By the end of the experiment (after 168 h) bare $GdPO_4$ nanorods (Figure 54 f1) were completely precipitated, whereas modified $GdPO_4$ nanorods were only slightly settled (Figure 54 f2) but still in the state of stable aqueous colloid. Also, a more rapid sedimentation of bare hexagonal nanoprisms (Figure 54 f3) becomes more noticeable over time, as after 168 h bare prisms were clearly more settled if compared to modified hexagonal nanoprisms (Figure 54 f4). The difference in colloidal stability of bare and modified hexagonal nanoprisms could indicate possible agglomeration of bare hexagonal nanoprisms. Both bare and modified $GdPO_4$ submicrospheres completely precipitated after 168 h (Figure 54 f5 and Figure 54 f6). The reason for such sedimentation of submicrospheres could probably be related to relatively large mass and dimensions (>100 nm) of $GdPO_4$ submicrospheres (if compared to $GdPO_4$ nanorods and hexagonal nanoprisms). We would like to emphasize that it is not accurate to evaluate particle agglomeration only by judging the visually observed sedimentation of particles. Zeta potential values of both bare and modified submicrospheres in

observed colloids are rather high, i.e., -18.6 and +22.7 mV, respectively. Such zeta potential values should be high enough to induce strong electrostatic repulsion force to prevent submicrosphere agglomeration. So to conclude, this sedimentation is likely to be caused by gravity accompanied by relatively high weight of $GdPO_4$ submicrospheres.

Up to this moment colloidal stability during this experiment was evaluated only visually. However, such approach does not really tell anything about real scale of particle agglomeration. In order to justify our claims and hypotheses derived from visual observations of $GdPO_4$ colloids during this experiment, dynamic light scattering measurements were conducted. After visual experiment ended (colloids were observed for 168 hours), aqueous dispersions were prepared for DLS measurements by simply shaking $GdPO_4$ colloids for 20-30 seconds (no ultrasonic treatment was used). After that, DLS measurements were performed and particle size distribution was determined (Figure 55). Additional DLS measurements were conducted again after 3 weeks from initial re-dispersion of particles.

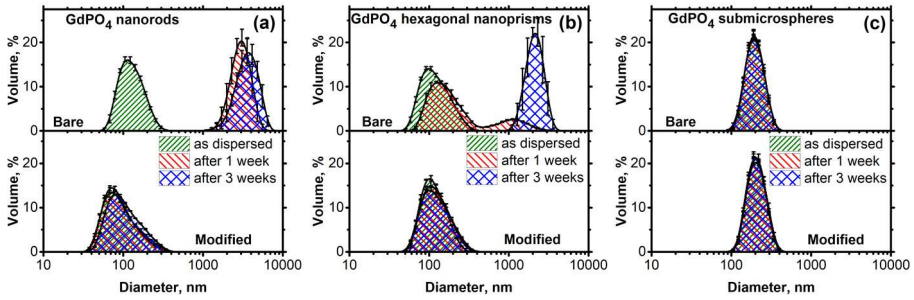

Figure 55. Particle size distribution in aqueous dispersions (pH 6.5) of $GdPO_4$ particles with different morphology after a different period of storage (as dispersed, after 1 week and after 3 weeks): nanorods (a), hexagonal nanoprisms (b) and submicrospheres (c).

DLS measurements revealed that after 168 hours (1 week) bare $GdPO_4$ nanorods were in agglomerated state (Figure 55 a) with agglomerate size varying around 2700 nm. Additional DLS measurements after 504 h (3 weeks) indicated further agglomeration of bare $GdPO_4$ nanorods (Figure 55 a) with agglomerate size increasing up to around 3600 nm. Such result was expected as bare $GdPO_4$ nanorods are close to their isoelectric point ($\zeta = +0.56$ mV) in neutral media (pH 6.5). These particles are completely unstable and, therefore, are inapplicable in any of intended applications. According to the DLS measurements, $GdPO_4$ nanorods modified with p(METAC-*stat*-PEO_{19}MEMA) cationic brush polyelectrolytes are perfectly

stable with their size varying approximately around 70 nm even after 3 weeks of storage. Contrary to bare $GdPO_4$ nanorods, $GdPO_4$ hexagonal nanoprisms have slightly expressed negative zeta potential value of -9.0 mV under pH value of 6.5. Such zeta potential value is enough to inhibit agglomeration of particles, but not to ensure overall colloidal stability of $GdPO_4$ hexagonal nanoprisms over the extended periods of time. Complete agglomeration of bare $GdPO_4$ hexagonal nanoprisms, with agglomerate size varying around 2300 nm, was observed after three weeks from initial re-dispersion (Figure 55 b). Therefore, under the given conditions, hexagonal nanoprisms are more stable if compared to rod-like $GdPO_4$ nanoparticles, but still their colloidal stability is far from superior. PSD curves, obtained by volume means of DLS, show a bimodal distribution in aqueous colloid of bare $GdPO_4$ hexagonal nanoprisms after one week (Figure 55 b) – one peak representing particles of around 105 nm in size can be attributed to stable particles and other peak represents hexagonal nanoprisms agglomerates around 1100 nm in size. PSD curve of bare hexagonal nanoprisms indicate complete agglomeration after three weeks from the initial re-dispersion with agglomerate size varying around 2300 nm (Figure 55 b). As expected, PSD curves of modified $GdPO_4$ nanoprisms (Figure 55 b) shows monomodal distribution; therefore, indicates that no agglomeration processes occurred during 3 weeks of experiment.

Further DLS measurements revealed that even though after one-week observation both bare and modified $GdPO_4$ submicrospheres were completely settled, due to relatively large values of zeta potential (-18.6 and +22.7 mV, for bare and modified particles, respectively) these particles show no agglomeration. As to be seen from Figure 55 c, PSD is monomodal with maximum value around 180 nm. DLS measurements indicated no signs of agglomeration were observed even after three weeks from the initial re-dispersion. Such results confirmed hypothesis that sedimentation of submicrospheres was induced only by relatively large particle weight.

This work leads to a conclusion that visual evaluation of nanoparticle colloidal stability, very typical in many papers, is not sufficient. Such visual stability evaluation in scientific papers and research is inappropriate and could even be referred to as incorrect. Indeed, if evaluated particles are observably unstable, as it was with bare $GdPO_4$ nanorods in case of this work, it can be concluded that aqueous colloid is unstable, even though it takes time for visual sedimentation to occur. Meanwhile, if particles have relatively large surface charge (as with $GdPO_4$ submicrospheres in this work), but they sediment over time as well (as discussed above, sedimentation of stable $GdPO_4$

submicrospheres occurred due to particle weight) they can be wrongly considered as agglomerates. Therefore, we strongly suggest that colloidal stability of aqueous dispersions should be confirmed not only visually, but also by means of light scattering measurements.

10.6. Long-term empirical stability experiment of modified $GdPO_4$ particles with different morphology

One of the most remarkable features of this study is that described concept of particle stabilization could be successfully applied in biological media. To prove this statement, the additional experiment was carried out by dispersing both bare and modified $GdPO_4$ in protein-rich aqueous media (consisting 10 vol. % of human blood plasma, pH 6.5). Firstly, particle dispersions were observed visually. It was noticed that bare particles, regardless their morphology (nanorods, hexagonal nanoprisms or submicrospheres), have higher tendency to sediment if compared to modified particles. The visual stability observations are presented in Figure 56.

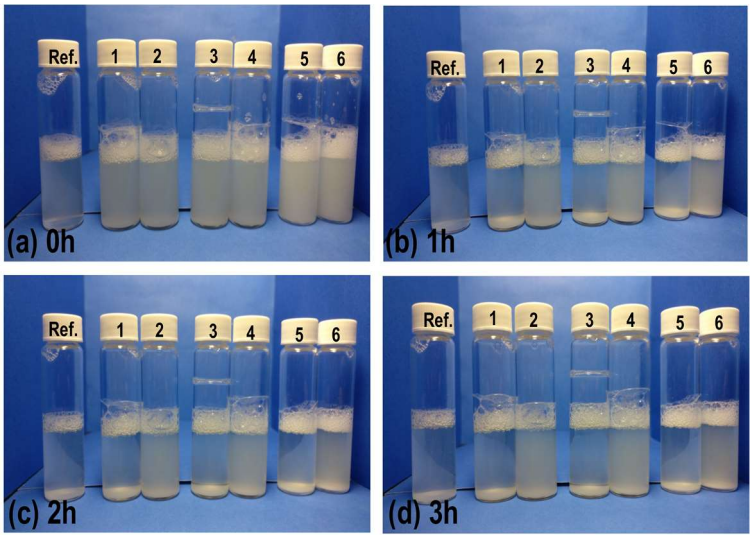

Figure 56. Visual evaluation of $GdPO_4$ particles ((nanorods (1 bare, 2 modified), hexagonal nanoprisms (3 bare, 4 modified), submicrospheres (5 bare, 6 modified)) stability in biological aqueous media (consisting 10 vol. % human blood plasma, pH 6.5 (Ref.)) over time: (a) 0 h; (b) 1 h; (c) 2 h; (d) 3 h.

The dry $GdPO_4$ powders (both bare and modified) were dispersed in protein-rich aqueous media and incubated for 3 hours. Then the dispersion was centrifuged (10000 rpm x 15 min, using Centrifuge 5804 by Eppendorf)

and particles washed with DI water (procedure repeated 3 times) to remove the excess amount of proteins. Washed particles were re-dispersed in water (pH 6.5) and the PSD of nanoparticle-protein conjugates were measured via DLS as shown in Figure 57.

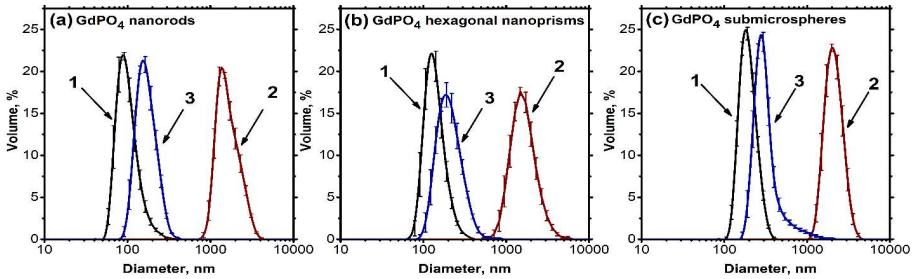

Figure 57. Particle size distribution in aqueous dispersions (pH 6.5) of $GdPO_4$ particles with different morphologies (nanorods (a), hexagonal nanoprisms (b) and submicrospheres (c)) after incubation in protein-rich aqueous media (consisting 10 vol. % human blood plasma, pH 6.5). 1 − the initial PSD; 2 – bare particles; 3 – modified particles.

The protein antifouling properties of modified particles were also evaluated by comparing the change in zeta potential of particles incubated in protein-rich media with those dispersed in protein-free aqueous media (pH 6.5). The obtained results are presented in Figure 58.

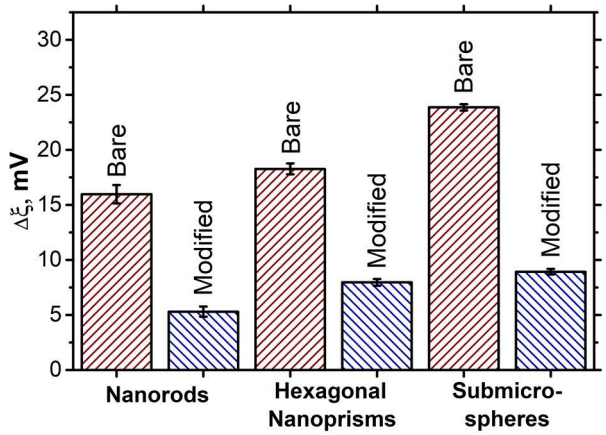

Figure 58. The change in zeta potential of particles in protein-rich aqueous media (consisting 10 vol. % of human blood plasma) compared to those dispersed in protein-free aqueous media (pH 6.5).

The smaller change in zeta potential of modified $GdPO_4$ particles (more than twice regardless the particle morphology) indicates that lower amount of

proteins is adsorbed (surrounds) the particles. Significant differences in zeta potential change proves that PEG substituents existing on the surfaces of modified $GdPO_4$ particles provides antifouling properties and significantly reduce protein binding. Therefore, these results are in perfect correlation with results obtained by measuring PSD, where modified particle-polymer conjugates exhibited smaller size if compared to bare particle-protein ones, which were non-stable and sediment rapidly (see Figure 57).

11. Nanofibrous ultralight magnetic $GdPO_4$ aerogel

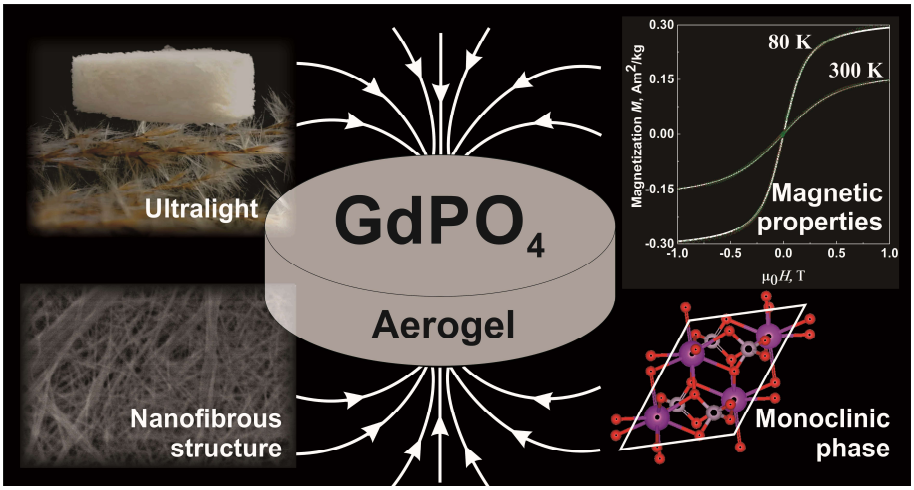

Figure 59. Representation of $GdPO_4$ aerogel unique properties.

Anisotropic aerogels are promising bulk materials with porous 3D structure, which are best known for their large surface area, low density and extremely low thermal conductivity. In this chapter synthesis of novel ultralight magnetic $GdPO_4$ aerogel is reported (Figure 59). The reported synthesis route is eco-friendly and does not require any harsh precursors or conditions. The most common route for magnetic aerogel preparation is via introduction of magnetic nanoparticles into the structure. However, $GdPO_4$ aerogel reported in this work is magnetic by itself already and no additives are required. Hydrogel used for $GdPO_4$ aerogel preparation was synthesized via hydrothermal route. Hydrogel was freeze-dried and heat treated to induce phase transformation from non-magnetic trigonal to magnetic monoclinic phase. The density of obtained magnetic nanofibrous monoclinic $GdPO_4$ aerogel is ca. 8 mg/cm^3.

11.1. Morphology and structural properties of $GdPO_4$ aerogel

The idea of this research started by preparation of $GdPO_4$ nanoparticles with different morphologies via hydrothermal synthesis route at relatively high pH values and different Gd^{3+}/PO_4^{3-} ratio in the solution [15]. It was observed that long and interwoven $GdPO_4$ nanofibers also can be obtained if pH of the synthesis solution is lowered to 7 and Gd^{3+}/PO_4^{3-} ratio is fixed to 1. Such fibers were sucessfully used for $GdPO_4$ aerogel preparation. The schematic

representation of synthesis process conducted to obtain $GdPO_4$ nanowires, hydrogel and aerogel is provided in Figure 60.

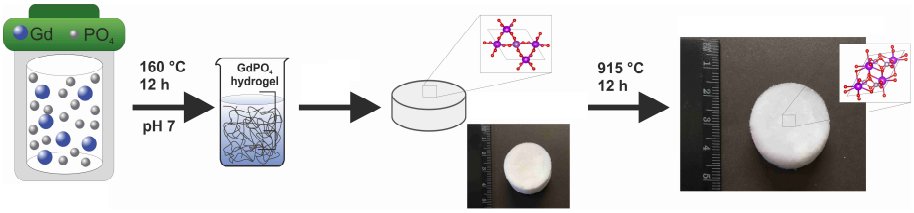

Figure 60. Preparation scheme for as-prepared aerogel (trigonal phase) and annealed $GdPO_4$ aerogel (monoclinic phase).

It was known from previous experience that increase of pH to 10 yields much shorter nanofibers; therefore, they cannot interweave sufficiently enough to form a hydrogel. The stirring should also be avoided since it breaks the delicate nanofibers. The synthesis at pH = 7 yielded nearly transparent hydrogel with the final volume of 10 mL. The obtained hydrogel was also diluted this hydrogel to 20 and 30 mL before the freeze-drying in order to check whether there is any influence to the aerogel formation. The best results were obtained for 10 mL sample, where no anisotropic pore structures were detected. However, the samples with higher volume possessed the large pores formed by ice crystals. This is supported by low resolution SEM images given in Figure 61.

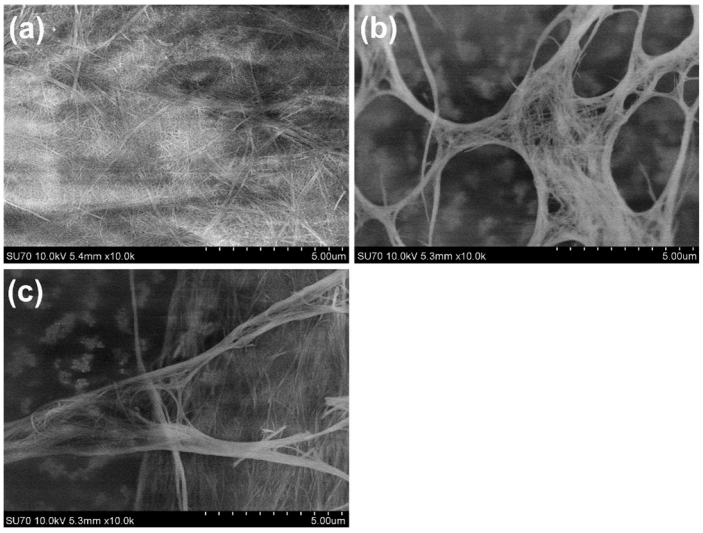

Figure 61. Low resolution SEM images of aerogels obtained after freeze-drying 10 mL (a), 20 mL (b) and 30 mL (c) hydrogel.

If hydrogel samples were diluted to 30 mL the aerogel structure collapsed during the freeze-drying procedure. The 10 mL volume hydrogel was washed and freeze dried resulting in the "as-prepared" aerogel. Subsequently, this aerogel was annealed at 915 °C for 12 h in air in order to induce phase transformation from trigonal to monoclinic.

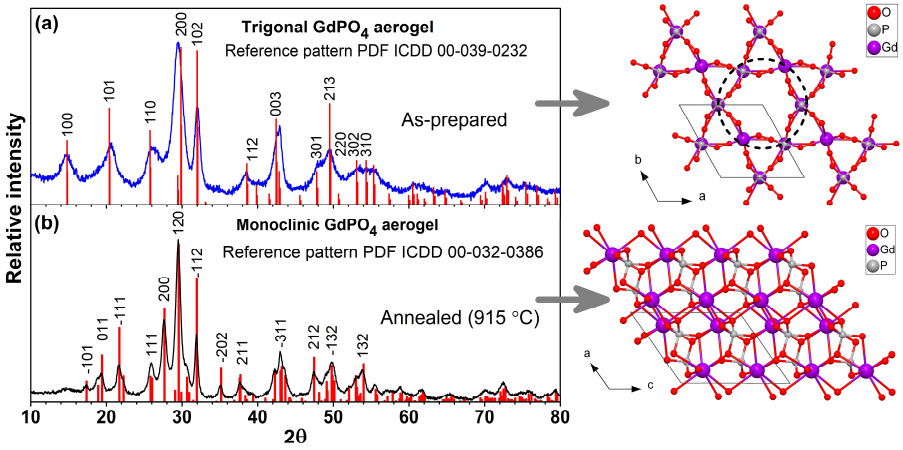

Figure 62. XRD patterns of as-prepared (a) aerogel (trigonal phase) and annealed (b) $GdPO_4$ aerogel (monoclinic phase).

Both, as-prepared and annealed aerogels were investigated by powder XRD to evaluate phase composition and purity. The obtained XRD patterns for as-prepared and annealed gadolinium phosphate aerogels are given in Figure 62 a and Figure 62 b, respectively. XRD analysis reveals that as-prepared $GdPO_4$ aerogel consists of pure rhabdophane-type phase with composition of $GdPO_4 \cdot nH_2O$, which has trigonal lattice symmetry with space group $P3_121$ (#152) (Figure 62 a). The lattice parameters of the as-prepared $GdPO_4$ aerogels were also calculated by applying Le Bail method. The calculations yielded lattice parameters a = 0.6935 nm and c = 0.6349 nm, which are slightly larger than those reported in the reference structure $GdPO_4 \cdot H_2O$, PDF ICDD 00-039-0232 (a = 0.69055 nm, c = 0.63257 nm).

The crystalline structure of trigonal rhabdophane phase contains zeolitic channels (pointed out by the black dashed circle in Figure 62 a), which accommodate crystalline water yielding $GdPO_4 \cdot nH_2O$ stoichiometry. Water molecules, accommodated in zeolitic channels, goes along crystalline structure of anisotropic particles (in this case – nanofibers), or to be more exact – along *c*-axis of $GdPO_4 \cdot nH_2O$ structure [15]. This crystalline water is responsible for stabilization of trigonal phase. Therefore, loss of this crystalline water results in phase transformation to monoclinic [355].

Annealing the as-prepared $GdPO_4$ aerogel results in phase transformation from trigonal (rhabdophane) to monoclinic (monazite) with space group $P2_1/n$ (#14). The XRD pattern shows that the pure $GdPO_4$ phase is obtained (see Figure 62 b). Calculated lattice parameters for the annealed aerogel are as follows: a = 0.6334 nm, b = 0.6854 nm, c = 0.6664 nm, β = 104.1° and are very similar to the ones provided in ICCD database (PDF ICDD-00-032-0386 card) (a = 0.63342 nm, b = 0.68451nm, c = 0.66525 nm, β = 104.0°). It is necessary to mention that the monoclinic phase is more preferable as it possesses no crystalline water within its structure. The high content of crystalline water within trigonal rhabdophane structure is known to quench luminescence emission significantly [356, 357]. Therefore, such monoclinic phase aerogel is much more suitable to be doped with rare-earth ions to introduce luminescent properties. After annealing of the as-prepared aerogel at several temperatures, we found out that 915 °C is the highest temperature that the aerogel can withstand. Annealing at higher temperature resulted in collapse of porous aerogel structure. Even samples annealed at 915 °C have already shown some signs of nanofiber melting as demonstrated in TEM images given in Figure 63.

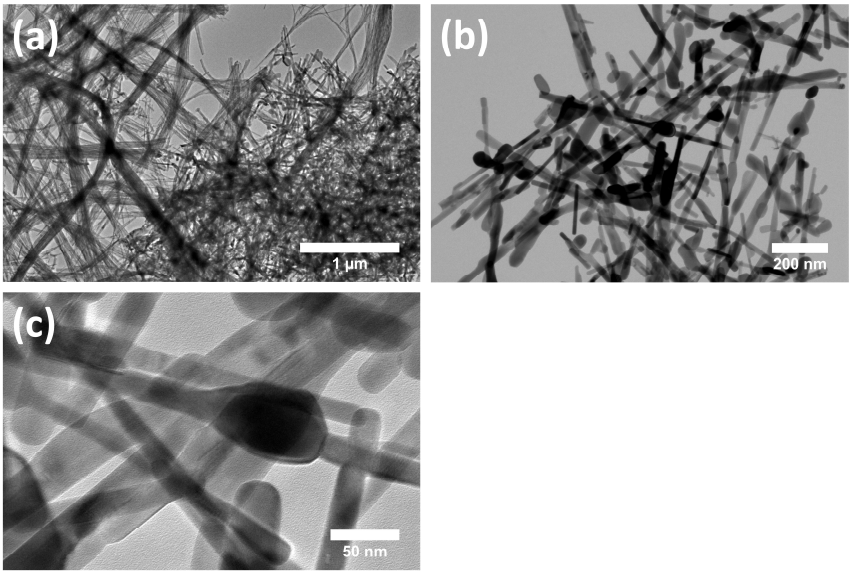

Figure 63. TEM images of annealed $GdPO_4$ aerogel indicate signs of melting.

Further, SEM and TEM were employed for morphological characterization of as-prepared and annealed $GdPO_4$ aerogel samples. The obtained images are given in Figure 64. Several studies reported that during annealing process at

900 °C temperature, when phase transformation occurs, anisotropic nanoparticles of trigonal $LnPO_4$ tend to deform and sinter badly [356, 358, 359]. This, however, is not true in this case, where virtually identical morphological features of both as-prepared and annealed aerogel samples were observed. This can be evaluated from Figure 64. Both as-prepared and annealed $GdPO_4$ aerogels are formed from high aspect ratio fibers; therefore, they can be regarded as porous, chaotically interwined nanofibrous structures. High porosity of the structure ensures effective accessibility of $GdPO_4$ aerogel surface throughout the entire volume. SEM images also revealed that $GdPO_4$ nanofibers within aerogel structure were randomly woven together, forming a three dimensional nanofibrous network. It is necessary to emphasize again that nanofibrous $GdPO_4$ aerogel withstands annealing process and phase transformation, while maintaining the original 3D structure undeformed and undamaged.

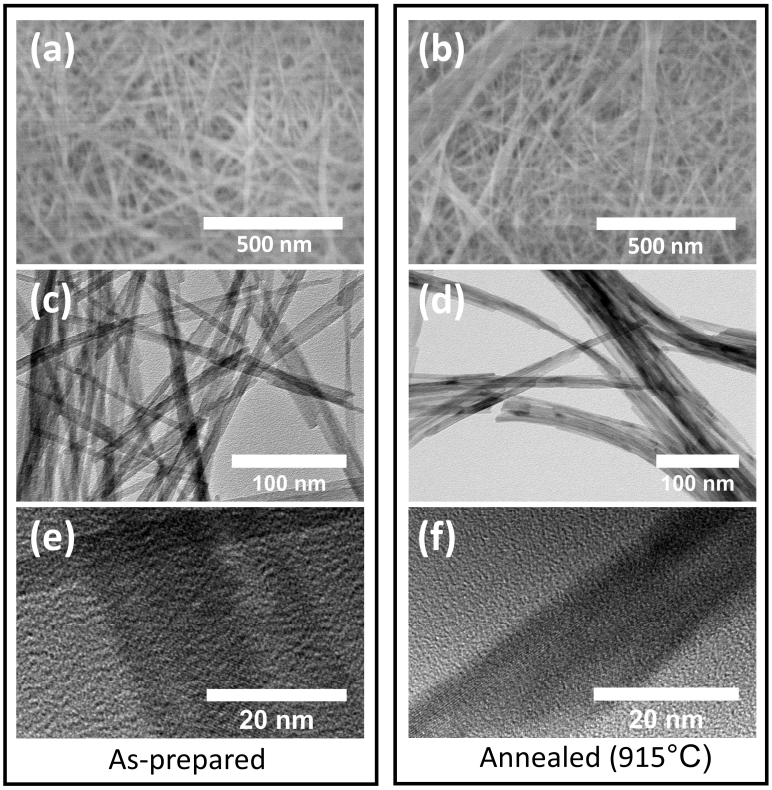

Figure 64. SEM and TEM images of $GdPO_4$ aerogel: as-prepared trigonal (a, c, e) and annealed monoclinic (b, d, f).

Taken TEM images confirm nanofibrous structure of both as-prepared and annealed $GdPO_4$ aerogels (see Figure 64 c-f and Figure 65). It is evident that wider in diameter fibers consist of axially agglomerated single crystalline nanofibers with a diameter ranging from 5 to 15 nm. TEM analysis of annealed samples has also confirmed that annealing process causes significant changes in the morphology of nanofiber junctions – they become noticeably more agglomerated. Figure 64 c demonstrates that prior sintering, individual nanofibers were mostly separate throughout the junctions and contact areas. Nanofibers in contact places were more agglomerated and sintered, while in as-prepared aerogel nanofibers were less affected by agglomeration. This claim is supported by numerous TEM images given in Figure 65.

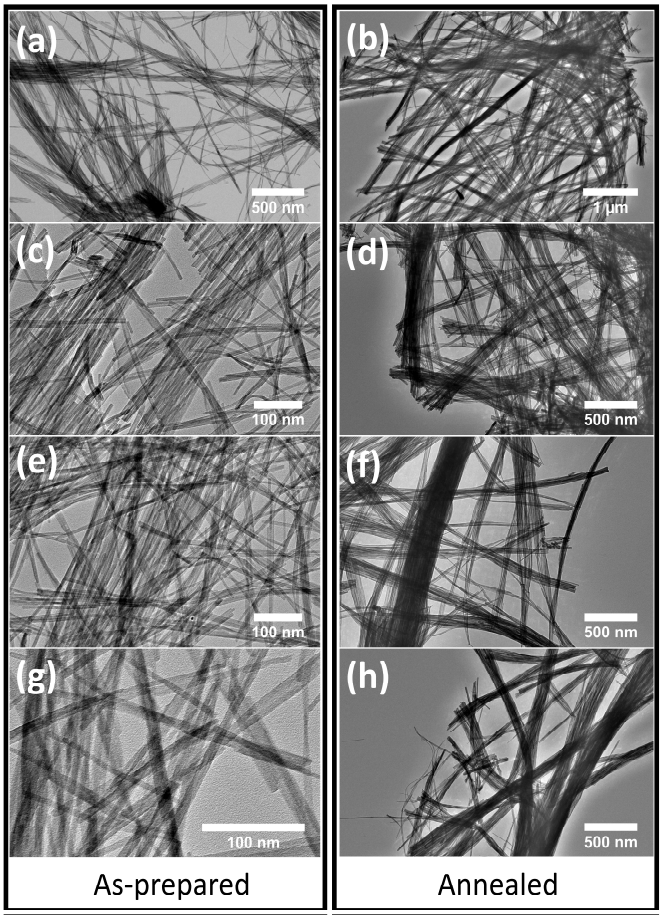

Figure 65. TEM images of as-prepared (a, c, e, g) and annealed (b, d, f, h) $GdPO_4$ aerogel samples.

Surface area and weight of obtained $GdPO_4$ aerogels were also evaluated, since these parameters are often referred to as the main characteristics defining aerogels. As-prepared $GdPO_4$ aerogel had density of around 10 mg/cm^3 and specific surface area of around 29 m^2/g. On the contrary, the density of annealed aerogel decreased even more, i.e. to around 8 mg/cm^3, and the determined specific surface area was around 35 m^2/g. It is evident that specific surface area of annealed $GdPO_4$ aerogels increases. Such increase in surface area is a result of crystalline water removal during the calcination step when trigonal rhabdophane phase transforms to monoclinic monazite phase. Since the total volume of the annealed aerogel virtually does not change, the weight loss results in increased surface area.

11.2. Magnetic properties of $GdPO_4$ aerogel

Since the magnetic properties are the most interesting feature of the reported $GdPO_4$ aerogels, the magnetization measurements were performed in order to analyze magnetic behavior of the annealed $GdPO_4$ aerogel. Figure 66 shows magnetization versus applied field at T = 300 and 80 K of the sample containing annealed $GdPO_4$ aerogel which consists of randomly oriented $GdPO_4$ nanofibers. We point out the absence of any hysteresis either at 300 or 80 K temperature. The observed nonlinear (S-shaped) magnetization curves have been fitted well using a standard Langevin function that is usually used to describe magnetization of superparamagnetic (SPM) systems [360]:

$$M(H,T) = N\, m\, L\left(\frac{\mu_0 m\, H}{k_B T}\right) \qquad \text{(Eq. 4)}$$

where N is the number of magnetic nanoparticles in the sample, m is the averaged magnetic moment of a particle, k_B is the Boltzmann's constant and $L(x)$ is the Langevin function: $L(x) = coth(x)-1/x$. Magnetic moment per nanoparticle of about 762 and 1190 Bohr magnetons at 300 and 80 K, respectively, was estimated in this work, and corresponds to the best fitting of the magnetization curves with the Langevin function (see red solid curves in Figure 66). The observed nonlinear M–H relation of the Langevin type and absence of hysteresis certify that the rod-like $GdPO_4$ nanofibers may be considered as a system of SPM particles. Similar nonlinear M–H relation and absence of hysteresis both at RT and low temperatures have been reported earlier for crystalline $GdPO_4$ material exhibiting monoclinic crystalline structure and prepared in various forms, namely, polycrystals [361], star-like nanocrystals [26] as well as Tb and Eu-doped nanotubes [30, 362]. It is worth noting, however, that room temperature magnetization value, indicated in this

work, is by factor 2 to 5 lower compared to those reported earlier. The observed magnetic properties of the nanotubes is a result of competing antiferromagnetic and ferromagnetic interaction of the paramagnetic Gd^{3+} ions with unpaired inner 4f electrons in the outer orbital in the monoclinic unit cell [361]. The reduced magnetization value at room temperature may probably be understood taking into account importance of the surface effects on magnetisation of the nanocrystalline material and significant shape anisotropy of the rod-like nanocrystals.

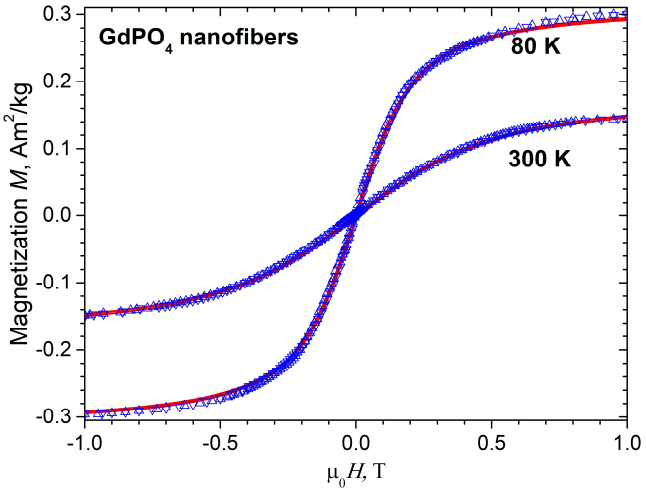

Figure 66. Mass magnetization versus magnetic field of the $GdPO_4$ nanotubes. Solid (red) lines show fitting of the experimental data by Langevin function.

12. General conclusions

- $GdPO_4 \cdot nH_2O$ particles with various sizes and morphologies were synthesized via hydrothermal route. It was demonstrated that altering molar ratio of $NH_4H_2PO_4/Gd^{3+}$ enables effective control over morphology of the synthesized nanoparticles. When $NH_4H_2PO_4/Gd^{3+}$ molar ratio was set to 10, 50 and 100, formation of nanorods, hexagonal nanoprisms and submicrospheres was observed, respectively.
- It was shown that particles with different morphology possess different zeta potential values; therefore, their colloidal stability can be adjusted relative to the application field.
- Bare $GdPO_4$ particles of different morphologies (nanorods, hexagonal nanoprisms, and submicrospheres) were modified with cationic brush-type p(METAC-*stat*-PEO_{19}MEMA) polyelectrolytes. Such cationic brush-type polymers had positive effect over colloidal stability of $GdPO_4$ particles. Apparently, the p(METAC-*stat*-PEO_{19}MEMA) polyelectrolytes with the highest amount of charged groups (65 mol%) had the most noticeable positive impact on stability of $GdPO_4$ particles. $GdPO_4$ particles modified with such polymer were successfully redispersed from the dry-state. Such dispersions remained stable up to three weeks with no signs of agglomeration.
- The stability experiment of $GdPO_4$ particles in protein-rich aqueous media (consisting 10 vol. % of human blood plasma (pH 6.5)) showed that p(METAC-*stat*-PEO_{19}MEMA) modified polymers on the surface of nanoparticles not only significantly improve dispersion stability, but also has protein-repellent properties. The sorption of proteins on the surface of modified particles is at least twice lower than that of unmodified particles.
- Lyophilization of $GdPO_4$ nanofiber hydrogel yielded $GdPO_4$ aerogel of trigonal rhabdophane phase. Further annealing of such aerogel, under temperature of 915 °C, induced phase transformation from trigonal rhabdophane phase to monoclinic monazite phase without disrupting its nanofibrous structure. The monazite phase $GdPO_4$ aerogel displayed superparamagnetic properties, had large surface area and was ultralight.

13. References

[1] S. M. Ng, M. Koneswaran, R. Narayanaswamy, A review on fluorescent inorganic nanoparticles for optical sensing applications. *RSC Advances* **2016,** *6* (26), 21624-21661.

[2] J. Liu, A. M. Kaczmarek, R. Van Deun, Advances in tailoring luminescent rare-earth mixed inorganic materials. *Chemical Society Reviews* **2018,** *47* (19), 7225-7238.

[3] H. Dong, S.-R. Du, X.-Y. Zheng, G.-M. Lyu, L.-D. Sun, L.-D. Li, P.-Z. Zhang, C. Zhang, C.-H. Yan, Lanthanide Nanoparticles: From Design toward Bioimaging and Therapy. *Chemical Reviews* **2015,** *115* (19), 10725-10815.

[4] Y. Zhang, W. Wei, G. K. Das, T. T. Yang Tan, Engineering lanthanide-based materials for nanomedicine. *Journal of Photochemistry and Photobiology C: Photochemistry Reviews* **2014,** *20*, 71-96.

[5] J.-C. G. Bünzli, Rising Stars in Science and Technology: Luminescent Lanthanide Materials. *European Journal of Inorganic Chemistry* **2017,** *2017* (44), 5058-5063.

[6] Happy, A. I. Y. Tok, L. T. Su, F. Y. C. Boey, S. H. Ng, Homogeneous precipitation of Dy_2O_3 nanoparticles-effects of synthesis parameters. *Journal of Nanoscience and Nanotechnology* **2007**, *7*, 907-915

[7] D. Wawrzynczyk, M. Nyk, A. Bednarkiewicz, W. Strek, M. Samoc, Morphology- and size-dependent spectroscopic properties of Eu^{3+}-doped Gd_2O_3 colloidal nanocrystals. *Journal of Nanoparticle Research* **2014,** *16* (11), 2690.

[8] R. M. Pallares, R. J. Abergel, Transforming lanthanide and actinide chemistry with nanoparticles. *Nanoscale* **2020,** *12* (3), 1339-1348.

[9] S. Y. Lee, M. Lin, A. Lee, Y. I. Park, Lanthanide-Doped Nanoparticles for Diagnostic Sensing. *Nanomaterials* **2017,** *7* (12), 411.

[10] G. A. Mandl, D. R. Cooper, T. Hirsch, J. Seuntjens, J. A. Capobianco, Perspective: lanthanide-doped upconverting nanoparticles. *Methods and Applications in Fluorescence* **2019,** *7* (1), 012004.

[11] Y. Tang, R. Mei, S. Yang, H. Tang, W. Yin, Y. Xu, Y. Gao, Hollow $GdPO_4$:Eu^{3+} microspheres: Luminescent properties and applications as drug carrier. *Superlattices and Microstructures* **2016,** *92*, 256-263.

[12] M. A. Hassairi, A. Garrido Hernández, M. Dammak, D. Zambon, G. Chadeyron, R. Mahiou, Tuning white upconversion emission in $GdPO_4$:Er/Yb/Tm phosphors. *Journal of Luminescence* **2018,** *203*, 707-713.

[13] V. Kumar, S. Singh, S. Chawla, Fabrication of dual excitation, dual emission nanophosphor with broad UV and IR excitation through simultaneous doping of triple rare earth ions Er^{3+}, Yb^{3+}, Eu^{3+} in $GdPO_4$. *Superlattices and Microstructures* **2015,** *79*, 86-95.

[14] T. T. N. Nguyen, V. Bellière-Baca, P. Rey, J. M. M. Millet, Efficient catalysts for simultaneous dehydration of light alcohols in gas phase. *Catalysis Science & Technology* **2015,** *5* (7), 3576-3584.

[15] M. Janulevicius, V. Klimkevicius, A. Vanetsev, V. Plausinaitiene, S. Sakirzanovas, A. Katelnikovas, Controlled hydrothermal synthesis, morphological design and colloidal stability of $GdPO_4 \cdot nH_2O$ particles. *Materials Today Communications* **2020,** *23*, 100934.
[16] V. Kumar, S. Singh, R. K. Kotnala, S. Chawla, $GdPO_4:Eu^{3+}$ nanoparticles with intense orange red emission suitable for solar spectrum conversion and their multifunctionality. *Journal of Luminescence* **2014,** *146*, 486-491.
[17] Y. Xing, M. Li, S. A. Davis, S. Mann, Synthesis and Characterization of Cerium Phosphate Nanowires in Microemulsion Reaction Media. *The Journal of Physical Chemistry B* **2006,** *110* (3), 1111-1113.
[18] A. Phuruangrat, T. Thongtem, S. Thongtem, Sonochemical synthesis and characterization of uniform lanthanide orthophosphate ($LnPO_4$, Ln = La and Ce) nanorods. *Rare Metals* **2015,** *34* (5), 301-307.
[19] E. V. Samsonova, A. V. Popov, A. S. Vanetsev, K. Keevend, E. O. Orlovskaya, V. Kiisk, S. Lange, U. Joost, K. Kaldvee, U. Maeorg, N. A. Glushkov, A. V. Ryabova, I. Sildos, V. V. Osiko, R. Steiner, V. B. Loschenov, Y. V. Orlovskii, An energy transfer kinetic probe for OH-quenchers in the $Nd(3+):YPO_4$ nanocrystals suitable for imaging in the biological tissue transparency window. *Physical Chemistry Chemical Physics* **2014** *16* (48), 26806-26815.
[20] A. Ochiai, S. Utsunomiya, Crystal Chemistry and Stability of Hydrated Rare-Earth Phosphates Formed at Room Temperature. *Minerals* **2017,** *7* (5), 84-105.
[21] N. Ekthammathat, T. Thongtem, A. Phuruangrat, S. Thongtem, Facile Hydrothermal Synthesis and Optical Properties of Monoclinic $CePO_4$ Nanowires with High Aspect Ratio. *Journal of Nanomaterials* **2012,** *2012*, 958593, 1-6.
[22] H. Khajuria, J. Ladol, S. Khajuria, M. S. Shah, H. N. Sheikh, Surfactant mediated hydrothermal synthesis, characterization and luminescent properties of $GdPO_4:Ce^{3+}/Tb^{3+}@GdPO_4$ core shell nanorods. *Materials Research Bulletin* **2016,** *80*, 150-158.
[23] Z. Xu, Y. Cao, C. Li, P. a. Ma, X. Zhai, S. Huang, X. Kang, M. Shang, D. Yang, Y. Dai, J. Lin, Urchin-like $GdPO_4$ and $GdPO_4:Eu^{3+}$ hollow spheres – hydrothermal synthesis, luminescence and drug-delivery properties. *Journal of Materials Chemistry* **2011,** *21* (11), 3686-3694.
[24] N. O. Nuñez, S. R. Liviano, M. Ocaña, Citrate mediated synthesis of uniform monazite $LnPO_4$ (Ln=La, Ce) and $Ln:LaPO_4$ (Ln=Eu, Ce, Ce+Tb) spheres and their photoluminescence. *Journal of Colloid and Interface Science* **2010,** *349* (2), 484-491.
[25] X. Li, H. Bi, Template-free synthesis of $LaPO_4:Eu^{3+}$ hollow spheres with enhanced luminescent properties. *Journal of Alloys and Compounds* **2012,** *532*, 72-77.

[26] G. A. Kumar, N. R. Balli, M. Kailasnath, L. C. Mimun, C. Dannangoda, K. S. Martirosyan, C. Santhosh, D. K. Sardar, Spectroscopic and magnetic properties of neodymium doped in $GdPO_4$ sub-micron-stars prepared by solvothermal method. *Journal of Alloys and Compounds* **2016,** *672*, 668-673.
[27] Z. Wang, X. Shi, X. Wang, Q. Zhu, B.-N. Kim, X. Sun, J.-G. Li, Breaking the strong 1D growth habit to yield quasi-equiaxed $REPO_4$ nanocrystals (RE = La–Dy) via solvothermal reaction and investigation of photoluminescence. *CrystEngComm* **2018,** *20* (6), 796-806.
[28] M. Saraf, P. Kumar, G. Kedawat, J. Dwivedi, S. A. Vithayathil, N. Jaiswal, B. A. Kaipparettu, B. K. Gupta, Probing Highly Luminescent Europium-Doped Lanthanum Orthophosphate Nanorods for Strategic Applications. *Inorganic Chemistry* **2015,** *54* (6), 2616-2625.
[29] H. Xu, B. Xu, R. Liu, X. Li, S. Zhang, C. Ouyang, S. Zhong, Facile microwave synthesis of $ScPO_4{\cdot}2H_2O$ flowerlike superstructures: morphology control, electronic structure and multicolor tunable luminescent properties. *CrystEngComm* **2017,** *19* (38), 5787-5796.
[30] B. Abécassis, F. Lerouge, F. Bouquet, S. Kachbi, M. Monteil, P. Davidson, Aqueous Suspensions of $GdPO_4$ Nanorods: A Paramagnetic Mineral Liquid Crystal. *The Journal of Physical Chemistry B* **2012,** *116* (25), 7590-7595.
[31] H. Hifumi, S. Yamaoka, A. Tanimoto, D. Citterio, K. Suzuki, Gadolinium-Based Hybrid Nanoparticles as a Positive MR Contrast Agent. *Journal of the American Chemical Society* **2006,** *128* (47), 15090-15091.
[32] G. H. Lee, Y. Chang, T.-J. Kim, Blood-Pool and Targeting MRI Contrast Agents: From Gd-Chelates to Gd-Nanoparticles. *European Journal of Inorganic Chemistry* **2012,** *2012* (12), 1924-1933.
[33] J. Huang, Z. Lv, Y. Wang, Z. Wang, T. Gao, N. Zhang, M. Guo, H. Zou, P. Zhang, In Vivo MRI and X-Ray Bifunctional Imaging of Polymeric Composite Supplemented with $GdPO_4{\cdot}H_2O$ Nanobundles for Tracing Bone Implant and Bone Regeneration. *Advanced Healthcare Materials* **2016,** *5* (17), 2182-2190.
[34] ISO, ISO/TS 80004-2:2015. In *Nanotechnologies — Vocabulary — Part 2: Nano-objects*, 2015-06 ed.; 2015; p 10.
[35] B. S. Institution, Nanoparticles. Vocabulary. British Standards Institution: 2011; p 36.
[36] J.-M. Kim, Y.-S. Chung, H. J. Jo, N.-J. Lee, M. S. Kim, S. H. Woo, S. Park, J. W. Kim, H. M. Kim, M.-G. Han, Identification of Coronavirus Isolated from a Patient in Korea with COVID-19. *Osong Public Health and Research Perspectives* **2020,** *11* (1), 3-7.
[37] H. P. Erickson, Size and Shape of Protein Molecules at the Nanometer Level Determined by Sedimentation, Gel Filtration, and Electron Microscopy. *Biological Procedures Online* **2009,** *11* (1), 32.
[38] M. Reth, Matching cellular dimensions with molecular sizes. *Nature Immunology* **2013,** *14* (8), 765-767.

[39] S. Rodriguez-Liviano, A. I. Becerro, D. Alcántara, V. Grazú, J. M. de la Fuente, M. Ocaña, Synthesis and Properties of Multifunctional Tetragonal Eu:$GdPO_4$ Nanocubes for Optical and Magnetic Resonance Imaging Applications. *Inorganic Chemistry* **2013,** *52* (2), 647-654.
[40] S. Sankar, B. N. Nair, T. Suzuki, G. M. Anilkumar, M. Padmanabhan, U. N. S. Hareesh, K. G. Warrier, Hydrophobic and Metallophobic Surfaces: Highly Stable Non-wetting Inorganic Surfaces Based on Lanthanum Phosphate Nanorods. *Scientific Reports* **2016,** *6* (1), 22732.
[41] M. Janulevicius, V. Klimkevičius, L. Mikoliunaite, B. Vengalis, R. Vargalis, S. Sakirzanovas, V. Plausinaitiene, A. Zilinskas, A. Katelnikovas, Ultralight Magnetic Nanofibrous $GdPO_4$ Aerogel. *ACS Omega* **2020,** *5* (23), 14180-14185.
[42] G. E. Fair, R. S. Hay, E. E. Boakye, Precipitation Coating of Rare-Earth Orthophosphates on Woven Ceramic Fibers—Effect of Rare-Earth Cation on Coating Morphology and Coated Fiber Strength. *Journal of the American Ceramic Society* **2008,** *91* (7), 2117-2123.
[43] C. P. Aoife, G. Brian, C. Shaneel, C. James, Carbon nanomaterials and their application to electrochemical sensors: a review. *Nanotechnology Reviews* **2018,** *7* (1), 19-41.
[44] M. Notarianni, J. Liu, K. Vernon, N. Motta, Synthesis and applications of carbon nanomaterials for energy generation and storage. *Beilstein Journal of Nanotechnology* **2016,** *7*, 149-96.
[45] A. Nimibofa, E. A. Newton, A. Y. Cyprain, W. Donbebe, Fullerenes: Synthesis and Applications. *Journal of Materials Science Research* **2018,** *7* (3), 22-36.
[46] A. Zieleniewska, F. Lodermeyer, A. Roth, D. M. Guldi, Fullerenes – how 25 years of charge transfer chemistry have shaped our understanding of (interfacial) interactions. *Chemical Society Reviews* **2018,** *47* (3), 702-714.
[47] S.-E. Zhu, F. Li, G.-W. Wang, Mechanochemistry of fullerenes and related materials. *Chemical Society Reviews* **2013,** *42* (18), 7535-7570.
[48] A. Mageswari, R. Srinivasan, P. Subramanian, N. Ramesh, K. M. Gothandam, Nanomaterials: Classification, Biological Synthesis and Characterization. In *Nanoscience in Food and Agriculture 3*, S. Ranjan, N. Dasgupta, E. Lichtfouse, Eds. Springer International Publishing: Cham, 2016; pp 31-71.
[49] N. Saifuddin, A. Z. Raziah, A. R. Junizah, Carbon Nanotubes: A Review on Structure and Their Interaction with Proteins. *Journal of Chemistry* **2013,** *2013*, 676815.
[50] J. Prasek, J. Drbohlavova, J. Chomoucka, J. Hubalek, O. Jasek, V. Adam, R. Kizek, Methods for carbon nanotubes synthesis—review. *Journal of Materials Chemistry* **2011,** *21* (40), 15872-15884.
[51] G. Rahman, Z. Najaf, A. Mehmood, S. Bilal, A. U. Shah, S. A. Mian, G. Ali, An Overview of the Recent Progress in the Synthesis and Applications of Carbon Nanotubes. *C — Journal of Carbon Research* **2019,** *5* (1), 3.

[52] K. Kobashi, S. Ata, T. Yamada, D. N. Futaba, T. Okazaki, K. Hata, Classification of Commercialized Carbon Nanotubes into Three General Categories as a Guide for Applications. *ACS Applied Nano Materials* **2019,** *2* (7), 4043-4047.
[53] H. Dai, Carbon Nanotubes: Synthesis, Integration, and Properties. *Accounts of Chemical Research* **2002,** *35* (12), 1035-1044.
[54] E. P. Randviir, D. A. C. Brownson, C. E. Banks, A decade of graphene research: production, applications and outlook. *Materials Today* **2014,** *17* (9), 426-432.
[55] P. Avouris, C. Dimitrakopoulos, Graphene: synthesis and applications. *Materials Today* **2012,** *15* (3), 86-97.
[56] X. J. Lee, B. Y. Z. Hiew, K. C. Lai, L. Y. Lee, S. Gan, S. Thangalazhy-Gopakumar, S. Rigby, Review on graphene and its derivatives: Synthesis methods and potential industrial implementation. *Journal of the Taiwan Institute of Chemical Engineers* **2019,** *98*, 163-180.
[57] M. Hernaez, C. Zamarreño, S. Melendi-Espina, L. Bird, A. Mayes, F. Arregui, Optical Fibre Sensors Using Graphene-Based Materials: A Review. *Sensors* **2017,** *17* (12), 155.
[58] A. Nag, A. Mitra, S. C. Mukhopadhyay, Graphene and its sensor-based applications: A review. *Sensors and Actuators A: Physical* **2018,** *270*, 177-194.
[59] L. Farzin, M. Shamsipur, L. Samandari, S. Sheibani, HIV biosensors for early diagnosis of infection: The intertwine of nanotechnology with sensing strategies. *Talanta* **2020,** *206*, 120201.
[60] P. T. Yin, S. Shah, M. Chhowalla, K.-B. Lee, Design, Synthesis, and Characterization of Graphene–Nanoparticle Hybrid Materials for Bioapplications. *Chemical Reviews* **2015,** *115* (7), 2483-2531.
[61] Z. Abdullaeva. Classification of Nanomaterials. *Nano- and Biomaterials.* Wiley: **2017**, pp 27-56.
[62] E. Abbasi, S. F. Aval, A. Akbarzadeh, M. Milani, H. T. Nasrabadi, S. W. Joo, Y. Hanifehpour, K. Nejati-Koshki, R. Pashaei-Asl, Dendrimers: synthesis, applications, and properties. *Nanoscale Research Letters* **2014,** *9* (1), 247.
[63] M. T. McMahon, J. W. M. Bulte, Two decades of dendrimers as versatile MRI agents: a tale with and without metals. *Wiley Interdiscip Rev Nanomed Nanobiotechnol* **2018,** *10* (3), e1496-e1496.
[64] C. Kojima, B. Turkbey, M. Ogawa, M. Bernardo, C. A. S. Regino, L. H. Bryant Jr., P. L. Choyke, K. Kono, H. Kobayashi, Dendrimer-based MRI contrast agents: the effects of PEGylation on relaxivity and pharmacokinetics. *Nanomedicine* **2011** *7*(6), 1001-1008.
[65] C. Sandoval-Yañez, C. Castro Rodriguez, Dendrimers: Amazing Platforms for Bioactive Molecule Delivery Systems. *Materials* **2020,** *13* (3), 570.

[66] A. Akbarzadeh, R. Rezaei-Sadabady, S. Davaran, S. W. Joo, N. Zarghami, Y. Hanifehpour, M. Samiei, M. Kouhi, K. Nejati-Koshki, Liposome: classification, preparation, and applications. *Nanoscale Research Letters* **2013,** *8* (1), 102.
[67] E. Beltrán-Gracia, A. López-Camacho, I. Higuera-Ciapara, J. B. Velázquez-Fernández, A. A. Vallejo-Cardona, Nanomedicine review: clinical developments in liposomal applications. *Cancer Nanotechnology* **2019,** *10* (1), 11.
[68] L. Sercombe, T. Veerati, F. Moheimani, S. Y. Wu, A. K. Sood, S. Hua, Advances and Challenges of Liposome Assisted Drug Delivery. *Front Pharmacol* **2015,** *6*, 286-286.
[69] Y. Panahi, M. Farshbaf, M. Mohammadhosseini, M. Mirahadi, R. Khalilov, S. Saghfi, A. Akbarzadeh, Recent advances on liposomal nanoparticles: synthesis, characterization and biomedical applications. *Artificial Cells, Nanomedicine, and Biotechnology* **2017,** *45* (4), 788-799.
[70] A. Puri, K. Loomis, B. Smith, J.-H. Lee, A. Yavlovich, E. Heldman, R. Blumenthal, Lipid-based nanoparticles as pharmaceutical drug carriers: from concepts to clinic. *Crit Rev Ther Drug Carrier Syst* **2009,** *26* (6), 523-580.
[71] M. E. R. O'Brien, N. Wigler, M. Inbar, R. Rosso, E. Grischke, A. Santoro, R. Catane, D. G. Kieback, P. Tomczak, S. P. Ackland, F. Orlandi, L. Mellars, L. Alland, C. Tendler, Reduced cardiotoxicity and comparable efficacy in a phase IIItrial of pegylated liposomal doxorubicin HCl(CAELYX/Doxil) versus conventional doxorubicin forfirst-line treatment of metastatic breast cancer. *Annals of Oncology* **2004,** *15* (3), 440-449.
[72] H. M. Trinh, M. Joseph, K. Cholkar, R. Mitra, A. K. Mitra, Chapter 3 - Nanomicelles in Diagnosis and Drug Delivery∗. In *Emerging Nanotechnologies for Diagnostics, Drug Delivery and Medical Devices*, A. K. Mitra, K. Cholkar, A. Mandal, Eds. Elsevier: Boston, 2017; pp 45-58.
[73] C. Guo, Y. Zhang, Z. Yang, M. Li, F. Li, F. Cui, T. Liu, W. Shi, X. Wu, Nanomicelle formulation for topical delivery of cyclosporine A into the cornea: in vitro mechanism and in vivo permeation evaluation. *Scientific Reports* **2015,** *5* (1), 12968.
[74] Z. Ahmad, A. Shah, M. Siddiq, H.-B. Kraatz, Polymeric micelles as drug delivery vehicles. *RSC Advances* **2014,** *4* (33), 17028-17038.
[75] H. Cabral, K. Miyata, K. Osada, K. Kataoka, Block Copolymer Micelles in Nanomedicine Applications. *Chemical Reviews* **2018,** *118* (14), 6844-6892.
[76] A. Nasir, A. Kausar, A. Younus, A Review on Preparation, Properties and Applications of Polymeric Nanoparticle-Based Materials. *Polymer-Plastics Technology and Engineering* **2015,** *54* (4), 325-341.
[77] J. Karlsson, H. J. Vaughan, J. J. Green, Biodegradable Polymeric Nanoparticles for Therapeutic Cancer Treatments. *Annual Review of Chemical and Biomolecular Engineering* **2018,** *9* (1), 105-127.

[78] M.-C. Chen, K. Sonaje, K.-J. Chen, H.-W. Sung, A review of the prospects for polymeric nanoparticle platforms in oral insulin delivery. *Biomaterials* **2011,** *32* (36), 9826-9838.
[79] B. L. Banik, P. Fattahi, J. L. Brown, Polymeric nanoparticles: the future of nanomedicine. *WIREs Nanomedicine and Nanobiotechnology* **2016,** *8* (2), 271-299.
[80] A. Mahapatro, D. K. Singh, Biodegradable nanoparticles are excellent vehicle for site directed in-vivo delivery of drugs and vaccines. *J Nanobiotechnology* **2011,** *9*, 55-55.
[81] K. Zhao, D. Li, C. Shi, X. Ma, G. Rong, H. Kang, X. Wang, B. Sun, Biodegradable Polymeric Nanoparticles as the Delivery Carrier for Drug. *Current Drug Delivery* **2016** *13* (4), 494-499.
[82] M. Auffan, J. Rose, J.-Y. Bottero, G. V. Lowry, J.-P. Jolivet, M. R. Wiesner, Towards a definition of inorganic nanoparticles from an environmental, health and safety perspective. *Nature Nanotechnology* **2009,** *4* (10), 634-641.
[83] R. Ladj, A. Bitar, M. Eissa, Y. Mugnier, R. Le Dantec, H. Fessi, A. Elaissari, Individual inorganic nanoparticles: preparation, functionalization and in vitro biomedical diagnostic applications. *Journal of Materials Chemistry B* **2013,** *1* (10), 1381-1396.
[84] J. Wallyn, N. Anton, T. F. Vandamme, Synthesis, Principles, and Properties of Magnetite Nanoparticles for In Vivo Imaging Applications—A Review. *Pharmaceutics* **2019,** *11* (11), 601.
[85] X. Huang, M. A. El-Sayed, Gold nanoparticles: Optical properties and implementations in cancer diagnosis and photothermal therapy. *Journal of Advanced Research* **2010,** *1* (1), 13-28.
[86] P. Slepička, N. Slepičková Kasálková, J. Siegel, Z. Kolská, V. Švorčík, Methods of Gold and Silver Nanoparticles Preparation. *Materials* **2020,** *13* (1), 1.
[87] L. Bai, Y. Ouyang, J. Song, Z. Xu, W. Liu, J. Hu, Y. Wang, F. Yuan, Synthesis of Metallic Nanocrystals: From Noble Metals to Base Metals. *Materials* **2019,** *12* (9), 1497.
[88] S. M. Shakil Hussain, M. S. Kamal, M. K. Hossain, Recent Developments in Nanostructured Palladium and Other Metal Catalysts for Organic Transformation. *Journal of Nanomaterials* **2019,** *2019*, 1562130.
[89] Y. Xu, L. Chen, X. Wang, W. Yao, Q. Zhang, Recent advances in noble metal based composite nanocatalysts: colloidal synthesis, properties, and catalytic applications. *Nanoscale* **2015,** *7* (24), 10559-10583.
[90] S. H. Lee, B.-H. Jun, Silver Nanoparticles: Synthesis and Application for Nanomedicine. *International Journal of Molecular Sciences* **2019,** *20* (4).
[91] K. J. Klabunde, J. Stark, O. Koper, C. Mohs, D. G. Park, S. Decker, Y. Jiang, I. Lagadic, D. Zhang, Nanocrystals as Stoichiometric Reagents with Unique Surface Chemistry. *The Journal of Physical Chemistry* **1996,** *100* (30), 12142-12153.

[92] A. Tamilvanan, K. Balamurugan, K. Ponappa, B. M. Kumar, Copper Nanoparticles: Synthetic Strategies, Properties and Multifunctional Application. *International Journal of Nanoscience* **2014,** *13* (02), 1430001.
[93] N. Tarannum, Divya, Y. K. Gautam, Facile green synthesis and applications of silver nanoparticles: a state-of-the-art review. *RSC Advances* **2019,** *9* (60), 34926-34948.
[94] Y.-C. Yeh, B. Creran, V. M. Rotello, Gold nanoparticles: preparation, properties, and applications in bionanotechnology. *Nanoscale* **2012,** *4* (6), 1871-1880.
[95] F. Tian, F. Bonnier, A. Casey, A. E. Shanahan, H. J. Byrne, Surface enhanced Raman scattering with gold nanoparticles: effect of particle shape. *Analytical Methods* **2014,** *6* (22), 9116-9123.
[96] T. Mitsudome, K. Kaneda, Gold nanoparticle catalysts for selective hydrogenations. *Green Chemistry* **2013,** *15* (10), 2636-2654.
[97] S. A. C. Carabineiro, Supported Gold Nanoparticles as Catalysts for the Oxidation of Alcohols and Alkanes. *Frontiers in Chemistry* **2019,** *7*, 702.
[98] S. Liu, G. Chen, P. N. Prasad, M. T. Swihart, Synthesis of Monodisperse Au, Ag, and Au–Ag Alloy Nanoparticles with Tunable Size and Surface Plasmon Resonance Frequency. *Chemistry of Materials* **2011,** *23* (18), 4098-4101.
[99] M. Larguinho, P. V. Baptista, Gold and silver nanoparticles for clinical diagnostics — From genomics to proteomics. *Journal of Proteomics* **2012,** *75* (10), 2811-2823.
[100] R. A. Hamouda, M. H. Hussein, R. A. Abo-elmagd, S. S. Bawazir, Synthesis and biological characterization of silver nanoparticles derived from the cyanobacterium Oscillatoria limnetica. *Scientific Reports* **2019,** *9* (1), 13071.
[101] S. Pal, R. Nisi, M. Stoppa, A. Licciulli, Silver-Functionalized Bacterial Cellulose as Antibacterial Membrane for Wound-Healing Applications. *ACS Omega* **2017,** *2* (7), 3632-3639.
[102] R. X. He, R. Liang, P. Peng, Y. Norman Zhou, Effect of the size of silver nanoparticles on SERS signal enhancement. *Journal of Nanoparticle Research* **2017,** *19* (8), 267.
[103] D. Pedone, M. Moglianetti, E. De Luca, G. Bardi, P. P. Pompa, Platinum nanoparticles in nanobiomedicine. *Chemical Society Reviews* **2017,** *46* (16), 4951-4975.
[104] E. Ramirez, L. Eradès, K. Philippot, P. Lecante, B. Chaudret, Shape Control of Platinum Nanoparticles. *Advanced Functional Materials* **2007,** *17* (13), 2219-2228.
[105] X. Chen, Z. Cai, Z. Huang, M. Oyama, Y. Jiang, X. Chen, Non-enzymatic oxalic acid sensor using platinum nanoparticles modified on graphene nanosheets. *Nanoscale* **2013,** *5* (13), 5779-5783.

[106] Z. Jin, D. Nackashi, W. Lu, C. Kittrell, J. M. Tour, Decoration, Migration, and Aggregation of Palladium Nanoparticles on Graphene Sheets. *Chemistry of Materials* **2010,** *22* (20), 5695-5699.
[107] T. T. Phan, T.-C. Huynh, P. Manivasagan, S. Mondal, J. Oh, An Up-To-Date Review on Biomedical Applications of Palladium Nanoparticles. *Nanomaterials* **2020,** *10* (1), 66.
[108] Y. Wang, A. Biby, Z. Xi, B. Liu, Q. Rao, X. Xia, One-Pot Synthesis of Single-Crystal Palladium Nanoparticles with Controllable Sizes for Applications in Catalysis and Biomedicine. *ACS Applied Nano Materials* **2019,** *2* (7), 4605-4612.
[109] J. Jiang, P. Zhang, Y. Liu, H. Luo, A novel non-enzymatic glucose sensor based on a Cu-nanoparticle-modified graphene edge nanoelectrode. *Analytical Methods* **2017,** *9* (14), 2205-2210.
[110] S. Chandra, A. Kumar, P. K. Tomar, Synthesis and characterization of copper nanoparticles by reducing agent. *Journal of Saudi Chemical Society* **2014,** *18* (2), 149-153.
[111] Y. Kamikoriyama, H. Imamura, A. Muramatsu, K. Kanie, Ambient Aqueous-Phase Synthesis of Copper Nanoparticles and Nanopastes with Low-Temperature Sintering and Ultra-High Bonding Abilities. *Scientific Reports* **2019,** *9* (1), 899.
[112] H. Amani, R. Habibey, F. Shokri, S. J. Hajmiresmail, O. Akhavan, A. Mashaghi, H. Pazoki-Toroudi, Selenium nanoparticles for targeted stroke therapy through modulation of inflammatory and metabolic signaling. *Scientific Reports* **2019,** *9* (1), 6044.
[113] A. Khurana, S. Tekula, M. A. Saifi, P. Venkatesh, C. Godugu, Therapeutic applications of selenium nanoparticles. *Biomedicine & Pharmacotherapy* **2019,** *111*, 802-812.
[114] L. D. Geoffrion, T. Hesabizadeh, D. Medina-Cruz, M. Kusper, P. Taylor, A. Vernet-Crua, J. Chen, A. Ajo, T. J. Webster, G. Guisbiers, Naked Selenium Nanoparticles for Antibacterial and Anticancer Treatments. *ACS Omega* **2020,** *5* (6), 2660-2669.
[115] A. Pal, S. Shah, S. Devi, Synthesis of Au, Ag and Au–Ag alloy nanoparticles in aqueous polymer solution. *Colloids and Surfaces A: Physicochemical and Engineering Aspects* **2007,** *302* (1), 51-57.
[116] A. V. Nikam, B. L. V. Prasad, A. A. Kulkarni, Wet chemical synthesis of metal oxide nanoparticles: a review. *CrystEngComm* **2018,** *20* (35), 5091-5107.
[117] Y.-J. Zhu, F. Chen, Microwave-Assisted Preparation of Inorganic Nanostructures in Liquid Phase. *Chemical Reviews* **2014,** *114* (12), 6462-6555.
[118] M. S. Chavali, M. P. Nikolova, Metal oxide nanoparticles and their applications in nanotechnology. *SN Applied Sciences* **2019,** *1* (6), 607.

[119] G. Shen, P.-C. Chen, K. Ryu, C. Zhou, Devices and chemical sensing applications of metal oxide nanowires. *Journal of Materials Chemistry* **2009,** *19* (7), 828-839.
[120] D. Ziental, B. Czarczynska-Goslinska, D. T. Mlynarczyk, A. Glowacka-Sobotta, B. Stanisz, T. Goslinski, L. Sobotta, Titanium Dioxide Nanoparticles: Prospects and Applications in Medicine. *Nanomaterials* **2020,** *10* (2), 387.
[121] A. J. Haider, Z. N. Jameel, I. H. M. Al-Hussaini, Review on: Titanium Dioxide Applications. *Energy Procedia* **2019,** *157*, 17-29.
[122] J. Jiang, J. Pi, J. Cai, The Advancing of Zinc Oxide Nanoparticles for Biomedical Applications. *Bioinorganic Chemistry and Applications* **2018,** *2018*, 1062562.
[123] P. Ruenraroengsak, D. Kiryushko, I. G. Theodorou, M. M. Klosowski, E. R. Taylor, T. Niriella, C. Palmieri, E. Yagüe, M. P. Ryan, R. C. Coombes, F. Xie, A. E. Porter, Frizzled-7-targeted delivery of zinc oxide nanoparticles to drug-resistant breast cancer cells. *Nanoscale* **2019,** *11* (27), 12858-12870.
[124] J. Wang, J. S. Lee, D. Kim, L. Zhu, Exploration of Zinc Oxide Nanoparticles as a Multitarget and Multifunctional Anticancer Nanomedicine. *ACS Applied Materials & Interfaces* **2017,** *9* (46), 39971-39984.
[125] T. G. Smijs, S. Pavel, Titanium dioxide and zinc oxide nanoparticles in sunscreens: focus on their safety and effectiveness. *Nanotechnol Sci Appl* **2011,** *4*, 95-112.
[126] X. Wang, H.-F. Wu, Q. Kuang, R.-B. Huang, Z.-X. Xie, L.-S. Zheng, Shape-Dependent Antibacterial Activities of Ag_2O Polyhedral Particles. *Langmuir* **2010,** *26* (4), 2774-2778.
[127] S. Iqbal, M. Fakhar-e-Alam, F. Akbar, M. Shafiq, M. Atif, N. Amin, M. Ismail, A. Hanif, W. A. Farooq, Application of silver oxide nanoparticles for the treatment of cancer. *Journal of Molecular Structure* **2019,** *1189*, 203-209.
[128] M. E. Grigore, E. R. Biscu, A. M. Holban, M. C. Gestal, A. M. Grumezescu, Methods of Synthesis, Properties and Biomedical Applications of CuO Nanoparticles. *Pharmaceuticals* **2016,** *9* (4), 75.
[129] N. Verma, N. Kumar, Synthesis and Biomedical Applications of Copper Oxide Nanoparticles: An Expanding Horizon. *ACS Biomaterials Science & Engineering* **2019,** *5* (3), 1170-1188.
[130] S. Ortelli, A. L. Costa, M. Blosi, A. Brunelli, E. Badetti, A. Bonetto, D. Hristozov, A. Marcomini, Colloidal characterization of CuO nanoparticles in biological and environmental media. *Environmental Science: Nano* **2017,** *4* (6), 1264-1272.
[131] S. Laurent, D. Forge, M. Port, A. Roch, C. Robic, L. Vander Elst, R. N. Muller, Magnetic Iron Oxide Nanoparticles: Synthesis, Stabilization, Vectorization, Physicochemical Characterizations, and Biological Applications. *Chemical Reviews* **2008,** *108* (6), 2064-2110.
[132] V. Patsula, L. Kosinová, M. Lovrić, L. Ferhatovic Hamzić, M. Rabyk, R. Konefal, A. Paruzel, M. Šlouf, V. Herynek, S. Gajović, D. Horák,

Superparamagnetic Fe_3O_4 Nanoparticles: Synthesis by Thermal Decomposition of Iron(III) Glucuronate and Application in Magnetic Resonance Imaging. *ACS Applied Materials & Interfaces* **2016,** *8* (11), 7238-7247.
[133] H. Mu, Y. Chen, N. Xiao, Effects of metal oxide nanoparticles (TiO_2, Al_2O_3, SiO_2 and ZnO) on waste activated sludge anaerobic digestion. *Bioresource Technology* **2011,** *102* (22), 10305-10311.
[134] Z. Li, J. C. Barnes, A. Bosoy, J. F. Stoddart, J. I. Zink, Mesoporous silica nanoparticles in biomedical applications. *Chemical Society Reviews* **2012,** *41* (7), 2590-2605.
[135] Y. Liu, J. Zhou, X. Yuan, T. Jiang, L. Petti, L. Zhou, P. Mormile, Hydrothermal synthesis of gold polyhedral nanocrystals by varying surfactant concentration and their LSPR and SERS properties. *RSC Advances* **2015,** *5* (84), 68668-68675.
[136] A. J. Frank, N. Cathcart, K. E. Maly, V. Kitaev, Synthesis of Silver Nanoprisms with Variable Size and Investigation of Their Optical Properties: A First-Year Undergraduate Experiment Exploring Plasmonic Nanoparticles. *Journal of Chemical Education* **2010,** *87* (10), 1098-1101.
[137] J. L. Cuya Huaman, K. Sato, S. Kurita, T. Matsumoto, B. Jeyadevan, Copper nanoparticles synthesized by hydroxyl ion assisted alcohol reduction for conducting ink. *Journal of Materials Chemistry* **2011,** *21* (20), 7062-7069.
[138] M. Rehan, X. Lai, G. M. Kale, Hydrothermal synthesis of titanium dioxide nanoparticles studied employing in situ energy dispersive X-ray diffraction. *CrystEngComm* **2011,** *13* (11), 3725-3732.
[139] J. A. Alvarado, A. Maldonado, H. Juarez, M. Pacio, Synthesis of Colloidal ZnO Nanoparticles and Deposit of Thin Films by Spin Coating Technique. *Journal of Nanomaterials* **2013,** *2013*, 903191.
[140] G. Gao, X. Liu, R. Shi, K. Zhou, Y. Shi, R. Ma, E. Takayama-Muromachi, G. Qiu, Shape-Controlled Synthesis and Magnetic Properties of Monodisperse Fe_3O_4 Nanocubes. *Crystal Growth & Design* **2010,** *10* (7), 2888-2894.
[141] S. Liu, X. Su, The synthesis and application of I–III–VI type quantum dots. *RSC Advances* **2014,** *4* (82), 43415-43428.
[142] D. Bera, L. Qian, T.-K. Tseng, P. H. Holloway, Quantum Dots and Their Multimodal Applications: A Review. *Materials* **2010,** *3* (4), 2260–2345.
[143] M. L. Landry, T. E. Morrell, T. K. Karagounis, C.-H. Hsia, C.-Y. Wang, Simple Syntheses of CdSe Quantum Dots. *Journal of Chemical Education* **2014,** *91* (2), 274-279.
[144] H. Lu, G. M. Carroll, N. R. Neale, M. C. Beard, Infrared Quantum Dots: Progress, Challenges, and Opportunities. *ACS Nano* **2019,** *13* (2), 939-953.
[145] L. Tong, F. Qiu, T. Zeng, J. Long, J. Yang, R. Wang, J. Zhang, C. Wang, T. Sun, Y. Yang, Recent progress in the preparation and application of quantum dots/graphene composite materials. *RSC Advances* **2017,** *7* (76), 47999-48018.

[146] H. Wen, F. Wang, 4 - Lanthanide-Doped Nanoparticles: Synthesis, Property, and Application. In *Nanocrystalline Materials (Second Edition)*, S.-C. Tjong, Ed. Elsevier: Oxford, 2014; pp 121-160.
[147] G. Blasse, B.C. Grabmaier, *Luminescent Materials*, Springer-Verlag, Berlin, 1994.
[148] M. Tan, B. del Rosal, Y. Zhang, E. Martín Rodríguez, J. Hu, Z. Zhou, R. Fan, D. H. Ortgies, N. Fernández, I. Chaves-Coira, Á. Núñez, D. Jaque, G. Chen, Rare-earth-doped fluoride nanoparticles with engineered long luminescence lifetime for time-gated in vivo optical imaging in the second biological window. *Nanoscale* **2018,** *10* (37), 17771-17780.
[149] C. Bouzigues, T. Gacoin, A. Alexandrou, Biological Applications of Rare-Earth Based Nanoparticles. *ACS Nano* **2011,** *5* (11), 8488-8505.
[150] J. Shen, L.-D. Sun, C.-H. Yan, Luminescent rare earth nanomaterials for bioprobe applications. *Dalton Transactions* **2008,** (42), 5687-5697.
[151] W. Xu, B. A. Bony, C. R. Kim, J. S. Baeck, Y. Chang, J. E. Bae, K. S. Chae, T. J. Kim, G. H. Lee, Mixed lanthanide oxide nanoparticles as dual imaging agent in biomedicine. *Scientific Reports* **2013,** *3* (1), 3210.
[152] T. Tegafaw, W. Xu, M. W. Ahmad, J. S. Baeck, Y. Chang, J. E. Bae, K. S. Chae, T. J. Kim, G. H. Lee, Dual-mode T1 and T2 magnetic resonance imaging contrast agent based on ultrasmall mixed gadolinium-dysprosium oxide nanoparticles: synthesis, characterization, and in vivo application. *Nanotechnology* **2015,** *26* (36), 365102.
[153] T. Tsuzuki, Lanthanides: Oxide and Sulfide Nanomaterials. *Encyclopedia of Inorganic and Bioinorganic Chemistry* **2012**.
[154] L. Li, N. Zhang, R. Wu, L. Song, G. Zhang, H. He, Comparative Study of Moisture-Treated Pd@CeO_2/Al_2O_3 and Pd/CeO_2/Al_2O_3 Catalysts for Automobile Exhaust Emission Reactions: Effect of Core–Shell Interface. *ACS Applied Materials & Interfaces* **2020,** *12* (9), 10350-10358.
[155] K. Kattel, J. Y. Park, W. Xu, H. G. Kim, E. J. Lee, B. A. Bony, W. C. Heo, J. J. Lee, S. Jin, J. S. Baeck, Y. Chang, T. J. Kim, J. E. Bae, K. S. Chae, G. H. Lee, A Facile Synthesis, In vitro and In vivo MR Studies of d-Glucuronic Acid-Coated Ultrasmall Ln_2O_3 (Ln = Eu, Gd, Dy, Ho, and Er) Nanoparticles as a New Potential MRI Contrast Agent. *ACS Applied Materials & Interfaces* **2011,** *3* (9), 3325-3334.
[156] L. Zong, Z. Wang, R. Yu, Lanthanide-Doped Photoluminescence Hollow Structures: Recent Advances and Applications. *Small* **2019,** *15* (29), 1804510.
[157] R. Naccache, Q. Yu, J. A. Capobianco, The Fluoride Host: Nucleation, Growth, and Upconversion of Lanthanide-Doped Nanoparticles. *Advanced Optical Materials* **2015,** *3* (4), 482-509.
[158] B. Chen, F. Wang, Recent advances in the synthesis and application of Yb-based fluoride upconversion nanoparticles. *Inorganic Chemistry Frontiers* **2020,** *7* (5), 1067-1081.

[159] J. Huang, X. Wang, A. Shao, G. Du, N. Chen, Growth of β-$NaYF_4$:Eu^{3+} Crystals by the Solvothermal Method with the Aid of Oleic Acid and Their Photoluminescence Properties. *Materials* **2019,** *12* (22).
[160] C. Gao, Y. Jin, G. Jia, X. Suo, H. Liu, D. Liu, X. Yang, K. Ge, X.-J. Liang, S. Wang, J. Zhang, Y_2O_3 Nanoparticles Caused Bone Tissue Damage by Breaking the Intracellular Phosphate Balance in Bone Marrow Stromal Cells. *ACS Nano* **2019,** *13* (1), 313-323.
[161] S. Gai, P. Yang, D. Wang, C. Li, N. Niu, F. He, X. Li, Monodisperse Gd_2O_3:Ln (Ln = Eu^{3+}, Tb^{3+}, Dy^{3+}, Sm^{3+}, Yb^{3+}/Er^{3+}, Yb^{3+}/Tm^{3+}, and Yb^{3+}/Ho^{3+}) nanocrystals with tunable size and multicolor luminescent properties. *CrystEngComm* **2011,** *13* (17), 5480-5487.
[162] A. Xie, S. Wang, W. Liu, J. Zhang, Y. Yang, J. Han, Rapid hydrothermal synthesis of CeO_2 nanoparticles with (220)-dominated surface and its CO catalytic performance. *Materials Research Bulletin* **2015,** *62*, 148-152.
[163] L. Dong, P. Zhang, P. Lei, S. Song, X. Xu, K. Du, J. Feng, H. Zhang, PEGylated GdF_3:Fe Nanoparticles as Multimodal T1/T2-Weighted MRI and X-ray CT Imaging Contrast Agents. *ACS Applied Materials & Interfaces* **2017,** *9* (24), 20426-20434.
[164] L. Zi, D. Zhang, G. De, Self-assembly NaGdF4nanoparticles: phase controlled synthesis, morphology evolution, and upconversion luminescence properties. *Materials Research Express* **2016,** *3* (2), 025009.
[165] H. Li, L. Xu, G. Chen, Controlled Synthesis of Monodisperse Hexagonal $NaYF_4$:Yb/Er Nanocrystals with Ultrasmall Size and Enhanced Upconversion Luminescence. *Molecules* **2017,** *22* (12), 2113.
[166] J.-L. Lemyre, A. M. Ritcey, Synthesis of Lanthanide Fluoride Nanoparticles of Varying Shape and Size. *Chemistry of Materials* **2005,** *17* (11), 3040-3043.
[167] P. Rahman, M. Green, The synthesis of rare earthfluoride based nanoparticles. *Nanoscale* **2009,** *1* (2), 214-224.
[168] R. Rafique, S. H. Baek, C. Y. Park, S.-J. Chang, A. R. Gul, S. Ha, T. P. Nguyen, H. Oh, S. Ham, M. Arshad, H. Lee, T. J. Park, Morphological evolution of upconversion nanoparticles and their biomedical signal generation. *Scientific Reports* **2018,** *8* (1), 17101.
[169] J. Y. Park, *Current Trends of Surface Science and Catalysis*. Springer, New York, 2014; p 1-262.
[170] C. Cao, H. K. Yang, B. K. Moon, B. C. Choi, J. H. Jeong, Host Sensitized White Luminescence of Dy^{3+} Activated $GdPO_4$ Phosphors. *Journal of The Electrochemical Society* **2011,** *158* (2), J6-J9.
[171] M. R. Rafiuddin, A. P. Grosvenor, A Structural Investigation of Hydrous and Anhydrous Rare-Earth Phosphates. *Inorganic Chemistry* **2016,** *55* (19), 9685-9695.
[172] W. Ren, G. Tian, L. Zhou, W. Yin, L. Yan, S. Jin, Y. Zu, S. Li, Z. Gu, Y. Zhao, Lanthanide ion-doped $GdPO_4$ nanorods with dual-modal bio-optical

and magnetic resonance imaging properties. *Nanoscale* **2012,** *4* (12), 3754-3760.
[173] A. I. Becerro, S. Rodríguez-Liviano, A. J. Fernández-Carrión, M. Ocaña, A Novel 3D Architecture of $GdPO_4$ Nanophosphors: Multicolored and White Light Emission. *Crystal Growth & Design* **2013,** *13* (2), 526-535.
[174] K. Rajesh, P. Shajesh, O. Seidel, P. Mukundan, K. G. K. Warrier, A Facile Sol–Gel Strategy for the Synthesis of Rod-Shaped Nanocrystalline High-Surface-Area Lanthanum Phosphate Powders and Nanocoatings. *Advanced Functional Materials* **2007,** *17* (10), 1682-1690.
[175] M. A. Ahmadzadeh, S. F. Chini, A. Sadeghi, Size and shape tailored sol-gel synthesis and characterization of lanthanum phosphate ($LaPO_4$) nanoparticles. *Materials & Design* **2019,** *181*, 108058.
[176] C. Yu, M. Yu, C. Li, X. Liu, J. Yang, P. Yang, J. Lin, Facile sonochemical synthesis and photoluminescent properties of lanthanide orthophosphate nanoparticles. *Journal of Solid State Chemistry* **2009,** *182* (2), 339-347.
[177] L. Zhu, X. Liu, X. Liu, Q. Li, J. Li, S. Zhang, J. Meng, X. Cao, Facile sonochemical synthesis of $CePO_4$:Tb/LaPO4core/shell nanorods with highly improved photoluminescent properties. *Nanotechnology* **2006,** *17* (16), 4217-4222.
[178] H. Dong, Y. Shuang, Q. Sun, Q. Ren, W. Ma, Preparation of $LaPO_4$ Nanoparticles by Coprecipitation Method, *Advanced Functional Materials CMC2017 Book*, Ed. Springer Singapore: Singapore, 2018; pp 643-649.
[179] M. Yang, H. You, K. Liu, Y. Zheng, N. Guo, H. Zhang, Low-Temperature Coprecipitation Synthesis and Luminescent Properties of $LaPO_4:Ln^{3+}$ (Ln^{3+} = Ce^{3+}, Tb^{3+}) Nanowires and $LaPO_4:Ce^{3+},Tb^{3+}/LaPO_4$ Core/Shell Nanowires. *Inorganic Chemistry* **2010,** *49* (11), 4996-5002.
[180] Z. Zhu, K. Zhang, H. Zhao, J. Zhu, UV-light driven photocatalytic performance of hydrothermally-synthesized hexagonal $CePO_4$ nanorods. *Solid State Sciences* **2017,** *72*, 28-32.
[181] X.-y. Kuang, H. Liu, W.-y. Hu, Y.-z. Shao, Hydrothermal synthesis of core–shell structured $TbPO_4:Ce^{3+}@TbPO_4:Gd^{3+}$ nanocomposites for magnetic resonance and optical imaging. *Dalton Transactions* **2014,** *43* (32), 12321-12328.
[182] Y. Cao, P. Sun, Y. Liang, R. Wang, X. Zhang, Sol-precipitation-hydrothermal synthesis and luminescence of $GdPO_4:Tb^{3+}$ submicron cubes. *Chemical Physics Letters* **2016,** *651*, 80-83.
[183] M. T. Colomer, A. L. Ortiz, Effect of Tb^{3+} doping and self-generated pressure on the crystallographic/morphological features and thermal stability of $LaPO_4 \cdot nH_2O$ single-crystal nanorods obtained by microwave-assisted hydrothermal synthesis. *Ceramics International* **2016,** *42* (16), 18074-18086.
[184] E. V. Samsonova, A. V. Popov, A. S. Vanetsev, K. Keevend, E. O. Orlovskaya, V. Kiisk, S. Lange, U. Joost, K. Kaldvee, U. Mäeorg, N. A. Glushkov, A. V. Ryabova, I. Sildos, V. V. Osiko, R. Steiner, V. B. Loschenov,

Y. V. Orlovskii, An energy transfer kinetic probe for OH-quenchers in the Nd^{3+}:YPO_4 nanocrystals suitable for imaging in the biological tissue transparency window. *Physical Chemistry Chemical Physics* **2014,** *16* (48), 26806-26815.
[185] Z. Huo, C. Chen, D. Chu, H. Li, Y. Li, Systematic Synthesis of Lanthanide Phosphate Nanocrystals. *Chemistry – A European Journal* **2007,** *13* (27), 7708-7714.
[186] Y. Zhan, X. Wan, Y. He, Z. Long, H. Hu, X. Liu, Improving the properties of poly(arylene ether nitrile) composites reinforced by covalently modified multi-walled carbon nanotubes. *High Performance Polymers* **2016,** *29* (9), 1058-1068.
[187] F. Shi, J. Wang, D. Zhang, G. Qin, W. Qin, Greatly enhanced size-tunable ultraviolet upconversion luminescence of monodisperse β-$NaYF_4$:Yb,Tm nanocrystals. *Journal of Materials Chemistry* **2011,** *21* (35), 13413-13421.
[188] D. Meroni, S. Ardizzone, Preparation and Application of Hybrid Nanomaterials. *Nanomaterials (Basel)* **2018,** *8* (11), 891.
[189] A. Mehdi, Organic–Inorganic Hybrid Nanomaterials: Organization, Functionalization, and Potential Applications in Environmental Domain. *Hybrid Nanomaterials* **2011**, 299-329.
[190] Q. Zhang, P. Wang, X. Li, Y. Yang, X. Liu, F. Zhang, Y. Ling, Y. Zhou, Preparation of highly dispersed γ-Fe_2O_3 and $GdPO_4$ co-functionalized mesoporous carbon spheres for dual-mode MR imaging and anti-cancer drug carrying. *Journal of Materials Chemistry B* **2017,** *5* (20), 3765-3770.
[191] D. Li, W.-Y. Lai, Q. Shao, W. Huang, Multifunctional $NaYF_4$:Yb^{3+},Er^{3+}@SiO_2@Au heterogeneous nanocomposites for upconversion luminescence, temperature sensing and photothermal conversion. *RSC Advances* **2017,** *7* (19), 11491-11495.
[192] Z. Yi, W. Lu, C. Qian, T. Zeng, L. Yin, H. Wang, L. Rao, H. Liu, S. Zeng, Urchin-like Ce/Tb co-doped $GdPO_4$ hollow spheres for in vivo luminescence/X-ray bioimaging and drug delivery. *Biomaterials Science* **2014,** *2* (10), 1404-1411.
[193] F. Liebner, N. Aigner, C. Schimper, A. Potthast, T. Rosenau, Bacterial Cellulose Aerogels: From Lightweight Dietary Food to Functional Materials. In *Functional Materials from Renewable Sources*, American Chemical Society: 2012; Vol. 1107, pp 57-74.
[194] I. Smirnova, P. Gurikov, Aerogels in Chemical Engineering: Strategies Toward Tailor-Made Aerogels. *Annual Review of Chemical and Biomolecular Engineering* **2017,** *8* (1), 307-334.
[195] H. D. Gesser, P. C. Goswami, Aerogels and related porous materials. *Chemical Reviews* **1989,** *89* (4), 765-788.
[196] K. J. De France, T. Hoare, E. D. Cranston, Review of Hydrogels and Aerogels Containing Nanocellulose. *Chemistry of Materials* **2017,** *29* (11), 4609-4631.

[197] E. Barrios, D. Fox, Y. Y. Li Sip, R. Catarata, J. E. Calderon, N. Azim, S. Afrin, Z. Zhang, L. Zhai, Nanomaterials in Advanced, High-Performance Aerogel Composites: A Review. *Polymers* **2019,** *11* (4), 726.
[198] İ. Şahin, Y. Özbakır, Z. İnönü, Z. Ulker, C. Erkey, Kinetics of Supercritical Drying of Gels. *Gels* **2018,** *4* (1), 3.
[199] Š. Jan, P. Eva, P. Monika, B. Jaroslav, K. Mariana, K. Jaroslav, B. Petr, S. Helena, Titania aerogels with tailored nano and microstructure: comparison of lyophilization and supercritical drying. *Pure and Applied Chemistry* **2017,** *89* (4), 501-509.
[200] A. Venkateswara Rao, G. M. Pajonk, D. Haranath, Synthesis of hydrophobic aerogels for transparent window insulation applications. *Materials Science and Technology* **2001,** *17* (3), 343-348.
[201] A. C. Pierre, G. M. Pajonk, Chemistry of Aerogels and Their Applications. *Chemical Reviews* **2002,** *102* (11), 4243-4266.
[202] V. C.-F. Li, C. K. Dunn, Z. Zhang, Y. Deng, H. J. Qi, Direct Ink Write (DIW) 3D Printed Cellulose Nanocrystal Aerogel Structures. *Scientific Reports* **2017,** *7* (1), 8018.
[203] H. Maleki, M.-A. Shahbazi, S. Montes, S. H. Hosseini, M. R. Eskandari, S. Zaunschirm, T. Verwanger, S. Mathur, B. Milow, B. Krammer, N. Hüsing, Mechanically Strong Silica-Silk Fibroin Bioaerogel: A Hybrid Scaffold with Ordered Honeycomb Micromorphology and Multiscale Porosity for Bone Regeneration. *ACS Applied Materials & Interfaces* **2019,** *11* (19), 17256-17269.
[204] M. Power, B. Hosticka, E. Black, C. Daitch, P. Norris, Aerogels as biosensors: viral particle detection by bacteria immobilized on large pore aerogel. *Journal of Non-Crystalline Solids* **2001,** *285* (1), 303-308.
[205] B. Gao, I. W. Wang, L. Ren, J. Hu, Catalytic Methane Decomposition over Bimetallic Transition Metals Supported on Composite Aerogel. *Energy & Fuels* **2019,** *33* (9), 9099-9106.
[206] K. Li, Q. Luo, J. Xu, K. Li, W. Zhang, L. Liu, J. Ma, H. Zhang, A Novel Freeze-Drying-Free Strategy to Fabricate a Biobased Tough Aerogel for Separation of Oil/Water Mixtures. *Journal of Agricultural and Food Chemistry* **2020,** *68* (12), 3779-3785.
[207] J. P. Randall, M. A. B. Meador, S. C. Jana, Tailoring Mechanical Properties of Aerogels for Aerospace Applications. *ACS Applied Materials & Interfaces* **2011,** *3* (3), 613-626.
[208] T. Feng, X. Ye, Y. Zhao, Z. Zhao, S. Hou, N. Liang, L. Zhao, Magnetic silica aerogels with high efficiency for selective adsorption of pyrethroid insecticides in juices and tea beverages. *New Journal of Chemistry* **2019,** *43* (13), 5159-5166.
[209] Y. Li, Q. Liu, A. J. Hess, S. Mi, X. Liu, Z. Chen, Y. Xie, I. I. Smalyukh, Programmable Ultralight Magnets via Orientational Arrangement of Ferromagnetic Nanoparticles within Aerogel Hosts. *ACS Nano* **2019,** *13* (12), 13875-13883.

[210] D. Faivre, Dry but flexible magnetic materials. *Nature Nanotechnology* **2010,** *5* (8), 562-563.
[211] R. T. Olsson, M. A. S. Azizi Samir, G. Salazar-Alvarez, L. Belova, V. Ström, L. A. Berglund, O. Ikkala, J. Nogués, U. W. Gedde, Making flexible magnetic aerogels and stiff magnetic nanopaper using cellulose nanofibrils as templates. *Nature Nanotechnology* **2010,** *5* (8), 584-588.
[212] K. E. Yorov, T. O. Shekunova, A. E. Baranchikov, G. P. Kopitsa, L. Almásy, L. S. Skogareva, V. V. Kozik, A. N. Malkova, S. A. Lermontov, V. K. Ivanov, First rare-earth phosphate aerogel: sol–gel synthesis of monolithic ceric hydrogen phosphate aerogel. *Journal of Sol-Gel Science and Technology* **2018,** *85* (3), 574-584.
[213] Y.-P. Fang, A.-W. Xu, R.-Q. Song, H.-X. Zhang, L.-P. You, J. C. Yu, H.-Q. Liu, Systematic Synthesis and Characterization of Single-Crystal Lanthanide Orthophosphate Nanowires. *Journal of the American Chemical Society* **2003,** *125* (51), 16025-16034.
[214] Y. Ni, J. M. Hughes, A. N. Mariano, Crystal chemistry of the monazite and xenotime structures. *American Mineralogist* **1995,** *80* (1-2), 21-26.
[215] L. Mezentseva, Synthesis and Thermal Behavior of Nanopowders in LaPO4-YPO4(-H2O), $LaPO_4$-$LuPO_4$(-H_2O) and YPO_4-$ScPO_4$(-H_2O) Systems for Ceramic Matrices. *Journal of Nanomedicine Research* **2017,** *6* (1), 1-6.
[216] T. Subramani, M. R. Rafiuddin, A. Shelyug, S. Ushakov, A. Mesbah, N. Clavier, D. Qin, S. Szenknect, E. Elkaim, N. Dacheux, A. Navrotsky, Synthesis, Crystal Structure, and Enthalpies of Formation of Churchite-type $REPO_4 \cdot 2H_2O$ (RE = Gd to Lu) Materials. *Crystal Growth & Design* **2019,** *19* (8), 4641-4649.
[217] Y.-P. Fang, A.-W. Xu, A.-M. Qin, R.-J. Yu, Selective Synthesis of Hexagonal and Tetragonal Dysprosium Orthophosphate Nanorods by a Hydrothermal Method. *Crystal Growth & Design* **2005,** *5* (3), 1221-1225.
[218] A. Shelyug, A. Mesbah, S. Szenknect, N. Clavier, N. Dacheux, A. Navrotsky, Thermodynamics and Stability of Rhabdophanes, Hydrated Rare Earth Phosphates $REPO_4 \cdot nH_2O$. *Frontiers in Chemistry* **2018,** *6*, 604.
[219] H. Assaaoudi, A. Ennaciri, A. Rulmont, Vibrational spectra of hydrated rare earth orthophosphates. *Vibrational Spectroscopy* **2001,** *25* (1), 81-90.
[220] K. M. Heffernan, N. L. Ross, E. C. Spencer, L. A. Boatner, The structural response of gadolinium phosphate to pressure. *Journal of Solid State Chemistry* **2016,** *241*, 180-186.
[221] M. R. Rafiuddin, E. Mueller, A. P. Grosvenor, X-ray Spectroscopic Study of the Electronic Structure of Monazite- and Xenotime-Type Rare-Earth Phosphates. *The Journal of Physical Chemistry C* **2014,** *118* (31), 18000-18009.
[222] A. Mesbah, N. Clavier, E. Elkaim, S. Szenknect, N. Dacheux, In pursuit of the rhabdophane crystal structure: from the hydrated monoclinic $LnPO_4 \cdot 0.667H_2O$ to the hexagonal $LnPO_4$ (Ln = Nd, Sm, Gd, Eu and Dy). *Journal of Solid State Chemistry* **2017,** *249*, 221-227.

[223] R. Yan, X. Sun, X. Wang, Q. Peng, Y. Li, Crystal Structures, Anisotropic Growth, and Optical Properties: Controlled Synthesis of Lanthanide Orthophosphate One-Dimensional Nanomaterials. *Chemistry – A European Journal* **2005,** *11* (7), 2183-2195.
[224] Z. Wang, J.-G. Li, Q. Zhu, Z. Ai, X. Li, X. Sun, B.-N. Kim, Y. Sakka, EDTA-assisted phase conversion synthesis of $Gd_{0.95}RE_{0.05}PO_4$ nanowires (RE = Eu, Tb) and investigation of photoluminescence. *Science and Technology of Advanced Materials* **2017,** *18* (1), 447-457.
[225] L. Mezentseva, A. Osipov, V. Ugolkov, I. Kruchinina, V. Popova, A. Yakovlev, T. Maslennikova, Solid solutions and thermal transformations in nanosized $LaPO_4$-YPO_4-H_2O and $LaPO_4$-$LuPO_4$-H_2O systems. *Journal of Ceramic Science and Technology* **2014,** *5*, 237-244.
[226] T. Anfimova, Q. Li, J. O. Jensen, N. Bjerrum, Thermal Stability and Proton Conductivity of Rare Earth Orthophosphate Hydrates. *International Journal of Electrochemical Science* **2014,** *9*, 2285-2300.
[227] Y. Hikichi, K.-i. Hukuo, J. Shiokawa, Syntheses of Rare Earth Orthophosphates. *Bulletin of the Chemical Society of Japan* **1978,** *51* (12), 3645-3646.
[228] E. Bandiello, D. Errandonea, S. Ferrari, J. Pellicer-Porres, D. Martínez-García, S. N. Achary, A. K. Tyagi, C. Popescu, Pressure-Induced Hexagonal to Monoclinic Phase Transition of Partially Hydrated $CePO_4$. *Inorganic Chemistry* **2019,** *58* (7), 4480-4490.
[229] R. Kijkowska, E. Cholewka, B. Duszak, X-ray diffraction and Ir-absorption characteristics of lanthanide orthophosphates obtained by crystallisation from phosphoric acid solution. *Journal of Materials Science* **2003,** *38* (2), 223-228.
[230] A. Garrido Hernández, A. García Murillo, F. d. J. Carrillo Romo, D. Boyer, A. Potdevin, G. Chadeyron, J. R. Miranda, Photoluminescence behavior of YPO_4:Tb^{3+} crystallized in monoclinic, hexagonal or tetragonal phase obtained by hydrothermal process. *Materials Research Bulletin* **2016,** *84*, 225-231.
[231] A. I. Becerro, M. Ocaña, Quick synthesis, functionalization and properties of uniform, luminescent $LuPO_4$-based nanoparticles. *RSC Advances* **2015,** *5* (44), 34517-34524.
[232] H. Lai, Y. Du, M. Zhao, K. Sun, L. Yang, Controlled synthesis and luminescent properties of $DyPO_4$:Eu nanostructures. *RSC Advances* **2014,** *4* (92), 50731-50738.
[233] M. Ding, D. Chen, S. Yin, Z. Ji, J. Zhong, Y. Ni, C. Lu, Z. Xu, Simultaneous morphology manipulation and upconversion luminescence enhancement of β-$NaYF_4$:Yb^{3+}/Er^{3+} microcrystals by simply tuning the KF dosage. *Scientific Reports* **2015,** *5* (1), 12745.
[234] E. E. Boakye, P. Mogilevsky, R. S. Hay, G. E. Fair, Synthesis and Phase Composition of Lanthanide Phosphate Nanoparticles $LnPO_4$ (Ln=La, Gd, Tb,

Dy, Y) and Solid Solutions for Fiber Coatings. *Journal of the American Ceramic Society* **2008,** *91* (12), 3841-3849.
[235] W. Di, M.-G. Willinger, R. A. S. Ferreira, X. Ren, S. Lu, N. Pinna, Citric Acid-Assisted Hydrothermal Synthesis of Luminescent $TbPO_4$:Eu Nanocrystals: Controlled Morphology and Tunable Emission. *The Journal of Physical Chemistry C* **2008,** *112* (48), 18815-18820.
[236] C. G. Granqvist, R. A. Buhrman, J. Wyns, A. J. Sievers, Far-Infrared Absorption in Ultrafine Al Particles. *Physical Review Letters* **1976,** *37* (10), 625-629.
[237] J. Siegel, O. Kvitek, Z. Kolska, P. Slepicka, V. Svorcik, Gold Nanostructures Prepared on Solid Surface. In *Metallurgy - Advances in Materials and Processes*, 2012; pp 40 - 70.
[238] P. Tc, L. Mathew, N. Chandrasekaran, A. Raichur, A. Mukherjee, Biomimetic Synthesis of Nanoparticles: Science, Technology & Applicability, Biomimetics, Learning. 2010; pp 1 - 20.
[239] W. Shi, S. Song, H. Zhang, Hydrothermal synthetic strategies of inorganic semiconducting nanostructures. *Chemical Society Reviews* **2013,** *42* (13), 5714-5743.
[240] S. Bayda, M. Adeel, T. Tuccinardi, M. Cordani, F. Rizzolio, The History of Nanoscience and Nanotechnology: From Chemical–Physical Applications to Nanomedicine. *Molecules* **2020,** *25* (1), 112.
[241] S. Anu Mary Ealia, M. P. Saravanakumar, A review on the classification, characterisation, synthesis of nanoparticles and their application. *IOP Conference Series: Materials Science and Engineering* **2017,** *263*, 032019.
[242] A. Majid, M. Bibi, Wet Chemical Synthesis Methods. In *Cadmium based II-VI Semiconducting Nanomaterials: Synthesis Routes and Strategies*, A. Majid, M. Bibi, Eds. Springer International Publishing: Cham, 2018; pp 43-101.
[243] Z. Wu, S. Yang, W. Wu, Shape control of inorganic nanoparticles from solution. *Nanoscale* **2016,** *8* (3), 1237-1259.
[244] C. Dhand, N. Dwivedi, X. J. Loh, A. N. Jie Ying, N. K. Verma, R. W. Beuerman, R. Lakshminarayanan, S. Ramakrishna, Methods and strategies for the synthesis of diverse nanoparticles and their applications: a comprehensive overview. *RSC Advances* **2015,** *5* (127), 105003-105037.
[245] Y. Chen, Z. Lai, X. Zhang, Z. Fan, Q. He, C. Tan, H. Zhang, Phase engineering of nanomaterials. *Nature Reviews Chemistry* **2020,** *4* (5), 243-256.
[246] C. Chen, L. Xie, Y. Wang, Recent advances in the synthesis and applications of anisotropic carbon and silica-based nanoparticles. *Nano Research* **2019,** *12* (6), 1267-1278.
[247] T. Cele, Preparation of Nanoparticles. IntechOpen: February 16th 2020; pp 1 - 14.

[248] Y. X. Gan, A. H. Jayatissa, Z. Yu, X. Chen, M. Li, Hydrothermal Synthesis of Nanomaterials. *Journal of Nanomaterials* **2020,** *2020*, 8917013.
[249] K. I. Bryukhanova, G. Nikiforova, K. Gavrichev, Synthesis and study of anhydrous lanthanide orthophosphate (Ln = La, Pr, Nd, Sm) nanowhiskers. *Nanosystems: Physics, Chemistry, Mathematics* **2016**, 451-458.
[250] G. Yang, S.-J. Park, Conventional and Microwave Hydrothermal Synthesis and Application of Functional Materials: A Review. *Materials* **2019,** *12* (7).
[251] W. Lv, W. He, X. Wang, Y. Niu, H. Cao, J. H. Dickerson, Z. Wang, Understanding the oriented-attachment growth of nanocrystals from an energy point of view: a review. *Nanoscale* **2014,** *6* (5), 2531-2547.
[252] R. R. Chada, S. S. Enumula, S. Reddy K, M. D. Gudimella, S. R. Rao Kamaraju, D. R. Burri, Direct and facile synthesis of $LaPO_4$ containing SBA-15 catalyst for selective O-methylation of phenol to anisole in continuous process. *Microporous and Mesoporous Materials* **2020,** *300*, 110144.
[253] K. Maciejewska, B. Poźniak, M. Tikhomirov, A. Kobylińska, Ł. Marciniak, Synthesis, Cytotoxicity Assessment and Optical Properties Characterization of Colloidal $GdPO_4$:Mn^{2+}, Eu^{3+} for High Sensitivity Luminescent Nanothermometers Operating in the Physiological Temperature Range. *Nanomaterials* **2020,** *10* (3), 421.
[254] K. Byrappa, N. Keerthiraj, S. M. Byrappa, 14 - Hydrothermal Growth of Crystals—Design and Processing. In *Handbook of Crystal Growth (Second Edition)*, P. Rudolph, Ed. Elsevier: Boston, 2015; pp 535-575.
[255] P. R. Sajanlal, T. S. Sreeprasad, A. K. Samal, T. Pradeep, Anisotropic nanomaterials: structure, growth, assembly, and functions. *Nano Reviews* **2011,** *2* (1), 5883.
[256] K. Byrappa, Hydrothermal Growth of Polyscale Crystals. In *Springer Handbook of Crystal Growth*, G. Dhanaraj, K. Byrappa, V. Prasad, M. Dudley, Eds. Springer Berlin Heidelberg: Berlin, Heidelberg, 2010; pp 599-653.
[257] J. Ortiz-Landeros, C. Gómez-Yáñez, R. López-Juárez, I. Dávalos-Velasco, H. Pfeiffer, Synthesis of advanced ceramics by hydrothermal crystallization and modified related methods. *Journal of Advanced Ceramics* **2012,** *1* (3), 204-220.
[258] J. Li, Q. Wu, J. Wu, Synthesis of Nanoparticles via Solvothermal and Hydrothermal Methods. 2016; pp 295-328.
[259] K. Byrappa, M. Yoshimura, 2 - History of Hydrothermal Technology. In *Handbook of Hydrothermal Technology*, K. Byrappa, M. Yoshimura, Eds. William Andrew Publishing: Norwich, NY, 2001; pp 53-81.
[260] C.-C. Huang, Y.-W. Lo, W.-S. Kuo, J.-R. Hwu, W.-C. Su, D.-B. Shieh, C.-S. Yeh, Facile Preparation of Self-Assembled Hydrogel-like $GdPO_4 \cdot H_2O$ Nanorods. *Langmuir* **2008,** *24* (15), 8309-8313.

[261] P. C. de Sousa Filho, O. A. Serra, Red, green, and blue lanthanum phosphate phosphors obtained via surfactant-controlled hydrothermal synthesis. *Journal of Luminescence* **2009,** *129* (12), 1664-1668.
[262] H. Dong, Y. Liu, P. Yang, W. Wang, J. Lin, Controlled synthesis and characterization of $LaPO_4$, $LaPO_4$:Ce^{3+} and $LaPO_4$:Ce^{3+}, Tb^{3+} by EDTA assisted hydrothermal method. *Solid State Sciences* **2010,** *12* (9), 1652-1660.
[263] H. Song, L. Zhou, L. Li, F. Hong, X. Luo, Hydrothermal synthesis, characterization and luminescent properties of $GdPO_4 \cdot H_2O$:Tb^{3+} nanorods and nanobundles. *Materials Research Bulletin* **2013,** *48* (12), 5013-5018.
[264] J. Polte, Fundamental growth principles of colloidal metal nanoparticles – a new perspective. *CrystEngComm* **2015,** *17* (36), 6809-6830.
[265] G. Dhanaraj, K. Byrappa, V. Prasad, M. Dudley, Crystal Growth Techniques and Characterization: An Overview. In *Springer Handbook of Crystal Growth*, G. Dhanaraj, K. Byrappa, V. Prasad, M. Dudley, Eds. Springer Berlin Heidelberg: Berlin, Heidelberg, 2010; pp 3-16.
[266] B. Gilbert, H. Zhang, F. Huang, M. P. Finnegan, G. A. Waychunas, J. F. Banfield, Special phase transformation and crystal growth pathways observed in nanoparticles†. *Geochemical Transactions* **2003,** *4* (1), 20.
[267] J. D. Chen, Y. J. Wang, K. Wei, S. H. Zhang, X. T. Shi, Self-organization of hydroxyapatite nanorods through oriented attachment. *Biomaterials* **2007,** *28* (14), 2275-2280.
[268] J. Fang, B. Ding, H. Gleiter, Mesocrystals: Syntheses in metals and applications. *Chemical Society Reviews* **2011,** *40* (11), 5347-5360.
[269] G. Cravotto, D. Carnaroglio, editors. *Microwave Chemistry*. De Gruyter: Berlin, Boston, **2017** (ISBN 9873110479928).
[270] L. A. Kolahalam, I. V. Kasi Viswanath, B. S. Diwakar, B. Govindh, V. Reddy, Y. L. N. Murthy, Review on nanomaterials: Synthesis and applications. *Materials Today: Proceedings* **2019,** *18*, 2182-2190.
[271] C. Feldmann, H. O. Jungk, Preparation of sub-micrometer $LnPO_4$ particles (Ln = La, Ce). *Journal of Materials Science* **2002,** *37* (15), 3251-3254.
[272] Z. Wang, Z. Quan, J. Lin, J. Fang, Polyol-mediated synthesis and photoluminescent properties of Ce^{3+} and/or Tb^{3+}-doped $LaPO_4$ nanoparticles. *Journal of Nanoscience and Nanotechnology* **2005,** *5* (9), 1532-6.
[273] L. Ma, L.-M. Xu, W.-X. Chen, Z.-D. Xu, Microwave-assisted synthesis and characterization of $LaPO_4$:Re (Re=Ce^{3+}, Eu^{3+}, Tb^{3+}) nanorods. *Materials Letters* **2009,** *63* (18), 1635-1637.
[274] N. Ekthammathat, T. Thongtem, A. Phuruangrat, S. Thongtem, Microwave-assisted synthesis and characterisation of uniform $LaPO_4$ nanorods. *Journal of Experimental Nanoscience* **2012,** *7* (6), 616-623.
[275] G. Bühler, C. Feldmann, Microwave-Assisted Synthesis of Luminescent $LaPO_4$:Ce,Tb Nanocrystals in Ionic Liquids. *Angewandte Chemie International Edition* **2006,** *45* (29), 4864-4867.

[276] M. J. Burger, B. J. Robinson, L. F. Pease, Sol-Gel-Derived Nanoscale Materials. In *Handbook of Nanoparticles*, M. Aliofkhazraei, Ed. Springer International Publishing: Cham, 2016; pp 691-714.
[277] S. Esposito, "Traditional" Sol-Gel Chemistry as a Powerful Tool for the Preparation of Supported Metal and Metal Oxide Catalysts. *Materials* **2019,** *12* (4), 668.
[278] G. J. Owens, R. K. Singh, F. Foroutan, M. Alqaysi, C.-M. Han, C. Mahapatra, H.-W. Kim, J. C. Knowles, Sol–gel based materials for biomedical applications. *Progress in Materials Science* **2016,** *77*, 1-79.
[279] M. J. Fisher, W. Wang, P. K. Dorhout, E. R. Fisher, Synthesis of $LaPO_4$:Eu Nanostructures Using the Sol−Gel Template Method. *The Journal of Physical Chemistry C* **2008,** *112* (6), 1901-1907.
[280] H. Xu, B. W. Zeiger, K. S. Suslick, Sonochemical synthesis of nanomaterials. *Chemical Society Reviews* **2013,** *42* (7), 2555-2567.
[281] J. Kis-Csitári, Z. Kónya, I. Kiricsi In *Sonochemical Synthesis of Inorganic Nanoparticles*, Functionalized Nanoscale Materials, Devices and Systems, Dordrecht, 2008; A. Vaseashta, I. N. Mihailescu, Eds. Springer Netherlands: Dordrecht, 2008; pp 369-372.
[282] B. Richard, J.-L. Lemyre, A. M. Ritcey, Nanoparticle Size Control in Microemulsion Synthesis. *Langmuir* **2017,** *33* (19), 4748-4757.
[283] M. Sanchez-Dominguez, K. Pemartin, M. Boutonnet, Preparation of inorganic nanoparticles in oil-in-water microemulsions: A soft and versatile approach. *Current Opinion in Colloid & Interface Science* **2012,** *17* (5), 297-305.
[284] P. C. de Sousa Filho, O. A. Serra, Reverse Microemulsion Synthesis, Structure, and Luminescence of Nanosized $REPO_4$:Ln^{3+} (RE = La, Y, Gd, or Yb, and Ln = Eu, Tm, or Er). *The Journal of Physical Chemistry C* **2011,** *115* (3), 636-646.
[285] R. Chai, H. Lian, P. Yang, Y. Fan, Z. Hou, X. Kang, J. Lin, In situ preparation and luminescent properties of $LaPO_4$:Ce^{3+}, Tb^{3+} nanoparticles and transparent LaPO4:Ce^{3+}, Tb^{3+}/PMMA nanocomposite. *Journal of Colloid and Interface Science* **2009,** *336* (1), 46-50.
[286] A. Nayfeh, N. El-Atab, 6 - Agglomeration-based nanoparticle fabrication. In *Nanomaterials-Based Charge Trapping Memory Devices*, A. Nayfeh, N. El-Atab, Eds. Elsevier: 2020; pp 133-153.
[287] R. Hufschmid, E. Teeman, B. L. Mehdi, K. M. Krishnan, N. D. Browning, Observing the colloidal stability of iron oxide nanoparticles in situ. *Nanoscale* **2019,** *11* (27), 13098-13107.
[288] D. Doblas, T. Kister, M. Cano-Bonilla, L. González-García, T. Kraus, Colloidal Solubility and Agglomeration of Apolar Nanoparticles in Different Solvents. *Nano Letters* **2019,** *19* (8), 5246-5252.
[289] V. Klimkevicius, M. Janulevicius, A. Babiceva, A. Drabavicius, A. Katelnikovas, Effect of Cationic Brush-Type Copolymers on the Colloidal

Stability of $GdPO_4$ Particles with Different Morphologies in Biological Aqueous Media. *Langmuir* **2020** 36, 7533-7544.
[290] H. Ohshima, The Derjaguin–Landau–Verwey–Overbeek (DLVO) Theory of Colloid Stability. In *Electrical Phenomena at Interfaces and Biointerfaces*, Wiley: 2012; pp 27-34.
[291] S. Shrestha, B. Wang, P. Dutta, Nanoparticle processing: Understanding and controlling aggregation. *Advances in Colloid and Interface Science* **2020,** *279*, 102162.
[292] S.-J. Park, M.-K. Seo, Chapter 1 - Intermolecular Force. In *Interface Science and Technology*, S.-J. Park, M.-K. Seo, Eds. Elsevier: 2011; Vol. 18, pp 1-57.
[293] S. G. J. Heijman, H. N. Stein, Electrostatic and Sterical Stabilization of TiO_2 Dispersions. *Langmuir* **1995,** *11* (2), 422-427.
[294] V. Klimkevicius, T. Graule, R. Makuska, Effect of Structure of Cationic Comb Copolymers on Their Adsorption and Stabilization of Titania Nanoparticles. *Langmuir* **2015,** *31* (7), 2074-2083.
[295] T. Kegl, A. Košak, A. Lobnik, Z. Novak, A. K. Kralj, I. Ban, Adsorption of rare earth metals from wastewater by nanomaterials: A review. *Journal of Hazardous Materials* **2020,** *386*, 121632.
[296] Principles and Mechanisms of Nanoparticle Stabilization by Polymers. In *Metallopolymer Nanocomposites*, A. D. Pomogailo, V. N. Kestelman, Eds. Springer Berlin Heidelberg: Berlin, Heidelberg, 2005; pp 65-113.
[297] J. H. Adair, E. Suvaci, J. Sindel, Surface and Colloid Chemistry. In *Encyclopedia of Materials: Science and Technology*, K. H. J. Buschow, R. W. Cahn, M. C. Flemings, B. Ilschner, E. J. Kramer, S. Mahajan, P. Veyssière, Eds. Elsevier: Oxford, 2001; pp 1-10.
[298] J. N. Israelachvili, *Intermolecular and Surface Forces*. Elsevier Science: 2015.
[299] W. Zhang, R. Honaker, Surface charge of rare earth phosphate (monazite) in aqueous solutions. *Powder Technology* **2017,** *318*, 263-271.
[300] R. J. Pugh, Dispersions and stability of ceramic powders in liquids. In *Surface and Colloid Chemistry in Advanced Ceramics Processing*, R. J. Pugh, L. Bergström, Eds. Marcel Dekker: 1993; pp 127-192.
[301] S. Barcikowski, V. Amendola, G. Marzun, C. Rehbock, S. Reichenberger, D. Zhang, B. Gökce. *Handbook of Laser Synthesis of Colloids*, Universität Duisburg-Essen, 2016.
[302] M. O. Fatehah, H. A. Aziz, S. Stoll, Nanoparticle Properties, Behavior, Fate in Aquatic Systems and Characterization Methods. *Journal of Colloid Science and Biotechnology* **2014,** *3* (2), 111-140.
[303] E. Piacenza, A. Presentato, R. J. Turner, Stability of biogenic metal(loid) nanomaterials related to the colloidal stabilization theory of chemical nanostructures. *Critical Reviews in Biotechnology* **2018,** *38* (8), 1137-1156.

[304] R. J. Hunter, *Zeta Potential in Colloid Science: Principles and Applications*, Academic Press, London ; New York, 1988.
[305] A. J. Worthen, V. Tran, K. A. Cornell, T. M. Truskett, K. P. Johnston, Steric stabilization of nanoparticles with grafted low molecular weight ligands in highly concentrated brines including divalent ions. *Soft Matter* **2016,** *12* (7), 2025-2039.
[306] T. Tadros, Electrostatic and Steric Stabilization of Colloidal Dispersions. In *Electrical Phenomena at Interfaces and Biointerfaces*, H. Ohshima, Ed. pp 153-172.
[307] L. Guerrini, R. A. Alvarez-Puebla, N. Pazos-Perez, Surface Modifications of Nanoparticles for Stability in Biological Fluids. *Materials* **2018,** *11* (7), 1154.
[308] W. Ren, G. Tian, S. Jian, Z. Gu, L. Zhou, L. Yan, S. Jin, W. Yin, Y. Zhao, TWEEN coated $NaYF_4$:Yb,Er/$NaYF_4$ core/shell upconversion nanoparticles for bioimaging and drug delivery. *RSC Advances* **2012,** *2* (18), 7037-7041.
[309] Z. Khan, S. A. Al-Thabaiti, A. Y. Obaid, Z. A. Khan, A. O. Al-Youbi, Effects of solvents on the stability and morphology of CTAB-stabilized silver nanoparticles. *Colloids and Surfaces A: Physicochemical and Engineering Aspects* **2011,** *390* (1), 120-125.
[310] D. S. Gaikwad, K. A. Undale, D. B. Patil, D. M. Pore, A. A. Kamble, Triton X-100 stabilized Pd nanoparticles and their catalytic application in one-pot sequential Heck and Hiyama coupling in water. *Research on Chemical Intermediates* **2018,** *44* (1), 265-275.
[311] S. Farrokhpay, A review of polymeric dispersant stabilisation of titania pigment. *Advances in Colloid and Interface Science* **2009,** *151* (1), 24-32.
[312] M. Rahaman, M. N. Rahaman, *Ceramic Processing*. Taylor & Francis: 2006.
[313] V. Klimkevicius, R. Makuska, T. Graule, Rheology of titania based ceramic nanodispersions stabilized by cationic comb copolymers. *Applied Rheology* **2016,** *26,* 15199.
[314] K. McNamara, S. A. M. Tofail, Nanoparticles in biomedical applications. *Advances in Physics: X* **2017,** *2* (1), 54-88.
[315] V. Prakash Sharma, U. Sharma, M. Chattopadhyay, V. N. Shukla, Advance Applications of Nanomaterials: A Review. *Materials Today: Proceedings* **2018,** *5* (2, Part 1), 6376-6380.
[316] R. Thiruppathi, S. Mishra, M. Ganapathy, P. Padmanabhan, B. Gulyás, Nanoparticle Functionalization and Its Potentials for Molecular Imaging. *Advanced Science* **2017,** *4* (3), 1600279.
[317] J. Shen, M. Shafiq, M. Ma, H. Chen, Synthesis and Surface Engineering of Inorganic Nanomaterials Based on Microfluidic Technology. *Nanomaterials* **2020,** *10* (6), 1177.

[318] R. Mout, D. F. Moyano, S. Rana, V. M. Rotello, Surface functionalization of nanoparticles for nanomedicine. *Chemical Society Reviews* **2012,** *41* (7), 2539-2544.
[319] J. Conde, J. T. Dias, V. Grazú, M. Moros, P. V. Baptista, J. M. de la Fuente, Revisiting 30 years of biofunctionalization and surface chemistry of inorganic nanoparticles for nanomedicine. *Frontiers in Chemistry* **2014,** *2*, 48.
[320] T. S. Atabaev, Y. C. Shin, S.-J. Song, D.-W. Han, N. H. Hong, Toxicity and T2-Weighted Magnetic Resonance Imaging Potentials of Holmium Oxide Nanoparticles. *Nanomaterials* **2017,** *7* (8), 216.
[321] C.-H. Huang, A. Tsourkas, Gd-based macromolecules and nanoparticles as magnetic resonance contrast agents for molecular imaging. *Current Topics in Medicinal Chemistry* **2013,** *13* (4), 411-421.
[322] R. Northrop, D. Hristov, Noninvasive Instrumentation and Measurements in Medical Diagnosis. *Medical Physics* **2003,** *30*, 2565-2565.
[323] F. Li, D. Zhi, Y. Luo, J. Zhang, X. Nan, Y. Zhang, W. Zhou, B. Qiu, L. Wen, G. Liang, Core/shell Fe_3O_4/Gd_2O_3 nanocubes as T1–T2 dual modal MRI contrast agents. *Nanoscale* **2016,** *8* (25), 12826-12833.
[324] Q. Yang, X. Li, Z. Xue, Y. Li, M. Jiang, S. Zeng, Short-wave near-infrared emissive $GdPO_4:Nd^{3+}$ theranostic probe for in vivo bioimaging beyond 1300 nm. *RSC Advances* **2018,** *8* (23), 12832-12840.
[325] R. Lv, G. Yang, S. Gai, Y. Dai, F. He, P. Yang, Multifunctional $LaPO_4$:Ce/Tb@Au mesoporous microspheres: synthesis, luminescence and controllable light triggered drug release. *RSC Advances* **2014,** *4* (108), 63425-63435.
[326] M. Kumari, S. Mondal, P. K. Sharma, Synthesis, characterization and electrochemical monitoring of drug release properties of dual stimuli responsive mesoporous $GdPO_4:Eu^{3+}$ nanoparticles. *Journal of Alloys and Compounds* **2019,** *776*, 654-665.
[327] B. I. A. Chisca S., and Popa K., Radioactive Waste Treatment and Disposal: Phosphates for Actinides Conditioning. *Acta Chemica Iasi* **2009,** *17*, 73-84.
[328] L. A. Boatner, G. W. Beall, M. M. Abraham, C. B. Finch, P. G. Huray, M. Rappaz, Monazite and Other Lanthanide Orthophosphates as Alternate Actinide Waste Forms. In *Scientific Basis for Nuclear Waste Management*, C. J. M. Northrup, Ed. Springer US: Boston, MA, 1980; pp 289-296.
[329] F. Nieto, K. J. Livi, *Minerals at the nanoscale*. The Mineralogical Society of Great Britain and Ireland: 2013; Vol. 14.
[330] O. Terra, N. Clavier, N. Dacheux, R. Podor, Preparation and characterization of lanthanum–gadolinium monazites as ceramics for radioactive waste storage. *New Journal of Chemistry* **2003,** *27* (6), 957-967.
[331] R. Lacomba-Perales, D. Errandonea, Y. Meng, M. Bettinelli, High-pressure stability and compressibility of APO_4 (A=La, Nd, Eu, Gd, Er, and Y) orthophosphates: An x-ray diffraction study using synchrotron radiation. *Physical Review B* **2010,** *81* (6), 064113.

[332] S. A. P. b. MDPI, *High-Pressure Studies of Crystalline Materials*. MDPI: 2018.
[333] S. Hartmut, H. Julia, N. Andreas, S. Stephan, B. Dirk, Monazite as a suitable actinide waste form. *Zeitschrift für Kristallographie - Crystalline Materials* **2013,** *228* (3), 113-123.
[334] V. Klimkevicius, M. Steponaviciute, R. Makuska, Kinetics of RAFT polymerization and copolymerization of vinyl monomers by size exclusion chromatography. *European Polymer Journal* **2020,** *122*, 109356.
[335] A. S. Vanetsev, E. V. Samsonova, O. M. Gaitko, K. Keevend, A. V. Popov, U. Mäeorg, H. Mändar, I. Sildos, Y. V. Orlovskii, Phase composition and morphology of nanoparticles of yttrium orthophosphates synthesized by microwave-hydrothermal treatment: The influence of synthetic conditions. *Journal of Alloys and Compounds* **2015,** *639*, 415-421.
[336] H. Deng, C. Liu, S. Yang, S. Xiao, Z.-K. Zhou, Q.-Q. Wang, Additive-Mediated Splitting of Lanthanide Orthovanadate Nanocrystals in Water: Morphological Evolution from Rods to Sheaves and to Spherulites. *Crystal Growth & Design* **2008,** *8* (12), 4432-4439.
[337] X. Wang, M. Gao, A facile route for preparing rhabdophane rare earth phosphate nanorods. *Journal of Materials Chemistry* **2006,** *16* (14), 1360-1365.
[338] T. Sugimoto, *Monodispersed particles*. Elsevier: 2019.
[339] L. I. Katzin, E. Gulyas, Dissociation constants of tartaric acid with the aid of polarimetry. *The Journal of Physical Chemistry* **1960,** *64* (11), 1739-1741.
[340] S. Wu, J. Yin, H. Qu, A. Li, L. Liu, Y. Shao, Photoluminescence properties of gadolinium phosphate nanoprisms doped with lanthanide ions for multicolor live cell imaging. *Journal of Materials Science: Materials in Electronics* **2019,** *30* (12), 11336-11345.
[341] A. Mayence, J. R. G. Navarro, Y. Ma, O. Terasaki, L. Bergström, P. Oleynikov, Phase Identification and Structure Solution by Three-Dimensional Electron Diffraction Tomography: Gd–Phosphate Nanorods. *Inorganic Chemistry* **2014,** *53* (10), 5067-5072.
[342] F. Mpambani, Multifunctional Magnetic and Fluorescent Nanoparticles for Betaamyloid Targeting in Neurodegenerative Disease Diagnosis, Anal. Chem. Université Claude Bernard, Lyon, 2013, p. 222.
[343] M. Toro-González, D. M. Clifford, R. Copping, S. Mirzadeh, J. V. Rojas, Synthesis and characterization of intrinsically radiolabeled lanthanide phosphate nanoparticles toward biomedical and environmental applications. *Journal of Nanoparticle Research* **2018,** *20* (9), 238.
[344] Z. Li, Y. Tao, S. Huang, N. Gao, J. Ren, X. Qu, Lanthanide-based hollow mesoporous nanoparticles: a novel multifunctional platform for simultaneous gene delivery and cell imaging. *Chemical Communications* **2013,** *49* (64), 7129-7131.

[345] M. Runowski, T. Grzyb, A. Zep, P. Krzyczkowska, E. Gorecka, M. Giersig, S. Lis, Eu^{3+} and Tb^{3+} doped $LaPO_4$ nanorods, modified with a luminescent organic compound, exhibiting tunable multicolour emission. *RSC Advances* **2014,** *4* (86), 46305-46312.
[346] S. K. Rhodes, R. H. Lambeth, J. Gonzales, J. S. Moore, J. A. Lewis*, Cationic Comb Polymer Superdispersants for Colloidal Silica Suspensions. *Langmuir* **2009,** *25* (12), 6787-6792.
[347] V. B. Pawade, S. J. Dhoble, *Phosphors for Energy Saving and Conversion Technology*. CRC Press/Taylor & Francis Group, 2019.
[348] R. Skaudzius, A. Katelnikovas, D. Enseling, A. Kareiva, T. Jüstel, Dependence of the $^5D_0 \rightarrow {}^7F_4$ transitions of Eu^{3+} on the local environment in phosphates and garnets. *Journal of Luminescence* **2014,** *147*, 290-294.
[349] Z. Karimi, L. Karimi, H. Shokrollahi, Nano-magnetic particles used in biomedicine: Core and coating materials. *Materials Science and Engineering: C* **2013,** *33* (5), 2465-2475.
[350] A. Albanese, W. C. W. Chan, Effect of Gold Nanoparticle Aggregation on Cell Uptake and Toxicity. *ACS Nano* **2011,** *5* (7), 5478-5489.
[351] J. Wu, X. Zhang, T. Yao, J. Li, H. Zhang, B. Yang, Improvement of the Stability of Colloidal Gold Superparticles by Polypyrrole Modification. *Langmuir* **2010,** *26* (11), 8751-8755.
[352] P. J. Sugumaran, X.-L. Liu, T. S. Herng, E. Peng, J. Ding, GO-Functionalized Large Magnetic Iron Oxide Nanoparticles with Enhanced Colloidal Stability and Hyperthermia Performance. *ACS Applied Materials & Interfaces* **2019,** *11* (25), 22703-22713.
[353] P. Rivera Gil, G. Oberdörster, A. Elder, V. Puntes, W. J. Parak, Correlating Physico-Chemical with Toxicological Properties of Nanoparticles: The Present and the Future. *ACS Nano* **2010,** *4* (10), 5527-5531.
[354] J. S. Suk, Q. Xu, N. Kim, J. Hanes, L. M. Ensign, PEGylation as a strategy for improving nanoparticle-based drug and gene delivery. *Advanced Drug Delivery Reviews* **2016,** *99*, 28-51.
[355] B. Yan, X. Xiao, Hydrothermal Synthesis, Microstructure and Photoluminescence of Eu^{3+}-Doped Mixed Rare Earth Nano-Orthophosphates. *Nanoscale Research Letters* **2010,** *5* (12), 1962.
[356] J. Cho, C. H. Kim, Solid-state phase transformation mechanism from hexagonal $GdPO_4 : Eu^{3+}$ nanorods to monoclinic nanoparticles. *RSC Advances* **2014,** *4* (59), 31385-31392.
[357] X. Zou, L. He, D. Tan, F. Lei, N. Jiang, Q. Zheng, D. Lin, C. Xu, Y. Liu, Anneal-induced transformation of phase structure, morphology and luminescence of $GdPO_4:Sm^{3+}$ nanomaterials synthesized by a hydrothermal method. *Dalton Transactions* **2017,** *46* (9), 2948-2956.
[358] M. N. Luwang, R. S. Ningthoujam, Jagannath, S. K. Srivastava, R. K. Vatsa, Effects of Ce^{3+} Codoping and Annealing on Phase Transformation and Luminescence of Eu^{3+}-Doped YPO_4 Nanorods: D_2O

Solvent Effect. *Journal of the American Chemical Society, 132* (8), 2759–2768.
[359] A. G. Hernández, D. Boyer, A. Potdevin, G. Chadeyron, A. G. Murillo, F. de J. Carrillo Romo, R. Mahiou, Hydrothermal synthesis of lanthanide-doped $GdPO_4$ nanowires and nanoparticles for optical applications. *Physica Status Solidi (a)* **2014,** *211* (2), 498-503.
[360] K. A. GschneidnerJr, V. K. Pecharsky, A. O. Tsokol, Recent developments in magnetocaloric materials. *Reports on Progress in Physics* **2005,** *68* (6), 1479-1539.
[361] F. F. Y. Wang, Magnetic Susceptibilities of Gadolinium Orthophosphate ($GdPO_4$). *Physica Status Solidi (b)* **1966,** *14* (1), 193-203.
[362] Q. Du, Z. Huang, Z. Wu, X. Meng, G. Yin, F. Gao, L. Wang, Facile preparation and bifunctional imaging of Eu-doped $GdPO_4$ nanorods with MRI and cellular luminescence. *Dalton Transactions* **2015,** *44* (9), 3934-3940.

1. Įvadas

Medžiagotyra yra viena labiausiai besivystančių šiuolaikinio mokslo krypčių. Įvairių neorganinių nanomedžiagų kūrimas ir jų tobulinimas yra svarbi šių mokslų sritis. Mokslininkai daug laiko skiria įvairių nanomedžiagų kūrimui. Nanostruktūrų unikalias savybes lema jų mažas dydis, tačiau ne tik medžiagų dydis, bet ir forma yra svarbi apsprendžiant unikalias nanomedžiagų savybes ir pritaikomumą. Neorganinės lantanoidų medžiagos (fluoridai, oksidai, fosfatai) dėl savo plataus pritaikomumo ir funkcionalumo yra perspektyvios naujos funkcinės nanomedžiagos.

Paskutinius du-tris dešimtmečius lantanoidų ortofosfatai ir jų keramika buvo intensyviai tiriamos. Šie tyrimai ženkliai prisidėjo prie technologinės pažangos LED technologijose, lazerių kūrime, magnetų kūrime ir t. t. Įvairių lantanoidų ortofosfatų ir jų keramikos kūrimas ir sintezė ir toliau išlieka svarbi mokslinių tyrimų kryptis, tačiau neorganinių lantanoidais grįstų nanodalelių kūrimas savo populiarumu sparčiai vejasi kitas medžiagotyros mokslų kryptis. Nanodalelės ir nanostruktūros gali turėti skirtingas savybes lyginant su jų makroanalogais. Mažėjant lantanoidų jonų turinčių medžiagų dalelėms, dėl didėjančio paviršiaus ploto prastėja jų liuminescencinės savybės. Nepaisant to šios medžiagos pasižymi geresnėmis savybėmis lyginant su kitomis nanodalelėmis. Pavyzdžiui, lantanoidų neorganinės nanodalelės, skirtingai nuo kvantinių taškų ar organinių šviestukų nepasižymi fotoblukimu ar fotodegradacija. Neorganinės nanodalelės išsiskiria savo specifine liuminescencija, t. y. siauromis emisijos linijomis lyginant su plačiomis kvantinių taškų, organinių šviestukų emisijos linijomis, kurios dėl savo platumo dažnai persikloja.

Iš visų tyrinėjamų neorganinių lantanoidais grįstų medžiagų, įdomi medžiagų klasė yra lantanoidų ortofosfatai ($LnPO_4$). Dėl didelio šių medžiagų funkcionalumo susidomėjimas lantanoidų ortofosfatais tik auga. Lantanoidų ortofosfatų dalelės yra tyrinėjamos kaip potencialūs biologiniai žymekliai (medicinai), liuminescenciniai nanofosforai (optoelektronikai), aukštynvertės medžiagos, katalizatoriai ir t. t. Egzistuoja ne vienas sintezės metodas (hidroterminė sintezė, išsodinimas, atvirkštinių micelių metodas, sonocheminė sintezė, mikrobangomis asistuojama hidroterminė sintezė ir kt. metodai), kuriuo pasinaudojus galima gauti lantanoidų ortofosfatų nanodaleles.

Dėl savo įvairiapusiškumo, lantanoidai yra labai įdomios medžiagos tyrinėjimams. Visų pirma, priklausomai nuo lantanoido joninio spindulio ir pasirinkto sintezės metodo, lantanoidų ortofosfatai gali sudaryti skirtingas

kritalines struktūras: trigoninę rabdofano, monoklininą monazito, tetragoninę ksenotimo. Priešingai nei lantanoidų fluoridai, galima ir labai plati manipuliacija lantanoidų ortofosfatų dalelių morfologijomis – nanopluoštai, nanolazdelės, heksagoninės nanoprizmės, submikrosferos, submikrožvaigždės, tuščiavidurės sferos ir t. t. Be to, lantanoidų ortofosfatai yra biologiškai inertiškos medžiagos, pasižymimčios geru terminiu ir cheminiu stabilumu, yra labai mažai tirpios vandenyje, jų sintezių metu nereikalingi toksiški reagentai.

Lantanoidų ortofosfatai taip pat žinomi kaip magnetinių savybių turintys junginiai. Gadolinio magnetinės savybės atsiranda dėl Gd^{3+} jonuose esančių 7 nesuporuotų 4f sluoksnio elektronų. Dėl tokios unikalios elektroninės konfigūracijos gadolinio junginiai (tiek neorganiniai, tiek organiniai kompleksai) yra patrauklios platformos kaip magnetinio rezonanso kontrastiniai agentai, multifunkcinės nanodalelės ($GdPO_4$, GdF_3, $NaGdF_4$, Gd_2O_3) suteikia sudėtinę bio-vaizdinimo ir magnetinio rezonanso vaizdinimo galimybę.

Mokslinis naujumas ir aktualumas:

- Išdirbta ir optimizuota hidroterminės sintezės metodika, leidžianti lengvai, nesudėtingai ir su geru atsikartojamumu susintetinti įvairių morfologijų rabdofano fazės $GdPO_4$ nano ir submikro daleles.
- Pirmą kartą literatūroje palyginti nemodifikuotų skirtingų morfologijų lantanoidų ortofosfatų nanodalelių zeta potencialai. Keičiant nanodalelių morfologiją galima pasiekti elektrostatinį stabilumą vandeniniuose koloiduose plačiame pH intervale.
- Susintetintas aukštos kokybės rabdofano fazės $GdPO_4$ nanopluoštas.
- Efektyvios augimo kontrolės dėka pirmąkart susintetintas ir charakterizuotas monoklininės monazito fazės $GdPO_4$ aerogelis, sudarytas iš nanogijų.

Šio darbo tikslas buvo susintetinti įvairias nano/submikro lantanoidų ortofosfatų nanodaleles, kurios galėtų būtų pritaikytos kaip funkcinės nanomedžiagos technologijų ir/ar biomedicinos srityse. Šiam tikslui įgyvendinti buvo suformuluoti šie uždaviniai:

1. Išdirbti paprastą, toksiškų prekursorių ir sudėtingų sąlygų nereikalaujantį sintezės metodą, leidžiantį gauti aukštos kokybės lantanoidų ortofosfatų daleles ir efektyviai manipuliuoti jų morfologija;
2. Ištirti ir įvertinti nemodifikuotų lantanoidų ortofosfatų dalelių stabilumą vandeniniuose koloiduose;

3. Užtikrinti lantanoidų ortofosfatų dalelių stabilumą biologinėje terpėje.

Ginamieji disertacijos teiginiai:

1. Hidroterminis metodas yra tinkamas būdas sintetinti monodispersiškoms, lantanoidų ortofosfatų nano ir mikro dalelėms. Keičiant fosfatų šaltinio ir lantanoidų jonų molinį santykį (1 - 100 ribose), galima efektyviai kontroliuoti augančių dalelių morfologiją ir dydį.
2. Skirtingų morfologijų $GdPO_4$ nano ir submikro dalelės turi skirtingas zeta-potencialo vertes. Keičiant dalelių morfologiją, galima pasiekti elektrostatinį nemodifikuotų $GdPO_4$ dalelių stabilumą plačiame pH ruože.
3. Lyginant su nemodifikuotomis $GdPO_4$ dalelėmis, katijoniniais p(METAC-*stat*-PEO_{19}MEMA) polimeriniais šepečiais modifikuotos $GdPO_4$ nano ir submikro dalelės pasižymi puikiu koloidiniu stabilumu vandeninėje terpėje ir nėra linkusios aglomeruotis laikui bėgant.
4. p(METAC-*stat*-PEO_{19}MEMA) polimeriniais šepečiais modifikuotos $GdPO_4$ dalelės gali būti redisperguotos iš sauso būvio. Tai yra naudinga savybė, kadangi tiek praktiniams, tiek komerciniams pritaikymams naudojamos dalelės dažniausiai yra transportuojamos ir parduodamos kaip koloidai ir negali būti redisperguojamos iš sauso būvio.
5. Disertacijos metu susintetintos $GdPO_4$ nanovielos buvo panudotos gauti $GdPO_4$ aerogelį. Gautas $GdPO_4$ aerogelis yra ypač lengvas ir pasižymi įdomiomis magnetinėmis savybėmis.

2. Eksperimento metodika

Disertacijos Eksperimento metodikos dalis yra suskirstyta į du poskyrius. Pirmajame poskyryje pateikti medžiagų charakterizavimui naudota įranga: medžiagų sintezei naudotas hidroterminis reaktorius *highpreactor* (gamintojas BERGHOF), susintetintos dalelės buvo centrifūguojamos naudojant centrifūgą Centrifuge 5804 (gamintojas Eppendorf), $GdPO_4$ hidrogelio liofilizacija buvo atlikta naudojant liofilizatorių Labconco FreeZone 2.5 freeze-dryer, kristalinėms fazėms nustatyti buvo naudojami Rentgeno spindulių difraktometrai Bruker D8 Advance ir Rigaku MiniFlexII, skenuojanti elektronų mikroskopija buvo atlikta naudojantis mikroskopu Hitachi SU-70 (greitinanti įtampa 10 kV), peršviečiamoji elektronų mikroskopija buvo atlikta naudojant FEI Tecnai F20 X-TWIN mikroskopą (TEM matavimai atlikti esant 200 kV greitinančiai įtampai), dinaminės šviesos sklaidos ir zeta potencialų matavimai buvo atlikti naudojant prietaisą ZetaSizer Nano ZS (gamintojas Malvern), termogravimetrinė analizė buvo atlikta naudojant prietaisą Perkin Elmer STA 6000 (oro atmosfera, kaitinimas

10 °C/min., mėginių svoris apie 5.5 mg), infraraudonisios spektroskopijos (FTIR) matavimai buvo atlikti naudojant spektrometrą Perkin Elmer FT IR Spectrometer Frontier, mėginių paviršiaus plotas buvo įvertinas BET (Brunauer−Emmett−Teller) analizės metodu naudojant prietaisą Micromeretics ASAP 2020, magnetinės aerogelio savybės buvo įvertintos matuojant bandinių įmagnetėjimo (*M*) priklausomybę nuo magnetinio lauko (*H*), optinėms medžiagų savybėms įvertinti buvo naudojantis spektrometru Edinburgh Instruments FLS980.

Antrajame poskyryje pateikti išsamūs $GdPO_4$ nano ir mikro dalelių, nanopluošto sintezių aprašymai ir naudoti prekursoriai, nurodant jų grynumą ir gamintoją.

3. Rezultatai ir jų aptarimas

3.1 Hidroterminė $GdPO_4$ nano ir submikro dalelių sintezė

Šiame skyriuje buvo ištirta ir pateikta įvairių hidroterminės sintezės parametrų (sintezės trukmė, pH, pradinės koncentracijos, moliniai prekursorių santykiai) įtaka $GdPO_4$ dalelių augimui. Buvo nustatyta, jog fosfatų šaltinio ir lantanoidų jonų molinis santykis leidžia efektyviai kontroliuoti augančių dalelių morfologiją. Taip pat buvo parinkti optimalūs sintezės parametrai dalelių morfologijai kontroliuoti. Dalelės buvo auginamos esant šioms hidroterminėms sąlygoms: temperatūra 160 °C, sintezės trukmė 12 valandų, pH vertė 10 (reguliuota su 25 % NH_4OH), kaip augimą koordinuojantis agentas naudota vyno rūgštis. Sintezės metu reakcijos tirpalas buvo maišomas. Naudojantis šia išdirbta hidroterminės sintezės metodika buvo susintetintos trijų skirtingų morfologijų $GdPO_4 \cdot nH_2O$ dalelės – nanolazdelės, heksagoninės nanoprizmės ir submikrosferos. Fosfatų šaltinio ir lantanoidų jonų molinam santykiui esant 10 formuojasi nanolazdelės (atvaizduota 1 pav. a, d). Didinant šį santykį iki 50 gaunamos heksagoninės nanoprizmės (1 pav. b, e). Fosfatų šaltinio ir lantanoidų jonų molinam santykiui esant 100 gaunamos submikrosferos (1 pav. c, f).

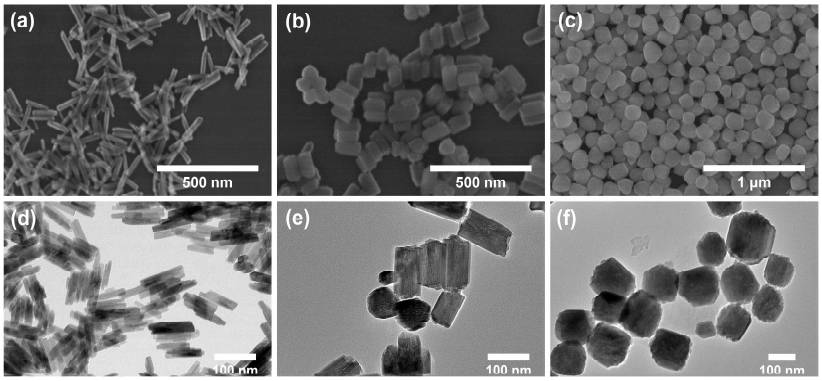

1 pav. $GdPO_4 \cdot nH_2O$ dalelių SEM (a-c) ir TEM (d-f) mikrografos. Nanolazdelės (a, d), heksagoninės nanoprizmės (b, e) ir submikrosferos (c, f).

Iš SEM ir TEM mikrografų matyti, kad susintetintos dalelės yra monodispersiškos. Dalelės kristalizuojasi į trigoninę rabdofano fazę. Tai patvirtino atlikta šių dalelių Rentgeno spindulių difrakcinė analizė. Be to, visų morfologijų dalelės yra faziškai grynos, t. y. lyginant dalelių difraktogramas su PDF ICDD 00-039-0232 standartu nėra stebima jokių pašalinių smailių (2 pav).

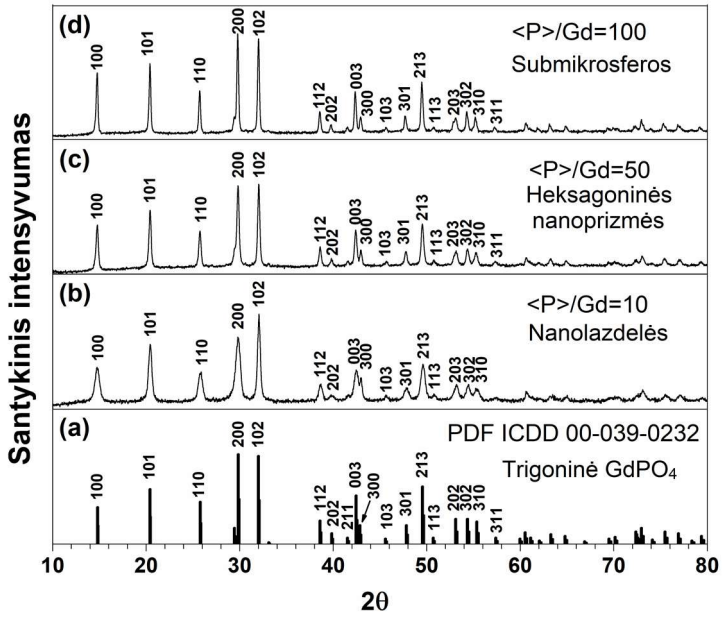

2 pav. $GdPO_4 \cdot nH_2O$ dalelių difraktogramos. Trigoninės $GdPO_4$ difraktogramos standartas (a), nanolazdelės (b), heksagoninės nanoprizmės (c) ir submikrosferos (d).

3.2 Koloidinis $GdPO_4$ nano ir submikro dalelių stabilumas

3.2.1 Nemodifikuotų $GdPO_4$ dalelių koloidinio stabilumo įvertinimas

Šiame skyriuje buvo įvertintas koloidinis susintetintų $GdPO_4$ nano ir submikro dalelių stabilumas vandeniniuose tirpaluose, pasitelkiant zeta potencialo ir dinaminės šviesos sklaidos (DLS) matavimus bei vizualinį vertinimą laike.

Nemodifikuotų $GdPO_4$ nanodalelių vandeninių koloidų stabilumas yra pasiekiamas elektrostatiškai, t. y. kada elektrostatinio atostūmio jėga yra stipresnė už Van der Valso tarpusiavio traukos jėgas. $GdPO_4$ dalelių koloidinis stabilumas stipriai priklauso nuo pH vertės, kuriai kintant keičiasi ir pačių dalelių paviršiaus krūvis, kuris įvertinamas remiantis zeta potencialo verte. Nustatyta, kad $GdPO_4$ dalelės yra linkusios formuoti stabilius koloidus, kada jų zeta potencialo vertė yra apytikriai |30| mV ar daugiau.

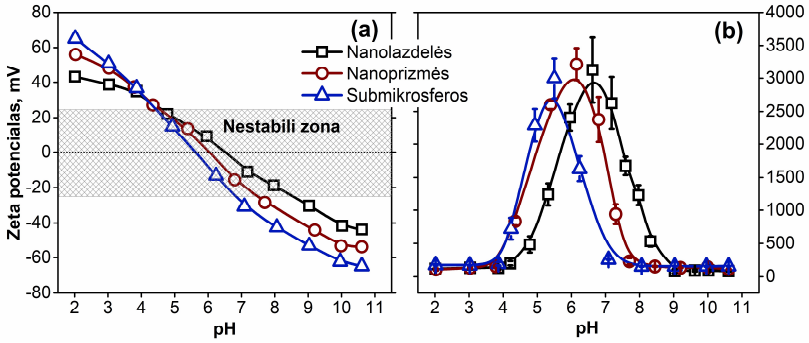

3 pav. $GdPO_4 \cdot nH_2O$ dalelių zeta-potencialo (a) ir jų dydžių pasiskirstymo (b) priklausomybė nuo pH vertės.

Iš 3 pav. matyti, kad skirtingų morfologijų $GdPO_4$ dalelės turi skirtingas zeta potencialo vertes (3 pav. a). Dalelių stabilumas buvo įvertintas atlikus dalelių koloidinių tirpalų DLS matavimus (3 pav. b). Remiantis gautais rezultatais, galima teigti, kad skirtingų morfologijų $GdPO_4$ dalelės yra stabilios skirtinguose pH intervaluose. Identiškomis sąlygomis (pH = 10,6), nemodifikuotų nanolazdelių zeta potencialo vertė yra -43,8 mV, hesagoninių nanoprizmių -53,8 mV, o submikrosferų -64,7 mV. Taip pat, priklausomai nuo morfologijos, $GdPO_4$ dalelės turi ir skirtingus izoelektrinius taškus. Izoelektrinis nanolazdelių taškas pasiekiamas pH vertei esant 6,53, heksagoninių nanoprizmių – pH vertei esant 6,03, o submikrosferų pH vertei esant 5,61.

Daroma prielaida, kad, priklausomai nuo morfologijos, $GdPO_4$ dalelės turi skirtingą funkcinių grupių, galinčių protonizuotis/deprotonizuotis, skaičių savo paviršiuje. Šios funkcinės grupės nulemia skirtingus dalelių paviršiaus krūvius, izoelektrinius taškus ir koloidinį stabilumą skirtinguose pH ruožuose.

3.2.2 $GdPO_4$ dalelių, modifikuotų katijoniniais p(METAC-*stat*-PEO_{19}MEMA) šepetiniais polimerais, koloidinio stabilumo įvertinimas

Elektrostatiškai pasiekta stabilizacija neužtikrina patikimo $GdPO_4$ dalelių koloidų stabilumo. Dalelės pH intervale tarp maždaug 5-7 yra linkusios aglomeruotis (3 pav. b). Be to, temperatūros, joninės jėgos ar dalelių koncentracijų pokyčiai taip pat gali būti neplanuotos aglomeracijos priežastimis.

Siekiant pagerinti $GdPO_4$ dalelių koloidinį stabilumą, dalelės buvo modifikuotos p(METAC-*stat*-PEO_{19}MEMA) polimeriniais šepečiais. Tam tikslui, keičiant pradinius monomerų (METAC ir PEO_{19}MEMA) santykius (žr. 1 lentelę), buvo susintetinti trys skirtingų sudėčių polimerai. Ketvirtinės amino grupės, esančios METAC momomeriniuose segmentuose, suteikia p(METAC-*stat*-PEO_{19}MEMA) kopolimerams teigiamą krūvį. Modifikuojant $GdPO_4$ daleles, šios teigiamą krūvį turinčios amino grupės elektrostatiškai sorbuojasi ant neigiamą krūvį turinčių $GdPO_4$ dalelių paviršiaus.

1 lentelė. $GdPO_4$ dalelių stabilizacijai naudoti skirtingus katijoninių grupių tankius turintys katijoniniai p(METAC-*stat*-PEO_{19}MEMA) šepetiniai polimerai.

Nr.	Kopolimero krūvis	$[METAC]_0$: $[PEO_{19}MEMA]_0$	[METAC]: [PEO_{19}MEMA]*	M_n, kDa*
1.	Žemas	25:75	27:73	28.5
2.	Vidutinis	45:55	47:53	24.6
3.	Didelis	65:35	65:35	19.4

* Išskaičiuota iš ^{1}H BMR spektrų.

$GdPO_4$ dalelių modifikacijai susintetinti katijoniniai p(METAC-*stat*-PEO_{19}MEMA) polimerai gali būti išskirstyti pagal ketvirtinių amino grupių kiekį sudėtyje: turintys mažą krūvį, turintys vidutinį krūvį ir turintys didelį krūvį. Atitinkamai (pagal 1 lentelę) mažą krūvį turintys polimerai turi 27 mol%, vidutinį krūvį turintys polimerai turi 47 mol% ir didelį

krūvį turintys polimerai turi 65 mol% METAC fragmentų, turinčių funkcinę grupę su teigiamu krūviu.

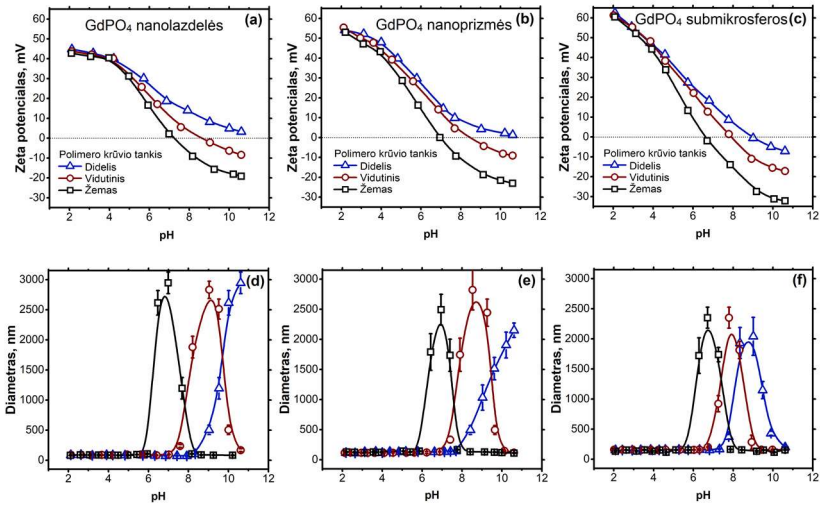

4 pav. Skirtingas morfologijas turinčių modifikuotų $GdPO_4$ dalelių zeta-potencialo (a-c) ir dalelių dydžių pasiskirstymo (d-f) priklausomybės nuo pH vertės, naudojant skirtingos sudėties p(METAC-*stat*-PEO_{19}MEMA) polielektrolitus.

Visų skirtingų morfologijų $GdPO_4$ dalelių paviršius buvo modifikuotas naudojant skirtingus katijoninių grupių tankius turinčius p(METAC-*stat*-PEO_{19}MEMA) polielektrolitus. Koloidinis dalelių stabilumas buvo vertinamas paruošiant jų koloidus (1 mg/mL) iš sausų dalelių ir atliekant šių koloidų zeta potencialo ir dinaminės šviesos sklaidos matavimus (žr. 4 pav.). Matavimai buvo atlikti pH intervale nuo ~2 iki 10,6. Koloidinių tirpalų pH vertėms koreguoti buvo naudoti 0,1 M koncentracijos HNO_3 ir NH_4OH tirpalai.

Sėkmingai modifikuotos visų morfologijų $GdPO_4$ dalelės tapo stabilesnės biologiniame pH ruože (pH 6,6 – 7,4). Tai, kad nanodalelės sėkmingai „apsivilko“ polimeru patvirtina ir pasikeitusios $GdPO_4$ dalelių izoelektrinių taškų pH vertės (4 pav. a-c).

Labiausiai pagerėjo modifikuotų $GdPO_4$ nanolazdelių stabilumas. Palyginimui, nemodifikuotos $GdPO_4$ nanolazdelės (IET 6,53) pH ruože nuo 4,2 iki 9,1 yra linkusios formuoti aglomeratus (3 pav. b). Po $GdPO_4$ dalelių paviršiaus modifikacijos katijoniniu polielektrolitu, jos tampa stabilios gerokai platesniame ir tinkamesniame praktiniams pritaikymams pH intervale: nuo 2 iki 5,6, 7,2 ir 8,3 atitinkamai naudojant mažą, vidutinį ir didelį

krūvį turinčius polimerus. Kitų morfologijų nanodalelės taip pat rodo ženkliai geresnį kolodinį stabilumą (4 pav.).

Nepriklausomai nuo tiriamų dalelių morfologijos, geriausi rezultatai stebimi daleles modifikuojant didelį krūvį (65 mol%) turinčiais p(METAC-*stat*-PEO_{19}MEMA) polimerais, kurių sudėtyje yra didžiausias teigiamą krūvį turinčių grupių tankis. Šis polimeras yra tinkamiausias $GdPO_4$ dalelių stabilizacijai.

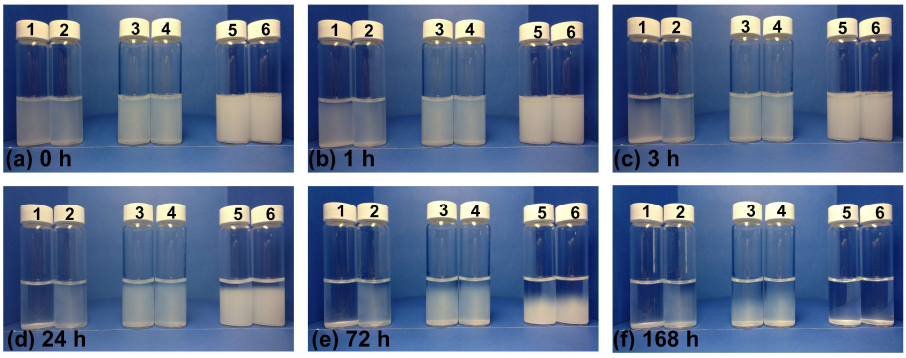

5 pav. Vizualus vandeninių (pH 6,5) $GdPO_4$ dalelių (nanolazdelės (**1** nemodifikuotos, **2** modifikuotos), heksagoninės nanoprizmės (**3** nemodifikuotos, **4** modifikuotos), submikrosferos (**5** nemodifikuotos, **6** modifikuotos)) koloidų stabilumo vertinimas laike: 0 val. (a), 1 val. (b), 3 val. (c), 24 val. (d), 72 val. (d) ir 168 val. (e).

Modifikuotų $GdPO_4$ dalelių stabilumą lemia elektrosterinė stabilizacija. Polimeras, esantis ant dalelių paviršiaus, sukuria ne tik sterinį barjerą, trukdantį dalelėms aglomeruotis, tačiau modifikuotos dalelės turi ir paviršiaus krūvį, atsirandantį dėl daugybės teigiamų funkcinių grupių, esančių polimero sudėtyje. Dėl šio krūvio atsiranda teigiamai dalelių stabilumą veikiantis elektrostatinis atostūmis tarp vienodą krūvį turinčių dalelių.

Tam, kad palyginti nemodifikuotų ir modifikuotų didelį krūvį turinčiu p(METAC-*stat*-PEO_{19}MEMA) polielektrolitu $GdPO_4$ dalelių stabilumą, buvo atliktas vizualus stebėjimo eksperimentas. Tuo tikslu buvo paruošti visų morfologijų $GdPO_4$ dalelių vandeniniai koloidai (1 mg/ml) ir buvo stebimas jų stabilumas laike. Visų dalelių vandeninių koloidų pH vertė buvo 6,5. Esant šiai pH vertei, nemodifikuotų $GdPO_4$ nanolazdelių zeta potencialo vertė buvo +0,56 mV, nemodifikuotų heksagoninių nanoprizmių -9,0 mV, o nemodifkuotų submikrosferų -18,6 mV. Tuo tarpu visų morfologijų modifikuotų $GdPO_4$ dalelių zeta potencialų vertės buvo apie +22 mV. Po 168 valandų nuo eksperimento pradžios nemodifikuotos $GdPO_4$ nanolazdelės

(5 pav. f1) buvo visiškai išsėdusios, o modifikuotos $GdPO_4$ nanolazdelės – neženkliai pasėdę (5 pav. f2). Modifikuotų $GdPO_4$ hesagoninių nanoprizmių atveju (5 pav. f4) taip pat buvo stebima mažesnė sedimentacija, lyginant su nemodifikuotomis prizmėmis (5 pav. f3).

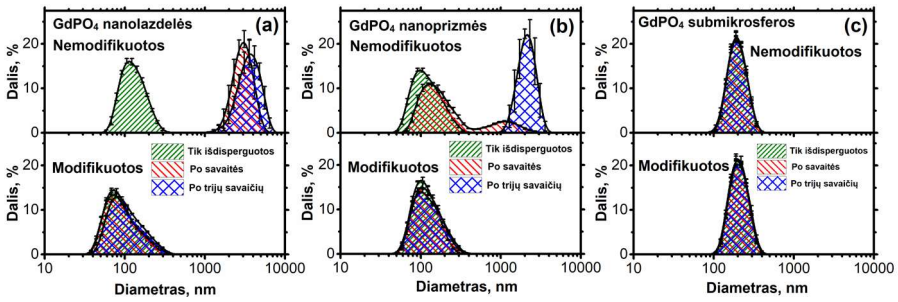

6 pav. $GdPO_4$ dalelių (nanolazdelių (**a**), heksagoninių nanoprizmių (**b**) ir submikrosferų (**c**)) dydžio pasiskirstymo kreivės (vandeniniai koloidai, pH 6,5). Matavimai atlikti tik išdispergavus daleles, po savaitės ir po trijų savaičių.

Remiantis vien tik vizualiais stebėjimais vertinti dalelių agomeraciją nėra visiškai tikslu. Norint tiksliai įvertinti dalelių aglomeraciją ir jos mastą, buvo atlikti papildomi dinaminės šviesos sklaidos matavimai bei įvertintas dalelių dydžių pasiskirstymas (6 pav. a-c). Atlikus 6 pav. pateiktus DLS matavimus, $GdPO_4$ dalelių (modifikuotų ir nemodifikuotų) koloidiniai tirpalai buvo 30 sekundžių purtomi, bet redispergavimui ultragarsas naudojamas nebuvo.

Iš 6 pav. pateiktų dalelių dydžių pasiskirstymo kreivių matyti, kad po 168 valandų (po vienos savaitės) nemodifikuotos $GdPO_4$ nanolazdelės jau buvo „sulipę“ (6 pav. a) į maždaug 2700 nm dydžio aglomeratus. Po 504 valandų (trijų savaičių) atlikti DLS matavimai leidžia teigti, jog vyksta tolimesnė nanolazdelių aglomeracija (aglomeratų dydis pasiekė maždaug 3600 nm). Panašių rezultatų buvo galima tikėtis, kadangi pH vertei esant 6,5 nanolazdelių zeta potencialas ($\zeta = +0.56$ mV) yra labai arti izoelektrinio taško. Analogiškai, tiriant p(METAC-*stat*-PEO_{19}MEMA) polimeru modifikuotas nanolazdeles jokių aglomeracijos ženklų nebuvo pastebėta nei po 168 valandų, nei po 504 valandų (dydis išliko apie 70 nm).

Lyginant su nanolazdelėmis, pH vertei esant 6,5, heksagoninės $GdPO_4$ nanoprizmės turi šiek tiek didesnį paviršiaus krūvį ($\zeta = -9.0$ mV). Nors heksagoninių nanoprizmių paviršiaus krūvis ir nėra didelis, tačiau jo užtenka pristabdyti šios morfologijos dalelių aglomeraciją. Nuo eksperimento pradžios praėjus 168 valandoms (vienai savaitei), matomi pirmieji heksagoninių $GdPO_4$ nanoprizmių aglomeracijos ženklai (6 pav. b). Nors iš

dalelių dydžių pasiskirstymo kreivės matyti, kad dominuoja maždaug 105 nm dydžio dalelės, tačiau yra stebima papildoma išplatėjusi smailė, rodanti maždaug 1100 nm dydžio aglomeratus. Nuo eksperimento pradžios praėjus 504 valandoms (3 savaitėms), nemodifikuotos heksagoninės nanoprizmės buvo susiaglomeravę (aglomeratų dydis apie 2300 nm). Heksagoninės nanoprizmės, modifikuotos p(METAC-*stat*-PEO_{19}MEMA) polimeru, nerodė jokių aglomeracijos ženklų net ir praėjus 504 valandoms nuo eksperimento pradžios (6 pav. b).

Nors po 504 valandų tiek modifikuotos, tiek nemodifikuotos $GdPO_4$ submikrosferos buvo visiškai nusėdusios, tačiau DLS matavimai parodė, kad nevyko jokia šių dalelių agregacija. Tai galima paaiškinti tuo, kad tiek modifikuotos, tiek nemodifikuotos $GdPO_4$ submikrosferos, pH vertei esant 6,5, turi pakankamai dideles zeta potencialo vertes, atitinkamai +22.7 mV modifikuotoms ir -18.6 mV nemodifikuotoms. Kadangi submikrosferos (lyginant su nanolazdelėmis ir nanoprizmėmis) yra pakankamai didelės, jų sedimentacija vyko dėl jų svorio.

3.2.3 $GdPO_4$ dalelių, modifikuotų katijoniniais p(METAC-*stat*-PEO_{19}MEMA) šepetiniais polimerais, koloidinio stabilumo biologinėje terpėje įvertinimas

Dažnai nanodalelės, kurios rodo gerą koloidinį stabilumą vandenyje, vis tik yra nestabilios biologinėje terpėje. Tai gali nulemti įvairūs faktoriai, tokie kaip joninė jėga, makromolekulių „atsikabinimas“ nuo dalelės paviršiaus, baltymų adsorbcija ant dalelės paviršiaus (baltymų karūnos formavimasis).

Tam, kad įvertinti potencialų p(METAC-*stat*-PEO_{19}MEMA) polimeru modifikuotų $GdPO_4$ dalelių stabilumą biologinėje terpėje, buvo atliktas papildomas eksperimentas. Šio eksperimento metu tiek modifikuotos, tiek nemodifikuotos $GdPO_4$ dalelės buvo redisperguotos (iš sauso būvio) 10 % v/v žmogaus kraujo plazmos vandeniniame tirpale (pH 6,5). Eksperimento metu buvo pastebėta, kad nemodifikuotos $GdPO_4$ dalelės (nepriklausomai nuo dalelių morfologijos) yra linkę sedimentuoti gerokai sparčiau, negu modifikuotos $GdPO_4$ dalelės (7 pav.). Visų morfologijų nemodifikuotos $GdPO_4$ dalelės po trijų valandų nuo eksperimento pradžios buvo visiškai išsėdusios, o modifikuotos $GdPO_4$ dalelės nerodė jokių sedimentacijos ženklų.

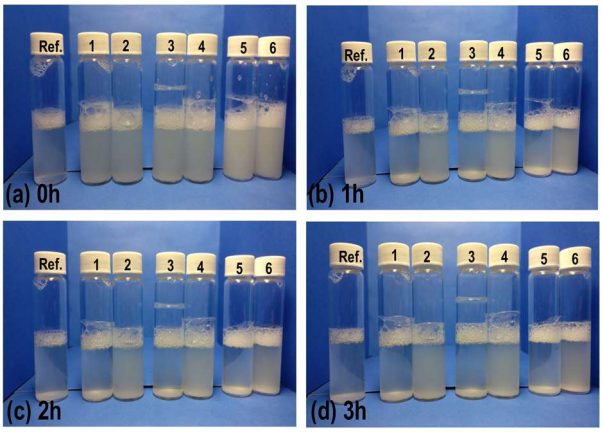

7 pav. Vizualus (pH 6,5) $GdPO_4$ dalelių (nanolazdelės (1 nemodifikuotos, 2 modifikuotos), heksagoninės nanoprizmės (3 nemodifikuotos, 4 modifikuotos), submikrosferos (5 nemodifikuotos, 6 modifikuotos)) koloidų stabilumo vertinimas biologinėje terpėje: 0 val. (a), 1 val. (b), 2 val. (c), 3 val.

Tiek modifikuotos, tiek nemodifikuotos $GdPO_4$ dalelės, išlaikytos 10 % v/v žmogaus kraujo plazmos vandeniniame tirpale (pH 6,5) buvo centrifuguotos (10000 apsisukimų per minutę, 15 minučių) ir praplautos dejonizuotu vandeniu. Plovimo procedūra kartota tris kartus tam, kad pašalinti perteklinius baltymus, neprisikabinusius prie plaunamų dalelių paviršiaus. Tokiu būdu praplautos $GdPO_4$ dalelės buvo vėl redisperguotos vandenyje (pH 6,5) ir atlikti koloidų DLS matavimai, siekiant įvertinti baltymų adsorbciją ant dalelių paviršiaus. Dalelių dydžio pasiskirstymo kreivės pateiktos 8 pav. Remiantis dalelių dydžio pasiskirstymo kreivių duomenimis, galima teigti, kad, nepriklausomai nuo morfologijos, modifikuotos $GdPO_4$ dalelės yra mažiau linkusios adsorbuoti baltymų molekules savo paviršiuje, lyginant su nemodifikuotomis $GdPO_4$ dalelėmis.

Taip pat buvo papildomai įvertintos šių praplautų bei redisperguotų $GdPO_4$ dalelių zeta potencialų vertės (9 pav.). Nemodifikuotų dalelių zeta potencialų vertės pasikeitė beveik dvigubai daugiau, lyginant su modifikuotomis dalelėmis. $GdPO_4$ dalelių zeta potencialų pokyčius galima sieti su baltymų adsorbcija ant dalelių paviršiaus. Visi atlikti eksperimentai leidžia teigti, jog PEO grandinės formuoja ne tik sterinį barjerą apsaugantį daleles nuo aglomeracijos, tačiau ir suteikia dalelių paviršiui baltymus atstumiančių savybių.

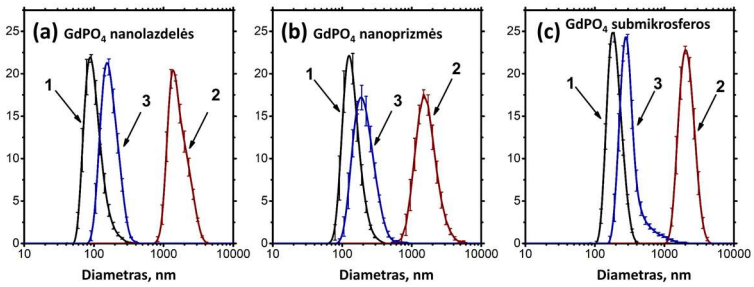

8 pav. $GdPO_4$ dalelių (nanolazdelių **a**, heksagoninių nanoprizmių **b** ir submikrosferų **c**) dydžių pasiskirstymo kreivės po inkubacijos biologinėje terpėje (10 % v/v žmogaus kraujo plazmos vandeniniame tirpale, pH 6,5). **1** – $GdPO_4$ dalelių dydžių pasiskirstymo kreivė daleles tiesiog redisperguojant vandeninėje terpėje. **2** - nemodifikuotų $GdPO_4$ dalelių dydžių pasiskirstymo kreivė po inkubacijos biologinėje terpėje. **3** - modifikuotų $GdPO_4$ dalelių dydžių pasiskirstymo kreivė po inkubacijos biologinėje terpėje.

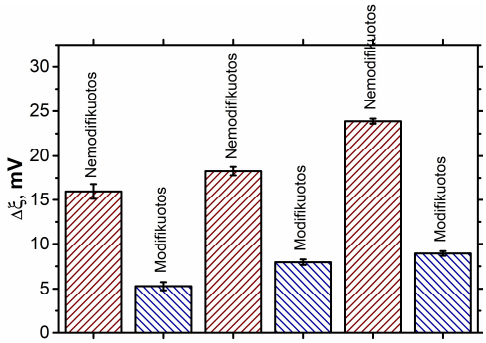

9 pav. Modifikuotų ir nemodifikuotų $GdPO_4$ dalelių, redisperguotų biologinėje terpėje zeta-potencialo pokytis (lyginama su dalelių, redisperguotų vandeninėje terpėje (pH 6,5), zeta potencialu).

3.3 Ypač lengvas magnetinis $GdPO_4$ aerogelis

Ypač lengvas ir magnetinėmis savybėmis pasižymintis $GdPO_4$ aerogelis buvo gautas panaudojant $GdPO_4$ nanopluoštą, susintetintą hidroterminės sintezės būdu. Iš susintetinto nanopluošto paruoštas hidrogelis buvo liofilizuojamas, o gautas aerogelis toliau kaitinamas 915 °C temperatūroje (10 pav.).

10 pav. $GdPO_4$ dalelių aerogelio paruošimo schema.

Trigoninė rabdofano fazė yra metastabili ir aukštose temperatūrose (maždaug nuo 550 °C) persitvarko į monoklininę monazito fazę. Monazito fazė yra patrauklesnė praktiniam pritaikymui, nes į jos struktūrą neįeina kristalizacinis vanduo. Yra žinoma, kad trigoninės rabdofano fazės lantanoidų ortofosfatai gali turėti net iki 8-10 procentų kristalizacinio vandens. Kristalizacinio vandens molekulės išsidėsto struktūriniuose rabdofano fazės kanaluose, einančiuose išilgai *c* ašies (apvesta punktyrine linija 11 pav. a). Kristalizacinis vanduo gali neigiamai veikti medžiagos liuminescencines savybes. Dėl šių priežasčių monoklininės fazės $GdPO_4$ aerogelis yra labiau tinkamas legiravimui optiškai aktyviais jonais.

Atlikta Rentgeno spidulių difrakcinė analizė parodė (11 pav.), kad nekaitintas $GdPO_4$ aerogelis yra trigoninės rabdofano kristalinės fazės ($GdPO_4 \cdot nH_2O$, PDF ICDD 00-039-0232). Atitinkamai, iškaitintas (915 °C, 12 valandų) $GdPO_4$ aerogelis turi monoklininę monazito struktūrą ($GdPO_4$, PDF ICDD-00-032-0386).

Nekaitinto $GdPO_4$ aerogelio tankis yra maždaug 10 mg/cm^3, o paviršiaus plotas (nustatytas BET metodu) – apie 29 m^2/g. Iškaitinto $GdPO_4$ aerogelio tankis yra maždaug 8 mg/cm^3, o jo paviršiaus plotas – apie 35 m^2/g. Iškaitinto aerogelio tankio sumžėjimą ir paviršiaus ploto padidėjimą galima priskirti kristalizacinio vandens netekčiai vykstant virsmui iš rabdofano fazės į monazito fazę kaitinant. Kaitinant aerogelį, jo tūris praktiškai nekinta, tačiau dėl vandens netekties sumažėja masė, todėl padidėja paviršiaus plotas.

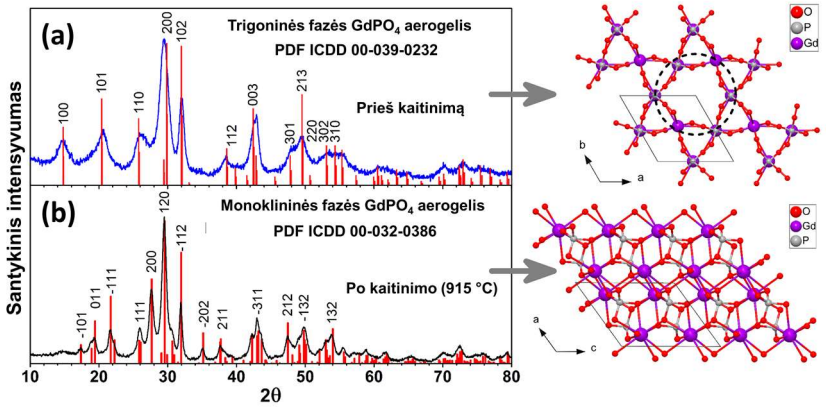

11 pav. Nekaitinto (a) ir iškaitinto (b) $GdPO_4$ aerogelių Rentgeno spindulių difraktogramos ir kristalinių struktūrų vizualizacija.

Iš SEM ir TEM mikrografų, pateiktų 12 pav., matyti, kad tiek nekaitintas rabdofano fazės, tiek iškaitintas monoklininės fazės aerogelis yra sudarytas iš chaotiškai orientuotų $GdPO_4$ nanogijų. Gijų storis svyruoja nuo 5 iki 15 nm, o ilgis nuo kelių šimtų nanometrų iki kelių mikrometrų. Skenuojančiu elektronų mikroskopu užfiksuotose mikrografose (12 pav. a ir b) abiejų aerogelių morfologija yra labai panaši, tačiau iš TEM mikrografų (12 pav. c ir d) matyti, kad neiškaitintame aerogelyje dauguma nanogijų yra individualios ir nesusiaglomeravę, o iškaitintame aerogelyje nanogijos yra pastebimai sulipę lygiagrečiai viena kitai.

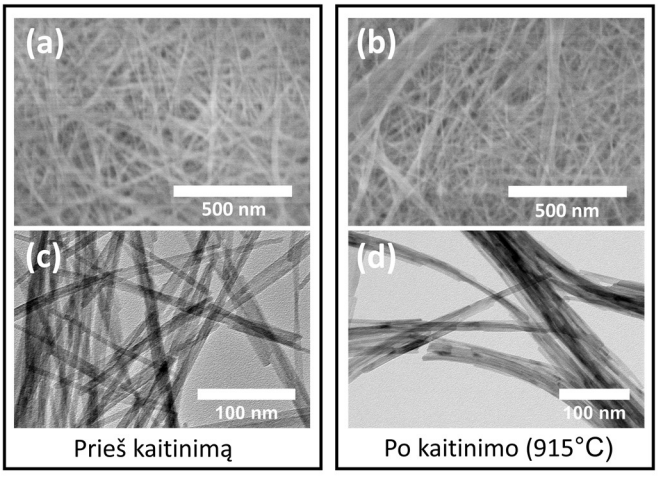

12 pav. $GdPO_4$ aerogelio SEM (a, b) ir TEM (c, d) mikrografos.

Darbe buvo nustatyta, kad $GdPO_4$ aerogelis pasižymi magnetinėmis savybėmis. Šios savybės buvo tiriamos matuojant bandinių įmagnetėjimo (M) priklausomybę nuo magnetinio lauko (H), esant 80 ir 300 K temperatūroms (13 pav.). Tiek kambario, tiek ir skysto azoto temperatūroje išmatuotos įmagnetėjimo kreivės buvo netiesinės (S formos) ir nepasižymėjo histereze, kuri yra būdinga daugeliui feromagnetikų. Eksperimentinės $M(H)$ priklausomybės buvo aprašytos naudojant Lanževeno funkciją (13 pav.), kuri yra dažnai naudojama paramagnetikų ir superparamagnetikų magnetinėms savybėms paaiškinti. Šiame darbe gautas geras eksperimentinių ir teorinių duomenų sutapimas leidžia teigti, jog $GdPO_4$ aerogelis gali būti apibūdinamas kaip silpnai tarpusavyje sąveikaujančių superparamagnetinių nanogijų sistema. Šias savybes lemia nesuporuoti Gd^{3+} jonų elektronai. Tikėtina, kad magnetinėms $GdPO_4$ aerogelio savybėms svarbią įtaką taip pat gali turėti paviršiaus efektai (pvz., paviršiaus magnetizmas), nanogijų formos anizotropija.

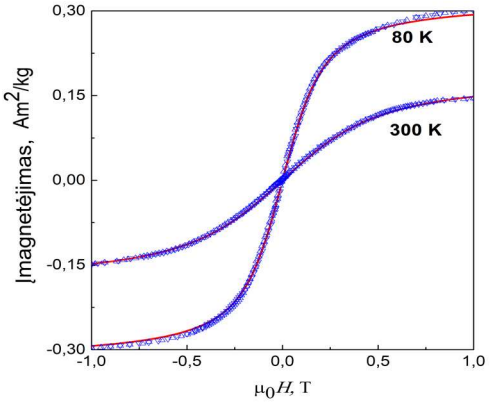

13 pav. $GdPO_4$ dalelių įmagnetėjimas magnetiniame lauke. Raudonos kreivės - eksperimentinių duomenų aprašymas Lanževeno funkcija.

4. Išvados

- Hidroterminės sintezės metodu buvo susintetintos įvairių morfologijų $GdPO_4$ dalelės. Nustatyta, kad keičiant $NH_4H_2PO_4/Gd^{3+}$ molinius santykius galima efektyviai kontroliuoti gaunamų dalelių morfologiją. $NH_4H_2PO_4/Gd^{3+}$ moliniam santykiui esant 10, 50, 100 gaunamos atitinkamai nanolazdelių, heksagoninių nanoprizmių ir submikrosferų morfologijos dalelės.
- Skirtingų morfologijų $GdPO_4$ dalelės turi skirtingas zeta potencialų vertes, todėl, keičiant morfologiją, įmanoma reguliuoti dalelių stabilumą įvairiose terpėse (plačiame pH intervale).
- Skirtingos morfologijos $GdPO_4$ daleles (nanolazdelės, hesagoninės nanoprizmės ir submikrosferos) modifikavus p(METAC-*stat*-PEO_{19}MEMA) polimerais, pagerėjo jų vandeninių koloidų stabilumas. Nepriklausomai nuo dalelių morfologijos, geriausiai vandenines dispersijas stabilizavo polimerai, turintys didžiausią katijoninių grupių (65 mol%) tankį. Šiais polimerais modifikuotos dalelės, redisperguotos iš sauso būvio, išlieka stabilios dispersijose iki 3 savaičių be jokių aglomeracijos požymių.
- Ištyrus p(METAC-*stat*-PEO_{19}MEMA) polimerais modifikuotų skirtingos morfologijos $GdPO_4$ dalelių stabilumą biologinėje terpėje (10 % v/v žmogaus kraujo plazmos vandeninis tirpalas (pH 6,5), pastebėta, kad šie polimerai, esantys nanodalelių paviršiuje net tik pagerina dispersijų stabilumą, bet ir pasižymi baltymus atstumiančiomis savybėmis. Baltymų sorbcija modifikuotų dalelių paviršiuje yra bent du kartus mažesnė lyginant su nemodifikuotomis dalelėmis.
- Liofilizuojant $GdPO_4$ nanogijų hidrogelį, buvo gautas didelio paviršiaus ploto rabdofano kristalinės fazės aerogelis, kurį kaitinant 915 °C temperatūroje galima gauti monazito kristalinės fazės $GdPO_4$ aerogelį, nesuardant trimatės nanopluošto struktūros. Ištyrus monazito kristalinės fazės aerogelių magnetines savybes, nustatyta, kad šios medžiagos pasižymi superparamagnetinėmis savybėmis.

Summary

Detailed study on $GdPO_4$ nanoparticles, their synthesis (i), surface modification with polymers and stability study (ii), development of nanofibrous $GdPO_4$ aerogel (iii) is presented in this thesis.

The first part of the study is focused on hydrothermal synthesis of $GdPO_4$ nanostructures. The main object of this part was to determine influence of synthesis parameters (PO_4^{3-}/Gd^{3+} molar ratio, Gd^{3+} absolute concentration, pH and duration of synthesis) upon $GdPO_4$ particle formation and in order to enable selective synthesis of monodisperse $GdPO_4$ particles with high quality. It turns out that by tuning PO_4^{3-}/Gd^{3+} molar ratio (in the range from 1 to 100) it is possible to effectively control $GdPO_4$ particle formation and, thus, their morphology. In total, several different morphologies were obtained: nanofiber, nanorods, hexagonal nanoprisms, submicrospheres. The obtained particles were investigated by means of XRD, FTIR, DT/TGA, SEM and TEM.

Stability study of bare (as-prepared) $GdPO_4$ particles indicated that particles of different morphology have different stability ranges. Therefore, by altering particle morphology, it is possible to achieve colloidal stability in relatively wide pH range. On the contrary, $GdPO_4$ particles, which were redispersed from dry state, exhibited poor colloidal stability, especially in biological range (ca. pH 6.6 -7.4). Therefore, additional stabilization was required. In order to enhance particle stability and applicability, obtained $GdPO_4$ nano and submicro particles were modified with purposely synthesized cationic p(METAC-*stat*-PEO_{19}MEMA) brush polymers with different compositions. The best results were observed when particles were modified with p(METAC-*stat*-PEO_{19}MEMA) polymer with the highest density of positively charged groups (65 mol%). Furthermore, $GdPO_4$ particle stability in biological media (protein rich aqueous solution consisting 10 vol.% of human blood plasma, pH 6.5) was evaluated. Stability study revealed that p(METAC-*stat*-PEO_{19}MEMA) modified $GdPO_4$ particles show superior stability in aqueous colloids (particles showed no agglomeration signs even 3 weeks after being redispersed from the dry state) and also had enhanced stability in protein rich biological media. Both bare and modified $GdPO_4$ particle stabilities were evaluated by performing DLS measurements and measuring zeta potential values.

Hydrothermally synthesized $GdPO_4$ nanofibers further were used for development of novel nanofibrous $GdPO_4$ aerogel. Firstly, $GdPO_4$ fibers were

used for hydrogel preparation, which during liophilization process turned into three dimensional nanofibrous $GdPO_4$ aerogel of trigonal rhabdophane phase. Further annealing of such aerogel, under temperature of 915 °C, induced phase transformation from trigonal rhabdophane phase to monoclinic monazite phase, which was more preferable due to lower crystalline water content. The monazite phase $GdPO_4$ aerogel displayed superparamagnetic properties, had large surface area (ca. 35 m^2/g) and was ultralight (ca. 8 mg/cm^3). Such $GdPO_4$ aerogel was not reported in literature before and represents a new class of lanthanide-based materials.

All research in this thesis confirm that $GdPO_4$ is a very interesting and diverse material, which can be hydrothermally synthesized in numerous morphologies.

List of publications and conference participation

Publications included in the thesis

1. **M. Janulevicius**, V. Klimkevicius, L. Mikoliunaite, B. Vengalis, R. Vargalis, S. Sakirzanovas, V. Plausinaitiene, A. Zilinskas, A. Katelnikovas. „Ultralight Magnetic Nanofibrous $GdPO_4$ Aerogel“. *ACS Omega* **5** (2020) 14180-14185.
2. V. Klimkevicius‡, **M. Janulevicius**‡, A. Babiceva, A. Drabavicius, A. Katelnikovas, Effect of Cationic Brush-Type Copolymers on Colloidal Stability of $GdPO_4$ Particles with Different Morphology in Biological Aqueous Media“. *Langmuir* **36** (2020) 7533-7544.
3. **M. Janulevicius**, V. Klimkevicius, A. Vanetsev, V. Plausinaitiene, S. Sakirzanovas, A. Katelnikovas. „Controlled Hydrothermal Synthesis, Morphological Design and Colloidal Stability of $GdPO_4 \cdot nH_2O$ Particles“. *Materials Today Communications* **23** (2020) 100934.

‡ Authors contributed equally.

Attended conferences on the subject of the thesis

1. V. Klimkevičius, A. Babičeva, **M. Janulevičius**, R. Makuška, A. Katelnikovas, „Surface Modification of Various Morphology $GdPO_4$ Particles using Cationic Brush Polymers“, *Chemistry and Chemical Technology 2019*, Vilnius, Lithuania, May 16 (2019).
2. **M. Janulevicius**, Hydrothermal synthesis route to mixed-metal oxides, *OXYGENALIA*, Vilnius, Lithuania, October 11 (2018).
3. **M. Janulevičius**, Y. Orlovskii, A. Katelnikovas. Synthesis via Hydrothermal Route, Morphology Control and Luminescent Properties of Rare-earth doped $GdPO_4$ Particles. *19th World Congress on Materials Science and Engineering,* Barcelona, Spain, June 11-33 (2018).

4. **M. Janulevicius**, A. Katelnikovas. *Hydrothermal Synthesis and Morphology Control of $GdPO_4$ particles assisted by Tartaric Acid* Stendinis pranešimas tarptautinėje konferencijoje *NATO/NANOAPP 2017*, Bled, Slovenia.

Publications not included in the thesis

1. J. Grigorjevaite, **M. Janulevicius**, A. Kruopyte, E. Ezerskyte, R. Vargalis, S. Sakirzanovas, A. Katelnikovas. Synthesis and optical properties of efficient orange emitting $GdB_5O_9:Sm^{3+}$ phosphors. *Journal of Sol-Gel Science and Technology* **94** (2020) 80-87.
2. I. Mackevic, J. Grigorjevaite, **M. Janulevicius**, A. Linkeviciute, S. Sakirzanovas, A. Katelnikovas. Synthesis and optical properties of highly efficient red-emitting $K_2LaNb_5O_{15}:Eu^{3+}$ phosphors. *Optical Materials* **89** (2019) 25-33.
3. **M. Janulevicius**, P. Marmokas, M. Misevicius, J. Grigorjevaite, L. Mikoliunaite, S. Sakirzanovas, A. Katelnikovas. Luminescence and Luminescence Quenching of Highly Efficient $Y_2Mo_4O_{15}:Eu^{3+}$ Phosphors and Ceramics. *Scientific Reports* **6** (2016) 26098.
4. **M. Janulevicius**, J. Grigorjevaite, G. Merkininkaite, S. Sakirzanovas, A. Katelnikovas. Luminescence and Luminescence Quenching of $Eu_2Mo_4O_{15}$. *Journal of Luminescence* **179** (2016) 35-39.
5. S. Visniakova, I. Urbanaviciute, L. Dauksaite, **M. Janulevicius**, B. Lenkeviciute, I. Sychugov, K. Arlauskas, A. Zilinskas. Luminescent benzo- and naphthoquinolines: Synthesis and investigation of photophysical properties. *Journal of Luminescence.* **167** (2015) 261-267.

Acknowledgements

Firstly, I want to thank my supervisor Prof. Artūras Katelnikovas for realiable guidance throughout my journey up to this point. I am very grateful to him for all his efforts, patience and help in my development as a scientist and professional in my field of activity.

Also, I would like to thank Dr. Vaidas Klimkevičius for all his invaluable help, insights, advice and good company while preparing this thesis. I think he could be referred to as my unofficial scientific consultant during the Doctoral studies.

I am very grateful to Prof. Aivaras Kareiva and Prof. Albinas Žilinskas. They never refused to advice and help me whenever I needed.

I want to thank Prof. Simas Šakirzanovas for his help and providing me access to necessary equipment that I needed to conduct my research and carry out experiments during the preparation of this thesis. Throughout these years, I always felt welcome in his laboratory, and, in case of any technical or scientific obstacles, was always provided with a viable solution.

I find it necessary to thank my colleagues and friends, and namely Assist. Prof. Ramūnas Skaudžius, Dr. Aleksandra Prichodko, Dr. Živilė Stankevičiūtė, Dr. Lina Mikoliūnaitė, Dr. Giedrė Nenartavičienė, Dr. Jolanta Raudonienė, Dr. Sigita Višniakova, Rokas Vargalis, Greta Merkininkaitė, Mantas Jonušis. Thanks to these people, I could always in university as in my second home. I will forget neither of you!

I want to thank my friends Antanas, Simonas and Martynas. Their contribution to this thesis is greater than they realise. Thank you guys!

Lastly and most importantly, I would like to thank my family for their unconditional support and caring through all the years that I have spent studying. Thank you!

Curriculum Vitae

Personal information	
Name, Surname	Matas Janulevičius
Date and place of birth	1990/07/29, Vilnius, Lithuania
E-mail address	mata.janu@gmail.com
Education	
2013 – 2015	Master of Science in Nanomaterial Chemistry Vilnius University
2009 – 2013	Bachelor of Science in Chemistry Vilnius University
Scientific mobility and iternships	
MAR 2019 – SEP 2019	Tartu University (Tartu, Estonia), visiting scientist in the Spectroscopy group of the Institute of Physics.
SEP 2018	Scientific visit (2019/09/03 - 2019/09/07), Department of Supramolecular Chemistry and Catalysis, Artois Univeristy, France.
APR 2018 – MAY 2018	Tartu University (Tartu, Estonia), visiting scientist in the Spectroscopy group of the Institute of Physics.
MAR 2017 – JUN 2017	Hasselt University (Hasselt, Belgium), visiting scientist in the Inorganic and Physical Chemistry Group.
Work experience	
SEP 2019 – SEP 2020	Junior assistant, Faculty of Chemistry and Geosciences, Vilnius University.
SEP 2019 – DEC 2019	Junior researcher, Faculty of Chemistry and Geosciences, Vilnius University.
SEP 2017 – MAR 2019	Junior researcher, Faculty of Chemistry and Geosciences, Vilnius University.

1

Controlled Hydrothermal Synthesis, Morphological Design and Colloidal Stability of $GdPO_4 \cdot nH_2O$ Particles

Matas Janulevičius, Vaidas Klimkevičius, Alexander Vanetsev, Valentina Plaušinaitienė, Simas Šakirzanovas, Artūras Katelnikovas

Materials Today Communications 23 (2020) 100934

Contents lists available at ScienceDirect

Materials Today Communications

journal homepage: www.elsevier.com/locate/mtcomm

Controlled hydrothermal synthesis, morphological design and colloidal stability of $GdPO_4{\cdot}nH_2O$ particles

Matas Janulevicius[a], Vaidas Klimkevicius[a], Alexander Vanetsev[b,c], Valentina Plausinaitiene[a], Simas Sakirzanovas[a], Arturas Katelnikovas[a,*]

[a] Institute of Chemistry, Vilnius University, Naugarduko 24, LT-03225, Vilnius, Lithuania
[b] Institute of Physics, University of Tartu, 1 W. Ostwald str., Tartu, Estonia
[c] A.M. Prokhorov General Physics Institute RAS, 38 Vavilov str., Moscow, Russia

ARTICLE INFO

Keywords:
Hydrothermal synthesis
Gadolinium orthophosphate
Nanorods
Hexagonal nanoprisms
Nanospheres
Zeta-potential

ABSTRACT

A number of different morphologies of rhabdophane-type $GdPO_4{\cdot}nH_2O$ particles were synthesized via hydrothermal route with presence of tartaric acid as a coordinating/capping agent. Nanorods, hexagonal nanoprisms and nanospheres of different sizes were obtained. An impact of PO_4^{3-}/Gd^{3+} molar ratio, Gd^{3+} absolute concentration, pH and duration of synthesis on the phase composition, particle morphology and colloidal stability in water was investigated. These synthesis parameters greatly influenced the particle size and morphology. It turned out that the best way to control the particle shape and size is to change the PO_4^{3-}/Gd^{3+} ratio in the reaction mixture. The measured zeta potential values showed that the stability range of $GdPO_4{\cdot}nH_2O$ nanoparticles in aqueous solutions are influenced by the shape of particles; therefore, the appropriate $GdPO_4{\cdot}nH_2O$ nanoparticles could be synthesized for the desired applications.

1. Introduction

Development of various nano- and micro- sized particles and structures has attracted lots of scientists' attention recently. It is well known that rare-earth doped inorganic materials possess unique luminescent and magnetic properties. Among many inorganic host matrices that can be doped with rare earth (RE) ions, orthophosphates are widely studied as a promising media for RE ions because of their thermal and chemical stability, low toxicity, and appropriate optical properties [1–3].

Rare-earth doped nano– and submicro– sized orthophosphate particles are promising materials for multiple purposes and have a wide field of applications including, but not limited to, phosphors, electronics, photon up-conversion materials, catalysis, counterfeiting pigments, composite films and so on [2,4,5]. Another important field for $LnPO_4$ (here Ln is any lanthanide ion) particles application is biolabeling, drug-delivery and/or bio-imaging probes as they possess necessary properties for bio-application field, such as low toxicity and luminescence stability [6,7].

Not only the particle size but morphology as well is an important aspect of this research area, responsible for unique luminescent and physical properties (density, specific surface area, solubility, reactivity) of synthesized particles [8,9]. Synthesis of various $LnPO_4$ particles has been studied extensively lately and various morphologies such as nanorods, nanowires, nanofibers, nanocubes, hexagonal nanoprisms, microspheres, submicrostars were reported [1,4,10–12]. Yet, effectiveness in synthesis of $LnPO_4$ particles with the aim to obtain desired morphology, narrow particle size distribution, good dispersability in various solvents is still to be improved [13]. Various synthesis routes and methods (combustion [14], solid state [15], sol-gel [16], ultrasound [17], co-precipitation [18], solvothermal synthesis [1], hydrothermal microwave treatment [19]) have been developed and applied to obtain rare-earth orthophosphates. Hydrothermal route was employed to obtain rare-earth phosphate particles, as this route is relatively simple and easy to perform, does not require harsh synthesis conditions, high temperatures and hazardous precursors.

In many cases the morphology, formation and dispersability of various nano– and micro– sized particles ($LnPO_4$, $NaLnF_4$, LnF_3, etc.) are assisted by employing organic surfactants (i.e., oleic acid, triton and so on), which coat particle surface. However, application of these surfactants has some drawbacks, such as decreased solubility in water (in case of oleic acid presence on the particle surface, this particle can be dispersed only in non-polar solvents, etc.), reduced accessibility of particles surface as surfactants remain attached on it [20–22]. In this

* Corresponding author.
E-mail address: arturas.katelnikovas@chf.vu.lt (A. Katelnikovas).

https://doi.org/10.1016/j.mtcomm.2020.100934
Received 14 November 2019; Received in revised form 14 January 2020; Accepted 14 January 2020
Available online 24 January 2020

case particle surface is blocked from further modifications in order to develop multifunctional nanoparticles. Another drawback is decreased efficiency of luminescence, as organic molecules may absorb both incoming and outgoing radiation. The use of small, water soluble organic acids as a coordinating agent is a good alternative in order to avoid these drawbacks as these molecules not only assist in controlling particle morphology, but also can be easily removed by washing particles with distilled water.

Herein, we report an alternative approach to obtain $GdPO_4{\cdot}nH_2O$ particles by changing only one parameter. We state that particles obtained via this route are easier and cheaper to obtain. We employed hydrothermal synthesis of $GdPO_4{\cdot}nH_2O$ particles assisted by tartaric acid as a coordinating agent. Several different morphologies such as nanofibers, nanorods, hexagonal nanoprisms, and submicrospheres were synthesized. The impact of synthesis conditions on particle phase and morphology was investigated and is discussed in this work. As far as we know, there are little to no information in scientific literature on impact of phosphorus source/Gd^{3+} ratio to $GdPO_4{\cdot}nH_2O$ particle formation via hydrothermal route. In addition, there are quite few reports on impact of coordinating agent (citric acid and EDTA mainly) as well.

2. Experimental

The starting materials were Gd_2O_3 (99.99%, Tailorlux), $NH_4H_2PO_4$ (99.9%, EuroChemicals), concentrated HNO_3 (EuroChemicals), concentrated ammonia (35%, EuroChemicals), tartaric acid (99.99%, EuroChemicals). $Gd(NO_3)_3$ was obtained by dissolving Gd_2O_3 in warm diluted nitric acid. The obtained transparent solution was then evaporated to dryness to remove excessive nitric acid. The dry residue was dissolved in appropriate amount of distilled water to obtain of 0.8 mol/L concentration stock solution of $Gd(NO_3)_3$. All chemicals were used as received without any further purification.

For this work we used different sets of experimental conditions. The synthesis can be divided into multiple stages. During the first stage, certain amount (0.5 mL (0.4 mmol) in typical experiment) of $Gd(NO_3)_3$ stock solution was diluted to 20 mL using distilled water. Subsequently, 1.200 g (8 mmol) of tartaric acid was weighted, dissolved in 20 mL of distilled water, and added dropwise to $Gd(NO_3)_3$ solution. The obtained solution was stirred at room temperature for 30 min. in order to Gd-tartaric acid complex to form solution A. During the second stage, pH value was set to 10 by adding ammonia solution. Afterwards, during the third stage, certain amount of $NH_4H_2PO_4$ (from 0.4 mmol to 0.04 mol, depending on synthesis) was dissolved in 20 mL of distilled water and added dropwise to solution A under vigorous stirring, while maintaining pH value around 10 and left stirring for 15 min. The necessary pH value was adjusted by using HNO_3 and ammonia solutions and then the volume of reaction mixture was adjusted to 80 mL by adding distilled water. During the fourth stage, the reaction mixture was poured into Teflon bottle autoclave, which was sealed and placed into a hydrothermal reactor. The hydrothermal reaction temperature in a typical experiment was maintained at 160 °C for 12 h. During the fifth stage, the reactor was cooled to room temperature, then obtained precipitate was centrifuged at 7500 rpm (centrifuge model Eppendorf 5804), and washed with distilled water. This procedure was repeated 4 times, then the precipitate was left to dry in air at 80 °C. All the syntheses were repeated at least three times in order to evaluate the reproducibility of the obtained results.

Hydrothermal synthesis of particles was performed using hydrothermal reactor *highpreactor* by BERGHOF and BTC-3000 Temperature Controller and Data Logger by BERGHOF.

Crystalline phase of the particles was identified by performing powder XRD measurements using following devices:

XRD measurements for Fig. 1 were carried out using parallel beam geometry on a Bruker D8 Advance da Vinci design diffractometer. The patterns were analyzed with the software Topas version 4.2 (Bruker AXS).

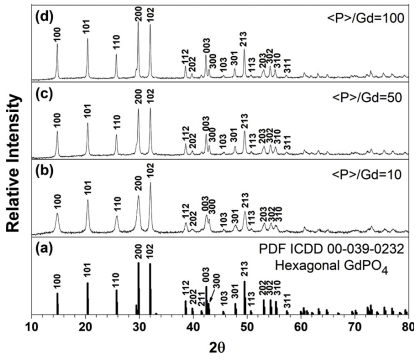

Fig. 1. XRD patterns of different $GdPO_4{\cdot}nH_2O$ samples (b, c, d) and a reference pattern of $GdPO_4{\cdot}H_2O$ (a).

Rigaku MiniFlexII working in Bragg-Brentano (θ/2θ) focusing geometry was used for remaining XRD measurements. The 2θ angle was scanned in the range of $10^\circ \le 2\theta \le 80^\circ$ (step width 0.02° and scanning speed 5 °/min.) using Ni-filtered Cu Kα radiation.

Le Bail method was used to calculate cell parameters.

The morphology and size of synthesized $GdPO_4{\cdot}nH_2O$ particles was investigated using scanning electron microscopy (SEM). SEM images were taken with high-resolution scanning electron microscope (FE SEM) Hitachi SU-70, with accelerating voltage up to 10 kV. Samples for SEM were prepared by dispersing particles in distilled water and adding 20 μL of aqueous dispersion on a Si plate.

Zeta-potential values of obtained particles in aqueous media were measured at 25 °C using Zetasizer Nano ZS by Malvern. The results were processed by applying Smoluchowski model.

TG-DTA measurements of the synthesized particles were performed using Perkin Elmer STA 6000 under air atmosphere. The heating rate was 10 °C/min. The weight of analyzed samples was ca. 5.5 mg.

FTIR measurements of rare-earth orthophosphate particles were performed in the range from 520 to 3800 cm^{-1} with resolution of 4 cm^{-1} using Perkin Elmer FT-IR Spectrometer Frontier.

3. Results

The main goal of this work was to study the influence of an array of synthetic conditions on phase composition, morphology and colloidal stability of $GdPO_4{\cdot}nH_2O$ particles obtained in hydrothermal solution. Among the conducted experiments four major series could be marked out varying: 1) PO_4^{3-}/Gd^{3+} molar ratio (for the sake of simplicity further referred to as < P > /Gd ratio), 2) Gd^{3+} absolute concentration, 3) pH, and 4) duration of synthesis.

3.1. Phase composition and thermal behavior

Phase composition and purity of synthesized gadolinium phosphate particles was investigated by means of XRD. As expected, the selected range of synthetic conditions does not affect the phase composition of final materials. All synthesized samples consist of pure rhabdophane-type phase with composition $GdPO_4{\cdot}nH_2O$. PDF ICDD 00-039-0232 card states that structure possess $P3_121$ space group. This structure is described as hexagonal in the ICCD database ($P6_222$, a = 6.9055 Å c = 6.3257 Å), but recent precise synchrotron experiments established that probably this is a monoclinic structure [23]. In our study we describe it as a hexagonal structure, due to lack of information such as atomic positions for the monoclinic structure. However, in order to

Table 1
Crystallite sizes and unit cell parameters of different $GdPO_4{\cdot}nH_2O$ samples. Reference unit cell parameters were taken from PDF ICDD 00-039-0232 card.

< P > /Gd ratio	Crystalite size (nm)	Cell parameter *a* (Å)	Cell parameter *c* (Å)
Reference	–	6.905	6.326
10	20 (± 3)	6.904 (± 0.001)	6.311 (± 0.001)
50	29 (± 1)	6.918 (± 0.001)	6.315 (± 0.001)
100	38 (± 2)	6.926 (± 0.001)	6.320 (± 0.001)

avoid confusion, it is necessary to notice, that several recent works refer to $GdPO_4{\cdot}nH_2O$ phase as monoclinic.

Despite the fact, that the phase is the same regardless the conditions of synthesis, the lattice parameters and the apparent crystallite sizes are different for different samples. XRD patterns of $GdPO_4{\cdot}nH_2O$ samples synthesized via hydrothermal route with different < P > /Gd molar ratios (other conditions: 12 h at 160 °C, synthesized amount 0.4 mmol) are presented on Fig. 1.

The lattice parameters of the synthesized samples were calculated using Le Bail method and the obtained values are tabulated in Table 1. Lattice parameter *a* for sample with < P > /Gd ratio = 10 is very close to this parameter in reference structure from ICCD database ($GdPO_4{\cdot}H_2O$, PDF ICDD 00-039-0232), but it grows and exceeds this value with the increase of < P > /Gd ratio. Meanwhile parameter *c* for all obtained samples is smaller than reported in ICCD database. It is worthy to note that both cell parameters, and, therefore, the volume of the unit cell, are growing with the increase of < P > /Gd ratio. This result indicates, that, although the phase remains the same, exact composition of the samples synthesized in different conditions is different.

The most obvious source of nonstoichiometry for rhabdophane phases is crystalline water. The amount of crystalline water molecules in zeolitic channels of rhabdophane structure is not strictly defined by structure and, as the water molecules are neutral, there's no problem with the electroneutrality. To prove this hypothesis and study condition and content of crystalline and absorbed water in samples synthesized in different conditions we conducted their analysis by means of IR spectroscopy and DT/TGA.

The recorded FTIR spectra of as prepared $GdPO_4{\cdot}nH_2O$ samples with different < P > /Gd molar ratios of 10, 50 and 100 are given in Fig. S1 a, b, and c, respectively. The obtained results can be divided into four regions of interest: 300-800 cm^{-1} (corresponding to PO_4 tetrahedron deformation modes), 900 – 1200 cm^{-1} (originating from the stretching PO_4 vibrations), and two remaining regions related to water: around 1615 cm^{-1} (corresponding to bending H_2O vibrations) and 2500-3800 cm^{-1} (corresponding to stretching H_2O vibrations). Wide vibration band at around 1000 cm^{-1} originates from P—O vibrations within PO_4^{3-} groups and actually consist of three peaks centered at 976 cm^{-1} (could be assigned to symmetrical stretching mode), 1001 cm^{-1} (shifts to 1004 cm^{-1} as < P > /Gd ratio increases to 50 or more,) and 1027 cm^{-1}. Both 1001 and 1027 cm^{-1} vibrational bands could be assigned to asymmetric stretching mode. A pair of sharp bands observed at 625 and 535 cm^{-1} are the result of O—P—O vibrations in PO_4^{3-} groups and can be assigned to bending modes of O = P—O and O—P—O groups. The vibrational bands at 1617, ca. 3210, ca. 3480, and ca. 3530 cm^{-1} (position of the bands shifts slightly with the change of < P > /Gd ratio) can be related to both physically adsorbed and bound within crystal structure water molecules. 1617 cm^{-1} band can be assigned to bending vibrations and ca. 3210, ca. 3480, and ca. 3530 cm^{-1} to

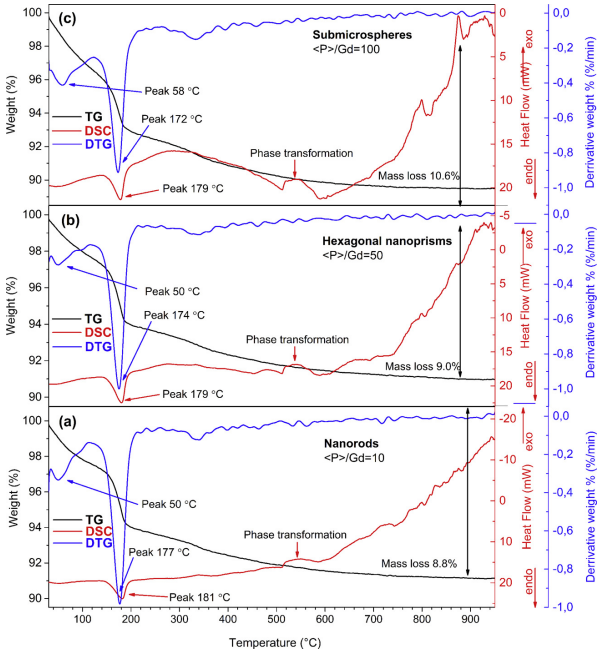

Fig. 2. TG-DTG-DSC curves of $GdPO_4{\cdot}nH_2O$ nanorods (a), hexagonal nanoprisms (b) and submicrospheres (c).

stretching vibrations of water, respectively. It is noticeable that with the increase of < P > /Gd ratio both bands of OH groups have more and more pronounced splitting and lower energy component emerges (3210 cm^{-1}). These components most likely can be attributed to structurally bound water of different coordination. Phosphate ions are known as one of the strongest positively-binding groups for water molecules and, therefore, significant shift towards lower energies of vibrations is to be expected for crystalline water molecules in orthophosphates [24]. Thus, it is reasonable to suggest, that the increase of < P > /Gd ratio leads to the increase of content of strongly bound, i.e., crystalline, water.

This suggestion is confirmed by results of DT/TGA analysis (see Fig. 2). The analyzed samples were heated up to 950 °C with heating speed of 10 °C/min under air atmosphere. The main decrease in mass for analyzed samples was observed until 500 °C.

Weight loss of all analyzed samples contain three main processes – loss of physically adsorbed water, loss of crystalline water from rhabdophane phase and phase transformation, when during dehydration process phase transition from rhabdophane to monoclinic structure occurs. The observed results are similar to those published by T. Anfimova et al. [25,26]

The loss of physically adsorbed water from the particle surface occurs in the interval from 30 to ca. 145 °C. The observed mass loss in this temperature interval leads to the conclusion that spherical particles contain more physically adsorbed water if compared to rod-like nanoparticles.

The second process, accompanied with an endothermic peak at around 145 − 200 °C, is observed in temperature range from 150 to 500 °C and is assigned to the loss of crystalline water of $GdPO_4{\cdot}nH_2O$ phase.

The third process is attributed to the beginning of rhabdophane phase transformation into the monoclinic phase and starts at around 500 °C and, even though it is not followed by significant weight loss, is accompanied by the exothermic peak observed at temperatures between 500 and 550 °C for all samples representing different morphologies. The weight loss in temperature interval 500 − 900 °C can be attributed to the remaining crystalline water (or even stronger bound OH groups within zeolitic channels, which is supporting the rhabdophane crystal structure [19]).

It was calculated that along with increase of < P > /Gd ratio the amount of physically adsorbed water increases and the amount of crystalline water decreases. The exact formulas for different $GdPO_4{\cdot}nH_2O$ morphologies were determined and are summarized in Table 2.

Possible explanation to this effect could be that water molecules in rhabdophane structure are forming strong hydrogen bonds between − OH groups and surrounding atoms forming zeolitic channels. Therefore, the increase of crystalline water content leads to gradual shrinkage of these channels. However, this hypothesis needs further experimental verification, which is out of the scope of the present work.

3.2. Morphology of synthesized particles

The choice of synthesis parameters is extremely important in morphology control of obtained $GdPO_4{\cdot}nH_2O$ particles. We have studied the influence of synthesis parameters such as ratio of < P > /Gd, Gd^{3+} concentration, pH, and synthesis duration. All syntheses were conducted in the presence of tartaric acid. Tartaric acid may affect the growth of $GdPO_4{\cdot}nH_2O$ crystals in several ways. It has two carboxylic groups −COOH and two hydroxyl groups −OH in its structure. The presence of these functional groups enables tartaric acid to chelate Gd^{3+} ions by forming TA–Gd^{3+} complex [27]. Therefore, in the presence of tartaric acid, the sedimentation of Gd^{3+} ions with $NH_4H_2PO_4$ proceeds at a slower rate, as Gd^{3+} ions are chelated. On the other hand, the nucleation process is also affected by the presence of tartaric acid. It was shown that short organic molecules (for example citric acid, EDTA, as a coordinating agents or EG as synthesis medium) may bind to {0001} facet and in this way inhibit the particle growth along *c* (001) axis or alter the morphology of forming particles [1,27,28]. Thus, one can expect the formation of anisotropic particles in presence of tartaric acid, given that degree of supersaturation is not very high.

Table 2
Crystalline and physically adsorbed water content within different $GdPO_4{\cdot}nH_2O$ samples.

< P > /Gd ratio	$GdPO_4{\cdot}nH_2O$	Physically adsorbed water
10	1.07	1.7%
50	1.03	2.1%
100	1.01	3.8%

This hypothesis was proved by series of experiments with varying < P > /Gd molar ratio (these syntheses were performed for 12 h at 160 °C, pH = 10). Fig. 3 and Fig. S2 represents SEM images of synthesized $GdPO_4{\cdot}nH_2O$ particles. By changing the molar ratio of < P > /Gd from 1 to 100 (in other words increasing the degree of supersaturation) the following morphologies were obtained subsequently: nanofibers, nanorods, nanoprisms and submicrospheres. At the lowest degree of supersaturation (< P > /Gd ratio is equal to 1, Fig. S2 a) a nanofiber net made from very thin (~10 nm) and long wires up to hundreds of nanometers is formed. As the ratio increases up to 10 (Figs. S2 b–d) – a well-shaped and monodisperse nanorods of ca. 100 nm in length and 15 nm in thickness form. These images also reveal that shorter and thicker nanorods are formed if larger < P > /Gd ratio is used. It is well-known that orientation and growth along one axis is due to specific nature of hexagonal (rhabdophane) phase. Rhabdophane phase possesses zeolitic channels with crystalline water within and generally rare-earth phosphates of rhabdophane phase (including hexagonal $GdPO_4{\cdot}nH_2O$) prefer to grow along the axis of zeolitic channel (*c* axis) as {0001} facet is more preferable for growth than others[Fang, 2003 #5] [1,26].

However, when the degree of supersaturation increases (< P > /Gd molar ratio reaches 50, Fig. 3b and Fig. S2 f), intensive growth and aggregation of nuclei prevents formation of anisotropic nanoparticles, hexagonal nanoprisms (ca. 80 nm in length and ca. 40 nm in diameter) start to form. Further increase of degree of supersaturation and, therefore, rate of growth, leads to formation of more and more isotropic particles. The formation of crude submicrospheres is observed when < P > /Gd ratio reached 75 (Fig. S2 g) and higher. Eventually, relatively uniform submicrospheres, although not perfect in shape, form if < P > /Gd^{3+} molar ratio reaches 100 (Fig. 3c and Fig. S2 h) (ca. 100 nm in diameter). The mean size of particles also increased with the increase of the degree of supersaturation.

It is interesting to compare evolution of microstructure and crystallinity of samples synthesized under different degree of supersaturation (Fig. 3). As the < P > /Gd ratio increases, the apparent crystallite size, calculated using Scherrer equation, increases too, thus resulting in narrowing of the peaks of corresponding XRD patterns (see Fig. 3d) (full information on SEM images and XRD patterns for the whole series can be found in Figs. S2 and S3). The mean apparent crystallite sizes for samples with < P > /Gd ratios of 10 (20 ± 3 nm), 50 (29 ± 1 nm) and 100 (38 ± 2 nm) were calculated using Scherrer's equation (see Table 1). It is expectable, as with increase of degree of supersaturation forming nuclei should grow more intensively. Less common is formation of uniform spherical particles with very narrow size distribution. Usually under such high degree of supersaturation shapeless micrometer-sized aggregates are formed as a result of unlimited growth and fast aggregation of particles. On the other hand, conditions for formation of uniform spherical particles is low concentration of reagents and minimal degree of supersaturation [29]. In our case the possible explanation of resulting morphology may be the chelating effect of tartaric acid. Binding of Gd^{3+} ions in complex may efficiently limit the velocity of growth, therefore, providing conditions

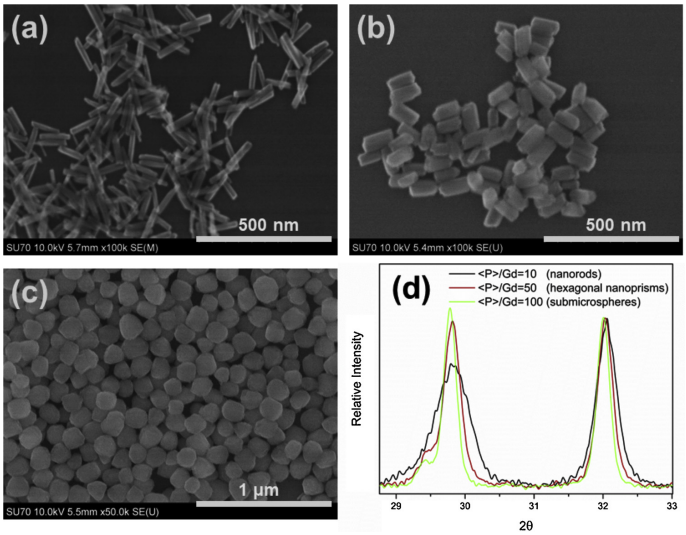

Fig. 3. SEM images of $GdPO_4{\cdot}nH_2O$ synthesized with different < P > /Gd molar ratio: (a) 10, (b) 50 (c) 100. (d) shows the change of $I_{(200)}/I_{(102)}$ ratio in the XRD patterns of samples with different morphology.

for uniform particles formation even at high degree of supersaturation.

It is also noticeable, that $I_{(200)}/I_{(102)}$ changes, indicating specific texture, in this case aggregation of particles. The powder XRD pattern of particles synthesized under < P > /Gd molar ratio of 10 (nanorod shaped) have a diffraction peak (102) a little less intensive than peak (200), i.e., $I_{(200)}/I_{(102)}$ value is 0.732. In the case of sample synthesized under < P > /Gd ratio of 50 (hexagonal nanoprisms, Fig. 1 c) intensity values of (200) and (102) peaks become similar as ratio $I_{(200)}/I_{(102)}$ reaches value of 0.977. For sample, synthesized under < P > /Gd molar ratio of 100 (submicrospheres, Fig. 1 d) intensity of (200) peak even exceeds intensity of (102) peak as observed $I_{(200)}/I_{(102)}$ ratio value reaches 1.05. The comparison of (200) and (102) peaks (normalized intensity) is given in Fig. 3 d. It is reasonable as nanorods grow along specific crystallographic axis and tend to form stacks of particles with the same orientation. On the other hand, isotropic particles do not have preferable orientation during aggregation.

It was figured out that concentration of Gd^{3+} ions does not affect morphology of the resulting nanoparticles once the < Gd > /P ratio is fixed. The SEM images of $GdPO_4{\cdot}nH_2O$ particles obtained for different starting amounts of Gd^{3+} ions with < P > /Gd ratio set to 100 given in Fig. 4 (conditions of synthesis – 12 h at 160 °C). This confirms the hypothesis that Gd^{3+} ions are chelated by tartaric acid and the release of Gd^{3+} ions occurs with low velocity determined by stability of complex, not the initial Gd^{3+} concentration.

The SEM images, given in Fig. 5, represent the impact of pH value (9, 10 and 10.5) on the $GdPO_4{\cdot}nH_2O$ particle size and morphology. Hydrothermal synthesis was performed for 12 h at 160 °C and the < P > /Gd ratio was set to 10. It is obvious (Fig. 5a–c) that an increase in pH value causes formation of shorter and thicker nanorods and, therefore, acts in the same way as the increase of < P > /Gd ratio. Though the concentration of phosphate ions does not change with the increase of pH, hydrolysis equilibria for phosphate ions shifts towards less protonated forms. This increases the activity of phosphate ions in the precipitation process and, therefore, acts the same way as the increase of degree of supersaturation. Additionally, the way how tartaric acid interacts with growing particles may depend on the pH value too, as it affects deprotonisation of tartaric acid molecules [30]. For reference the XRD patterns of specimens synthesized at different pH values are shown in Fig. S4.

We have also studied the influence of synthesis duration on particles morphology. Fig. S5 represent SEM images of $GdPO_4{\cdot}nH_2O$ particles synthesized for: 4 (Fig. S5 a), 8 (Fig. S5 b), 12 (Fig. S5 c), 16 (Fig. S5 d),

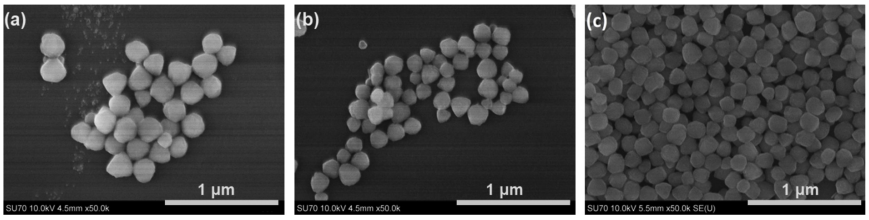

Fig. 4. SEM images of $GdPO_4{\cdot}nH_2O$ under magnification of x50 k (c). Samples were synthesized with different starting amounts of Gd^{3+} ions: (a) 0.1, (b) 0.2, and (c) 0.4 mmol of Gd^{3+} ions.

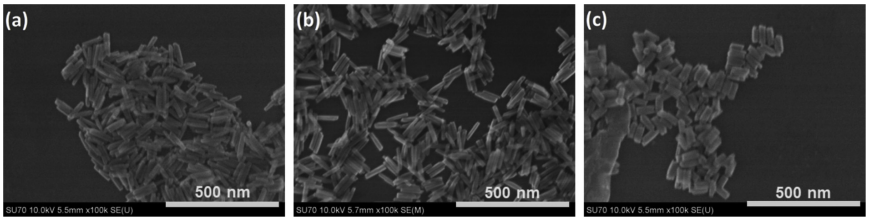

Fig. 5. SEM images of $GdPO_4{\cdot}nH_2O$ particles under magnification of x100 k. Particles were synthesized at several pH values: (a) 9, (b) 10, and (c) 10.5.

20 (Fig. S5 e), and 24 (Fig. S5 f) hours, respectively. These SEM images imply that the best quality nanorods are obtained when synthesis time is in the range of 12–16 h. Nanorods synthesized in the time range up to 12 h have broader size distribution and are not perfectly shaped. It indicates that growth and recrystallization of nanorods are not finished yet. On the other hand, particles synthesized with duration over 24 h already are not that well dispersed and tend to agglomerate along *c*-axis, what can actually be called self-assembly of nanorods. In this case, self-assembly occurs in order to minimize the surface area and, thus, defects. The XRD patterns of samples synthesized for different time are depicted in Fig. S6. The patterns look virtually identical; thus it can be concluded that single phase $GdPO_4{\cdot}nH_2O$ compounds are obtained even after 4 h synthesis.

3.3. Colloidal stability of $GdPO_4$ particles with different morphology in aqueous media

Fig. 6 demonstrates the dependence of zeta-potential values of $GdPO_4$ samples with different morphology as a function of pH. Zeta-potential is an important factor determining the stability of electrostatically stabilized nanoparticles. The value of zeta-potential is strongly dependent on pH value and ionic force of the solution. The obtained values of zeta-potentials varied from 52.9 mV at pH value of 2.5 for nanorods up to -65.6 mV at pH value of 10.0 for submicrospheres. According to the literature, the particles with absolute zeta-potential value higher than 28 mV exhibits colloidal stability, which is induced by electrostatic repulsion. This prevents them from forming agglomerates and coagulates [31]. In all cases, the measured zeta-potential values decreased alongside with increase in pH value. It was also noticed that isoelectric point of examined particles is highly dependent on the particles morphology. The isoelectric points of rod-like particles (< P > /Gd = 10), nanoprisms (< P > /Gd = 50), and submicrospheres (< P > /Gd = 100) are at pH values of 6.2, 5.6, and 4.5, respectively.

The main source of surface charge, determining zeta-potential of

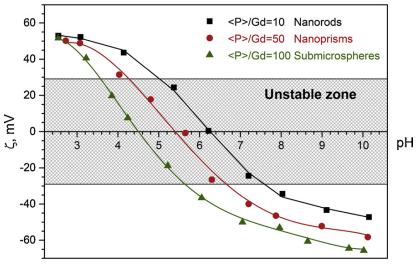

Fig. 6. Zeta-potentials of $GdPO_4{\cdot}nH_2O$ particles with different morphologies at different pH values.

electrostatically stabilized particles are anionic/cationic groups exposed to the particle surface. Particularly in this case, at pH value of 2.5, nanorod/hexagonal and nanoprism/submicrosphere shaped particles have very similar zeta-potential values, which are around 50 mV. This can be related to gadolinium located near the surface, responsible for the positive surface charge, which is measured when all phosphate groups are fully protonated under pH value of around 2. The change in remarkably different isoelectric points and zeta-potential values under basic pH values of nanoparticles can be explained by different amounts of phosphate groups on the particle surfaces. The difference may come from morphology and different surface areas of particles with different morphologies. As spherically shaped particles do have more phosphate groups due to formation mechanism compared to $GdPO_4$ nanorods/hexagonal nanoprisms. This explains why submicrospheres have isoelectric point under more acidic pH value of 4.5. Analogically, hexagonal nanoprisms have more phosphate groups if compared to nanorods. Therefore, their isoelectric point is located in less acidic pH value of 5.6. Under pH value of around 10, there is an obvious difference between zeta-potentials of investigated particles: -49 mV for nanorods, −58 mV for hexagonal nanoprisms, and −65 mV for submicrospheres. Under this pH value, it is most likely that most of the surface-exposed phosphate groups are deprotonised. The more deprotonised phosphate groups – the more negative surface charge is generated, which results in more negative zeta-potential value. The observed values are intact with presumption that submicrospheres > hexagonal nanoprisms > nanorods regarding number of surface exposed phosphate groups.

The obtained results suggest that $GdPO_4$ particles can be effectively dispersed in aqueous media forming stable solutions in different ranges of pH values. Furthermore, these morphology/surface area dependent changes in zeta-potential values enable to selectively choose desired morphologies of $GdPO_4$ particles to form stable dispersions under certain pH values.

4. Discussion

There are numerous papers reporting various different approaches to obtain $GdPO_4$ nano- and micro- sized particles (nanorods, nanoprisms, submicrospheres, submicrostars, nanocubes). To the best our knowledge there are only two papers reporting controlled growth of $GdPO_4$ nanoparticles. However, both of them have slightly different approaches. In 2018, Z. Wang et al. reported a study of $GdPO_4$ nanocrystals synthesis by solvothermal method, where the impact of pH and ethylene glycol (EG) to the particle morphology has been investigated. This report has shown that increasing EG concentration results in shortening of the obtained nanorods yielding quasi-equiaxed hexagonal $GdPO_4{\cdot}nH_2O$ nanocrystals when high amount of EG was used [1]. However, the control of particle shape was not that simple and, in some cases, particle size distribution was relatively large due to particle agglomeration. In 2019, S. Wu et al. published a research paper where morphology of obtained $GdPO_4$ particles was controlled by altering pH values from 1 to 4. Nanorods and hexagonal nanoprisms were obtained

[32]. Authors of this paper also claimed that they have also obtained $GdPO_4$ nanocubes; however, it is more likely that these cubes are the same hexagonal nanoprisms just lying on the side. This observation is also confirmed by the fact, that reported TEM images also contain hexagonal nanoprisms. Both publications discuss possible bio-applicability of obtained nanoparticles; however, none of them has any stability experiments done to support these claims.

As mentioned before, the surface charge and, therefore, stability range of electrostatically stabilized particles are characterized by zeta potential analysis. This analysis method of particle surface charge provides information about $GdPO_4$ particle stability in aqueous colloids and charge of the particle surface. The isoelectric points and stability range of particles were determined and are given in Fig. 6. These results define particle stability and, thus, help to evaluate potential applicability of $GdPO_4$ nanoparticles in biomedical and other possible fields, as particles which are not stable in biological pH range (biological pH value ranges from 7.35 to 7.45) cannot be applied in the fields where colloid stability under discussed pH is required.

There are only few reports discussing stability of $GdPO_4$ nanoparticles. A. Mayence et al. reported nanorods of ca. 300 nm in length and 15 nm in thickness with negative zeta potential values in pH range from 2.0 (around 0 mV) to 10.0 (around -70 mV) [33]. B. Abecassis et al. reported nanorods of 125 nm in length (with 40 nm deviation). According to this paper, the analyzed $GdPO_4$ nanorods possess similar stability range to $GdPO_4$ nanorods reported by us. However, zeta-potential values in this paper are not suitable to achieve colloidal stability for biological applications, as these particles seem not to be stable in biological pH range [34]. F. Mpambani reported research on $GdPO_4$ particle stability in his doctoral thesis. He discussed that instability range of $GdPO_4$ nanorods obtained by his group is between pH values 5.0–10.0 with isoelectric point around pH value of 6. According to thesis author, $GdPO_4$ particles can be considered as possible MRI agents if their stability is increased [35]. Mirzadeh et al. reported $GdPO_4$ particles, which possess -23.88 mV zeta potential values as prepared and -13.03 mV values after the dialysis. $GdPO_4$ particles doped with Eu^{3+} ions are reported to exhibit -28.52 mV zeta potential (deviation 7.78) and after dialysis value of zeta-potential decreased to -18.50 mV [36]. Zeta potential of $GdPO_4$:Eu submicrospheres was reported to be around -6 mV at pH value of 5.0, -15 mV at pH value of 7.4, and -22 mV at pH value 8.0. However, the reported values are not large enough for electrostatically stabilized colloids to form [37].

Some research reporting stability of some other similar $LnPO_4$ systems are also worth mentioning. Hexagonal $LaPO_4$ nanorods ($50-100$ nm in length and $5-10$ nm in thickness) doped with Tb^{3+} and Eu^{3+} ions were reported by T. Grzyb [38]. Particles, reported by his group, possess zeta potential values of $29-34$ mV at pH value of 7, which is almost the minimal satisfactory value for the stability, although if particles are stable - it seems to be suitable for biological applications. In 2015 Becerro et al. reported $LuPO_4$:5 %Eu nanoparticles (85 nm in length and 40 nm in thickness) with tetragonal crystal structure. These nanoparticles exhibited zeta potential value of 0.3 mV (very near to the isoelectric point) at pH value of 4.0, and value of -44 mV at pH value of 10.0. In comparison to this result, under similar pH values our particles possess zeta potential values of 30 mV (for nanoprisms) and 50 mV (for nanorods) which is more than enough for stable colloids to be acquired [39].

The pH instability range for particles obtained by us is 5.0–7.5 for nanorods, 4.5–6.5 for hexagonal nanoprisms and 3.5–5.5 for submicrospheres. According to these results, $GdPO_4$ nanoparticles, which may form stable aqueous colloids at pH values from 2.5 to 5.0 and from 5.5 to 10, may be obtained. These results show, that only at pH interval 5–5.5 none of our synthesized nanoparticles form stable aqueous colloids.

Our research was mainly focused on developing novel simple synthesis route allowing to control $GdPO_4$ nanoparticle growth and morphology. Moreover, to prove particle applicability in suggested fields, which require colloid stability in aqueous solutions, stability of colloids was evaluated. Besides, every so often scientific reports provide $LnPO_4$ synthesis routes, which yield $GdPO_4$ particles with large size distribution. These particles are also often agglomerated, possess poor crystallinity or are not single phase, or simply are too large to form stable colloids and to be applied in suggested application fields. It is well known, that colloidal stability of particles in dispersion is highly related to their size. If particles are larger than 1 μm, the tendency of sedimentation process is high due to their own weight. However, it is possible to find examples where relatively large particles are stable in aqueous media. Rhodes et al. reported the florescent SiO_2 particles with diameter of about 1 μm, which are stable in aqueous dispersion (at pH = 6) without any dispersant added [40]. On the other hand, there are also cases reporting that even small particles ($\sim$25 nm) in aqueous dispersions exhibit poor stability, despite high values of surface potential (-60 mV) [41].

Here we provide simple, clean, eco-friendly and quick synthesis route, which enables not only to obtain relatively small, single phase, monodisperse, well-shaped $GdPO_4$ particles but also to control their growth and morphology with great accuracy and reproducibility. Furthermore, most of the published research related to $GdPO_4$ nano– or micro–sized particle development nearly always mentions possible particle applications such as MRI agents, nanoprobes, security inks and so on. These applications require colloidal stability. In addition, we want to note that particle size plays an important role in overall applicability of such colloidal systems: smaller colloidal systems made from particles, which size varies from several to around 100 nm can potentially be applied in biological fields, whereas size of particles to be applied in development of security inks does not matter that much as long as aqueous colloids of such particles are stable.

However, only very few reports provide any experiments that the obtained particles can be dispersed in aqueous media at all. Our results, regardless of desired application (which requires colloidal stability), enable to obtain $GdPO_4$ particles, which will form stable aqueous colloids under nearly all pH values. Particles are easily synthesized and no surface modification is needed making the synthesis procedure simple, clean and quick. It is also important to mention that hexagonal nanoprisms and submicrospheres show colloidal stability in biological pH range (as most papers do not achieve such wide $GdPO_4$ stability). Moreover, particle surface remains unmodified; therefore, further functionalization of the particles is possible. All of the previously discussed insights are based on our stability research of rare-earth orthophosphate colloids. These insights can also be applied to nanoparticle systems where particle size varies in the range from several nanometers up to hundreds of nanometers in size.

5. Conclusions

$GdPO_4{\cdot}nH_2O$ particles with various sizes and morphologies were synthesized via hydrothermal route using tartaric acid as a chelating/capping agent. We have demonstrated that synthesis parameters, such as molar ratio of $NH_4H_2PO_4/Gd^{3+}$, pH and synthesis duration allow controlling the morphology of synthesized nanoparticles and producing final product in shapes from nanofibers to nanorods to spherical particles with narrow size distribution. Effects leading to the different morphologies were also discussed.

Moreover, we have also shown that particles with different morphology possess different zeta potential values; therefore, their colloidal stability can be adjusted relative to the application field.

The synthesized $GdPO_4{\cdot}nH_2O$ nanoparticles can potentially be applied as MRI contrast agents since they show good stability in aqueous media and can be further doped with rare-earth ions to introduce luminescence properties or surface-modified to introduce additional properties, such as drug delivery and so on.

CRediT authorship contribution statement

Matas Janulevicius: Methodology, Validation, Investigation, Writing - original draft, Visualization. **Vaidas Klimkevicius:** Investigation, Visualization. **Alexander Vanetsev:** Investigation. **Valentina Plausinaitiene:** Investigation, Formal analysis. **Simas Sakirzanovas:** Conceptualization, Writing - review & editing. **Arturas Katelnikovas:** Conceptualization, Resources, Writing - review & editing, Supervision, Funding acquisition.

Declaration of Competing Interest

The authors declare that they have no known competing financial interests or personal relationships that could have appeared to influence the work reported in this paper.

Acknowledgements

The authors gratefully thank Rokas Vargalis (Vilnius University) for taking SEM images. This research was funded by a grant (No. S-MIP-17-48) from the Research Council of Lithuania.

Appendix A. Supplementary data

Supplementary material related to this article can be found, in the online version, at doi:https://doi.org/10.1016/j.mtcomm.2020.100934.

References

[1] Z.H. Wang, X.F. Shi, X.J. Wang, Q. Zhu, B.N. Kim, X.D. Sun, J.G. Li, Breaking the strong 1D growth habit to yield quasi-equiaxed $REPO_4$ nanocrystals (RE = La-Dy) via solvothermal reaction and investigation of photoluminescence, Cryst. Eng. Comm 20 (2018) 796–806.

[2] M. Saraf, P. Kumar, G. Kedawat, J. Dwivedi, S.A. Vithayathil, N. Jaiswal, B.A. Kaipparettu, B.K. Gupta, Probing highly luminescent europium-doped lanthanum orthophosphate nanorods for strategic applications, Inorg. Chem. 54 (2015) 2616–2625.

[3] J. Yang, J.J. Cao, D.Y. Shen, J. Xiong, J.F. Tang, S.S. Hu, Morphology-controlled synthesis and luminescence properties of $ScPO_4{\cdot}2H_2O{:}Ln^{3+}$ nano/micro-crystals by a facile approach, Cryst. Eng. Comm 18 (2016) 8944–8952.

[4] A.G. Hernandez, D. Boyer, A. Potdevin, G. Chadeyron, A.G. Murillo, F.D.C. Romo, R. Mahiou, Hydrothermal synthesis of lanthanide-doped $GdPO_4$ nanowires and nanoparticles for optical applications, Phys. Status Solidi a-Appl. Mater. Sci. 211 (2014) 498–503.

[5] A.I. Becerro, S. Rodriguez-Liviano, A.J. Fernandez-Carrion, M. Ocana, A novel 3D architecture of $GdPO_4$ nanophosphors: multicolored and white light emission, Cryst. Growth Des. 13 (2013) 526–535.

[6] Q.H. Yang, X.L. Li, Z.L. Xue, Y.B. Li, M.Y. Jiang, S.J. Zeng, Short-wave near-infrared emissive $GdPO_4{:}Nd^{3+}$ theranostic probe for in vivo bioimaging beyond 1300 nm, RSC Adv. 8 (2018) 12832–12840.

[7] J. Xu, X.K. Shen, L. Jia, Z.J. Ge, D. Zhou, Y. Yang, T.L. Ma, Y.F. Luo, T.F. Zhu, $GdPO_4$-Based Nanoprobe for Bioimaging and Selective Recognition of Dipicolinic Acid and Cysteine by a Sensing Ensemble Approach, ACS Biomater. Sci. Eng. 5 (2019) 996–1004.

[8] A.S. Barnard, Using theory and modelling to investigate shape at the nanoscale, J. Mater. Chem. 16 (2006) 813–815.

[9] S.Z. Lu, J.H. Zhang, J.S. Zhang, H.F. Zhao, Y.S. Luo, X.G. Ren, Remarkably enhanced photoluminescence of hexagonal $GdPO_4{\cdot}nH_2O{:}Eu$ with decreasing size, Nanotechnology 21 (2010) 365709.

[10] J. Dai, G.C. Li, M. Lv, R.S. Zhou, X. Li, Hydrothermal synthesis and luminescent properties of spherical $LaPO_4{:}Ln^{3+}$ (Ln^{3+} = Eu^{3+}, Dy^{3+}, Ce^{3+}, Tb^{3+}), Adv. Mat. Res. 1120-1121 (2015) 396–400.

[11] H. Lai, Y. Du, M. Zhao, K.N. Sun, L. Yang, Effects of different organic additives on the formation of $YPO_4{:}Eu^{3+}$ nano-/microstructures under hydrothermal conditions with enhanced photoluminescence, Ceram. Int. 40 (2014) 1885–1891.

[12] G.A. Kumar, N.R. Balli, M. Kailasnath, L.C. Mimun, C. Dannangoda, K.S. Martirosyan, C. Santhosh, D.K. Sardar, Spectroscopic and magnetic properties of neodymium doped in $GdPO_4$ sub-micron-stars prepared by solvothermal method, J. Alloys. Compd. 672 (2016) 668–673.

[13] L.X. Yu, D.C. Li, M.X. Yue, J. Yao, S.Z. Lu, Dependence of morphology and photoluminescent properties of $GdPO_4{:}Eu^{3+}$ nanostructures on synthesis condition, Chem. Phys. 326 (2006) 478–482.

[14] M. Ferhi, S. Toumi, K. Horchani-Naifer, M. Ferid, Single phase $GdPO_4{:}Dy^{3+}$ microspheres blue, yellow and white light emitting phosphor, J. Alloys. Compd. 714 (2017) 144–153.

[15] P. Halappa, B. Devakumar, C. Shivakumara, Effect of Ca^{2+} ion co-doping on radiative properties via tuning the local symmetry around the Eu^{3+} ions in orange red light emitting $GdPO_4{:}Eu^{3+}$ phosphors, New J. Chem. 43 (2019) 63–71.

[16] M. Yu, J. Lin, J. Fu, H.J. Zhang, Y.C. Han, Sol-gel synthesis and photoluminescent properties of $LaPO_4$:a (A = Eu^{3+}, Ce^{3+}, Tb^{3+}) nanocrystalline thin films, J. Mater. Chem. 13 (2003) 1413–1419.

[17] Y.B. Wu, P. Sun, H.Q. Yu, S.S. Zeng, H.F. Xu, B.J. Chen, Synthesis and luminescent properties of $LaPO_4{:}Eu^{3+}$ nanocrystal with ultrasonic method, Proc. SPIE, 5th International Symposium on Advanced Optical Manufacturing and Testing Technologies: Optoelectronic Materials and Devices for Detector, Imager, Display, and Energy Conversion Technology 7658 (2010), p. 76583q.

[18] T. Grzyb, A. Gruszeczka, R.J. Wiglusz, Z. Sniadecki, B. Idzikowski, S. Lis, Multifunctionality of $GdPO_4{:}Yb^{3+}$,Tb^{3+} nanocrystals - luminescence and magnetic behaviour, J. Mater. Chem. 22 (2012) 22989–22997.

[19] A.S. Vanetsev, E.V. Samsonova, O.M. Gaitko, K. Keevend, A.V. Popov, U. Maeorg, H. Mandar, I. Sildos, Y.V. Orlovskii, Phase composition and morphology of nanoparticles of yttrium orthophosphates synthesized by microwave-hydrothermal treatment: the influence of synthetic conditions, J. Alloys. Compd. 639 (2015) 415–421.

[20] Z.Y. Huo, C. Chen, D. Chu, H.H. Li, Y.D. Li, Systematic synthesis of lanthanide phosphate nanocrystals, Chem. Eur. J. 13 (2007) 7708–7714.

[21] Q.Q. Zhan, H.C. Liu, B.J. Wang, Q.S. Wu, R. Pu, C. Zhou, B.R. Huang, X.Y. Peng, H. Gren, S.L. He, Achieving high-efficiency emission depletion nanoscopy by employing cross relaxation in upconversion nanoparticles, Nat. Commun. 8 (2017) 1058.

[22] F. Shi, J.S. Wang, D.S. Zhang, G.S. Qin, W.P. Qin, Greatly enhanced size-tunable ultraviolet upconversion luminescence of monodisperse β-$NaYF_4$:Yb,Tm nanocrystals, J. Mater. Chem. 21 (2011) 13413–13421.

[23] A. Mesbah, N. Clavier, E. Elkaim, C. Gausse, I. Ben Kacem, S. Szenknect, N. Dacheux, Monoclinic form of the rhabdophane compounds: $REEPO_4{\cdot}0.667H_2O$, Cryst. Growth Des. 14 (2014) 5090–5098.

[24] K.A.V. Karyakin, G.A. Krivencova, Water Content in Organic and Inorganic Compounds, Nauka, Moscow, 1973.

[25] T. Anfimova, Q.F. Li, J.O. Jensen, N.J. Bjerrum, Thermal stability and proton conductivity of rare earth orthophosphate hydrates, Int. J. Electrochem. Sci. 9 (2014) 2285–2300.

[26] Y.P. Fang, A.W. Xu, R.Q. Song, H.X. Zhang, L.P. You, J.C. Yu, H.Q. Liu, Systematic synthesis and characterization of single-crystal lanthanide orthophosphate nanowires, J. Am. Chem. Soc. 125 (2003) 16025–16034.

[27] W. Di, M.-G. Willinger, R.A.S. Ferreira, X. Ren, S. Lu, N. Pinna, Citric acid-assisted hydrothermal synthesis of luminescent $TbPO_4$:Eu nanocrystals: controlled morphology and tunable emission, J. Phys. Chem. C 112 (2008) 18815–18820.

[28] H. Deng, C.M. Liu, S.H. Yang, S. Xiao, Z.K. Zhou, Q.Q. Wang, Additive-mediated splitting of lanthanide orthovanadate nanocrystals in water: morphological evolution from rods to sheaves and to spherulites, Cryst. Growth Des. 8 (2008) 4432–4439.

[29] T. Sugimoto, Monodispersed Particles, 1st ed., Elsevier, Amsterdam; New York, 2001.

[30] L.I. Katzin, E. Gulyas, Dissociation constants of tartaric acid with the aid of Polarimetry[1], J. Phys. Chem. 64 (1960) 1739–1741.

[31] R.J. Hunter, Zeta Potential in Colloid Science: Principles and Applications, Academic Press, London ; New York, 1988.

[32] S. Wu, J. Yin, H. Qu, A. Li, L. Liu, Y. Shao, Photoluminescence properties of gadolinium phosphate nanoprisms doped with lanthanide ions for multicolor live cell imaging, J. Mater. Sci. Mater. Electron. 30 (2019) 11336–11345.

[33] A. Mayence, J.R.G. Navarro, Y. Ma, O. Terasaki, L. Bergström, P. Oleynikov, Phase identification and structure solution by three-dimensional Electron diffraction tomography: Gd–phosphate nanorods, Inorg. Chem. 53 (2014) 5067–5072.

[34] B. Abécassis, F. Lerouge, F. Bouquet, S. Kachbi, M. Monteil, P. Davidson, Aqueous suspensions of $GdPO_4$ nanorods: a paramagnetic mineral liquid crystal, J. Phys. Chem. B 116 (2012) 7590–7595.

[35] F. Mpambani, Multifunctional Magnetic and Fluorescent Nanoparticles for Beta-amyloid Targeting in Neurodegenerative Disease Diagnosis, Anal. Chem. Université Claude Bernard, Lyon, 2013, p. 222.

[36] M. Toro-González, D.M. Clifford, R. Copping, S. Mirzadeh, J.V. Rojas, Synthesis and characterization of intrinsically radiolabeled lanthanide phosphate nanoparticles toward biomedical and environmental applications, J. Nanopart. Res. 20 (2018) 238.

[37] Z. Li, Y. Tao, S. Huang, N. Gao, J. Ren, X. Qu, Lanthanide-based hollow mesoporous nanoparticles: a novel multifunctional platform for simultaneous gene delivery and cell imaging, Chem. Commun. 49 (2013) 7129–7131.

[38] M. Runowski, T. Grzyb, A. Zep, P. Krzyczkowska, E. Gorecka, M. Giersig, S. Lis, Eu^{3+} and Tb^{3+} doped LaPO4 nanorods, modified with a luminescent organic compound, exhibiting tunable multicolour emission, RSC Adv. 4 (2014) 46305–46312.

[39] A.I. Becerro, M. Ocana, Quick synthesis, functionalization and properties of uniform, luminescent $LuPO_4$-based nanoparticles, RSC Adv. 5 (2015) 34517–34524.

[40] S.K. Rhodes, R.H. Lambeth, J. Gonzales, J.S. Moore, J.A. Lewis, Cationic comb polymer superdispersants for colloidal silica suspensions, Langmuir 25 (2009) 6787–6792.

[41] V. Klimkevicius, T. Graule, R. Makuska, Effect of structure of cationic comb copolymers on their adsorption and stabilization of titania nanoparticles, Langmuir 31 (2015) 2074–2083.

2

Effect of Cationic Brush-Type Copolymers on the Colloidal Stability of $GdPO_4$ Particles with Different Morphologies in Biological Aqueous Media

Vaidas Klimkevičius[‡],, Matas Janulevičius[‡],, Aleksandra Babičeva, Audrius Drabavičius, Artūras Katelnikovas

LANGMUIR

pubs.acs.org/Langmuir Article

Effect of Cationic Brush-Type Copolymers on the Colloidal Stability of $GdPO_4$ Particles with Different Morphologies in Biological Aqueous Media

Vaidas Klimkevicius,[§] Matas Janulevicius,[§] Aleksandra Babiceva, Audrius Drabavicius, and Arturas Katelnikovas*

Cite This: *Langmuir* 2020, 36, 7533−7544 Read Online

ACCESS | Metrics & More | Article Recommendations | Supporting Information

ABSTRACT: In this study, we present the synthesis of cationic brush-type polyelectrolytes and their use in the stabilization of $GdPO_4$ particles in aqueous media. Polymers of various compositions were synthesized via the RAFT polymerization route. SEC equipped with triple detection (RI, DP, RALS, and LALS) was used to determine the molecular parameters (M_n, M_w, M_w/M_n). The exact composition of synthesized polymers was determined using NMR spectroscopy. Cationic brush-type polymers were used to improve the stability of aqueous $GdPO_4$ particle dispersions. First, the IEPs of $GdPO_4$ particles with different morphologies (nanorods, hexagonal nanoprisms, and submicrospheres) were determined by measuring the zeta potential of bare particle dispersions at various pH values. Afterward, cationic brush-type polyelectrolytes with different compositions were used for the surface modification of $GdPO_4$ particles (negatively charged in alkaline media under a pH value of ∼10.6). The concentration and composition effects of used polymers on the change in particle surface potential and stability (DLS measurements) in dispersions were investigated and presented in this work. The most remarkable result of this study is redispersible $GdPO_4$ nanoparticle colloids with increased biocompatibility and stability as well as new insights into possible cationic brush-type polyelectrolyte applicability in both scientific and commercial fields.

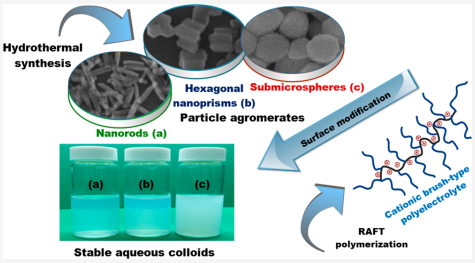

INTRODUCTION

The development of various novel nanomaterials and nanostructures is among the most rapidly progressing fields in a modern science. Due to their unique properties, which emerge as the size of the particle or structure decreases to the nanoscale, nanomaterials, regarding the application, frequently are far superior to micro- and macromaterials.[1−4] Newly developed functional nanomaterials often offer revolutionary properties and therefore are successfully applied in chemical, technological, biological, medical, and other fields.[5−9]

Most scientific papers, reporting the development of nanoparticles, claim possible nanoparticle applicability in fields which require colloidal stability (nanoparticles for biomedical applications, etc.). Colloidal stability (preferably over a wide pH range, including biological systems) is a crucial parameter and limiting factor in overall nanoparticle applicability in the mentioned fields because living organisms are commonly water-based.[10−14] Typically, nanoparticle colloidal stability is evaluated visually by conducting zeta potential measurements. In the ideal case, zeta potential measurements are supported by DLS experiments. However, such ideal case scenarios of nanoparticle stability evaluation are rather rare. Unfortunately, the authors of papers, despite intended applications, rarely evaluate the actual colloidal stability in aqueous media at all.[15−18]

Rare-earth-doped nanoparticles are materials of great interest lately.[19,20] The type of nanoparticle which can be excluded from the others would be those containing Gd^{3+} ions in their composition. Gadolinium-based particles can potentially be applied as MRI contrast agents because the Gd^{3+} ion has seven unpaired electrons in its 4f orbital.[21−23] There is plenty of published research regarding the synthesis and investigation of Gd-based nanoparticles such as $GdPO_4$, GdF_3, $NaGdF_4$, and Gd_2O_3. Gd-based nanoparticles are suitable hosts for doping with lanthanide ions in order to enrich these materials with additional luminescence properties.[5,19,20,23−25] One the most widely studied Gd-based particles is $NaGdF_4$ doped with various lanthanide ions. Such particles are often referred to as potential

Received: April 18, 2020
Revised: June 3, 2020
Published: June 3, 2020

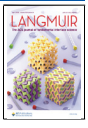

biomarkers in biomedicine.[26−28] However, the commonly used thermal decomposition[29] synthesis method leads to hydrophobic nanoparticles due to employed oleic acid, which remains on the particle surface.[30−32] A hydrophobic surface prevents any colloidal stability of $NaGdF_4$ particles in aqueous media; therefore, a change in surface ligands or additional surface modification is needed in order to achieve the colloidal stability of such particles in aqueous media.[33]

The necessity of novel Gd-based particles, which possess desired properties such as a ligand-free surface, chemical and thermal stability, and biological inertness, still exists. Orthophosphates proved to be promising host materials to satisfy such needs.[34−36] One of the approaches to obtaining rare-earth phosphate nanoparticles is hydrothermal synthesis. The main advantages of such a method are its repeatability, possibility to control the growth of the synthesized particles and, most importantly, the fact that it does not require any hydrophobic ligands (e.g., oleic acid).[37,38] Hydrothermally obtained particles typically have ligand-free surfaces and therefore are suitable for further surface modifications. There are numerous papers reporting the hydrothermal synthesis of $GdPO_4$ particles. Many of those claim that $GdPO_4$ particles can be applied in the biomedical field.[39−45] However, due to some limitations, such as reduced colloidal stability in aqueous media, $GdPO_4$ particles are not applied in vivo very frequently.

Recently, a paper reporting the controlled hydrothermal synthesis of $GdPO_4$ particles and their stability investigation was published.[46] It is important to notice that particles reported in this paper can form stable aqueous colloids. However, at neutral pH values all investigated particles are close to their isoelectric point, meaning that the surface charge of the particles is not high enough to ensure the stability of their colloids in aqueous media. Agglomeration, besides the observed $GdPO_4$ stability, remains a limiting factor for such nanoparticle applicability.

The stabilization of nanoparticles prevents the formation of agglomerates. Nanoparticle stability in aqueous colloids can be achieved either electrostatically or sterically. In most cases, electrostatic stabilization, induced by charge repulsion, does not ensure reliable-enough stability and the prevention of agglomeration.[38,47−49] Thus, steric stabilization, achieved by attaching a surfactant to a particle surface (either by chemical bonds or by electrostatic interactions), is more effective because the created steric barriers prevent particles from approaching an agglomerate too closely.[50,51] In order to apply any nano- or microsized particles, for example, $GdPO_4$ mentioned above, in fields which require superior colloidal stability (e.g., as nanoprobes), it is necessary to additionally enhance the particle stability. For this reason, various low-molecular-weight surfactants such as TWEEN, CTAB, and TRITON are used to enhance the stability of various nanoparticle systems.[23,39,52−55] Even though the use of various commercial surfactants often prevents particles from agglomerating, such surface modification cannot always ensure the desired stability of nanoparticles, especially in water. There is currently no effective universal way to ensure the colloidal stability of various nano- and microsized particles in aqueous colloids.

We believe that a viable solution for the discussed issues could be the use of cationic brush-type polymers. It is already known that polymeric brush-type electrolytes have a high potential for the surface modification and stabilization of nanoparticles (e.g., SiO_2, TiO_2).[51,56,57] In fact, studies show that the use of such brush-type polymers for the stabilization of particles is a more effective approach than using low-molecular-weight equivalents. However, no study on the stabilization of various morphology nanoparticles of the same crystalline phase using similar brush-type polymers exists.

In this work, we demonstrate a successful stabilization of $GdPO_4$ nanoparticles with different morphologies (nanorods, hexagonal nanoprisms, and submicrospheres) using cationic brush-type polyelectrolytes with different charge densities. The focus of this research was to investigate and determine the correlation among the zeta potential of $GdPO_4$ particles with different morphologies, the quantitative adsorption of different custom-made cationic brush-type copolymers on the particle surface, and the overall stability of $GdPO_4$ particle colloids. Redispersible $GdPO_4$ nanoparticle colloids with increased colloidal stability were obtained during this study. Not only the stability in aqueous media but also the biocompatibility of $GdPO_4$ particles is greatly enhanced after the surface modification with the p(METAC-*stat*-PEO_{19}MEMA) polyelectrolyte. The enhanced biocompatibility is due to PEO chains originating from p(METAC-*stat*-PEO_{19}MEMA). $GdPO_4$ particles are also suitable hosts for doping with rare-earth ions to enrich them with luminescence. We believe previously discussed benefits, such as increased nanoparticle stability and redispersibility from dry powder, suggest that the p(METAC-*stat*-PEO_{19}MEMA) polyelectrolyte, along with similar cationic brush-type polymers, can successfully be applied in both biomedical and commercial fields.

EXPERIMENTAL SECTION

Materials. Poly(ethylene glycol) methyl ether methacrylate (PEO_{19}MEMA, M_n 950, Aldrich) and [2-(methacryloyloxy)ethyl] trimethylammonium chloride (METAC, 80% aqueous solution, Aldrich) were purified of inhibitors by passing the monomers through a column filled with basic alumina (type S016A, Fluka). Methanol (MeOH, 99.8%, Aldrich), acetone (99%, Aldrich), ethylene glycol (EG, 99.5%, Fluka), diethyl ether (Et_2O, 99%, Aldrich), carbon disulfide (CS_2, 99.9%, Aldrich), 1-butanthiol (99%, Aldrich), sodium hydride (NaH, 60% dispersion in mineral oil, Aldrich), iodine (I_2, 99.8%, Aldrich), and 4,4′-azobis(4-cyanovaleric acid) (ACVA, 98%, Fluka) were used as received. Gd_2O_3 (99.99%, Tailorlux), ammonium dihydrogen phosphate ($NH_4H_2PO_4$, 99.9%, EuroChemicals), nitric acid (HNO_3, 70%, EuroChemicals), ammonium hydroxide (NH_4OH, 25%, EuroChemicals), and tartaric acid (99.99%, EuroChemicals) were used as received. $Gd(NO_3)_3$ was prepared by dissolving the required amount of Gd_2O_3 in nitric acid.

Synthesis of $GdPO_4$ Particles with Controlled Different Morphologies. Particles with different morphologies (nanorods, hexagonal nanoprisms, and submicrospheres) were synthesized by a hydrothermal route according to the previously published procedure with minor adjustments.[46] The morphology of synthesized particles was controlled by the variation of the initial molar ratio of Gd^{3+} to PO_4^{3-}. The morphological features of synthesized $GdPO_4$ particles were investigated using SEM (Scanning Electron microscopy) and TEM (transmission electron microscopy).

The crystalline phase (hexagonal rhabdophane; PDF ICDD 00-039-0232, space group $P3_121$) of particles was determined using XRD (X-ray powder diffraction) equipment. The synthesis procedure, analysis conditions, and XRD data in detail are provided in the Supporting Information (SI, Figure S1).

Synthesis of Cationic Brush-Type Polyelectrolytes. Cationic brush-type polyelectrolytes p(METAC-*stat*-PEO_{19}MEMA) were prepared via the RAFT (radical addition−fragmentation chain transfer) polymerization method from three different monomer feeds, METAC/PEO_{19}MEMA = 25:75, 45:55, and 65:35 mol %, according to the previously described procedure[51] with minor modifications. (Different chain-transfer agent 4-(((butylthio)carbonothioyl)thio)-4-cyano-pentanoic acid (BCPA) was used). BCPA was freshly synthesized before use according to the published data.[58] The synthesis scheme of

https://dx.doi.org/10.1021/acs.langmuir.0c01130
Langmuir 2020, 36, 7533−7544

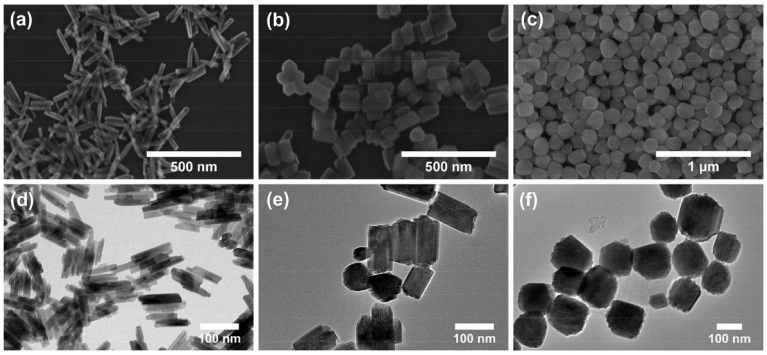

Figure 1. (a–c) SEM and (d–f) TEM images of $GdPO_4$ nanoparticles with different morphologies. Images represent the $NH_4H_2PO_4/Gd^{3+}$ molar ratio impact upon particle morphology: (a, d) 10, (b, e) 50, and (c, f) 100, respectively.

p(METAC-*stat*-PEO_{19}MEMA) with different morphologies is provided in Figure 2.

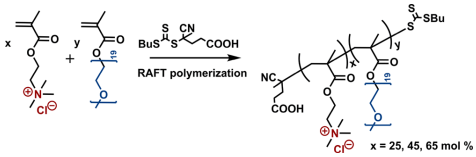

Figure 2. Synthesis scheme of cationic brush-type p(METAC-*stat*-PEO_{19}MEMA) polyelectrolytes via the RAFT method.

In all three cases, the molar ratio of initial synthesis components $[M]_0/[BCPA]_0/[ACVA]_0$ was the same (i.e., equal to 100:3:1, where $[M]_0$ represents the sum of the molar concentrations of both monomers in the reaction feed). RAFT copolymerization of METAC and PEO_{19}MEMA was carried out in a round-bottomed flask sealed with a silicone septum under an inert N_2 atmosphere in a 70:30 (v/v) mixture of ethylene glycol and water. The polymerization mixtures with an overall 15% monomer concentration were magnetically stirred for 12 h at 70 °C. After synthesis, the mixture was cooled and the flask was opened to air to quench the polymerization. Synthesized polymers were purified by ultrafiltration (10 kDa MWCO) against a 0.15 M NaCl aqueous solution and later against deionized water. Polymer solutions were concentrated using a rotary evaporator and separated by freeze-drying.

The NMR and SEC techniques (detailed analysis conditions in Figures S2 and S3) were applied to determine the composition and exact macromolecular parameters (number average molecular weight (M_n), dispersity ($Đ$), and calculated degrees of polymerization) of the synthesized polymers, respectively. The macromolecular parameter and exact composition of cationic polyelectrolytes used in this study are provided in Table 1.

Preparation of Dispersions. A colloidal 1 or 10 mg/mL dispersion was prepared by dispersing $GdPO_4$ particles with a particular morphology in Milli-Q water. The pH of each suspension was set to 10.6 using 1.0 M and then 0.1 M ammonium hydroxide (NH_4OH) solutions. All dispersions were treated with ultrasound in an ultrasonic bath for 15 min to disassemble nanoparticle agglomerates. Afterward, appropriate amounts of cationic brush-type polyelectrolytes p(METAC-*stat*-PEO_{19}MEMA) were added to the dispersion (up to 200 mg of polymer per gram of dry $GdPO_4$ particles) and ultrasonically treated again for 15 min.

Determination of the Isoelectric Point (IEP) of $GdPO_4$ Particles. The IEP point values of bare and modified $GdPO_4$ particles with different morphologies were determined by measuring zeta potentials under different pH values in aqueous dispersions. The pH of $GdPO_4$ dispersions was adjusted from 2 to 10 using 0.1 M HNO_3 and 0.1 M NH_4OH solutions, respectively. Zeta potential values were measured with a Malvern Zetasizer Nano ZS using the Smoluchowski model at 25 °C.

Determination of Polymer Adsorption and Surface Potential. The adsorbed amount of cationic polyelectrolyte on the surface of $GdPO_4$ particles was evaluated by measuring the change in zeta potential as a function of the amount of polymer added to alkaline aqueous (pH 10.6) dispersions.

The equilibrium polymer adsorption is observed at the point where the value of the zeta potential reached the plateau. Cationic polyelectrolytes with three different compositions were evaluated, and thus the effectiveness of all three polyelectrolytes was compared.

Determination of the Colloidal Stability of Aqueous $GdPO_4$ Dispersions. The colloidal stability of bare and modified $GdPO_4$ dispersions at different pH values was evaluated by measuring the particle size distribution using the dynamic light scattering (DLS) method. DLS measurements were carried out using a ZetaSizer Nano ZS (Malvern) equipped with a 4 mW He–Ne laser emitting at a wavelength of 633 nm. Measurements were performed at 25 °C and an angle of 173° using noninvasive backscattering (NIBS) technology. Using NIBS, the particle size detection range was 0.3 nm–10 μm. The

Table 1. Characteristics of the Synthesized p(METAC-*stat*-PEO_{19}MEMA) Copolymers[a]

no.	copolymer charge	$[METAC]_0/[PEO_{19}MEMA]_0$	M_n, kDa[b]	$Đ$	DP	[METAC]/ [PEO_{19}MEMA][c]
1.	low	25:75	28.5	1.15	38	27:73
2.	medium	45:55	24.6	1.16	41	47:53
3.	high	65:35	19.4	1.12	42	65:35

[a]Polymerization conditions: $[M]_0/[CTA]_0/[I]_0$ = 100:3:1, T = 70 °C, t = 12 h. [b]Determined using size exclusion chromatography (SEC). [c]Calculated from ^{1}H NMR spectra.

https://dx.doi.org/10.1021/acs.langmuir.0c01130
Langmuir 2020, 36, 7533–7544

size distribution data was analyzed using Zetasizer software from Malvern.

RESULTS AND DISCUSSION

Surface Potential and Colloidal Stability of Bare $GdPO_4$ Particles with Different Morphologies. The main object of this investigation was $GdPO_4$ particles with three different morphologies (i.e., nanorods, hexagonal nanoprisms, and submicrospheres). The change in the $GdPO_4$ particle surface potential was evaluated by measuring zeta potential values in aqueous colloidal dispersions in the pH range from 2 to 10 (Figure 3a). Zeta potential values of the synthesized $GdPO_4$ particles slightly differ and are dependent on the particle morphology. For example, the zeta potential value of submicrospheres in aqueous alkaline media (pH 10.6) is −64.7 mV. Under identical conditions, the measured zeta potential values for hexagonal nanoprisms and nanorods are observed to be higher, −53.8 and −43.8 mV, respectively. It is interesting that $GdPO_4$ particles with different morphologies possess different isoelectric points. (The isoelectric point is determined by the pH value, where the zeta potential is equal to 0, which will be referred to as the IEP.) The determined IEP value for nanorods is 6.53. IEP values of hexagonal nanoprisms and submicrospheres are shifted to lower pH values, 6.03 and 5.61, respectively. These differences in IEP could be related to different phosphate group density on differently shaped $GdPO_4$ particle surfaces since the surface potential of the particles is related to the number of surface-exposed PO_4^{3-} groups. The shape of template $GdPO_4$ particles and therefore the number of such surface-exposed phosphate groups were manipulated by varying the $NH_4H_2PO_4/Gd^{3+}$ molar ratio by employing a hydrothermal synthesis route as reported in the literature.[46] $NH_4H_2PO_4/Gd^{3+}$ molar ratios of 10, 50, and 100 were used for the hydrothermal synthesis of nanorods, hexagonal nanoprisms, and submicrospheres, respectively.

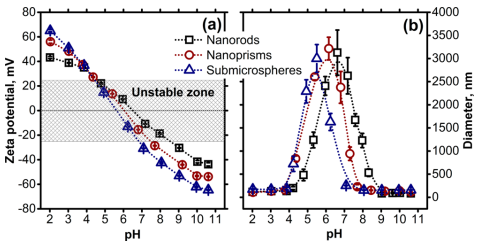

Figure 3. (a) Zeta potential and (b) particle size of bare $GdPO_4$ particles with different morphologies in aqueous dispersions at various pH values: nanorods (□), nanoprisms (○), and submicrospheres (Δ).

The colloidal stability of bare $GdPO_4$ particles with different morphologies in aqueous media under various pH values was measured using DLS equipment (Figure 3b). Typical unstable zones were observed during stability measurements of bare $GdPO_4$ particle dispersions. Regardless of particle morphology, agglomeration and fast sedimentation of particles in an aqueous dispersion occurred if absolute values of the zeta potentials of particles were lower than |22| mV. Almost identical $GdPO_4$ particle agglomeration and sedimentation due to changes in electric repulsion forces were reported in our earlier studies of particle stabilization.[46]

Surface Modification of Different $GdPO_4$ Particles Using Cationic Brush-Type Polyelectrolytes in Alkaline Media. For the surface modification of $GdPO_4$, three p(METAC-*stat*-PEO_{19}MEMA) polyelectrolytes with different compositions were synthesized. Different polymer compositions were obtained by the variation of the initial molar ratio of METAC and PEO_{19}MEMA (Table 1). METAC groups contain positively charged quaternary ammonium groups that could electrostatically anchor to the negatively charged surface of $GdPO_4$ particles. Moreover, the PEO_{19}MEMA polymer can be additionally defined as an inert, biocompatible macromonomer containing relatively long PEO substituents. These substituents are responsible for a steric barrier that prevents other particles from approaching too closely; therefore, agglomeration is avoided. PEO-stabilized particles are also known to possess good biocompatibility.[59] According to the number of quaternary ammonium groups in the copolymer composition, different p(METAC-*stat*-PEO_{19}MEMA) copolymers were classified as having low, medium, and high charge, where low means that the copolymer consist of 27 mol %; medium, 47 mol %; and high, 65 mol % METAC groups in composition.

The adsorption of a cationic brush-type polyelectrolyte on oppositely charged surfaces of $GdPO_4$ particles with different morphologies was evaluated by measuring the change in the particle zeta potential. Measurements were carried out in alkaline media (pH 10.6), where $GdPO_4$ particles have a highly

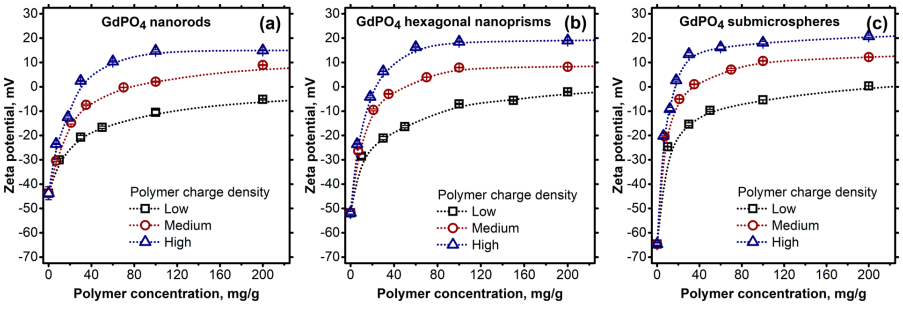

Figure 4. Dependence of the zeta potential of $GdPO_4$ particles in alkaline aqueous media (pH 10.6) as a function of polymer concentration: (a) nanorods, (b) nanoprisms, and (c) submicrospheres.

https://dx.doi.org/10.1021/acs.langmuir.0c01130
Langmuir 2020, 36, 7533−7544

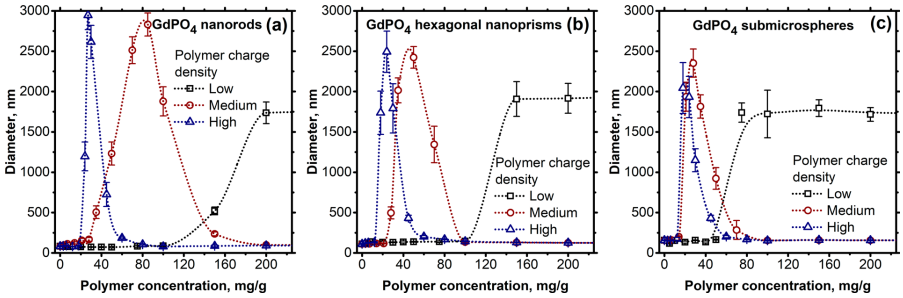

Figure 5. Dependence of the $GdPO_4$ particles size in alkaline aqueous media (pH 10.6) as a function of polymer concentration and polymer charge density: (a) nanorods, (b) nanoprisms, and (c) submicrospheres.

expressed negative charge. The effect of the amount of copolymer on the change in zeta potential of $GdPO_4$ particles with different morphologies in aqueous dispersions is presented in Figure 4.

During the addition of copolymer, the change in the zeta potential value and thus the charge on the $GdPO_4$ particle surface are affected by both the polymer charge density and the particle morphology (Figure 4.). Clearly, the charge density of polymers has a greater effect. For example, during the addition of a low-charge-density polymer to an aqueous dispersion with rod-like $GdPO_4$ nanoparticles, the full charge compensation is not achieved, and the surface of $GdPO_4$ nanorods remains negative (−5.1 mV) even when using a large amount of polymer (200 mg per gram of $GdPO_4$ particles in dispersion). Different behavior was observed using polymers with medium or high charge density. Surface charge inversion was observed during the physical adsorption of polymers with both medium and high densities of positively charged quaternary ammonium groups (METAC units). This behavior is explained in the literature,[51] where similarly structured cationic brush-type polyelectrolytes were applied for the stabilization of TiO_2 particles in aqueous media. The charge inversion effect is induced by an excess number of METAC groups on the particle surface during adsorption. The surface charge of $GdPO_4$ nanorods after the addition of medium- and high-density polymers (200 mg/g) reached +8.9 and +15.0 mV, respectively. Similar effects were observed during the investigation of $GdPO_4$ hexagonal nanoprisms. The zeta potential values of $GdPO_4$ hexagonal nanoprisms treated with low-, medium-, and high-charge p(METAC-*stat*-PEO_{19}MEMA) polyelectrolytes (amount of 200 mg/g) reached −2.1, +8.2, and +19.1 mV, respectively. Different from nanorods and hexagonal nanoprisms, the negatively charged surface of $GdPO_4$ submicrospheres after treatment with polymers was fully compensated for (+0.35 mV) using even a low-charge-density (27 mol % charged groups) polyelectrolyte. The medium- and high-charge p(METAC-*stat*-PEO_{19}MEMA) polyelectrolytes that were used led to the described charge inversion effect, and the zeta potentials of submicrosphere $GdPO_4$ particles were +12.2 and +20.8 mV, respectively.

Colloidal stability was evaluated and observed throughout all $GdPO_4$ particle treatment with the p(METAC-*stat*-PEO_{19}MEMA) procedure by measuring the particle size distribution (PSD) using dynamic light scattering equipment. A colloidal stability evaluation of differently shaped $GdPO_4$ particles is presented in Figure 5. Note that particles were treated using three different cationic brush-type polymers with different charge densities (low, medium, and high).

Regardless of the morphology, all $GdPO_4$ particles are stable in alkaline aqueous media (pH 10.6) without added polymer. In such cases, the stability of particles is ensured by electrostatic repulsion forces between highly (negatively) charged particles. Zeta potential values of $GdPO_4$ with the morphology of nanorods, hexagonal nanoprisms, and submicrospheres in alkaline media (pH 10.6) were observed to be −43.8, −53.8, and −64.7 mV, respectively.

The amount of polymer in such dispersions plays an important role. After the addition of a certain amount of polymer, dispersions became unstable. For example, during the treatment of $GdPO_4$ nanorods, particle dispersions were stable for up to 100 mg/g of added low-charge-density polymer. The addition of a larger amount of such a polymer in a dispersion led to the formation of agglomerates of up to 1800 nm. The addition of medium- and high-charge polymers to $GdPO_4$ particle dispersions showed different behavior. In these cases, $GdPO_4$ nanorod dispersions had typical zones of instability if the amount of polymer in the dispersion was insufficient. Instability zones of identical $GdPO_4$ nanorod dispersions stabilized using medium- and high-charge p(METAC-*stat*-PEO_{19}MEMA) polymers were determined to be from 30 to 150 and from 20 to 60 mg/g, respectively. In these zones, particles existed in an agglomerated state, and the measured PSD showed values of up to 3000 nm. After increasing the amount of polymer over these ranges, dispersions of $GdPO_4$ nanorods became stable again. The determined PSDs of modified $GdPO_4$ nanorods in alkaline media were ∼80 nm using both medium- and high-charge polyelectrolytes. The determined PSD values using DLS were relatively close to those measured using TEM and SEM (Figure 1). The unstable zones that occurred during the study could be related to the particle zeta potential. During treatment with polymers, the change in particle surface potential mainly depends on the amount of polymer added and the density of positively charged quaternary ammonium groups within the polymer itself. It was found that p(METAC-*stat*-PEO_{19}MEMA) polymers with a high charge density had the greatest impact on the zeta potential values of $GdPO_4$ particles. A smaller amount of such polymers was needed to reach the same value of the zeta potential in comparison to polyelectrolytes containing a small number of positively charged groups. Similar results were obtained during the stability study of $GdPO_4$ particles with other morphologies (hexagonal nanoprisms and submicrospheres) and are summarized in Table 2. It is important to note that

https://dx.doi.org/10.1021/acs.langmuir.0c01130
Langmuir 2020, 36, 7533−7544

Table 2. Stability Results of $GdPO_4$ Particles with Different Morphologies during Treatment with Different Polymers in Alkaline Aqueous Media (pH 10.6)

	nanorods		hexagonal nanoprisms		submicrospheres	
	unstable zone		unstable zone		unstable zone	
polymer charge density	polymer amount, mg/g	ζ, mV	polymer amount, mg/g	ζ, mV	polymer amount, mg/g	ζ, mV
low	>125	>−8.9	>100	>−8.4	>50	>−8.7
medium	35 to 150	−8.5 to +7.4	22.5 to 100	−8.9 to +7.8	15 to 70	−9.3 to +7.4
high	20 to 60	−9.5 to +10.9	15 to 50	−8.9 to +11.3	12.5 to 45	−9.1 to +11.9

Table 3. Zeta Potential and Calculated Equilibrium Adsorption of Cationic Polyelectrolytes on $GdPO_4$ Particles with Different Morphologies in Alkaline Aqueous Media (pH 10.6)

	polymer charge density								
	low			medium			high		
$GdPO_4$ morphology	ζ, mV[a]	ζ, mV[b]	equilibrium adsorption, mg/g[c]	ζ, mV[a]	ζ, mV[b]	equilibrium adsorption, mg/g[c]	ζ, mV[a]	ζ, mV[b]	equilibrium adsorption, mg/g[c]
nanorods	−5.2	−17.0	39.2	+8.9	−8.3	36.5	+15.0	+3.2	36.8
hexagonal nanoprisms	−2.1	−23.3	23.0	+8.2	−8.9	21.8	+19.1	+1.0	23.4
submicrospheres	+0.35	−32.3	8.7	+12.2	−17.3	11.1	+20.8	−6.8	13.3

[a]Zeta potential of $GdPO_4$ in alkaline aqueous media (pH 10.6) before washing. [b]Zeta potential of $GdPO_4$ in alkaline aqueous media (pH 10.6) after washing with Milli-Q water (three times). [c]Equilibrium adsorption of p(METAC-*stat*-PEO_{19}MEMA) with different charge density on the surface of $GdPO_4$ particles, calculated from the curves presented in Figure 4.

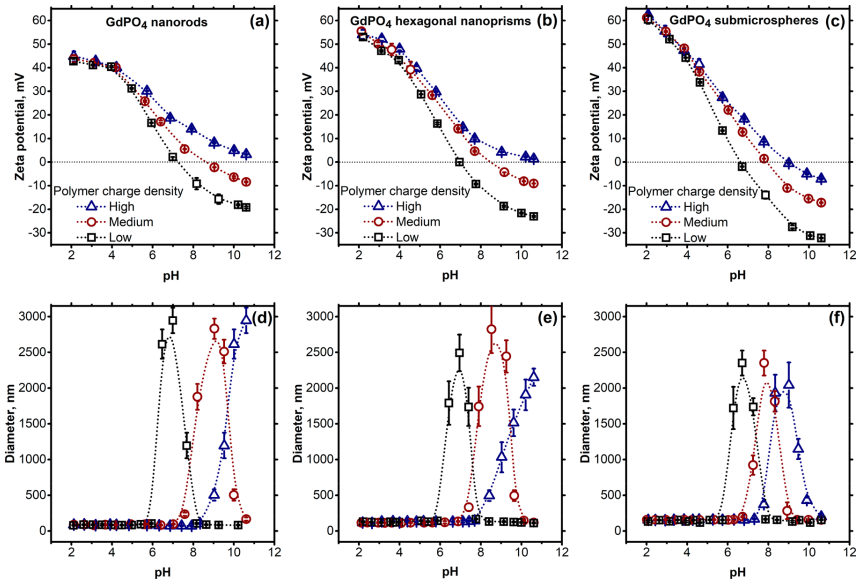

Figure 6. Dependence of the (a−c) zeta potential and (d−f) size of modified $GdPO_4$ particles as a function of the pH of the medium: (a, d) nanorods, (b, e) nanoprisms, and (c, f) submicrospheres.

instability zones of $GdPO_4$ particles, regardless of particle morphology, are observed when the absolute zeta potential value of particles was in the range of |12| mV (Figure 4).

Determination of the Equilibrium Polymer Adsorption of $GdPO_4$ with Different Morphologies. The equilibrium quantity of cationic brush-type polyelectrolyte adsorption on oppositely charged surfaces of $GdPO_4$ particles with three different morphologies (nanorods, hexagonal nanoprisms, and submicrospheres) was evaluated by measuring zeta potential values of particles treated with 200 mg/g polymers (low, medium, and high charge density). For this purpose, nanoparticles which were used for these measurements were washed three times by centrifuging and redispersing them in Milli-Q water employing ultrasonic treatment (Table 3).

https://dx.doi.org/10.1021/acs.langmuir.0c01130
Langmuir 2020, 36, 7533−7544

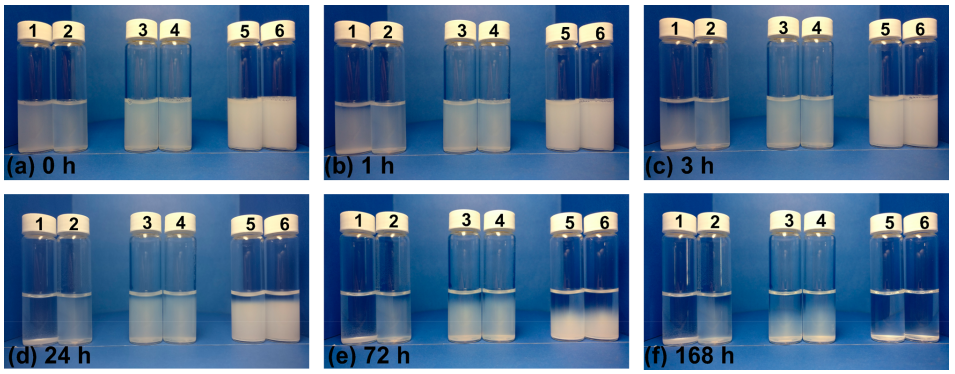

Figure 7. Visual evaluation of the aqueous dispersion stability (pH 6.5) of $GdPO_4$ particles with different morphologies ((nanorods (**1** bare, **2** modified), hexagonal nanoprisms (**3** bare, **4** modified), and submicrospheres (**5** bare, **6** modified)) over time: (a) 0, (b) 1, (c) 3, (d) 24, (e) 72, and (f) 168 h.

The results presented in Table 3 suggest that the equilibrium adsorption (independent of that of the used polymers) on $GdPO_4$ nanorods is higher in comparison to that of particles with other morphologies (hexagonal nanoprisms and submicrospheres). For example, the equilibrium adsorption of low-charge-density p(METAC-*stat*-PEO_{19}MEMA) on $GdPO_4$ nanorods is 39.2 mg/g if compared to 23.0 and 8.7 mg/g on hexagonal nanoprisms and submicrospheres, respectively. It can be explained through the particle size because it is well known that the surface area of particles is inversely proportional to the particle size, meaning that $GdPO_4$ nanorods are the smallest particles used in this study (Figure 1). To support this claim, nitrogen gas adsorption using the BET (Brunauer–Emmett–Teller) technique was conducted. During this analysis, the surface area was determined to be 47 m^2/g for nanorods, 24 m^2/g for hexagonal nanoprisms, and 20 m^2/g for submicrospheres.

Surface Potential and Colloidal Stability of Modified $GdPO_4$ Particles with Different Morphologies. Stable aqueous $GdPO_4$ particle dispersions (1 mg/mL) of each morphology were prepared by using dry $GdPO_4$ particles, which previously were washed and dried. The pH values of prepared $GdPO_4$ dispersions were then adjusted from ~2 to 10.6 using 0.1 M HNO_3 and NH_4OH solutions, respectively. The zeta potential and particle size distribution were measured at different pH values for all $GdPO_4$ particle morphologies and are presented in Figure 6.

The IEPs of particles determined independently of the $GdPO_4$ particle morphology are shifted to the alkaline pH region. The p(METAC-*stat*-PEO_{19}MEMA) containing the largest number of charged groups (67 mol %) affected the IEP of the studied particles the most noticeably. For example, the IEPs of $GdPO_4$ nanorods modified with low- and medium-charge polymers were 7.23 and 8.65, respectively, whereas the IEP of nanorods stabilized with high-charge p(METAC-*stat*-PEO_{19}MEMA) was shifted to highly alkaline pH values (>11). The IEPs of $GdPO_4$ hexagonal nanoprisms were 6.99, 8.51, and ~10.60 for particles modified using p(METAC-*stat*-PEO_{19}MEMA) with low, medium, and high charge densities, respectively. In the case of $GdPO_4$ submicrospheres, IEPs were determined to be 6.61, 7.96, and 8.98, respectively.

After $GdPO_4$ particle modification using cationic brush-type p(METAC-*stat*-PEO_{19}MEMA) polymers with different compositions, the stability range of $GdPO_4$ dispersions was expanded. It is important to notice that good stability is observed in the biological range (pH 6.6–7.4). The best results for the stabilization of $GdPO_4$ particles was achieved for rod-like particles. For comparison, bare $GdPO_4$ nanorods (IEP 6.53) were extremely unstable in the pH range from 4.2 to 9.1 (Figure 3b). Hence, after stabilization with polyelectrolytes, nanorods demonstrate perfect stability in the pH range from 2 up to 5.6, 7.2, and 8.3 using low-, medium- and high-charge polymers, respectively. The study of $GdPO_4$ particle stabilization with particles with other morphologies (hexagonal nanoprisms and submicrospheres) produced comparable results, which also suggest greatly increased colloidal stability (Figure 6).

The results obtained during this research imply that the most suitable investigated polymer for the stabilization of $GdPO_4$ particles tends to be the cationic brush-type p(METAC-*stat*-PEO_{19}MEMA) polyelectrolyte with the highest density of positively charged quaternary ammonium groups in its composition (65 mol %). The observed increase in $GdPO_4$ particle stability after surface modification was achieved as a combination of both steric and electrostatic stabilization because polymer-coated particles tend to possess positive surface charge, which provides additional electrostatic repulsion forces among modified particles. Therefore, this surface charge additionally enhances the particle stability.

Nanoparticles are often claimed to be potential candidates for biomedical (nanoprobes) and anticounterfeiting (security ink) applications. Low toxicity and good biocompatibility are highly desired properties for such nanoparticle systems, whereas superior colloidal stability is an absolute necessity.[60−63]

Long-Term Empirical Stability Experiment of Modified $GdPO_4$ Particles with Different Morphologies. One of the most remarkable results of this study is that after a relatively simple nanoparticle surface modification they can be easily redispersed from the dry powder and still form stable colloids. This, however, was not the case for the uncoated nanoparticles. Both nanoparticle preparation and their surface modification procedures are rather quick, easy, and simple and, most importantly, exhibit nearly perfect reproducibility, what is

https://dx.doi.org/10.1021/acs.langmuir.0c01130
Langmuir 2020, 36, 7533−7544

crucial for scientific and commercial applications. It is also very important to notice that $GdPO_4$ particle surface modification using the p(METAC-*stat*-PEO_{19}MEMA) polyelectrolyte not only enhances the particle stability but also improves its biocompatibility.[64] Hence, we believe that the results achieved during this research may are important to the scientific community working in the field of nanoscience and colloid chemistry and could be applied in commercial applications.

In order to support our previous statement regarding nanoparticle stability and redispersibility, an additional experiment was planned and conducted. The main objective of this experiment was to evaluate the colloidal stability and redispersibility of both bare and modified nanoparticles. For this purpose, aqueous colloids (six colloids in total) were prepared using bare $GdPO_4$ nanoparticles with different morphologies (nanorods, hexagonal nanoprisms, and submicrospheres) and $GdPO_4$ particles (same morphology) modified with a high-charge-density (65 mol % quaternary ammonium groups) p(METAC-*stat*-PEO_{19}MEMA) polyelectrolyte. First, in order to evaluate the initial dispersibility, particles were redispersed from the dry state in neutral aqueous media (pH 6.5). It was noticed immediately that bare $GdPO_4$ nanorods, whose isoelectric point value is close to neutral pH values (Figure 3a), were redispersed considerably slower than $GdPO_4$ nanorods with modified surfaces. This observation was documented and can clearly be seen in a video (SI video). In a vial on the left-hand side there are bare $GdPO_4$ nanorods that were dried, whereas in a vial on the right-hand side there are the same $GdPO_4$ nanorods whose surfaces were modified with the polyelectrolyte. After the shaking of both vials, the bare $GdPO_4$ nanorods precipitate readily, while the surface-modified particles are disperses into the water and remain stable.

Another experiment involved the observation of $GdPO_4$ colloidal suspension stability in a time frame of up to 168 h (1 week). For this purpose, aqueous colloids of $GdPO_4$ particles (both bare and modified) with different morphologies were prepared and documented over the given time. Visual colloidal stability over time is represented in Figure 7. All samples were redispersed by treating the colloids in an ultrasonic bath for 5 min.

It is important to notice that differently shaped $GdPO_4$ nanoparticles possess different zeta potential values at the same pH value. This means that in the same aqueous media (for example, during this experiment) they also have to have different zeta-potential values. This is because the isoelectric point (and therefore the zeta potential value) is dependent on the particle morphology, as discussed above. During this experiment (in which the pH of aqueous media was set to 6.5), zeta potential values of bare $GdPO_4$ nanoparticles were +0.56, −9.0, and −18.6 mV for nanorods, hexagonal nanoprisms, and submicrospheres, respectively. Meanwhile, identical aqueous colloids (pH 6.5) were prepared by dispersing $GdPO_4$ particles modified with the high-charge-density p(METAC-*stat*-PEO_{19}MEMA) polyelectrolyte. Zeta potential values of such colloids were ca. +22 mV for all morphologies identical to those presented in Figure 6a−c. Because modified $GdPO_4$ particles of all morphologies have almost identical zeta potential values, it is possible to additionally evaluate the effectiveness of cationic brush-type polymers as a function of the shape of the modified particles. It is known that due to the electrostatic repulsion forces even insignificant nanoparticle surface charge could affect the overall stability of such particle colloids. Therefore, according to Figure 3b, bare $GdPO_4$ hexagonal nanoprisms and submicrospheres should exhibit better colloidal stability during this experiment in comparison to bare $GdPO_4$ nanorods.

No obvious visual difference between colloids of the same morphology was observed after ultrasonically redispersing both bare and modified $GdPO_4$ particles of various morphologies in aqueous media (pH 6.5) (Figure 7a). However, it should be noticed that the aqueous colloid of bare $GdPO_4$ nanorods (Figure 7a, **1**) was slightly hazier in comparison to the colloid obtained by redispersing modified $GdPO_4$ nanorods (Figure 7a, **2**). After 1 h (Figure 7b), a transparent layer developed and is observed in the upper part of the bare $GdPO_4$ nanorod colloids (Figure 7b, **1**). This indicates the sedimentation of bare $GdPO_4$ nanorods. This transparent layer broadens over time and becomes more highly expressed in images taken after 3 h (Figure 7c, **1**). In the case of $GdPO_4$ nanoprisms (**3** and **4**) and submicrospheres (**5** and **6**), no obvious differences between bare and modified aqueous colloids were observed in the time frame of up to 3 h (Figure 7c). Twenty-four hours after the beginning of the experiment, the sedimentation of bare $GdPO_4$ nanorods (Figure 7d, **1**) becomes even more evident, while modified $GdPO_4$ nanorod colloids show no signs of sedimentation (Figure 7d, **2**). Controversially, dispersions of both bare and modified $GdPO_4$ hexagonal nanoprisms (**3** and **4**) even after 24 h remain in the state of stable aqueous colloids (Figure 7d, **3** and **4**). Slight settling is observed for both bare and modified $GdPO_4$ submicrospheres (Figure 7d, **5** and **6**). Visual observations 72 h after the beginning of the experiment revealed that bare $GdPO_4$ nanorods have completely precipitated, whereas modified $GdPO_4$ nanorod colloids remained stable. Both bare and modified hexagonal nanoprism colloids show signs of sedimentation after 72 h of experiment, though modified prism settling is less expressed in comparison with that of bare prisms (Figure 7e, **3** and **4**). Regardless of modified or bare, particle-weight-related settling of submicrospheres continues 72 h after the start of the experiment (Figure 7e, **5** and **6**). By the end of the experiment (after 168 h), bare $GdPO_4$ nanorods (Figure 7f, **1**) were completely precipitated, whereas modified $GdPO_4$ nanorods were only slightly settled (Figure 7f, **2**) but were still in the state of stable aqueous colloids. Also, a more rapid sedimentation of bare hexagonal nanoprisms (Figure 7f, **3**) becomes more noticeable over time because after 168 h bare prisms were clearly more settled if compared to modified hexagonal nanoprisms (Figure 7f, **4**). The difference in the colloidal stability of bare and modified hexagonal nanoprisms could indicate the possible agglomeration of bare hexagonal nanoprisms. Both bare and modified $GdPO_4$ submicrospheres completely precipitated after 168 h (Figure 7f, **5** and Figure 7f, **6**). The reason for such sedimentation of submicrospheres could probably be related to the relatively large mass and dimensions (>100 nm) of $GdPO_4$ submicrospheres (if compared to those of $GdPO_4$ nanorods and hexagonal nanoprisms). We emphasize that it is not accurate to evaluate particle agglomeration only by judging the visually observed sedimentation of particles. Zeta potential values of both bare and modified submicrospheres in observed colloids are rather high (i.e., −18.6 and +22.7 mV, respectively). Such zeta potential values should be high enough to induce a strong enough electrostatic repulsion force to prevent submicrosphere agglomeration. So to conclude, this sedimentation is likely to be caused by gravity accompanied by the relatively large weight of $GdPO_4$ submicrospheres.

Until this moment, colloidal stability during this experiment was evaluated only visually. However, such an approach does not really tell us anything about the real scale of particle

https://dx.doi.org/10.1021/acs.langmuir.0c01130
Langmuir 2020, 36, 7533−7544

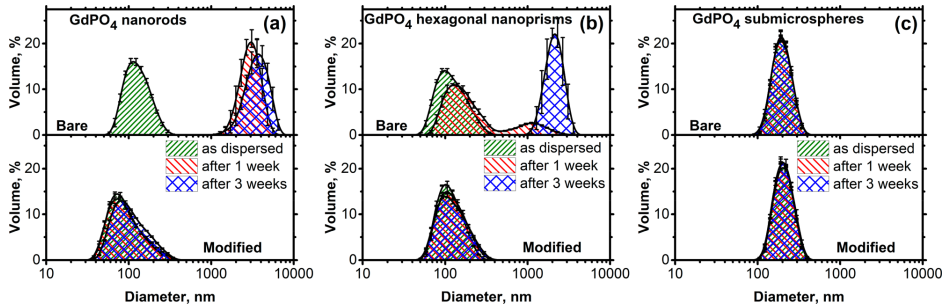

Figure 8. Particle size distribution in aqueous dispersions (pH 6.5) of $GdPO_4$ particles with different morphologies after different periods of storage (as dispersed, after 1 week and after 3 weeks): (a) nanorods, (b) hexagonal nanoprisms, and (c) submicrospheres.

agglomeration. In order to justify our claims and hypotheses derived from visual observations of $GdPO_4$ colloids during this experiment, dynamic light scattering measurements were conducted. After the visual experiment ended (colloids withstood 168 h), aqueous dispersions were prepared for DLS measurements by simply shaking $GdPO_4$ colloids for 20−30 s (no ultrasonic treatment was used). After that, DLS measurements were performed and the particle size distribution was determined (Figure 8). Additional DLS measurements were conducted again 3 weeks after the initial redispersion of particles.

DLS measurements revealed that after 168 h (1 week) bare $GdPO_4$ nanorods were in an agglomerated state (Figure 8a) with an agglomerate size varying around 2700 nm. Additional DLS measurements after 504 h (3 weeks) indicated the further agglomeration of bare $GdPO_4$ nanorods (Figure 8a), with the agglomerate size increasing up to around 3600 nm. Such a result was expected as bare $GdPO_4$ nanorods are close to their isoelectric point (ζ = +0.56 mV) in neutral media (pH 6.5). These particles are completely unstable and therefore are inapplicable in all intended applications. According to the DLS measurements, $GdPO_4$ nanorods modified with p(METAC-*stat*-PEO_{19}MEMA) cationic brush polyelectrolytes are perfectly stable, with a size of around 70 nm even after 3 weeks of storage. Contrary to bare $GdPO_4$ nanorods, $GdPO_4$ hexagonal nanoprisms have a slightly expressed negative zeta potential value of −9.0 mV at a pH value of 6.5. Such a zeta potential value is enough to inhibit the agglomeration of particles but not enough to ensure the overall colloidal stability of $GdPO_4$ hexagonal nanoprisms over extended periods of time. Complete agglomeration of bare $GdPO_4$ hexagonal nanoprisms, with the agglomerate size varying around 2300 nm, was observed 3 weeks after the initial redispersion (Figure 8b). Therefore, under the given conditions, hexagonal nanoprisms are more stable if compared to rod-like $GdPO_4$ nanoparticles, but their colloidal stability is still far from superior. PSD curves, obtained by volume means of DLS, show a bimodal distribution in aqueous colloids of bare $GdPO_4$ hexagonal nanoprisms after 1 week (Figure 8b). One peak representing particles of around 105 nm in size can be attributed to stable particles, and other peaks represent hexagonal nanoprism agglomerates of around 1100 nm in size. The PSD curve of bare hexagonal nanoprisms indicates complete agglomeration 3 weeks after the initial redispersion, with the agglomerate size varying around 2300 nm (Figure 8b). As expected, PSD curves of modified $GdPO_4$ nanoprisms (Figure 8b) show a monomodal distribution, indicating that no agglomeration processes occurred during the 3 weeks of the experiment.

Further DLS measurements revealed that even after 1 week of observation both bare and modified $GdPO_4$ submicrospheres were completely settled due to the relatively large values of the zeta potential (−18.6 and +22.7 mV for bare and modified particles, respectively), and these particles show no agglomeration. As seen in Figure 8c, PSD is monomodal with its maximum value at around 180 nm. DLS measurements indicated that no signs of agglomeration were observed even 3 weeks after the initial redispersion. Such results confirmed our hypothesis that the sedimentation of submicrospheres was induced only by a relatively large particle weight.

This work leads to the conclusion that the visual evaluation of nanoparticle colloidal stability, which is very typical in many papers, is not sufficient. Such visual stability evaluation in scientific papers and research is inappropriate and could even be referred to as incorrect. Indeed, if evaluated particles are observably unstable, as it was with bare $GdPO_4$ nanorods in our case, then it can be concluded that aqueous colloids are unstable, even though it takes time for visual sedimentation to occur. Meanwhile, if particles have relatively large surface charge (as with $GdPO_4$ submicrospheres in this work) but they sediment over time as well (as discussed above, the sedimentation of stable $GdPO_4$ submicrospheres occurred due to particle weight), then they can be wrongly considered to be agglomerates. Therefore, we strongly suggest that the colloidal stability of aqueous dispersions should be confirmed not only visually but also by means of light-scattering measurements (either dynamic or static).

Stability of $GdPO_4$ Particles in Biological Aqueous Media. One of the most remarkable features of this study is that the described concept of particle stabilization could be successfully applied in biological media. To prove this statement, an additional experiment was carried out by dispersing both bare and modified $GdPO_4$ in protein-rich aqueous media (consisting of 10 vol % human blood plasma, pH 6.5). First, particle dispersions were observed visually. It was noticed that bare particles, regardless their morphology (nanorods, hexagonal nanoprisms, or submicrospheres), have a greater tendency to sediment compared to modified particles. The visual stability observations are presented in Figure S4. The dry $GdPO_4$ powders (both bare and modified) were dispersed in protein-rich aqueous media and incubated for 3 h. Then the dispersion

https://dx.doi.org/10.1021/acs.langmuir.0c01130
Langmuir 2020, 36, 7533−7544

was centrifuged (10 000 rpm for 15 min) and particles were washed with DI water (procedure repeated three times) to remove the excess proteins. Washed particles were redispersed in water (pH 6.5), and the PSD of nanoparticle−protein conjugates was measured via DLS (Figure S5). The protein antifouling properties of modified particles were also evaluated by comparing the change in the zeta potential of particles incubated in protein-rich media with those dispersed in protein-free aqueous media (pH 6.5). The obtained results are presented in Figure 9.

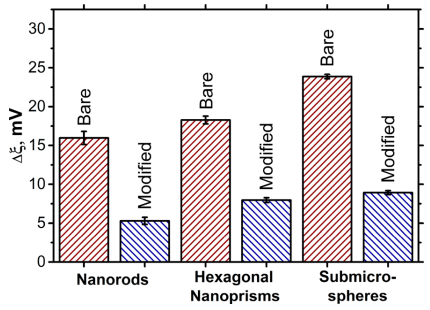

Figure 9. Change in the zeta potential of particles in protein-rich aqueous media (consisting of 10 vol % human blood plasma) compared to those dispersed in protein-free aqueous media (pH 6.5).

The smaller change in the zeta potential of modified $GdPO_4$ particles (more than twice regardless of the particle morphology) indicates that a smaller amount of proteins is adsorbed by (surrounds) the particles. Significant differences in the zeta potential change prove that PEG substituents existing on the surfaces of modified $GdPO_4$ particles provide antifouling properties and significantly reduce protein binding. Therefore, these results are in perfect correlation with the results obtained by measuring the PSD, where modified particle−polymer conjugates exhibited a smaller size if compared to bare particle−protein ones, which were nonstable and sedimented rapidly (Figure S5).

CONCLUSIONS

Cationic brush-type polyelectrolytes p(METAC-*stat*-PEO_{19}MEMA) with three different compositions were synthesized and applied with the aim of stabilizing aqueous dispersions of bare $GdPO_4$ particles (nanorods, hexagonal nanoprisms, and submicrospheres). Colloidal stability and zeta potential studies of bare $GdPO_4$ particles revealed that exhibited IEP values of $GdPO_4$ particles are dependent on their morphology and are 6.53, 6.03, and 5.61, for nanorods, hexagonal nanoprisms, and submicrospheres, respectively. Regardless of their morphology, particles had typical unstable zones if the absolute zeta potential is lower than |22| mV. Cationic brush-type p(METAC-*stat*-PEO_{19}MEMA) copolymers had a significant effect on the surface potential and overall stability of $GdPO_4$ particles. Apparently, the p(METAC-*stat*-PEO_{19}MEMA) polyelectrolytes with the largest number of charged groups (65 mol %) have the largest impact on the surface charge of $GdPO_4$ particles. During titrations using such polymers, the charge inversion effect was observed independently of the morphology of $GdPO_4$ particles used. The stability and zeta potential of modified $GdPO_4$ particle dispersions at different pH values were evaluated. The unstable zones of surface-modified $GdPO_4$ particles were narrowed, and the determined isoelectric point values were shifted to the alkaline region if compared to the bare particles. Highly charged p(METAC-*stat*-PEO_{19}MEMA) brush polyelectrolytes used to modify the surfaces of $GdPO_4$ particles enabled superior particle stability in the biological pH range, which could extend the applicability of such unique particles in the biotechnology field. Long-term stability measurements (DLS) indicated a monomodal PSD for all investigated modified $GdPO_4$ nanoparticles with no signs of agglomeration after 3 weeks from the initial redispersion. In the case of bare $GdPO_4$ nanoparticles, complete agglomeration is observed. The stability experiment in protein-rich aqueous media (consisting of 10 vol % human blood plasma) showed that PEG substituents on the surface of modified $GdPO_4$ particles provide antifouling properties that significantly reduce the formation of particle−protein conjugates.

We also point out that the most remarkable feature of the nanoparticle modification with the brush-type polyelectrolytes during this research is that such modified nanoparticles can be dried and later easily redispersed without any negative effects on the colloid stability. This approach has huge advantages in both scientific and commercial fields. For the former, it is much easier to prepare the desired nanoparticle concentration from the powder, whereas for the latter the handling, storage, and shipping of dry powders instead of diluted colloids are also much easier and more cost-effective. Moreover, particles whose surfaces are modified/covered with polymers containing PEO substituents tend to have reduced toxicity and improved biocompatibility.

ASSOCIATED CONTENT

Supporting Information

The Supporting Information is available free of charge at https://pubs.acs.org/doi/10.1021/acs.langmuir.0c01130.

Detailed $GdPO_4$ particle synthesis procedure; XRD patterns and SEC measurements; ^{1}H NMR spectra; and $GdPO_4$ particle stability in biological media: visual experiment and PSD curves (PDF)

Slow redispersion of bare $GdPO_4$ nanorods compared to that of $GdPO_4$ nanorods with a modified surface (MP4)

AUTHOR INFORMATION

Corresponding Author

Arturas Katelnikovas − *Institute of Chemistry, Vilnius University, LT-03225 Vilnius, Lithuania;* orcid.org/0000-0002-3295-8366; Email: arturas.katelnikovas@chf.vu.lt

Authors

Vaidas Klimkevicius − *Institute of Chemistry, Vilnius University, LT-03225 Vilnius, Lithuania*

Matas Janulevicius − *Institute of Chemistry, Vilnius University, LT-03225 Vilnius, Lithuania*

Aleksandra Babiceva − *Institute of Chemistry, Vilnius University, LT-03225 Vilnius, Lithuania*

Audrius Drabavicius − *Centre of Physical Science and Technology, LT-10257 Vilnius, Lithuania*

Complete contact information is available at: https://pubs.acs.org/10.1021/acs.langmuir.0c01130

Author Contributions

§V.K. and M.J. contributed equally.

Notes

The authors declare no competing financial interest.

■ ACKNOWLEDGMENTS

The Authors are indebted to Dr. Vitalijus Karabanovas (National Cancer Institute, Vilnius, Lithuania) for useful insights into particle stabilization in biological media. This project has received funding from the Research Council of Lithuania (LMTLT) (agreement no. S-MIP-17-48).

■ REFERENCES

(1) Talapin, D. V.; Shevchenko, E. V. Introduction: Nanoparticle Chemistry. *Chem. Rev.* **2016**, *116* (18), 10343−10345.
(2) Uglov, V. V.; Doroshevich, I. L.; Kvasov, N. T.; Remnev, G. E.; Shymanski, V. I. On Physical Properties of Nanoparticles: Size Effect and Scale of Nanoobjects. *Phys. status solidi c* **2016**, *13* (10−12), 903−907.
(3) Jeevanandam, J.; Barhoum, A.; Chan, Y. S.; Dufresne, A.; Danquah, M. K. Review on Nanoparticles and Nanostructured Materials: History, Sources, Toxicity and Regulations. *Beilstein J. Nanotechnol.* **2018**, *9*, 1050−1074.
(4) Mourdikoudis, S.; Pallares, R. M.; Thanh, N. T. K. Characterization Techniques for Nanoparticles: Comparison and Complementarity upon Studying Nanoparticle Properties. *Nanoscale* **2018**, *10* (27), 12871−12934.
(5) Teo, R. D.; Termini, J.; Gray, H. B. Lanthanides: Applications in Cancer Diagnosis and Therapy. *J. Med. Chem.* **2016**, *59* (13), 6012−6024.
(6) Björnmalm, M.; Thurecht, K. J.; Michael, M.; Scott, A. M.; Caruso, F. Bridging Bio-Nano Science and Cancer Nanomedicine. *ACS Nano* **2017**, *11* (10), 9594−9613.
(7) Cassano, D.; Pocoví-Martínez, S.; Voliani, V. Ultrasmall-in-Nano Approach: Enabling the Translation of Metal Nanomaterials to Clinics. *Bioconjugate Chem.* **2018**, *29* (1), 4−16.
(8) Levchenko, I.; Xu, S.; Teel, G.; Mariotti, D.; Walker, M. L. R.; Keidar, M. Recent Progress and Perspectives of Space Electric Propulsion Systems Based on Smart Nanomaterials. *Nat. Commun.* **2018**, *9* (1), 879.
(9) Giraldo, J. P.; Wu, H.; Newkirk, G. M.; Kruss, S. Nanobiotechnology Approaches for Engineering Smart Plant Sensors. *Nat. Nanotechnol.* **2019**, *14* (6), 541−553.
(10) Graf, C.; Gao, Q.; Schütz, I.; Noufele, C. N.; Ruan, W.; Posselt, U.; Korotianskiy, E.; Nordmeyer, D.; Rancan, F.; Hadam, S.; Vogt, A.; Lademann, J.; Haucke, V.; Rühl, E. Surface Functionalization of Silica Nanoparticles Supports Colloidal Stability in Physiological Media and Facilitates Internalization in Cells. *Langmuir* **2012**, *28* (20), 7598−7613.
(11) Fang, C.; Bhattarai, N.; Sun, C.; Zhang, M. Functionalized Nanoparticles with Long-Term Stability in Biological Media. *Small* **2009**, *5* (14), 1637−1641.
(12) Marins, J. A.; Montagnon, T.; Ezzaier, H.; Hurel, C.; Sandre, O.; Baltrunas, D.; Mazeika, K.; Petrov, A.; Kuzhir, P. Colloidal Stability of Aqueous Suspensions of Polymer-Coated Iron Oxide Nanorods: Implications for Biomedical Applications. *ACS Appl. Nano Mater.* **2018**, *1* (12), 6760−6772.
(13) Doblas, D.; Kister, T.; Cano-Bonilla, M.; González-García, L.; Kraus, T. Colloidal Solubility and Agglomeration of Apolar Nanoparticles in Different Solvents. *Nano Lett.* **2019**, *19* (8), 5246−5252.
(14) Phan, H. T.; Haes, A. J. What Does Nanoparticle Stability Mean? *J. Phys. Chem. C* **2019**, *123* (27), 16495−16507.
(15) Zhong, C.; Yang, P.; Li, X.; Li, C.; Wang, D.; Gai, S.; Lin, J. Monodisperse Bifunctional Fe_3O_4@$NaGdF_4$:Yb/Er@$NaGdF_4$: Yb/Er Core-Shell Nanoparticles. *RSC Adv.* **2012**, *2* (8), 3194−3197.
(16) Tian, J.; Zhang, F.; Han, Y.; Zhao, X.; Chen, C.; Zhang, C.; Jia, G. Template-Directed Synthesis, Properties, and Dual-Modal Bioapplications of Multifunctional $GdPO_4$ Hierarchical Hollow Spheres. *Appl. Surf. Sci.* **2019**, *475*, 264−272.
(17) Zhu, G.; Chen, L.; Zeng, F.; Gu, L.; Yu, X.; Li, X.; Jiang, J.; Guo, G.; Cao, J.; Tang, K.; Zhu, H.; Daldrup-Link, H. E.; Wu, M. $GdVO_4$:Eu^{3+}, Bi^{3+} Nanoparticles as a Contrast Agent for MRI and Luminescence Bioimaging. *ACS Omega* **2019**, *4* (14), 15806−15814.
(18) Kuang, X.; Liu, H.; Hu, W.; Shao, Y. Hydrothermal Synthesis of Core-Shell Structured $TbPO_4$:Ce^{3+}@$TbPO_4$:Gd^{3+} Nanocomposites for Magnetic Resonance and Optical Imaging. *Dalt. Trans.* **2014**, *43* (32), 12321−12328.
(19) Gai, S.; Li, C.; Yang, P.; Lin, J. Recent Progress in Rare Earth Micro/Nanocrystals: Soft Chemical Synthesis, Luminescent Properties, and Biomedical Applications. *Chem. Rev.* **2014**, *114* (4), 2343−2389.
(20) Bouzigues, C.; Gacoin, T.; Alexandrou, A. Biological Applications of Rare-Earth Based Nanoparticles. *ACS Nano* **2011**, *5* (11), 8488−8505.
(21) Cao, Y.; Xu, L.; Kuang, Y.; Xiong, D.; Pei, R. Gadolinium-Based Nanoscale MRI Contrast Agents for Tumor Imaging. *J. Mater. Chem. B* **2017**, *5* (19), 3431−3461.
(22) Jeong, Y.; Hwang, H. S.; Na, K. Theranostics and Contrast Agents for Magnetic Resonance Imaging. *Biomater. Res.* **2018**, *22*, 20.
(23) Xu, J.; Shen, X.; Jia, L.; Ge, Z.; Zhou, D.; Yang, Y.; Ma, T.; Luo, Y.; Zhu, T. $GdPO_4$-Based Nanoprobe for Bioimaging and Selective Recognition of Dipicolinic Acid and Cysteine by a Sensing Ensemble Approach. *ACS Biomater. Sci. Eng.* **2019**, *5* (2), 996−1004.
(24) Yan, Z.-G.; Yan, C.-H. Controlled Synthesis of Rare Earth Nanostructures. *J. Mater. Chem.* **2008**, *18* (42), 5046−5059.
(25) Yin, S.; Akita, S.; Shinozaki, M.; Li, R.; Sato, T. Synthesis and Morphological Control of Rare Earth Oxide Nanoparticles by Solvothermal Reaction. *J. Mater. Sci.* **2008**, *43* (7), 2234−2239.
(26) Rostami, I.; Rezvani Alanagh, H.; Hu, Z.; Shahmoradian, S. H. Breakthroughs in Medicine and Bioimaging with Up-Conversion Nanoparticles. *Int. J. Nanomed.* **2019**, *14*, 7759−7780.
(27) Wen, S.; Zhou, J.; Zheng, K.; Bednarkiewicz, A.; Liu, X.; Jin, D. Advances in Highly Doped Upconversion Nanoparticles. *Nat. Commun.* **2018**, *9* (1), 2415.
(28) Smith, B. R.; Gambhir, S. S. Nanomaterials for In Vivo Imaging. *Chem. Rev.* **2017**, *117* (3), 901−986.
(29) Cao, P.; Tong, L.; Hou, Y.; Zhao, G.; Guerin, G.; Winnik, M. A.; Nitz, M. Improving Lanthanide Nanocrystal Colloidal Stability in Competitive Aqueous Buffer Solutions Using Multivalent PEG-Phosphonate Ligands. *Langmuir* **2012**, *28* (35), 12861−12870.
(30) Boyer, J.-C.; Cuccia, L. A.; Capobianco, J. A. Synthesis of Colloidal Upconverting $NaYF_4$: Er^{3+}/Yb^{3+} and Tm^{3+}/Yb^{3+} Monodisperse Nanocrystals. *Nano Lett.* **2007**, *7* (3), 847−852.
(31) Abel, K. A.; Boyer, J.-C.; Veggel, F. C. J. M. van. Hard Proof of the $NaYF_4$/$NaGdF_4$ Nanocrystal Core/Shell Structure. *J. Am. Chem. Soc.* **2009**, *131* (41), 14644−14645.
(32) Liang, S.; Zhang, X.; Wu, Z.; Liu, Y.; Zhang, H.; Sun, H.; Sun, H.; Yang, B. Decoration of Up-Converting $NaYF_4$:Yb, Er(Tm) Nanoparticles with Surfactant Bilayer. A Versatile Strategy to Perform Oil-to-Water Phase Transfer and Subsequently Surface Silication. *CrystEngComm* **2012**, *14* (10), 3484−3489.
(33) Sedlmeier, A.; Gorris, H. H. Surface Modification and Characterization of Photon-Upconverting Nanoparticles for Bioanalytical Applications. *Chem. Soc. Rev.* **2015**, *44* (6), 1526−1560.
(34) Becerro, A. I.; Rodríguez-Liviano, S.; Fernández-Carrión, A. J.; Ocaña, M. A Novel 3D Architecture of $GdPO_4$ Nanophosphors: Multicolored and White Light Emission. *Cryst. Growth Des.* **2013**, *13* (2), 526−535.
(35) Achary, S. N.; Bevara, S.; Tyagi, A. K. Recent Progress on Synthesis and Structural Aspects of Rare-Earth Phosphates. *Coord. Chem. Rev.* **2017**, *340*, 266−297.
(36) Lai, H.; Bao, A.; Yang, Y.; Tao, Y.; Yang, H. Selective Synthesis and Luminescence Property of Monazite- and Hexagonal-Type $LaPO_4$:Eu Nanocrystals. *CrystEngComm* **2009**, *11* (6), 1109−1113.
(37) Patra, C. R.; Alexandra, G.; Patra, S.; Jacob, D. S.; Gedanken, A.; Landau, A.; Gofer, Y. Microwave Approach for the Synthesis of

Rhabdophane-Type Lanthanide Orthophosphate (Ln = La, Ce, Nd, Sm, Eu, Gd and Tb) Nanorods under Solvothermal Conditions. *New J. Chem.* **2005**, *29* (5), 733−739.
(38) Tsuda, A.; Venkata, N. K. The Role of Natural Processes and Surface Energy of Inhaled Engineered Nanoparticles on Aggregation and Corona Formation. *Nano Impact* **2016**, *2*, 38−44.
(39) Hifumi, H.; Yamaoka, S.; Tanimoto, A.; Citterio, D.; Suzuki, K. Gadolinium-Based Hybrid Nanoparticles as a Positive MR Contrast Agent. *J. Am. Chem. Soc.* **2006**, *128* (47), 15090−15091.
(40) Sahu, N. K.; Shanta Singh, N.; Ningthoujam, R. S.; Bahadur, D. Ce^{3+}-Sensitized $GdPO_4$:Tb^{3+} Nanorods: An Investigation on Energy Transfer, Luminescence Switching, and Quantum Yield. *ACS Photonics* **2014**, *1* (4), 337−346.
(41) Ren, W.; Tian, G.; Zhou, L.; Yin, W.; Yan, L.; Jin, S.; Zu, Y.; Li, S.; Gu, Z.; Zhao, Y. Lanthanide Ion-Doped $GdPO_4$ Nanorods with Dual-Modal Bio-Optical and Magnetic Resonance Imaging Properties. *Nanoscale* **2012**, *4* (12), 3754−3760.
(42) Yan, R.; Sun, X.; Wang, X.; Peng, Q.; Li, Y. Crystal Structures, Anisotropic Growth, and Optical Properties: Controlled Synthesis of Lanthanide Orthophosphate One-Dimensional Nanomaterials. *Chem. - Eur. J.* **2005**, *11* (7), 2183−2195.
(43) Yi, Z.; Lu, W.; Qian, C.; Zeng, T.; Yin, L.; Wang, H.; Rao, L.; Liu, H.; Zeng, S. Urchin-like Ce/Tb Co-Doped $GdPO_4$ Hollow Spheres for in Vivo Luminescence/X-Ray Bioimaging and Drug Delivery. *Biomater. Sci.* **2014**, *2* (10), 1404−1411.
(44) Xu, Z.; Cao, Y.; Li, C.; Ma, P.; Zhai, X.; Huang, S.; Kang, X.; Shang, M.; Yang, D.; Dai, Y.; Lin, J. Urchin-like $GdPO_4$ and $GdPO_4$:Eu^{3+} Hollow Spheres - Hydrothermal Synthesis, Luminescence and Drug-Delivery Properties. *J. Mater. Chem.* **2011**, *21* (11), 3686−3694.
(45) Rodriguez-Liviano, S.; Becerro, A. I.; Alcántara, D.; Grazú, V.; de la Fuente, J. M.; Ocaña, M. Synthesis and Properties of Multifunctional Tetragonal Eu:$GdPO_4$ Nanocubes for Optical and Magnetic Resonance Imaging Applications. *Inorg. Chem.* **2013**, *52* (2), 647−654.
(46) Janulevicius, M.; Klimkevicius, V.; Vanetsev, A.; Plausinaitiene, V.; Sakirzanovas, S.; Katelnikovas, A. Controlled Hydrothermal Synthesis, Morphological Design and Colloidal Stability of $GdPO_4$·nH2O Particles. *Mater. Today Commun.* **2020**, *23*, 100934.
(47) Singh, K.; Raghav, A.; Jha, P. K.; Satapathi, S. Effect of Size and Charge Asymmetry on Aggregation Kinetics of Oppositely Charged Nanoparticles. *Sci. Rep.* **2019**, *9* (1), 3762.
(48) Mohrhusen, L.; Osmić, M. Sterical Ligand Stabilization of Nanocrystals versus Electrostatic Shielding by Ionic Compounds: A Principle Model Study with TEM and XPS. *RSC Adv.* **2017**, *7* (21), 12897−12907.
(49) Moore, T. L.; Rodriguez-Lorenzo, L.; Hirsch, V.; Balog, S.; Urban, D.; Jud, C.; Rothen-Rutishauser, B.; Lattuada, M.; Petri-Fink, A. Nanoparticle Colloidal Stability in Cell Culture Media and Impact on Cellular Interactions. *Chem. Soc. Rev.* **2015**, *44* (17), 6287−6305.
(50) Heijman, S. G. J.; Stein, H. N. Electrostatic and Sterical Stabilization of TiO_2 Dispersions. *Langmuir* **1995**, *11* (2), 422−427.
(51) Klimkevicius, V.; Graule, T.; Makuska, R. Effect of Structure of Cationic Comb Copolymers on Their Adsorption and Stabilization of Titania Nanoparticles. *Langmuir* **2015**, *31* (7), 2074−2083.
(52) Yang, J.; Deng, Y.; Wu, Q.; Zhou, J.; Bao, H.; Li, Q.; Zhang, F.; Li, F.; Tu, B.; Zhao, D. Mesoporous Silica Encapsulating Upconversion Luminescence Rare-Earth Fluoride Nanorods for Secondary Excitation. *Langmuir* **2010**, *26* (11), 8850−8856.
(53) Heuer-Jungemann, A.; Feliu, N.; Bakaimi, I.; Hamaly, M.; Alkilany, A.; Chakraborty, I.; Masood, A.; Casula, M. F.; Kostopoulou, A.; Oh, E.; Susumu, K.; Stewart, M. H.; Medintz, I. L.; Stratakis, E.; Parak, W. J.; Kanaras, A. G. The Role of Ligands in the Chemical Synthesis and Applications of Inorganic Nanoparticles. *Chem. Rev.* **2019**, *119* (8), 4819−4880.
(54) Ramos Guivar, J. A.; Sanches, E. A.; Magon, C. J.; Ramos Fernandes, E. G. Preparation and Characterization of Cetyltrimethylammonium Bromide (CTAB)-Stabilized Fe_3O_4 Nanoparticles for Electrochemistry Detection of Citric Acid. *J. Electroanal. Chem.* **2015**, *755*, 158−166.
(55) Baziulyte-Paulaviciene, D.; Traskina, N.; Vargalis, R.; Katelnikovas, A.; Sakirzanovas, S. Thermal Decomposition Synthesis of Er^{3+}-Activated $NaYbF_4$ Upconverting Microparticles for Optical Temperature Sensing. *J. Lumin.* **2019**, *215*, 116672.
(56) Ran, Q.; Qiao, M.; Liu, J.; Miao, C. SMA-g-MPEG Comb-like Polymer as a Dispersant for Al_2O_3 Suspensions. *Appl. Surf. Sci.* **2012**, *258* (7), 2447−2453.
(57) Rhodes, S. K.; Lambeth, R. H.; Gonzales, J.; Moore, J. S.; Lewis, J. A. Cationic Comb Polymer Superdispersants for Colloidal Silica Suspensions. *Langmuir* **2009**, *25* (12), 6787−6792.
(58) Klimkevicius, V.; Steponaviciute, M.; Makuska, R. Kinetics of RAFT Polymerization and Copolymerization of Vinyl Monomers by Size Exclusion Chromatography. *Eur. Polym. J.* **2020**, *122*, 109356.
(59) Karimi, Z.; Karimi, L.; Shokrollahi, H. Nano-Magnetic Particles Used in Biomedicine: Core and Coating Materials. *Mater. Sci. Eng., C* **2013**, *33* (5), 2465−2475.
(60) Albanese, A.; Chan, W. C. W. Effect of Gold Nanoparticle Aggregation on Cell Uptake and Toxicity. *ACS Nano* **2011**, *5* (7), 5478−5489.
(61) Wu, J.; Zhang, X.; Yao, T.; Li, J.; Zhang, H.; Yang, B. Improvement of the Stability of Colloidal Gold Superparticles by Polypyrrole Modification. *Langmuir* **2010**, *26* (11), 8751−8755.
(62) Sugumaran, P. J.; Liu, X.-L.; Herng, T. S.; Peng, E.; Ding, J. GO-Functionalized Large Magnetic Iron Oxide Nanoparticles with Enhanced Colloidal Stability and Hyperthermia Performance. *ACS Appl. Mater. Interfaces* **2019**, *11* (25), 22703−22713.
(63) Rivera Gil, P.; Oberdörster, G.; Elder, A.; Puntes, V.; Parak, W. J. Correlating Physico-Chemical with Toxicological Properties of Nanoparticles: The Present and the Future. *ACS Nano* **2010**, *4* (10), 5527−5531.
(64) Suk, J. S.; Xu, Q.; Kim, N.; Hanes, J.; Ensign, L. M. PEGylation as a Strategy for Improving Nanoparticle-Based Drug and Gene Delivery. *Adv. Drug Delivery Rev.* **2016**, *99* (Pt A), 28−51.

3

Ultralight Magnetic Nanofibrous $GdPO_4$ Aerogel

Matas Janulevičius, Vaidas Klimkevičius, Lina Mikoliūnaitė, Bonifacas Vengalis, Rokas Vargalis, Simas Šakirzanovas, Valentina Plaušinaitienė, Albinas Žilinskas, Artūras Katelnikovas

ACS OMEGA

http://pubs.acs.org/journal/acsodf

Article

Ultralight Magnetic Nanofibrous $GdPO_4$ Aerogel

Matas Janulevicius, Vaidas Klimkevičius, Lina Mikoliunaite, Bonifacas Vengalis, Rokas Vargalis, Simas Sakirzanovas, Valentina Plausinaitiene, Albinas Zilinskas, and Arturas Katelnikovas*

Cite This: *ACS Omega* 2020, 5, 14180−14185

Read Online

ACCESS | Metrics & More | Article Recommendations | Supporting Information

ABSTRACT: Anisotropic aerogels are promising bulk materials with a porous 3D structure, best known for their large surface area, low density, and extremely low thermal conductivity. Herein, we report the synthesis and some properties of ultralight magnetic nanofibrous $GdPO_4$ aerogels. Our proposed $GdPO_4$ aerogel synthesis route is eco-friendly and does not require any harsh precursors or conditions. The most common route for magnetic aerogel preparation is the introduction of magnetic nanoparticles into the structure during the synthesis procedure. However, the nanofibrous $GdPO_4$ aerogel reported in this work is magnetic by itself already and no additives are required. The hydrogel used for nanofibrous $GdPO_4$ aerogel preparation was synthesized via a hydrothermal route. The hydrogel was freeze-dried and heat-treated to induce a phase transformation from the nonmagnetic trigonal to magnetic monoclinic phase. Density of the obtained magnetic nanofibrous monoclinic $GdPO_4$ aerogel is only ca. 8 mg/cm^3.

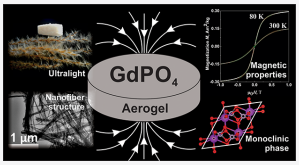

1. INTRODUCTION

An interest in synthesis and development of various rare-earth (RE)-based materials is consistently growing because of successful application of such materials in various high-tech and biomedical fields.[1−6] RE orthophosphates possess many beneficial features, such as high thermal (up to 2300 °C) and chemical stability, low solubility, and desirable optical properties [such as high refractive index (YPO_4 = 1.76, $LaPO_4$ = 1.85, and $GdPO_4$ = 1.97)].[7−9] Additionally, RE-based compounds are often referred as promising hosts for nuclear waste management.[10,11]

Aerogels are materials with a set of outstanding properties, such as extremely low density, large surface area, and low thermal conductivity. Despite a wide variety of materials that can be processed to very porous and low-density aerogel-like substances, there is still plenty room for specifically tailored and multifunctional systems. Aerogels can be prepared from a variety of different organic and inorganic substances, recent studies even report aerogels prepared from silver and gold.[12−14] Aerogel-based materials are considered for application in numerous fields ranging from tissue engineering and biosensing to catalysis and aerospace applications.[15−21] Introducing porosity in anisotropically structured magnetic materials would lead to the perfect supports for magnetic separations in biotechnology, environmental fields, or for magnetic field-assisted chemical reactions.[22−24] Typically, anisotropic aerogels are made from anisotropic particles (rods, fibers, wires, etc.), which are intertwined in all directions chaotically. The result of such chaotic interweaving of magnetic fibers is fully compensated overall magnetic momentum; therefore, magnetic properties of such an anisotropic aerogel would be significantly quenched.[25] Thus, obtaining a magnetic anisotropic aerogel as a homogeneous system with magnetic properties still remains an enormous challenge. Most of the recent papers report magnetic aerogels as composite materials, where magnetic properties are introduced by incorporating magnetic nanoparticles into an originally nonmagnetic aerogel matrix.[26−29]

RE elements, in turn, can be used to bring a whole new class of aerogels. RE elements would enable us to obtain homogeneous aerogel platforms with both magnetic and optical properties. Such materials could also be used in designing novel composite-based aerogels as templates. For example, Gd^{3+}-containing inorganic materials usually are magnetic because of the strong paramagnetic nature of Gd^{3+} ions.

Until now, there is only one scientific paper published on RE orthophosphate aerogels by Yorov et al., where the $CePO_4$ aerogel was successfully obtained and characterized.[30] However, the $CePO_4$ aerogel synthesis procedure, reported in this work, needed various organic solvents, was very time-consuming (more than 10 days), and required sophisticated supercritical drying in CO_2. Thus, the more environmentally friendly and time-effective synthesis route for RE phosphate aerogel preparation still needs to be developed. Additionally, to the best of our knowledge, there is no information describing synthesis or preparation of homogeneous anisotropically structured magnetic RE aerogels; therefore, such materials can be referred to as innovation.

Received: April 29, 2020
Accepted: May 21, 2020
Published: June 4, 2020

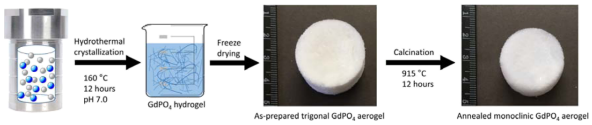

Figure 1. Preparation scheme for the as-prepared aerogel (trigonal phase) and annealed $GdPO_4$ aerogel (monoclinic phase).

The synthetic approach reported in this work can be applied to obtain various composite aerogels by simply incorporating different nanomaterials into the hydrogel, which further is used to produce aerogels. In such a way, gadolinium phosphate-based aerogels can be easily doped with other RE ions in order to tailor or enhance the desired properties.

In this work, we present the unique way for homogeneous fibrous magnetic $GdPO_4$ aerogel preparation. The method is simple, scalable, eco-friendly, and does not require any harsh precursors or conditions. The main characteristics of the synthesized nanofibrous $GdPO_4$ aerogel are also evaluated.

2. RESULTS AND DISCUSSION

The evolution of this research started by preparation of $GdPO_4$ nanoparticles with different morphologies via a hydrothermal synthesis route[31] at relatively high pH values and different Gd^{3+}/PO_4^{3-} ratios in the solution. Then, we observed that long and interwoven $GdPO_4$ nanofibers also can be obtained if pH of the synthesis solution is lowered to 7 and the Gd^{3+}/PO_4^{3-} ratio is fixed to 1 (Section S1 in the Supporting Information). Reducing the pH to 2 yields urchin-like microparticles, as shown in Figure S1a, whereas the increase in pH to 10 yields much shorter nanofibers (see Figure S1b); therefore, they cannot interweave sufficiently enough to form a hydrogel. The stirring should also be avoided because it breaks the delicate nanofibers (see Figure S1c). The synthesis at pH = 7 yielded a nearly transparent hydrogel with the final volume of 10 mL. We have also diluted this hydrogel to 20 and 30 mL before freeze-drying in order to check whether there is any influence to the aerogel formation. The best results were obtained for the 10 mL sample, where no anisotropic pore structures were detected. However, the samples with higher volume possessed the large anisotropic pores formed by ice crystals. This is supported by low-resolution scanning electron microscopy (SEM) images, as given in Figure S2. Moreover, if the samples were diluted to 30 mL, the aerogel structure collapsed during the freeze-drying procedure. The 10 mL volume hydrogel was washed and freeze-dried resulting in the "as-prepared" aerogel. Subsequently, this aerogel was annealed at 915 °C for 12 h in air in order to induce phase transformation from trigonal to monoclinic. The schematic representation of the synthesis process conducted to obtain $GdPO_4$ nanowires, hydrogel, and aerogel is provided in Figure 1.

Both, the as-prepared and annealed aerogels were investigated by powder X-ray diffraction (PXRD) to evaluate the phase composition and purity. The obtained XRD patterns for the as-prepared and annealed gadolinium phosphate aerogels are given in Figure 2a,b, respectively. XRD analysis reveals that the as-prepared $GdPO_4$ aerogel consists of the pure rhabdophane-type phase with the composition $GdPO_4{\cdot}nH_2O$, which has trigonal lattice symmetry with the space group $P3_121$ (#152) (Figure 2a). In the rhabdophane structure, Gd^{3+} ions are 8-coordinated with oxygen ions. The resulting

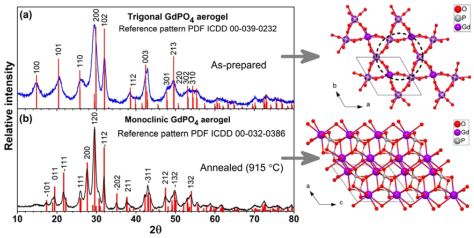

Figure 2. XRD patterns of the as-prepared (a) aerogel (trigonal phase) and annealed (b) $GdPO_4$ aerogel (monoclinic phase).

polyhedron, in turn, shares edges with four other GdO_8 polyhedrons and two PO_4 tetrahedra and vertexes with four PO_4 tetrahedrons. The visual representation of this building block is given in Figure S3. The lattice parameters of the as-prepared $GdPO_4$ aerogels were also calculated by applying the Le Bail method. The calculations yielded lattice parameters a = 0.6935 nm and c = 0.6349 nm, which are slightly larger than those reported in the reference structure $GdPO_4{\cdot}H_2O$, PDF ICDD 00-039-0232 (a = 0.69055 nm, c = 0.63257 nm).

One-dimensional growth of the rhabdophane structure is well-known.[32] Anisotropic particles (nanorods) of various RE orthophosphates are the result of such an anisotropic growth and are reported in numerous papers and is characteristic structural feature of such compounds.[32−34] The crystalline structure of the trigonal rhabdophane phase contains zeolitic channels (pointed out by the black dashed circle in Figure 2a), which accommodate crystalline water, yielding $GdPO_4{\cdot}nH_2O$ stoichiometry. Water molecules, accommodated in zeolitic channels, go along the crystalline structure of anisotropic particles (in our case—nanofibers) or to be more exact, along the c-axis of the $GdPO_4{\cdot}nH_2O$ structure.[31] This crystalline water is responsible for stabilization of the trigonal phase. Therefore, loss of this crystalline water results in phase transformation to monoclinic.[35]

The anisotropic nature of lanthanide orthophosphates can be related to their crystal structure. From the thermodynamic point of view, the activation energy of growth on the ab-plane is lower in comparison with other crystal planes (ac and bc), implying that the ab-plane is the preferable plane for growth.[8] Similarly, Wang et al.[32] explain that different chemical potentials on different crystalline planes are responsible for the anisotropic growth rhabdophane phase crystals. According to the Thompson−Gibbs theory, chemical potential is directly proportional to the number of dangling bonds on the particular crystal plane.[36] Because the ab-plane (perpendicular to the c-axis) has the largest number of dangling bonds, this plane is preferable for further growth.

Annealing the as-prepared $GdPO_4$ aerogel results in phase transformation from trigonal (rhabdophane) to monoclinic (monazite) with a space group $P2_1/n$ (#14). The XRD pattern

https://dx.doi.org/10.1021/acsomega.0c01980
ACS Omega 2020, 5, 14180−14185

shows that the pure $GdPO_4$ phase is obtained (see Figure 2b). In the monoclinic $GdPO_4$ structure, Gd^{3+} ions are nine-coordinated forming GdO_9 polyhedrons. Each GdO_9 polyhedron shares edges with six other GdO_9 polyhedrons and two PO_4 tetrahedra and vertexes with five PO_4 tetrahedrons.[37] The visual representation of this building block is given in Figure S4. Calculated lattice parameters for the annealed aerogel are as follows: a = 0.6334 nm, b = 0.6854 nm, c = 0.6664 nm, β = 104.1°, and are very similar to the ones provided in the ICCD database (PDF ICDD-00-032-0386 card) (a = 0.63342 nm, b = 0.68451 nm, c = 0.66525 nm, and β = 104.0°).

It is also necessary to mention that the monoclinic phase is more preferable as it possesses no crystalline water within its structure. The high content of crystalline water within the trigonal rhabdophane structure is known to quench luminescence emission significantly.[38,39] Therefore, such a monoclinic phase aerogel is much more suitable to be doped with RE ions to introduce luminescent properties. After annealing of the as-prepared aerogel at several temperatures, we found out that 915 °C is the highest temperature that the aerogel can withstand. Annealing at higher temperature resulted in collapse of the porous aerogel structure. Even samples annealed at 915 °C have already shown some signs of nanofiber melting, as demonstrated in transmission electron microscopy (TEM) images given in the Supporting Information Figure S5.

Furthermore, SEM and high-resolution TEM were used for morphological characterization of the as-prepared and annealed $GdPO_4$ aerogel samples. The obtained images are given in Figure 3. Several studies reported that during the annealing process at 900 °C temperature, when phase transformation occurs, anisotropic nanoparticles of trigonal $LnPO_4$ tend to deform and sinter badly.[38,40,41] This, however, is not true in our case, where virtually identical morphological features of both the as-prepared and annealed aerogel samples were observed. This can be evaluated from Figure 3. Both $GdPO_4$ aerogels are formed from high-aspect-ratio fibers; therefore, they can be regarded as anisotropic porous structures. High porosity of the structure ensures effective accessibility of the $GdPO_4$ aerogel surface throughout the entire volume. SEM images also revealed that $GdPO_4$ nanofibers within an aerogel structure were randomly woven together, forming a three-dimensional (3D) nanofibrous network. It is necessary to emphasize again that a nanofibrous $GdPO_4$ aerogel withstands the annealing process and phase transformation, while maintaining the original 3D structure undeformed and undamaged.

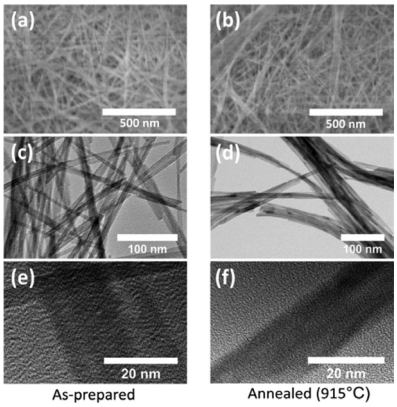

Figure 3. SEM and TEM images of the $GdPO_4$ aerogel: as-prepared trigonal (a,c,e) and annealed monoclinic (b,d,f).

The TEM images taken confirm the anisotropic nature of the nanofibrous structure of both the as-prepared and annealed $GdPO_4$ aerogels (see Figures 3c–f and S5). It is evident that fibers wider in diameter consist of axially agglomerated single crystalline nanofibers with a diameter ranging from 5 to 15 nm. TEM analysis of annealed samples has also confirmed that the annealing process causes significant changes in the morphology of nanofiber junctions—they become noticeably more agglomerated. Figure 3c demonstrates that prior to sintering, individual nanofibers were mostly separate throughout the junctions and contact areas. However, TEM images of the annealed aerogel (Figure 3d) show that nanofibers in contact places were more agglomerated and sintered, while in the as-prepared aerogel nanofibers were less affected by agglomeration. This is also supported by numerous TEM images given in Figure S6.

We have also evaluated the surface area and weight of the obtained $GdPO_4$ aerogels because these parameters are often referred to as the main characteristics defining aerogels. The as-prepared $GdPO_4$ aerogel had a density of around 10 mg/cm^3 and a specific surface area of around 29 m^2/g. On the contrary, the density of the annealed aerogel decreased even more, that is, to around 8 mg/cm^3, and the determined specific surface area was around 35 m^2/g. It is evident that the specific surface area of annealed $GdPO_4$ aerogels increases. Such an increase in the surface area is a result of crystalline water removal during the calcination step when the trigonal rhabdophane phase transforms to the monoclinic monazite phase. Because the total volume of the annealed aerogel virtually does not change, the weight loss results in the increased surface area.

Because the magnetic properties are the most interesting feature of the reported $GdPO_4$ aerogels, the magnetization measurements were performed in order to analyze magnetic behavior of the annealed $GdPO_4$ aerogel. Figure 4 shows magnetization versus applied field at T = 300 and 80 K of the sample containing randomly oriented fiber-like $GdPO_4$ nanocrystals. We point out the absence of any hysteresis either at

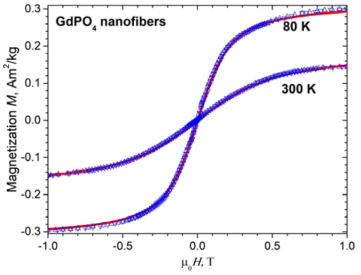

Figure 4. Mass magnetization vs magnetic field of the $GdPO_4$ nanotubes. Solid (red) lines show fitting of the experimental data by the Langevin function.

https://dx.doi.org/10.1021/acsomega.0c01980
ACS Omega 2020, 5, 14180−14185

300 or 80 K temperature. The observed nonlinear (S-shaped) magnetization curves have been fitted well using a standard Langevin function[42] that is usually used to describe magnetization of superparamagnetic (SPM) systems

$$M(H, T) = NmL\left(\frac{\mu_0 mH}{k_B T}\right) \quad (1)$$

where N is the number of magnetic nanoparticles in the sample, m is the averaged magnetic moment of a particle, k_B is the Boltzmann's constant, and $L(x)$ is the Langevin function: $L(x) = \coth(x) - 1/x$. The magnetic moment per nanoparticle of about 762 and 1190 Bohr magnetons at 300 and 80 K, respectively, was estimated in this work and corresponds to the best fitting of the magnetization curves with the Langevin function (see red solid curves in Figure 4). The observed nonlinear $M-H$ relation of the Langevin type and absence of hysteresis certify that the rod-like $GdPO_4$ nanofibers may be considered as a system of SPM particles. A similar nonlinear $M-H$ relation and absence of hysteresis both at RT and low temperatures have been reported earlier for the crystalline $GdPO_4$ material exhibiting the monoclinic crystalline structure and prepared in various forms, namely, polycrystals,[43] star-like nanocrystals,[44] and Tb- and Eu-doped nanotubes.[45,46] It is worth noting, however, that the room-temperature magnetization value, indicated in this work, is by factor 2−5 lower compared to those reported earlier. The observed magnetic properties of the nanotubes is a result of competing antiferromagnetic and ferromagnetic interaction of the paramagnetic Gd^{3+} ions with unpaired inner 4f electrons in the outer orbital in the monoclinic unit cell.[43] The reduced magnetization value at room temperature may probably be understood taking into account importance of the surface effects on magnetization of the nanocrystalline material and significant shape anisotropy of the rod-like nanocrystals.

3. CONCLUSIONS

In this work, we reported the synthesis and properties of the $GdPO_4$ aerogels composed of nanofiber-like crystals of a monoclinic phase, demonstrating chemical and thermal stability similar to that of a bulk material. Ultralight magnetic fibrous-structured $GdPO_4$ aerogels were prepared by a simple and eco-friendly aqueous hydrothermal synthesis method. The aerogel was produced by freeze-drying the hydrogel of $GdPO_4$ nanofibers, followed by a calcination step at 915 °C for 12 h. Various measurements were conducted to characterize the crystalline phase, structure, morphology, surface area, density, and magnetic properties. After the calcination step, the density of the aerogel decreased from ∼10 to ∼8 mg/cm^3. Morphological investigation revealed that both the as-prepared and annealed aerogels are highly anisotropic and possess a highly porous structure formed from the 3D network of overlapping $GdPO_4$ nanowires. The applied calcination step induced phase transformation from trigonal rhabdophane to monoclinic monazite.

One can expect that magnetic $GdPO_4$ aerogels (a promising platform for composite aerogels) are a very interesting class of novel materials because they offer magnetic properties, low density, and large surface area. These properties make $GdPO_4$ aerogels promising candidates in applications such as catalysts, nuclear waste management, electronic devices, neutron-absorbing materials, and so on.

We believe that fibrous, open-pore 3D-structured magnetic materials offer a flexible way for anisotropic texturing under a magnetic field. Magnetic RE orthophosphate-based aerogels offer a unique way for structuring because there is no need to introduce magnetic nanoparticles, leading to a homogeneous system. Finally, we enabled a relatively simple and fast route to obtain RE-based aerogels, which are yet emerging as a new class of materials.

4. METHODS

4.1. $GdPO_4$ Nanofiber Preparation. $GdPO_4$ nanofibers were prepared using an adopted procedure described in our previous publication with some minor adjustments.[31] The whole procedure in detail is provided in the Supporting Information Section S1. For the instrumental setup used for aerogel characterization, please see the Supporting Information Section S2.

4.2. $GdPO_4$ Aerogel Preparation. About 10 mL of the washed hydrogel was frozen in a freezer for 6 h at −24 °C. The frozen $GdPO_4$ hydrogel (containing $GdPO_4$ nanofibers) was then freeze-dried. As a result, a highly porous aerogel, composed of the 3D network of $GdPO_4$ nanofibers (with a diameter ranging from 5 to 15 nm), was obtained. This aerogel, hereafter, will be referred to as the "as-prepared". It should also be noted that the total volume of the as-prepared aerogel was virtually the same as the frozen $GdPO_4$ hydrogel, that is, ca. 10 mL. Finally, the as-prepared $GdPO_4$ aerogel was annealed at 915 °C for 12 h in order to induce phase transformation from trigonal to monoclinic.

■ ASSOCIATED CONTENT

Supporting Information

The Supporting Information is available free of charge at https://pubs.acs.org/doi/10.1021/acsomega.0c01980.

$GdPO_4$ nanofiber preparation; instrumental setup; SEM images of particles obtained under different pH values; SEM images of aerogels obtained from different volumes of the hydrogel; building block in the trigonal rhabdophane $GdPO_4 \cdot H_2O$ structure; building block in the monoclinic monazite $GdPO_4$ structure; and TEM images (PDF)

■ AUTHOR INFORMATION

Corresponding Author

Arturas Katelnikovas − *Institute of Chemistry, Vilnius University, 03225 Vilnius, Lithuania;* orcid.org/0000-0002-3295-8366; Email: arturas.katelnikovas@chf.vu.lt

Authors

Matas Janulevicius − *Institute of Chemistry, Vilnius University, 03225 Vilnius, Lithuania*

Vaidas Klimkevičius − *Institute of Chemistry, Vilnius University, 03225 Vilnius, Lithuania*

Lina Mikoliunaite − *Institute of Chemistry, Vilnius University, 03225 Vilnius, Lithuania; Center for Physical Sciences and Technology, 10223 Vilnius, Lithuania*

Bonifacas Vengalis − *Center for Physical Sciences and Technology, 10223 Vilnius, Lithuania*

Rokas Vargalis − *Institute of Chemistry, Vilnius University, 03225 Vilnius, Lithuania*

Simas Sakirzanovas − *Institute of Chemistry, Vilnius University, 03225 Vilnius, Lithuania*

Valentina Plausinaitiene − *Institute of Chemistry, Vilnius University, 03225 Vilnius, Lithuania*
Albinas Zilinskas − *Institute of Chemistry, Vilnius University, 03225 Vilnius, Lithuania*

Complete contact information is available at: https://pubs.acs.org/10.1021/acsomega.0c01980

Author Contributions

The manuscript was written through contributions of all authors. All authors have given approval to the final version of the manuscript.

Notes

The authors declare no competing financial interest.

■ ACKNOWLEDGMENTS

The authors gratefully thank Audrius Drabavicius for TEM imaging.

■ REFERENCES

(1) Huang, H.; Zhu, J.-J. The Electrochemical Applications of Rare Earth-Based Nanomaterials. *Analyst* **2019**, *144*, 6789−6811.
(2) Xu, C.; Qu, X. Cerium Oxide Nanoparticle: A Remarkably Versatile Rare Earth Nanomaterial for Biological Applications. *NPG Asia Mater.* **2014**, *6*, No. e90.
(3) Külah, E.; Marot, L.; Steiner, R.; Romanyuk, A.; Jung, T. A.; Wäckerlin, A.; Meyer, E. Surface Chemistry of Rare-Earth Oxide Surfaces at Ambient Conditions: Reactions with Water and Hydrocarbons. *Sci. Rep.* **2017**, *7*, 43369.
(4) Ignjatović, N. L.; Mančić, L.; Vuković, M.; Stojanović, Z.; Nikolić, M. G.; Škapin, S.; Jovanović, S.; Veselinović, L.; Uskoković, V.; Lazić, S.; et al. Rare-Earth (Gd^{3+},Yb^{3+}/Tm^{3+}, Eu^{3+}) Co-Doped Hydroxyapatite as Magnetic, up-Conversion and down-Conversion Materials for Multimodal Imaging. *Sci. Rep.* **2019**, *9*, 16305.
(5) Kong, T.; Zhang, C.; Gan, X.; Xiao, F.; Li, J.; Fu, Z.; Zhang, Z.; Zheng, H. Fast Transformation of a Rare-Earth Doped Luminescent Sub-Microcrystal via Plasmonic Nanoislands. *J. Mater. Chem. C* **2020**, *8*, 4338−4342.
(6) Sun, C.; Xue, D. Perspectives of Multiscale Rare Earth Crystal Materials. *CrystEngComm* **2019**, *21*, 1838−1852.
(7) Saltmarsh, N.; Kumar, G. A.; Kailasnath, M.; Shenoy, V.; Santhosh, C.; Sardar, D. K. Spectroscopic Characterizations of Er Doped $LaPO_4$ Submicron Phosphors Prepared by Homogeneous Precipitation Method. *Opt. Mater.* **2016**, *53*, 24−29.
(8) Fang, Y.-P.; Xu, A.-W.; Song, R.-Q.; Zhang, H.-X.; You, L.-P.; Yu, J. C.; Liu, H.-Q. Systematic Synthesis and Characterization of Single-Crystal Lanthanide Orthophosphate Nanowires. *J. Am. Chem. Soc.* **2003**, *125*, 16025−16034.
(9) Sun, C.; Xue, D. The Synergy Effect of Rare Earth Cations on Local Structure and PL Emission in a Ce^{3+}:$REPO_4$ (RE = La, Gd, Lu, Y) System. *Dalton Trans.* **2017**, *46*, 7888−7896.
(10) Terra, O.; Clavier, N.; Dacheux, N.; Podor, R. Preparation and Characterization of Lanthanum−Gadolinium Monazites as Ceramics for Radioactive Waste Storage. *New J. Chem.* **2003**, *27*, 957−967.
(11) Subramani, T.; Rafiuddin, M. R.; Shelyug, A.; Ushakov, S.; Mesbah, A.; Clavier, N.; Qin, D.; Szenknect, S.; Elkaim, E.; Dacheux, N.; et al. Synthesis, Crystal Structure, and Enthalpies of Formation of Churchite-Type $REPO_4{\cdot}2H_2O$ (RE = Gd to Lu) Materials. *Cryst. Growth Des.* **2019**, *19*, 4641−4649.
(12) Du, A.; Zhou, B.; Zhang, Z.; Shen, J. A Special Material or a New State of Matter: A Review and Reconsideration of the Aerogel. *Materials* **2013**, *6*, 941−968.
(13) Qian, F.; Troksa, A.; Fears, T. M.; Nielsen, M. H.; Nelson, A. J.; Baumann, T. F.; Kucheyev, S. O.; Han, T. Y.-J.; Bagge-Hansen, M. Gold Aerogel Monoliths with Tunable Ultralow Densities. *Nano Lett.* **2020**, *20*, 131−135.
(14) Qian, F.; Lan, P. C.; Freyman, M. C.; Chen, W.; Kou, T.; Olson, T. Y.; Zhu, C.; Worsley, M. A.; Duoss, E. B.; Spadaccini, C. M.; et al. Ultralight Conductive Silver Nanowire Aerogels. *Nano Lett.* **2017**, *17*, 7171−7176.
(15) Pierre, A. C.; Pajonk, G. M. Chemistry of Aerogels and Their Applications. *Chem. Rev.* **2002**, *102*, 4243−4266.
(16) Li, V. C.-F.; Dunn, C. K.; Zhang, Z.; Deng, Y.; Qi, H. J. Direct Ink Write (DIW) 3D Printed Cellulose Nanocrystal Aerogel Structures. *Sci. Rep.* **2017**, *7*, 8018.
(17) Maleki, H.; Shahbazi, M.-A.; Montes, S.; Hosseini, S. H.; Eskandari, M. R.; Zaunschirm, S.; Verwanger, T.; Mathur, S.; Milow, B.; Krammer, B.; et al. Mechanically Strong Silica-Silk Fibroin Bioaerogel: A Hybrid Scaffold with Ordered Honeycomb Micromorphology and Multiscale Porosity for Bone Regeneration. *ACS Appl. Mater. Interfaces* **2019**, *11*, 17256−17269.
(18) Power, M.; Hosticka, B.; Black, E.; Daitch, C.; Norris, P. Aerogels as Biosensors: Viral Particle Detection by Bacteria Immobilized on Large Pore Aerogel. *J. Non. Cryst. Solids* **2001**, *285*, 303−308.
(19) Gao, B.; Wang, I.-W.; Ren, L.; Hu, J. Catalytic Methane Decomposition over Bimetallic Transition Metals Supported on Composite Aerogel. *Energy Fuels* **2019**, *33*, 9099−9106.
(20) Li, K.; Luo, Q.; Xu, J.; Li, K.; Zhang, W.; Liu, L.; Ma, J.; Zhang, H. A Novel Freeze-Drying-Free Strategy to Fabricate a Biobased Tough Aerogel for Separation of Oil/Water Mixtures. *J. Agric. Food Chem.* **2020**, *68*, 3779−3785.
(21) Randall, J. P.; Meador, M. A. B.; Jana, S. C. Tailoring Mechanical Properties of Aerogels for Aerospace Applications. *ACS Appl. Mater. Interfaces* **2011**, *3*, 613−626.
(22) Maleki, H.; Durães, L.; Costa, B. F. O.; Santos, R. F.; Portugal, A. Design of Multifunctional Magnetic Hybrid Silica Aerogels with Improved Properties. *Microporous Mesoporous Mater.* **2016**, *232*, 227−237.
(23) Heiligtag, F. J.; Airaghi Leccardi, M. J. I.; Erdem, D.; Süess, M. J.; Niederberger, M. Anisotropically Structured Magnetic Aerogel Monoliths. *Nanoscale* **2014**, *6*, 13213−13221.
(24) Jung, S. M.; Preston, D. J.; Jung, H. Y.; Deng, Z.; Wang, E. N.; Kong, J. Porous Cu Nanowire Aerosponges from One-Step Assembly and Their Applications in Heat Dissipation. *Adv. Mater.* **2016**, *28*, 1413−1419.
(25) Shi, D.; He, P.; Lian, J.; Chaud, X.; Bud'ko, S. L.; Beaugnon, E.; Wang, L. M.; Ewing, R. C.; Tournier, R. Magnetic Alignment of Carbon Nanofibers in Polymer Composites and Anisotropy of Mechanical Properties. *J. Appl. Phys.* **2005**, *97*, 064312.
(26) Feng, T.; Ye, X.; Zhao, Y.; Zhao, Z.; Hou, S.; Liang, N.; Zhao, L. Magnetic Silica Aerogels with High Efficiency for Selective Adsorption of Pyrethroid Insecticides in Juices and Tea Beverages. *New J. Chem.* **2019**, *43*, 5159−5166.
(27) Li, Y.; Liu, Q.; Hess, A. J.; Mi, S.; Liu, X.; Chen, Z.; Xie, Y.; Smalyukh, I. I. Programmable Ultralight Magnets via Orientational Arrangement of Ferromagnetic Nanoparticles within Aerogel Hosts. *ACS Nano* **2019**, *13*, 13875−13883.
(28) Faivre, D. Dry but Flexible Magnetic Materials. *Nat. Nanotechnol.* **2010**, *5*, 562−563.
(29) Olsson, R. T.; Azizi Samir, M. A. S.; Salazar-Alvarez, G.; Belova, L.; Ström, V.; Berglund, L. A.; Ikkala, O.; Nogués, J.; Gedde, U. W. Making Flexible Magnetic Aerogels and Stiff Magnetic Nanopaper Using Cellulose Nanofibrils as Templates. *Nat. Nanotechnol.* **2010**, *5*, 584−588.
(30) Yorov, K. E.; Shekunova, T. O.; Baranchikov, A. E.; Kopitsa, G. P.; Almásy, L.; Skogareva, L. S.; Kozik, V. V.; Malkova, A. N.; Lermontov, S. A.; Ivanov, V. K. First Rare-Earth Phosphate Aerogel: Sol−Gel Synthesis of Monolithic Ceric Hydrogen Phosphate Aerogel. *J. Sol-Gel Sci. Technol.* **2018**, *85*, 574−584.
(31) Janulevicius, M.; Klimkevicius, V.; Vanetsev, A.; Plausinaitiene, V.; Sakirzanovas, S.; Katelnikovas, A. Controlled Hydrothermal Synthesis, Morphological Design and Colloidal Stability of $GdPO_4{\cdot}nH_2O$ Particles. *Mater. Today Commun.* **2020**, *23*, 100934.

(32) Wang, X.; Gao, M. A Facile Route for Preparing Rhabdophane Rare Earth Phosphate Nanorods. *J. Mater. Chem.* **2006**, *16*, 1360−1365.
(33) Yan, R.; Sun, X.; Wang, X.; Peng, Q.; Li, Y. Crystal Structures, Anisotropic Growth, and Optical Properties: Controlled Synthesis of Lanthanide Orthophosphate One-Dimensional Nanomaterials. *Chem.—Eur. J.* **2005**, *11*, 2183−2195.
(34) Wang, Z.; Shi, X.; Wang, X.; Zhu, Q.; Kim, B.-N.; Sun, X.; Li, J.-G. Breaking the Strong 1D Growth Habit to Yield Quasi-Equiaxed $REPO_4$ Nanocrystals (RE = La-Dy): Via Solvothermal Reaction and Investigation of Photoluminescence. *CrystEngComm* **2018**, *20*, 796−806.
(35) Yan, B.; Xiao, X. Hydrothermal Synthesis, Microstructure and Photoluminescence of Eu^{3+}-Doped Mixed Rare Earth Nano-Orthophosphates. *Nanoscale Res. Lett.* **2010**, *5*, 1962.
(36) Ding, M.; Chen, D.; Yin, S.; Ji, Z.; Zhong, J.; Ni, Y.; Lu, C.; Xu, Z. Simultaneous Morphology Manipulation and Upconversion Luminescence Enhancement of β-$NaYF_4$:Yb^{3+}/Er^{3+} Microcrystals by Simply Tuning the KF Dosage. *Sci. Rep.* **2015**, *5*, 12745.
(37) Heffernan, K. M.; Ross, N. L.; Spencer, E. C.; Boatner, L. A. The Structural Response of Gadolinium Phosphate to Pressure. *J. Solid State Chem.* **2016**, *241*, 180−186.
(38) Cho, J.; Kim, C. H. Solid-State Phase Transformation Mechanism from Hexagonal $GdPO_4$:Eu^{3+} Nanorods to Monoclinic Nanoparticles. *RSC Adv.* **2014**, *4*, 31385−31392.
(39) Zou, X.; He, L.; Tan, D.; Lei, F.; Jiang, N.; Zheng, Q.; Lin, D.; Xu, C.; Liu, Y. Anneal-Induced Transformation of Phase Structure, Morphology and Luminescence of $GdPO_4$:Sm^{3+} Nanomaterials Synthesized by a Hydrothermal Method. *Dalton Trans.* **2017**, *46*, 2948−2956.
(40) Wang, Z.; Li, J.-G.; Zhu, Q.; Ai, Z.; Li, X.; Sun, X.; Kim, B.-N.; Sakka, Y. EDTA-Assisted Phase Conversion Synthesis of $(Gd_{0.95}RE_{0.05})PO_4$ Nanowires (RE = Eu, Tb) and Investigation of Photoluminescence. *Sci. Technol. Adv. Mater.* **2017**, *18*, 447−457.
(41) Hernández, A. G.; Boyer, D.; Potdevin, A.; Chadeyron, G.; Murillo, A. G.; de J. Carrillo Romo, F.; Mahiou, R. Hydrothermal Synthesis of Lanthanide-Doped $GdPO_4$ Nanowires and Nanoparticles for Optical Applications. *Phys. Status Solidi A* **2014**, *211*, 498−503.
(42) Gschneidner, K. A., Jr.; Pecharsky, V. K.; Tsokol, A. O. Recent Developments in Magnetocaloric Materials. *Rep. Prog. Phys.* **2005**, *68*, 1479−1539.
(43) Wang, F. F. Y. Magnetic Susceptibilities of Gadolinium Orthophosphate ($GdPO_4$). *Phys. Status Solidi B* **1966**, *14*, 193−203.
(44) Kumar, G. A.; Balli, N. R.; Kailasnath, M.; Mimun, L. C.; Dannangoda, C.; Martirosyan, K. S.; Santhosh, C.; Sardar, D. K. Spectroscopic and Magnetic Properties of Neodymium Doped in $GdPO_4$ Sub-Micron-Stars Prepared by Solvothermal Method. *J. Alloys Compd.* **2016**, *672*, 668−673.
(45) Abécassis, B.; Lerouge, F.; Bouquet, F.; Kachbi, S.; Monteil, M.; Davidson, P. Aqueous Suspensions of $GdPO_4$ Nanorods: A Paramagnetic Mineral Liquid Crystal. *J. Phys. Chem. B* **2012**, *116*, 7590−7595.
(46) Du, Q.; Huang, Z.; Wu, Z.; Meng, X.; Yin, G.; Gao, F.; Wang, L. Facile Preparation and Bifunctional Imaging of Eu-Doped $GdPO_4$ Nanorods with MRI and Cellular Luminescence. *Dalton Trans.* **2015**, *44*, 3934−3940.

https://dx.doi.org/10.1021/acsomega.0c01980
ACS Omega 2020, 5, 14180−14185

NOTES

Vilniaus universiteto leidykla
Saulėtekio al. 9, III rūmai, LT-10222 Vilnius
El. p. info@leidykla.vu.lt, www.leidykla.vu.lt
Tiražas 33 egz.